

Stabilization of magnetic skyrmion bubbles and  
anomalous magneto-transport properties in  
centrosymmetric hexagonal magnets

*By*

Dola Chakrabartty

Enrolment No: PHYS11201704012

National Institute of Science Education and Research,  
Bhubaneswar

*A thesis submitted to the  
Board of Studies in Physical Sciences*

*In partial fulfillment of requirements  
for the Degree of*

DOCTOR OF PHILOSOPHY

*of*

HOMI BHABHA NATIONAL INSTITUTE



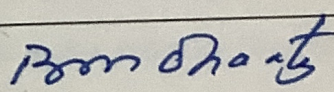
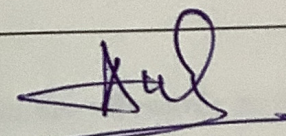
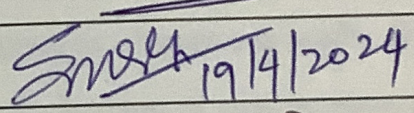
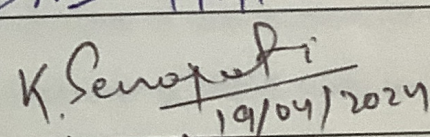
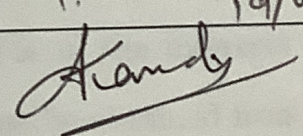
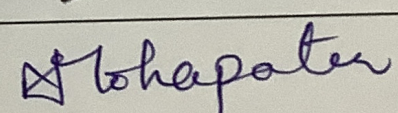
April, 2024



# Homi Bhabha National Institute

## Recommendations of the Viva Voce Committee

As members of the Viva Voce Committee, we certify that we have read the dissertation prepared by **Dola Chakrabartty** entitled "**Stabilization of magnetic skyrmion bubbles and anomalous magneto-transport properties in centrosymmetric hexagonal magnets**" and recommend that it may be accepted as fulfilling the thesis requirement for the award of Degree of Doctor of Philosophy.

Chairman - Prof. Bedangadas Mohanty		Date 19/4/2024
Guide/Convener - Dr. Ajaya K. Nayak		Date 19/04/2024
Examiner - Prof. K. G. Suresh		Date: 19/4/2024
Member 1- Dr. Kartikeswar Senapati		Date 19/04/2024
Member 2- Dr. Ashish Kumar Nandy		Date 19/04/2024
Member 3- Dr. Niharika Mohapatra		Date 19.04.2024

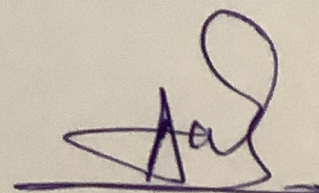
Final approval and acceptance of this thesis is contingent upon the candidate's submission of the final copies of the thesis to HBNI.

I/We hereby certify that I/we have read this thesis prepared under my/our direction and recommend that it may be accepted as fulfilling the thesis requirement.

Date: 19/04/2024

Place: NISER

Signature  
Co-guide(if applicable)



Signature  
Guide



CERTIFICATION ON ACADEMIC INTEGRITY

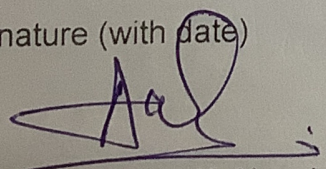
1. I Dola Chakrabartty (name of the student) HBNI Enrolment No. PHYS11201704012 hereby undertake that, the Thesis titled "***Stabilization of magnetic skyrmion bubbles and anomalous magneto-transport properties in centrosymmetric hexagonal magnets.***" (***bold & italics***) is prepared by me and is the original work undertaken by me and free of any plagiarism. That the document has been duly checked through a plagiarism detection tool and the document is plagiarism free.

2. I am aware and undertake that if plagiarism is detected in my thesis at any stage in future, suitable penalty will be imposed as per the applicable guidelines of the Institute / UGC.

*Dola Chakrabartty*  
19/04/2024  
Signature of the Student  
(With date)

Endorsed by the Thesis Supervisor:  
(I certify that the work done by the Researcher is plagiarism free)

Signature (with date)

  
Name: Dr. Ajaya K. Nayak

Designation: Associate Professor

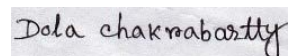
Department/ Centre: School of physical sciences

Name of the CI/ OCC: National institute of science Education and Research,  
Bhubaneswar

## STATEMENT BY AUTHOR

This dissertation has been submitted in partial fulfillment of requirements for an advanced degree at Homi Bhabha National Institute (HBNI) and is deposited in the Library to be made available to borrowers under rules of the HBNI.

Brief quotations from this dissertation are allowable without special permission, provided that accurate acknowledgement of source is made. Requests for permission for extended quotation from or reproduction of this manuscript in whole or in part may be granted by the Competent Authority of HBNI when in his or her judgment the proposed use of the material is in the interests of scholarship. In all other instances, however, permission must be obtained from the author.

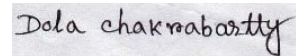
A handwritten signature in black ink on a light-colored background, reading "Dola chakrabartty".

Dola Chakrabartty



## DECLARATION

I, hereby declare that the investigation presented in the thesis has been carried out by me. The work is original and has not been submitted earlier as a whole or in part for a degree / diploma at this or any other Institution / University.

A handwritten signature in black ink on a light blue background, reading "Dola Chakrabartty".

Dola Chakrabartty

## List of Publications

### List of Publications arising from the thesis

- **Published**

1. “Tunable room temperature magnetic skyrmions in centrosymmetric kagome magnet  $\text{Mn}_4\text{Ga}_2\text{Sn}$ ”, **Dola Chakrabartty**, S. Jamaluddin, S. K. Manna, and A. K. Nayak, *Communications Physics*, **5**, 189 (2022).

**Author contribution:** Dola chakrabartty is the primary contributor who has prepared the sample, performed XRD measurement, magnetic measurements and LTEM measurements. She has analyzed the magnetic and LTEM data. She has performed micromagnetic simulations and contribute to the manuscript writing.

- **Communicated**

1. “Spin order dependent skyrmion stabilization in  $\text{MnFeCoGe}$  hexagonal magnets”, **Dola chakrabartty**, Mihir Sahoo, Amit Kumar, Sk Jamaluddin, Bimalesh Giri, Hitesh Chhabra, Kalpataru Pradhan and Ajaya. K. Nayak, arXiv preprint arXiv:2311.15823

**Author contribution:** Dola chakrabartty is the primary contributor who has prepared the sample, performed XRD measurement, magnetic measurements, EBSD and LTEM measurements. She also contribute to the TEM lamella preparation using focused ion beam. She has analyzed the powder neutron diffraction and LTEM data. She has performed micromagnetic simulations and contribute to the manuscript writing.

- **Manuscript under preparation**

1. “Anomalous magneto-transport properties due to inter-connected real and momentum space Berry curvature in skyrmion hosting kagome mag-



net  $\text{Mn}_4\text{Ga}_2\text{Sn}$ .”, **Dola chakrabartty**, Sk Jamaluddin and Ajaya. K. Nayak.

**Author contribution:** Dola chakrabartty is the primary contributor who has prepared the sample, performed XRD measurement, magnetic measurements. She also contribute to the device preparation using focused ion beam. She has made the connections using wire bonder and performed magneto-transport measurements and analyzed the data.

### Other publications

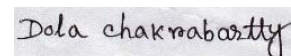
1. “ac susceptibility study of magnetic relaxation phenomena in the antiskyrmion-hosting tetragonal Mn-Pt(Pd)-Sn system. ”, P. V. P. Madduri, S. Sen, B. Giri, **Dola Chakrabartty**, S. K. Manna, S. S. P. Parkin, and A. K. Nayak, *Phys.Rev.B* **102**, 174402 (2020).
2. “Spontaneous interstitial (anti)merons in D2d symmetric Mn-Pt(Pd)SnIn system. ”, Bimalesh Giri, **Dola Chakrabartty**, S. S. P. Parkin and Ajaya K. Nayak, arXiv:2310.03427 (2023).
3. “Decoupling the topological antiskyrmion and non-topological phases in D2d symmetric Mn-Ni-Ga single crystalline device ”, Sk Jamaluddin, Subir Sen, **Dola Chakrabartty** and Ajaya K. Nayak, *Appl.Phys.Lett.* **123**, 19 (2023).

### Conferences and workshop

1. **Dola Chakrabartty**. Participated at “**International Conference on Magnetic Materials and Applications (ICMAGMA)-2018**”, National Institute of Science Education and Research (NISER), Bhubaneswar, India.
2. **Dola Chakrabartty**. Poster presented at “**Bringing The Nanoworld Together (BTNT)-2019**” conference, National Institute of Science Education

and Research (NISER), Bhubaneswar, India.

3. **Dola Chakrabartty.** Poster presented at “**Symposium on Magnetism and Spintronics (SMS 2021)**” conference, National Institute of Science Education and Research (NISER), Bhubaneswar, India.
4. **Dola Chakrabartty.** Oral presentation at “**Frontiers in Materials for Technological Applications (FIMTA-2022)**” conference, CSIR-Institute of Minerals and Materials Technology (IMMT), Bhubaneswar, India.
5. **Dola Chakrabartty.** Attended “**A Seven Day National Workshop cum Hands on Training program on Transmission Electron Microscopy**”, The University of Burdwan, University Science Instrumentation Centre (USIC), West Bengal, India.



Dola Chakrabartty



# DEDICATIONS

*The thesis is Dedicated to*

.....

My parents

Rajkumar Chakrabartty (Bapi) and Iva Chakrabartty (Ma)

My brother

Rajdeep Chakrabartty

## ACKNOWLEDGEMENTS

Firstly, I would like to thank my supervisor, Dr. Ajaya Kumar Nayak, for his continuous support and encouragement during my Ph.D. work. He permitted me to pursue independent research, which I greatly appreciate. I am grateful to him for his significant feedback and guidance in expanding my knowledge. I am also thankful for his critical suggestions to improve my thesis manuscript.

I want to thank Prof. Bedangadas Mohanty, chairman of my doctorate committee, for his continuous support and insightful recommendations that helped me improve my practical understanding. I am also thankful to Dr. Ashish Kumar Nandy and Dr. Kartikeswar Senapati, the members of my doctorate committee, for their continual assessment of my work. I would also like to thank Dr. Niharika Mohapatra of IIT Bhubaneswar for her comprehensive review of my work as an external member of the doctorate committee.

I would also like to thank our theoretical collaborators, Dr. Kalpataru Pradhan from SINP in India and Mihir Sahoo from RPTU Kaiserslautern-Landau in Kaiserslautern, Germany, for their ongoing cooperation and theoretical calculations to improve the visibility of our experimental results. I also want to thank our BARC collaborators, Amitabh Das sir and Amit Kumar sir, for recording the Neutron diffraction data.

I wish to thank the friends I met at NISER: Charanpreet Singh, Subir Sen, Rashmi Rekha Sahoo, Sk Jamaluddin, Bimalesh Giri, and Tanim Firdousi, for their support and help during my downtime. Special thanks go to Charanpreet, who, much like an elder brother, has consistently helped in every instance. I am also thankful to all my lab members for their help and support.

The Financial assistance provided by NISER during my Ph.D. tenure is gratefully acknowledged.

Finally, my heartfelt appreciation goes to my family, my parents, Rajkumar



Chakrabartty and Iva Chakrabartty, and my brother, Rajdeep Chakrabartty, for their unconditional love and selfless sacrifices. Their blessings, moral support, and unconditional dedication played a pivotal role in empowering me to undertake and complete my Ph.D. Additionally, I am grateful to my husband and best friend, Subir Sen, who stood by my side through the ups and downs, offering unwavering support no matter the circumstances.

# Contents

<b>Title page</b>	<b>i</b>
<b>Certificate of approval</b>	<b>ii</b>
<b>SUMMARY</b>	<b>xv</b>
<b>List of Figures</b>	<b>xxiv</b>
<b>1 Introduction</b>	<b>1</b>
1.1 Noncollinear magnetism . . . . .	3
1.2 Topology . . . . .	6
1.3 Topological aspects of noncollinear magnetic textures . . . . .	6
1.4 Magnetic skyrmions . . . . .	8
1.5 Magnetic Interactions . . . . .	12
1.5.1 Exchange interaction . . . . .	13
1.5.2 Magnetic anisotropy . . . . .	15
1.5.3 Dipole-dipole interaction . . . . .	18
1.5.4 Zeeman interaction . . . . .	19
1.6 Mechanisms of skyrmion stabilization . . . . .	19
1.7 Different degrees of freedom of skyrmion structures . . . . .	21
1.8 Skyrmions in centrosymmetric system . . . . .	22
1.9 Anomalous magneto-transport . . . . .	23
1.9.1 Anomalous Hall effect (AHE) . . . . .	25
1.9.2 Chiral anomaly . . . . .	30

1.9.3	Topological Hall effect (THE)	32
1.10	Important aspects of centrosymmetric hexagonal ferromagnets	34
<b>2</b>	<b>Experimental Techniques and Simulation Details</b>	<b>39</b>
2.1	Arc melting furnace	40
2.2	Scanning electron microscopy (SEM) and Energy dispersive X-ray spectroscopy (EDX)	41
2.3	Electron backscatter diffraction (EBSD)	44
2.4	X-ray diffraction (XRD)	46
2.5	Superconducting quantum interference device (SQUID)-Vibrating sample magnetometer (VSM)	48
2.6	Powder neutron diffraction (PND)	51
2.7	Physical property measurement system (PPMS)	53
2.7.1	Ac measurement system	54
2.7.2	Ac magneto-transport measurement	56
2.8	Transmission electron microscopy (TEM)	57
2.8.1	Selected area electron diffraction (SAED)	59
2.8.2	Lorentz transmission electron microscopy (LTEM)	62
2.9	TEM sample preparation technique	67
2.9.1	Focused ion beam (FIB)	67
2.10	Theoretical analysis	70
2.10.1	Micromagnetic simulations	70
2.10.2	Lorentz-TEM simulations	73
2.10.3	Transport of intensity equation (TIE) analysis	73
<b>3</b>	<b>Tunable magnetic skyrmions in a centrosymmetric kagome magnet <math>\text{Mn}_4\text{Ga}_2\text{Sn}</math></b>	<b>75</b>
3.1	Compositional homogeneity characterization of $\text{Mn}_4\text{Ga}_2\text{Sn}$	76
3.2	Structural characterization of $\text{Mn}_4\text{Ga}_2\text{Sn}$	78
3.3	Magnetic Properties of $\text{Mn}_4\text{Ga}_2\text{Sn}$	80
3.4	Real space observation of magnetic domains in $\text{Mn}_4\text{Ga}_2\text{Sn}$	82

3.4.1	Field evolution of magnetic domains at different temperatures	85
3.4.2	Magnetic states with zero sample tilting condition . . . . .	92
3.4.3	Controlled tuning/switching of magnetic spin textures at 250 K	94
3.4.4	Phase diagram . . . . .	97
3.5	Magnetocrystalline anisotropy in $\text{Mn}_4\text{Ga}_2\text{Sn}$ . . . . .	97
3.6	Micromagnetic simulation . . . . .	102
3.7	Discussion and conclusion . . . . .	107
<b>4</b>	<b>Magnetic-order dependent skyrmion stabilization in <math>\text{MnFeCoGe}</math> centrosymmetric hexagonal magnets</b>	<b>111</b>
4.1	Theoretical understanding . . . . .	113
4.2	Experimental results . . . . .	116
4.2.1	Compositional homogeneity characterization . . . . .	117
4.2.2	Structural characterization . . . . .	117
4.2.3	Magnetic characterization . . . . .	120
4.2.4	Magnetic ground states using powder neutron diffraction (PND) experiment . . . . .	124
4.2.5	Origin of easy-cone magnetic anisotropy for $\text{MnFe}_{0.2}\text{Co}_{0.8}\text{Ge}$ ( $x = 0.8$ ) . . . . .	137
4.2.6	Magnetic field dependent ac susceptibility measurements for $\text{MnFe}_{1-x}\text{Co}_x\text{Ge}$ . . . . .	141
4.2.7	Real space observation of magnetic domains in $\text{MnFe}_{1-x}\text{Co}_x\text{Ge}$ system . . . . .	141
4.3	Micromagnetic simulations for $\text{MnFe}_{1-x}\text{Co}_x\text{Ge}$ sample . . . . .	156
4.4	Discussion and conclusion . . . . .	158
<b>5</b>	<b>Anomalous magneto-transport properties due to inter-connected real and momentum space Berry curvature in the skyrmion hosting kagome magnet <math>\text{Mn}_4\text{Ga}_2\text{Sn}</math></b>	<b>163</b>
5.1	Magneto-transport measurements: . . . . .	165
5.1.1	Anomalous Hall effect: . . . . .	165



5.1.2	Magneto-resistance (MR) measurements: . . . . .	170
5.2	Discussion and conclusion: . . . . .	172
<b>6</b>	<b>Summary and Future prospective of the thesis</b>	<b>175</b>
6.1	Future outlook: . . . . .	180

## SUMMARY

Spintronics stands as one of the pivotal research domains, offering the promise of ushering in a new era of high-speed memory devices characterized by low power consumption. The most widely utilized data storage technologies in recent years are based on solid-state random access memory (RAMs) and magnetic hard disk drives (HDDs). Despite the cost-effectiveness of HDDs relative to RAMs, the principal drawback lies in their slower operational speed. Hence, it is our utmost priority to look for new memory devices that can be inexpensive, like HDDs, and have fast processing, like RAMs. In 2008, Parkin et al. proposed a new memory device based on domain wall motion, named racetrack memory (RM), where the controlled movement of domain walls with spin polarized current can be utilized to realize low-cost and efficient data storage technology. However, a significant hurdle emerged in the form of the high current density required for domain wall motion. In this direction, the recent discovery of magnetic skyrmions opens up a new horizon for their potential implementation in RM devices as an alternative to domain walls.

The magnetic skyrmions are topologically protected localized magnetic objects with swirling spin configurations. Their topological nature helps them to get depinned at low cut-off current density and avoid defects or pinning centers in their route. Magnetic skyrmions were first observed in B20 chiral magnet MnSi using a small angle neutron scattering (SANS) experiment, where their stabilization comes from the competing Dzyaloshinskii-Moriya interaction (DMI) and exchange interaction. Later, skyrmions with different topological numbers and helicity degrees of freedom are experimentally observed in a few uniaxial centrosymmetric magnets. In the latter case, the mechanism of skyrmion formation involves competing dipolar interaction and uniaxial magnetic anisotropy (UMA). The discovery of different types of topological spin textures in centrosymmetric systems adds a new direction

to these systems, as the observed spin textures with different vorticity and helicity may be used in multi-bit data storage devices where each bit contains more than one state and thus storing more information. This approach has the potential to broaden the concept of skyrmion-based racetrack memory devices. In addition, some recent publications suggest skyrmion's helicity degree of freedom as a potential approach to constructing quantum qubits for skyrmion-based quantum computations. Therefore, the fundamental goal of the present thesis is to find novel, skyrmion-hosting, centrosymmetric magnetic systems and explore their tunable physical properties in order to grasp their significance for application. Since the competition between dipolar energy and UMA acts as the primary mechanism for the stabilization of skyrmion in centrosymmetric magnets, the hexagonal centrosymmetric ferromagnets (FMs) with layered structures are potential candidates for skyrmion study. Although the skyrmion-like spin textures with different topologies are experimentally observed in some of the hexagonal magnets, in every instance, the size of the skyrmions at room temperature (RT) are larger than 200 nm. Therefore, the observation of nanometer sized skyrmions at or nearby RT in new hexagonal magnets might be a significant step forward for high-density data storage applications.

In the first part of the present thesis, a tunable skyrmion lattice with skyrmion size  $\approx 100$  nm is discovered near room temperature (RT) in a centrosymmetric kagome ferromagnet  $\text{Mn}_4\text{Ga}_2\text{Sn}$ . Polycrystalline samples of  $\text{Mn}_4\text{Ga}_2\text{Sn}$  are synthesized using an arc-melt furnace. The Rietveld refined RT powder X-ray diffraction (XRD) pattern confirms the hexagonal crystal structure ( $P6_3/mmc$ ) of  $\text{Mn}_4\text{Ga}_2\text{Sn}$ . From the temperature ( $T$ ) dependent magnetization ( $M$ ) measurement, it is observed that the sample exhibits a Curie temperature ( $T_c$ ) of 320 K and a spin reorientation transition (SRT) around 90 K. According to the earlier report, the magnetization of the sample rotates from the out-of-plane easy-axis configuration to an easy-plane configuration below the SRT. The field dependent magnetization

measurements on the sample reveal the presence of some transition anomaly in the sample above SRT. The field dependent ac susceptibility  $[\chi'(H)]$  of the system shows a typical ferromagnetic like behavior below the SRT, whereas the presence of peak/hump like anomalies are found above the SRT. This kind of peak/hump like anomalies are previously identified in the majority of the skyrmion hosting systems. Therefore, the magnetic measurements on the sample indirectly suggest the presence of the skyrmion phase in the present system. For the real space observation of magnetic textures, Lorentz transmission electron microscopy (LTEM) imaging is utilized. LTEM works based on the Lorentz force on the electrons due to the field from magnetic textures. Thin lamellae of approximately 100 nm thickness are prepared for the LTEM measurements using a  $\text{Ga}^+$  ion-based focused ion beam (FIB) technique. Prior to lamellae preparation, the desired oriented grain of the sample is selected using the Electron Back Scattered Diffraction (EBSD) technique. The  $c$ -orientation of the lamellae is confirmed using selected area electron diffraction (SAED). A very little magnetic contrast is seen at room temperature since the sample's  $T_c$  is near RT. Therefore, a double tilt Gatan cooling holder (GATAN-636) is used to cool down the sample to 100 K. A stripe domain of average periodicity of 100 nm is observed as a magnetic ground state (GS) at 100 K, and with increasing magnetic field, the stripe domains break into small bubble domains. The bubble domains contain alternative black and white half circles. To know the exact nature of the magnetic texture, a transport of intensity equation (TIE) analysis is carried out. The analysis clearly shows that the observed magnetic textures are type-II bubbles with zero topological number. With increasing temperature to 200 K and 250 K, a few different magnetic contrasts with black and white circular rings are observed. The magnetic contrasts are recognized as clockwise and counter-clockwise skyrmions with topological number 1. Here, the lack of DMI causes the stabilization of skyrmions with both helicities. While comparing the spin textures stabilized



at different temperatures, it is found that the number of skyrmions for an applied magnetic field increases with increasing temperature and reaches its maximum at 250 K. This observation demonstrates that the skyrmion stability is significantly influenced by the temperature-varying parameters. There is a one-to-one correlation between the effective uniaxial anisotropy and the measured skyrmion number, with both showing their maximum around 250 K. It is important to mention here that to avoid the bending contours, the LTEM images are usually taken by slightly tilting the sample. When the sample is tilted, the applied magnetic field has two components, one along the out-of-plane of the sample plate and the other in the sample plane. The sample is tilted almost three degrees for each of the LTEM images that are previously mentioned. Therefore, to know whether the present in-plane magnetic field affects our LTEM observation, the LTEM images are collected at almost zero sample tilting conditions. Although low density isolated skyrmions are found at 100 K and 200 K with field along the zone-axis, the significant bending contour, in this case, makes it difficult to convey the results accurately. The bending contour effect is significantly less at 250 K, and it is shown that when the magnetic field is increased to 0.3 T, the stripe domains split into a deformed hexagonal skyrmion lattice. This observation suggests that the skyrmions are in a stable state when a magnetic field is applied along the  $c$ -axis. Isolated skyrmions are seen when the magnetic field strength increases to 0.4 T. While reducing the field from saturation, the skyrmions stay in a remnant condition at zero magnetic field. To comprehend the role of an in-plane magnetic field on the stabilization of the observed magnetic spin textures, the LTEM experiments are performed under controlled tilting conditions. The experiment shows that the skyrmions are in a stable state with zero sample tilting, i.e., zero in-plane magnetic field, but the type-II bubble state appears as a metastable state in the presence of finite sample tilting from the zone axis or finite in-plane magnetic field. When the sample tilting direction is changed, the type-II

bubble spin textures align with the in-plane field directions. When the in-plane magnetic field is removed, the Type-II bubbles return to a stable state of skyrmions. All these observations suggest that the in-plane magnetic field acts as the deciding factor for the internal structure of the Type-II bubbles. The role of effective uniaxial magnetic anisotropy strength in determining the energy barrier between skyrmion and type-II bubble in a collinear ferromagnetic system is also demonstrated.

In part one tunability of skyrmions in a collinear centrosymmetric ferromagnetic systems is discussed in terms of external parameters such as magnetic field. The second part is dedicated to comprehending the stability and tunability of skyrmions concerning the internal energy parameters of a material. In this direction, a detailed study on the stabilization of the skyrmion phase is carried out in a series of non-collinear FM compounds  $\text{MnFe}_{1-x}\text{Co}_x\text{Ge}$ . According to the literature,  $\text{MnFeGe}$  shows an exchange frustration driven noncollinear FM ground state with an FM component along the  $c$ -direction and an AFM component along the in-plane direction. On the other hand,  $\text{MnCoGe}$  exhibits a collinear FM ground state. It is also theoretically shown that the strength of the underlying interactions can be modified by varying the inter-atomic distances of Mn along the  $c$  direction in  $\text{MnFeGe}$ . Therefore, the series of compound  $\text{MnFe}_{1-x}\text{Co}_x\text{Ge}$  is a potential choice to successfully control the magnetic ground state as well as the underlying interaction. Polycrystalline samples of  $\text{MnFe}_{1-x}\text{Co}_x\text{Ge}$  are prepared using the arc-melt furnace, and the RT powder XRD confirms the hexagonal crystal structure ( $\text{P6}_3/\text{mmc}$ ) of the samples. The  $M(T)$  measurements on the samples show an increase in  $T_c$  with increasing Co concentration ( $x$ ). Field dependent magnetization measurements [ $M(H)$ ] for the samples show that the saturation magnetization ( $M_s$ ) of the samples increases with increasing  $x$ . To verify the change in magnetic ground states with changing  $x$  and  $T$ , powder neutron diffraction (PND) experiments are performed on two of the samples with  $x = 0.4$  (Fe rich) and  $x = 0.8$  (Co rich). The appearance of the magnetic

reflection indexed (001) for the sample  $x = 0.4$  below 200 K signifies the presence of an in-plane AFM component in the sample, as also previously reported in the case of MnFeGe. Rietveld refinements of the data at different temperatures show that the  $x = 0.4$  sample exhibits a noncollinear-FM ground state with an FM component along the  $c$ -axis and an in-plane AFM component. From the refinement, it is also observed that the in-plane AFM component gradually decreases with increasing temperature and becomes zero nearby ordering temperature. Powder ND results for  $x = 0.8$  sample below  $T_c$  show the presence of nuclear reflections only, signifying the presence of a collinear FM ground state. Whereas careful observation of powder ND data reveals the increasing intensity of (002) and (102) reflections with decreasing temperature below 200 K. Rietveld refinement reveals the existence of an easy-cone phase for  $x = 0.8$  sample at or below 100 K with a magnetization tilting angle of  $25^\circ \pm 5^\circ$ . The change in magnetic ground state is also verified by the magnetic measurements, which show a transition around 125 K. For the real space observation, FIB lamellae of the samples  $x = 0.4, 0.5, 0.6, 0.8$  are prepared. The  $c$ -orientations of all the lamellae are confirmed using the SAED pattern. LTEM measurements for the  $x = 0.4$  sample show the presence of in-plane domain walls as a zero field state at 100 K due to a strong in-plane AFM component, i.e., stronger in-plane anisotropy ( $K_u^\parallel$ ) component. At 150 K, the superposition of stripe domain patterns with the in-plane domain patterns are observed. With increasing magnetic fields, the stripe domains start to vanish, and finally, a field polarized state is achieved without any skyrmion phase. LTEM measurements for  $x = 0.5, 0.6$  samples show the presence of a very few number of skyrmions along with the larger number of type-II bubbles with field applied along the  $c$ -axis. Comparing the  $M$  vs.  $T$  curves and DFT calculations, it is expected that the  $x = 0.5, 0.6$  samples also host noncollinear magnetic ground state, with a smaller expected canting angle than the  $x = 0.4$  sample. Therefore, in the noncollinear magnets depending on the ratio of  $K_u^\parallel$  and out-of-plane anisotropy

component ( $K_u^\perp$ ), the magnetic ground state can change from the in-plane domain to the stripe domain. Applying a magnetic field along the  $c$ -axis type-II bubbles can also be generated from the stripe domains. However, due to the presence of finite  $K_u^\parallel$  components in non-collinear magnets, the type-II bubbles become more stable in the systems rather than skyrmions. The  $x = 0.8$  sample with the collinear magnetic ground state shows stripe domains as zero field magnetic states all over the temperature range. The stripe domains in the easy-cone phase look more arranged. With the application of a magnetic field along the  $c$ -axis, the hexagonal skyrmion lattice is observed as a stable state at 220 K (easy-axis FM), whereas, the easy-cone phase (100 K) shows the presence of type-II bubbles. In the easy cone phase, the sample exhibits a finite  $K_u^\parallel$  component, which makes the type-II bubbles more stable. On the other hand, the zero in-plane anisotropy at 220 K ensures skyrmions as a stable state. The micromagnetic simulations carried out by using the experimental parameters validate the experimental results and explanations. Therefore, all the above observations suggest that the presence of  $K_u^\parallel$  component always hinders the skyrmions' stability in the system.

In the third section, magneto-transport studies are performed on the skyrmion hosting kagome ferromagnet  $\text{Mn}_4\text{Ga}_2\text{Sn}$  to investigate the effect of the observed real space spin textures on electronic transport and to determine the existence of electronic band topology and its correlation with real space topological spin texture such as skyrmion. A few recent articles have theoretically predicted that the dynamics of skyrmions can be modified by the presence of momentum space topology, where the generated torque is proportional to the intrinsic band topology driven anomalous Hall conductivity (AHC). On the other hand, a few recent articles also predict that the presence of skyrmion like spin textures can also lead to electronic band rearrangement. Skyrmions are already detected in the sample  $\text{Mn}_4\text{Ga}_2\text{Sn}$ , as discussed in the first part. The present sample  $\text{Mn}_4\text{Ga}_2\text{Sn}$  with kagome structure is also a



viable candidate for hosting band topologies. Hence, The material could be a potential choice to find a correlation between the real space topology and momentum space topology. The easiest way to incorporate the electronic band topology is the magneto-transport measurements. Site specific Micron-sized devices of  $\text{Mn}_4\text{Ga}_2\text{Sn}$  sample are prepared using EBSD and FIB techniques. In the present case, the fitting of experimental data with the scaling relation of AHE shows the presence of a dominant intrinsic AHC contribution of  $667 \text{ ohm}^{-1}\text{cm}^{-1}$  at temperatures above SRT where the spins are out-of-plane, whereas, below SRT the dominant contribution appears extrinsic. The experimentally observed AHC of  $170 \text{ ohm}^{-1}\text{cm}^{-1}$  at 100 K (above SRT) signifies the presence of a non-negligible amount of opposing extrinsic contribution from sources other than band topology. However, the presence of dominant intrinsic AHC contribution in the skyrmion phase indicates that the current material could be a potential candidate to experimentally explore the effect of momentum space topology on the dynamics of real space topological spin textures, such as skyrmion. On the other hand, a chiral anomaly like behavior is also observed in the magneto-resistance data for the out-of-plane device ( $I \parallel ab$ ,  $H \parallel c$ ) at temperatures where skyrmion spin textures exist. On the other hand, in the in-plane device with  $I \parallel c$ ,  $H \parallel ab$ , without any skyrmion structure, no such effect is observed. This type of chiral-anomaly effect is usually found in materials having Weyl / Dirac nodes or band ant-crossing. Therefore, the present system can give very important and essential information to experimentally verify the predicted correlation between skyrmion (real space) and electronic band structure (momentum space).

In conclusion, a comprehensive study on the stability of skyrmions in centrosymmetric ferromagnets is presented in the present thesis. In the first part, a new skyrmion hosting kagome ferromagnet  $\text{Mn}_4\text{Ga}_2\text{Sn}$  is explored. The tunability of the skyrmion using an in-plane magnetic field in the particular system is also studied

---

at an optimal anisotropy. In the second part, the stability of the skyrmion phase is studied in a series of non-collinear ferromagnets  $\text{MnFe}_{1-x}\text{Co}_x\text{Ge}$ , and their tunability with respect to material specific parameters are discussed. In the last part, the magneto-transport studies are performed in skyrmion host  $\text{Mn}_4\text{Ga}_2\text{Sn}$  to explore a potential platform to experimentally verify the possible correlation between real space topology and momentum space electronic band structure.



# List of Figures

1.1	Schematic diagrams of domain wall and skyrmion based racetrack memory devices. . . . .	2
1.2	Schematic diagrams of different types of non-collinear magnetic states. (a) Helical spin texture, (b) cycloid spin texture, and (c) longitudinal conical spin texture. Green arrows represent the spin direction and $q$ represents the propagation direction of the spin textures. . . . .	4
1.3	Physical objects with different topological properties. The physical objects with different numbers of holes like (a) zero (b) one, and (c) two. . . . .	5
1.4	2D real space spin configuration and its mapping on order parameter space. . . . .	7
1.5	A skyrmion and its mapping on a unit sphere. The figure is taken from the reference [30]. . . . .	8
1.6	First observation of hexagonal skyrmion lattice in MnSi. Magnetic field ( $H$ ) versus temperature ( $T$ ) phase diagram along with six spot small angle neutron scattering pattern in the A-phase and the corresponding hexagonal skyrmion lattice. The figures are taken from reference [20]. . . . .	9



1.7	First real-space observation of hexagonal skyrmion lattice in FeCoSi. (a)-(c) The Lorentz transmission electron microscopy (LTEM) images of helical (H), skyrmion (SKX), and ferromagnetic phases. (d) Magnetic field ( $H$ ) vs. temperature ( $T$ ) phase diagram. The figures are taken from the reference [21]. . . . .	9
1.8	(a)-(c) Schematic representation of magnetic spin textures of Bloch skyrmion (a), Neel skyrmion (b), Antiskyrmion (c), biskyrmion (d), merons (e) and hedgehog (f). Figure in (f) is taken from the reference [48] . . . . .	11
1.9	Schematic representation of (a) Direction cosine of magnetization of the sample, and (b) easy cone magnetic state. . . . .	16
1.10	Magnetic spin textures with different helicity ( $\gamma$ ) and vorticity ( $n$ ). (a,d) Neel skyrmion, (b,c) Bloch skyrmion, and (e-h) Antiskyrmion. The arrows represent the direction of the in plane magnetization component. The cross and dot sign represent the downward and upward spin direction respectively. . . . .	21
1.11	Normal and anomalous Hall resistivity. The figure is taken from the reference [81]. . . . .	24
1.12	(a) Band structure of bulk Fe along with the calculated berry curvature [ $\Omega^z(k)$ ] near the Fermi level. The figure is taken from reference [84]. . . . .	25

- 1.13 (a) The calculated band structure for ferromagnetic Weyl semimetal  $\text{Co}_3\text{Sn}_2\text{S}_2$  along with the corresponding calculated anomalous Hall conductivity  $[\sigma_{xy}]$ . (b) The calculated Band structure of ferromagnetic nodal line semimetal  $\text{MnAlGe}$  along with its calculated anomalous Hall conductivity  $[\sigma_{xy}^A]$ . The right side figure shows the confirmation of band touching using angle resolved photo emission spectroscopy at 14 K. The figures are taken from references [89, 90]. . . . . 27
- 1.14 Schematic representation of the scattering dependent extrinsic Hall contributions (a) skew scattering, (b) side jump. Here,  $Q$  is the scattering potential. The figure is taken from reference [91] . . . . . 28
- 1.15 Three different regions of AHE with different scaling relation depending on different longitudinal conductivity ( $\sigma_{xx}$ ) of the system. The figure is taken from the reference [81]. . . . . 28
- 1.16 Negative MR due to chiral anomaly effect in weyl semimetal  $\text{Co}_3\text{Sn}_2\text{S}_2$ . (a) Schematic representation depicting the Chiral anomaly effect, (b) Angular dependence of MR at 2 K, and (c) Magneto-conductance (MC) at 2 K. The inset shows a quadratic dependence of positive MC with respect to the applied magnetic field ( $B$ ). The figure is taken from the reference [90]. . . . . 31
- 1.17 Chiral anomaly effect due to avoided band crossing in half-Heusler compound  $\text{TbPtBi}$ . (a) Field dependent longitudinal MR at different temperatures, (b) Angular dependence of MR at 2 K. The figure is taken from the reference [109]. . . . . 32
- 1.18 Schematic representation of (a) classical example of real space Berry curvature, (b) noncoplanar spin texture with scalar spin chirality ( $\Omega$ ), (c) skyrmion spin texture, while deflecting the conduction electron. Figures (a) and (b) are taken from the references [30, 81] . . . . . 33

1.19	(a) The total Hall signal and (b) extracted THE in Gd <sub>2</sub> PdSi <sub>3</sub> . Figures are taken from the reference [13]. . . . .	33
1.20	Schematic representation of atomic arrangement in hexagonal (a) kagome ferromagnet, and (b) triangular lattice ferromagnet. . . . .	35
1.21	Schematic representation of topological band structure present in some of the kagome ferromagnets such as Fe <sub>3</sub> Sn <sub>2</sub> , Co <sub>3</sub> Sn <sub>2</sub> S <sub>2</sub> . The idea of the figure is taken from references [90, 110]. . . . .	35
2.1	(a) Schematic representation of an Arc melting furnace. (b) Physical view of an Arc melting furnace. . . . .	40
2.2	Schematic representation of SEM column. . . . .	42
2.3	Schematic representation of various interactions, possible between sample and primary electron beam. . . . .	42
2.4	Comparison between the SEM images and corresponding EDX patterns of two different samples having compositional double phase (a) and single phase (b). The images are taken with an SE detector at 20 keV energy. . . . .	43
2.5	Schematic representation of EBSD experiment. . . . .	45
2.6	Model orientation map for the MnFeCoGe sample. (a) SEM image, (b) inverse pole figure (IPF) EBSD mapping of the sample which shows different grains in different colors. (c) IPF color bar to evaluate the crystal orientation of the sample. (d) The crystal structure, the corresponding (110) plane, and the cutting direction are marked with a black rectangle. . . . .	45
2.7	Schematic of (a) characteristic X-ray production in an atom and (b) x-ray diffraction and Bragg's law. . . . .	47

2.8	Schematic diagram of SQUID detection technique. The picture is taken from Quantum Design MPMS3 user manual. For further references see <a href="https://qd-india.com">https://qd-india.com</a> . . . . .	49
2.9	(a) Sample mounting station for SQUID-VSM. (b) Physical view of Quantum Design SQUID-VSM. . . . .	50
2.10	Schematic representation of different magnetic states along with their corresponding possible neutron diffraction. The idea of the schematic is taken from the reference [118]. . . . .	52
2.11	Physical view of physical property measurement system (PPMS). . .	53
2.12	Schematic representation of ac measurement system (ACMS) coil. The picture is taken from the Quantum design website. For further references see <a href="https://qd-india.com">https://qd-india.com</a> . . . . .	54
2.13	Schematic diagram of (a) longitudinal and (b) Hall resistivity measurement setup. (c) The physical view of an ACT sample puck along with the sample. The connections are made using copper wire and indium soldering. . . . .	56
2.14	Schematic diagram of different parts of transmission electron microscopy (TEM). The idea of the image is taken from <a href="https://bitesizebio.com/29197/electron-microscopy-techniques">https://bitesizebio.com/29197/electron-microscopy-techniques</a> . . . . .	58
2.15	Schematic representation as well as real experimental images of two different measurement modes possible in TEM. (a) Imaging mode, (b) Diffraction mode. The idea of the schematic is taken from the reference [119]. . . . .	60
2.16	(a) A crystal lattice with lattice planes and (b) corresponding possible SAED pattern. (c) Schematic representation of the relation between different parameters for the indexing of diffraction spots. . . . .	61

2.17	Schematic ray diagram representation of electron beam and the images for LTEM in Fresnel mode. Black arrows in the sample specimen represent the moment direction in different magnetic domains. The arrows in the real experimental images point to the white line in under focused condition that turns to the black contrast in over-focused condition. The scale bars in experimental images represent 500 nm. The idea of the image is taken from [120] . . . . .	63
2.18	Schematic representation of electron beam deflection in LTEM by different types of skyrmions and the corresponding simulated as well as experimental real space LTEM images. (a) Neel skyrmion, (b-c) Bloch skyrmion, and (d) Anti-skyrmion. The maroon arrows represent the in plane component of spin texture and the black arrows represent the direction of electron deflection. The cross and dot sign represent the downward and upward spin direction. The picture of antiskyrmion are taken from the reference [44]. . . . .	64
2.19	External view of (a) TEM with model JEMF200, (b) double tilt beryllium cooling holder. . . . .	65
2.20	Schematic representation of FIB experiment. . . . .	67
2.21	Picture of a crossbeam dual column FIB/SEM system used for the TEM sample preparation. . . . .	68
2.22	Different steps of Lamella preparation for the sample $\text{Mn}_4\text{Ga}_2\text{Sn}$ using a FIB. The scale bars in each figure correspond to $5\ \mu\text{m}$ . . . . .	68
2.23	Schematic diagram of damping precession of magnetization according to the LLG equation. . . . .	71
3.1	Crystal structure of $\text{Mn}_4\text{Ga}_2\text{Sn}$ . (a) Unit cell, (b) Mn-Sn kagome layer, (c) Mn-Ga-Sn kagome layer. . . . .	77
3.2	SEM image of polycrystalline $\text{Mn}_4\text{Ga}_2\text{Sn}$ sample. . . . .	77

3.3	Fullprof fitted room temperature powder XRD pattern for $\text{Mn}_4\text{Ga}_2\text{Sn}$ sample. . . . .	78
3.4	(a) HRTEM image of the FIB lamella with $[001]$ orientation. The right inset shows the enlarged view of the reconstructed atomic arrangement after the inverse fast Fourier transformation (FFT) of the FFT of the actual image. The kagome structure formed with Mn atoms in the top Mn-Sn layer is marked with deep orange colored lines. The corresponding Mn-Sn kagome structure is shown in the left inset. The dark yellow balls represent the Mn atoms and the grey balls appear for the Sn atoms. (b) The SAED pattern of the FIB lamella with $[001]$ orientation. . . . .	79
3.5	Magnetic properties of $\text{Mn}_4\text{Ga}_2\text{Sn}$ sample. (a) Temperature dependent ZFC and FC data taken at a magnetic field of 0.5 kOe. The inset shows the temperature dependent first derivative ( $\frac{dM}{dT}$ ) of the FC $M$ vs $T$ curve. (b) Isothermal field dependent magnetization at various temperatures from 2.5 K to 300 K. The inset shows the first derivative of $M$ vs. $H$ data at selected temperatures with anomaly pointed by black arrows. . . . .	80
3.6	Magnetic field dependent ac susceptibility measurement of $\text{Mn}_4\text{Ga}_2\text{Sn}$ sample at different temperatures from 10 K to 300 K. (a) 10 K, (b) 100 K, (c) 200 K (d) 300 K. The black arrows mark the hump like anomalies. . . . .	81
3.7	Real space observation of magnetic domains for $\text{Mn}_4\text{Ga}_2\text{Sn}$ sample at room temperature. Zero field magnetic ground state in (a) under-focused, (b) in-focus, and (c) over-focused condition. The inset in Fig. (a) shows the intensity profile of the marked region. (d) Under-focused LTEM image for the sample at a magnetic field of 0.15 T. . .	83

- 3.8 Real space observation of magnetic ground states at 100 K for  $\text{Mn}_4\text{Ga}_2\text{Sn}$  sample at (a) in-focus, and (b) over-focused, condition. The inset shows the intensity profile. (c) The TIE reconstructed phase image of the magnetic domains. (d) The in-plane magnetization mapping of the domains constructed using the phase image. The color wheel in the inset of (d) represents the magnetization components at each point. . . . . 84
- 3.9 (a) Over-focused LTEM images for the  $\text{Mn}_4\text{Ga}_2\text{Sn}$  sample taken at  $T = 100$  K and field of 0.3 T. (b) The TIE field mapping of corresponding LTEM image. (c) Zoomed view of the LTEM images of the magnetic bubble structure, the TIE reconstructed phase image, and its magnetization mapping using TIE. (d) The LTEM simulated image corresponding to the type-II bubble constructed using PyLorentz code and its field mapping. The color wheel corresponds to the images shown in the insets. . . . . 86
- 3.10 Over-focused LTEM images of magnetic domains with varying temperatures for  $\text{Mn}_4\text{Ga}_2\text{Sn}$  sample. The images are taken at a magnetic field of 0.3 T for temperatures (a) 100 K, (b) 150 K, (c) 200 K, (d) 250 K, and at a magnetic field of 0.2 T for (e) 280 K. Observed skyrmions with clockwise (CW) and counter clockwise (CCW) helicity are marked with dashed and solid boxes, respectively. (f) Temperature variation of observed stripe domain size and skyrmion size. . 87

- 3.11 Real space LTEM images of field dependent magnetic domains for  $\text{Mn}_4\text{Ga}_2\text{Sn}$  sample in over-focused mode at 250 K. The images are taken at magnetic field of (a) 0 T, (b) 0.1 T, (c) 0.25 T, (d) 0.35 T, (e) 0.38 T, and (f) 0.43 T. The inset in Fig.(a) shows the intensity profile corresponding to stripe domains marked in box. The additional skyrmion like structures are marked with solid/dotted boxes. . . . . 88
- 3.12 (a)-(c) and (g)-(i) The LTEM images, the associated TIE phase image, and magnetization mapping of the additional contrast marked with dashed/solid boxes in Fig. 3.10 . The simulated spin texture of the CW/ CCW skyrmion along with the corresponding phase image and the LTEM simulated image using pylorentz-master code (d)-(f)/(j)-(l). . . . . 89
- 3.13 Over-focused LTEM images of field dependent magnetic domains at 100 K, 200 K for  $\text{Mn}_4\text{Ga}_2\text{Sn}$  sample taken at zero degree sample tilting condition. (a-b) The images at 100 K are taken at magnetic fields of 0 T (a), 0.5 T (b). (c-d) The images at 200 K are taken at magnetic fields of 0 T (c), 0.3 T (d). The skyrmions are marked with boxes. The observed magnetic contrast is very poor due to presence of strong bending contour. . . . . 91
- 3.14 Over-focused LTEM images of field dependent magnetic domains at 250 K for  $\text{Mn}_4\text{Ga}_2\text{Sn}$  sample in zero degree sample tilting condition. The images are taken at magnetic fields of (a) 0 T, (b) 0.15 T, (c) 0.3 T, (d) 0.4 T, (e) 0.25 T, and (f) 0 T. The hexagonal skyrmion lattice is marked with a hexagon in Figure (c). . . . . 93



- 3.15 Over-focused LTEM images showing magnetic domains along with their TIE analysis for the  $\text{Mn}_4\text{Ga}_2\text{Sn}$  sample at 250 K in various tilting conditions. The images are taken at an applied magnetic field of 0.2 T. (a) The schematic corresponding to different tilting conditions, (b) Zero tilting, (c) 6 degree  $\alpha$  tilting, (d) -6 degree  $\alpha$  tilting, (e) 6 degree  $\beta$  tilting. . . . . 95
- 3.16 Over-focused LTEM images showing magnetic domains at 250 K for  $\text{Mn}_4\text{Ga}_2\text{Sn}$  sample in 6 degree  $\beta$  tilting condition. The images are taken at an applied magnetic field of 0.2 T. (a) Zero tilting, (b) 6 degree  $\beta$  tilting, (c) zero tilting angle after decreasing  $\beta$  to zero. (d) The energy diagram for skyrmion and type-II bubble in the system. . 96
- 3.17  $H$ - $T$  phase diagram constructed using LTEM experiment performed with nearly 3 degree sample tilting. Star symbols represent the data points where the LTEM measurements are performed. The plus symbols represent the data points taken from ac susceptibility measurement at room temperature.  $n_{SKX+bubble}$  represents the density of skyrmions and bubbles per micrometer square area of the TEM lamella of the sample. . . . . 98
- 3.18 Fitting of  $M$  vs  $H^{-2}$  plots using the law of approach to saturation at different temperatures (a-c). Measured  $M_S$ , calculated  $a_2$ ,  $K_{eff}$  values at different temperatures (d). . . . . 99
- 3.19 Over-focused LTEM images of stripe domains at different temperatures and the calculated uniaxial magnetocrystalline anisotropy ( $K_u^\perp$ ). 100
- 3.20 The calculated uniaxial magnetocrystalline anisotropy ( $K_{eff}$ ) from approach to saturation method and domain wall width observation from LTEM ( $K_u^\perp$ ), and the number of observed isolated skyrmions ( $n_{SK}$ ) at 3 degree sample tilting condition at different temperatures. . 101

- 3.21 Micromagnetic simulated images with varying exchange stiffness constant ( $A$ ) and uniaxial anisotropy ( $K_u$ ) at zero magnetic field. other parameters like,  $M_S$  is taken  $5.35 \times 10^5$  A/m, Gilbert damping constant ( $\alpha$ ) 0.5. The color contrast represents the  $Z$ -direction magnetic moment. The white arrows represent the in plane spin direction. . . . 102
- 3.22 Micromagnetic simulated images with varying magnetic field by considering the stripe domain as an initial magnetic state. All the simulations are performed by completely relaxing the initial state. The parameters like  $A$ ,  $K_u$ ,  $M_S$ ,  $\alpha$  are taken as, 5 pJ/m,  $1 \times 10^5$  J/m<sup>3</sup>,  $5.35 \times 10^5$  A/m, and 0.5, respectively. The color contrast represents the  $Z$ -direction magnetic moment. The white arrows represent the in-plane spin direction. . . . . 104
- 3.23 Micromagnetic simulated images at 0.2 T out-of-plane magnetic field along with (a) 0 in-plane magnetic field, (b) 0.02 T in-plane magnetic field in negative  $x$ -direction, (c) 0.02 T in-plane magnetic field in positive  $x$ -direction, (d) 0.02 T in-plane magnetic field in positive  $y$ -direction, (e) 0.02 T in-plane magnetic field in negative  $y$ -direction. All the simulations are performed by completely relaxing the random magnetic domain as an initial state. The parameters like  $A$ ,  $K_u$ ,  $M_S$ ,  $\alpha$  are taken as, 5 pJ/m,  $1 \times 10^5$  J/m<sup>3</sup>,  $5.35 \times 10^5$  A/m, and 0.5, respectively. The color contrast represents the  $z$ -direction magnetic moment. The white arrows represent the in-plane spin direction. The index shows the LTEM simulated images of the simulated spin textures. The solid and dashed boxes in Figure (a) mark clockwise and counter-clockwise skyrmions, respectively. . . . . 105

3.24	The simulated magnetic textures for different uniaxial anisotropy constant values with out of plane magnetic field of 0.3 T and in-plane magnetic field of 0.02 T. The used parameters are, $A = 5 \times 10^{-12}$ J/m, $M_s = 6.68 \times 10^5$ A/m (saturation magnetization corresponding to 100 K). The white arrows represent the in-plane magnetization components. The simulations are performed considering a sample area of $1 \mu\text{m} \times 1 \mu\text{m}$ and thickness of 100 nm. The skyrmion spin textures are marked with white dashed boxes. . . . .	106
3.25	Variation of experimentally observed isolated skyrmion numbers at 3 degree sample tilting condition with changing anisotropy. The inset shows the simulated number of isolated skyrmions with changing anisotropy as observed in Fig. 3.24. . . . .	108
4.1	(a) Crystal structure of $\text{MnFe}_{1-x}\text{Co}_x\text{Ge}$ samples. The red, blue, orange, and green balls represent Mn, Co, Fe, and Ge atoms, respectively. (b) Top ( $c$ -axis) view of the triangular lattice arrangement of Mn atoms. . . . .	112
4.2	(a) Potential Magnetic Ground States for $\text{MnFe}_{1-x}\text{Co}_x\text{Ge}$ Samples. The red, blue, orange, and green colored atoms represent Mn, Co, Fe, and Ge, respectively. (b) The Variation in Energy with Non-Collinear Canting Angle in $\text{MnFe}_{1-x}\text{Co}_x\text{Ge}$ Sample. . . . .	113
4.3	(a) The d state projected density of state (DOS) of Mn, Fe, and Co for non-magnetic $\text{MnCoGe}$ and $\text{MnFe}_{0.75}\text{Co}_{0.25}\text{Ge}$ systems. (b) The schematic illustration of probable indirect exchange interactions between Mn-Mn localized moments with change in Co concentration. . . . .	114
4.4	SEM images of the samples $\text{MnFe}_{1-x}\text{Co}_x\text{Ge}$ ( $x = 0.2$ to $0.8$ ). The boxed areas in Figure 4.4a denote various locations on the sample from which the EDX spectra were collected. . . . .	117

4.5	Rietveld refined room temperature powder XRD patterns of the samples $\text{MnFe}_{1-x}\text{Co}_x\text{Ge}$ ( $x = 0.2$ to $0.8$ ). . . . .	119
4.6	Rietveld refined room temperature lattice parameters for the samples $\text{MnFe}_{1-x}\text{Co}_x\text{Ge}$ ( $x = 0.2$ to $0.8$ ). . . . .	120
4.7	Magnetization( $M$ ) vs. temperature( $T$ ) plots for the samples $\text{MnFe}_{1-x}\text{Co}_x\text{Ge}$ ( $x = 0.2$ to $0.8$ ) at a magnetic field of 1 kOe. The additional transitions are marked with arrows. The factors written beside the curves represent that the data shown in the Figure is actual data multiplied the factors. . . . .	121
4.8	(a) Magnetization ( $M$ ) vs. temperature ( $T$ ) plot for $\text{MnFe}_{0.2}\text{Co}_{0.8}\text{Ge}$ ( $x = 0.8$ ) at a magnetic field of 0.1 kOe. The additional transition is marked with an arrow. (b) Temperature dependent ac susceptibility [ $\chi'(T)$ ] for $\text{MnFe}_{0.2}\text{Co}_{0.8}\text{Ge}$ . . . . .	122
4.9	Curie temperature ( $T_C$ ) and additional magnetic transition temperature ( $T_t$ ) for different compositions of $\text{MnFe}_{1-x}\text{Co}_x\text{Ge}$ ( $x = 0.2$ to $0.8$ ). . . . .	122
4.10	(a) Magnetic moment ( $M$ ) vs. magnetic field ( $\mu_0 H$ ) plots for the samples $\text{MnFe}_{1-x}\text{Co}_x\text{Ge}$ ( $x = 0.2$ to $0.8$ ) at temperature of 5 K. (b) The variation of saturation magnetization ( $M_S$ ) of the samples with varying Co concentration ( $x$ ). . . . .	123
4.11	A comparison between the experimental saturation moment ( $M_S$ ) and the net moment calculated through DFT for samples with different potential magnetic ground states. The acronyms CFM, NCFM, and CAFM represent collinear ferromagnet, non-collinear ferromagnet, and collinear antiferromagnet, respectively. The $M_s$ values of nearby compositions (i.e, $x = 0.3, 0.5, 0.8$ ) are used for comparison, and the $M_s$ value for $x = 1$ is obtained from reference [133]. . . . .	124

4.12	The zoomed-in contour plot of (001) and (101) PND reflections for the $\text{MnFe}_{0.6}\text{Co}_{0.4}\text{Ge}$ ( $x = 0.4$ ) sample at different temperatures. The color bar represents the intensity profile of the PND data in arbitrary units. . . . .	125
4.13	(a) The zoomed view of (001) and (101) raw PND data with error bars for $\text{MnFe}_{0.6}\text{Co}_{0.4}\text{Ge}$ ( $x = 0.4$ ) sample at different temperatures. (b) Temperature variation of the relative intensity of (001) and (101) reflections with respect to (112) reflection. . . . .	125
4.14	Zoomed view of Rietveld refined PND patterns for $\text{MnFe}_{0.6}\text{Co}_{0.4}\text{Ge}$ ( $x = 0.4$ ) sample, considering both collinear and non-collinear spin arrangement. . . . .	127
4.15	Schematic representation of collinear and noncollinear Magnetic ground states for the sample $\text{MnFe}_{0.6}\text{Co}_{0.4}\text{Ge}$ ( $x = 0.4$ ). The red, blue, orange, and green balls represent Mn, Co, Fe, and Ge atoms, respectively.	127
4.16	Rietveld refined PND patterns for $\text{MnFe}_{0.6}\text{Co}_{0.4}\text{Ge}$ ( $x = 0.4$ ) sample at (a) 50 K, (b) 200 K. . . . .	128
4.17	(a) The Rietveld refined site specific moments of Mn (2a) and Co/Fe (2d) atoms in $\text{MnFe}_{0.6}\text{Co}_{0.4}\text{Ge}$ ( $x = 0.4$ ) sample at different temperatures. (b) The canting angles of MnI and MnII moments concerning the $c$ -axis at different temperatures. . . . .	129
4.18	Temperature dependence of the refined lattice parameters for $\text{MnFe}_{0.6}\text{Co}_{0.4}\text{Ge}$ ( $x = 0.4$ ) sample. . . . .	129
4.19	The zoomed-in contour plot of (002) and (102) PND reflections for the $\text{MnFe}_{0.2}\text{Co}_{0.8}\text{Ge}$ ( $x = 0.8$ ) sample at different temperatures. The color bar represents the intensity profile of the PND data in arbitrary units. . . . .	130

4.20	(a) The zoomed view of (002) and (102) raw PND data with error bars for $\text{MnFe}_{0.2}\text{Co}_{0.8}\text{Ge}$ ( $x = 0.8$ ) sample at different temperatures. (b) Temperature variation of the relative intensity of (002) and (102) reflections with respect to (112) reflection. . . . .	130
4.21	The Zoomed view of the simulated (002), (102) ND reflections with different tilting ( $\phi$ ) of the magnetic easy axis with respect to the $c$ -axis (a) and the corresponding relative intensity of the reflections with respect to (112) reflection (b). The moment is set to $2 \mu_B$ during the simulation. . . . .	131
4.22	The simulated ND pattern with increasing moment along the $c$ -axis and the corresponding relative intensity value of (102) reflection with respect to (112). . . . .	132
4.23	The Rietveld refined PND patterns for $\text{MnFe}_{0.2}\text{Co}_{0.8}\text{Ge}$ ( $x = 0.8$ ) at temperature 2.4 K, and 200 K. . . . .	133
4.24	The temperature dependence of the easy cone angle ( $\phi$ ) i.e., the angle by which the easy axis tilted away from $c$ -axis for $\text{MnFe}_{0.2}\text{Co}_{0.8}\text{Ge}$ ( $x = 0.8$ ). . . . .	134
4.25	The Rietveld refined magnetic structures for sample $\text{MnFe}_{0.2}\text{Co}_{0.8}\text{Ge}$ ( $x = 0.8$ ) at temperature 2.4 K, and 200 K. The red, blue, orange, and green balls represent the Mn, Co, Fe, and Ge atoms, respectively. . . . .	135
4.26	(a) The refined site-specific moment of Mn and Co in the sample $\text{MnFe}_{0.2}\text{Co}_{0.8}\text{Ge}$ ( $x = 0.8$ ) at different temperatures. (b) The temperature dependent refined lattice parameters for the sample. . . . .	135
4.27	LTEM observed zero field stripe domains for $\text{MnFe}_{0.2}\text{Co}_{0.8}\text{Ge}$ at various temperatures. The corresponding domain wall width( $\delta$ ) marked with black arrows. . . . .	137

- 4.28 Temperature dependent perpendicular magnetic anisotropy ( $K_u^\perp$ ) calculated using the average domain wall width ( $\delta$ ) of the zero field stripe domain observed in LTEM measurements. The anisotropy energy related to the dipolar effect is calculated using the saturation magnetization  $M_S$ . The effective leading anisotropy constant,  $K_1^{eff} = K_u^\perp - \mu_0 M_S^2/2$ . The solid symbols represent the experimental data points, and the open symbols in between show the interpolated points. 139
- 4.29 The MUMAX simulated magnetic ground states for the sample  $x = 0.8$  with varying 2nd order anisotropy constant  $K_2$ , while fixing the  $K_1$  value to  $-0.5 \times 10^5$  J/m<sup>3</sup>. The simulations are conducted in the sample dimension of  $1000 \times 1000 \times 100$  nm<sup>3</sup>, and cell size of  $4 \times 4 \times 4$  nm<sup>3</sup>. The parameters include exchange stiffness  $A$  of 8 pJ/m, saturation magnetization  $M_S$  of  $5.8 \times 10^5$  A/m, damping constant  $\alpha$  of 0.9, and external field  $H$  of 0 T. The color bar represents the out-of-plane moment. The arrows represent the direction of in plane moments. . . . . 140
- 4.30 Field dependent ac susceptibility measurements [ $\chi'(H)$ ] for MnFe<sub>(1-x)</sub>Co<sub>x</sub>Ge ( $x = 0.3, 0.4, 0.5, 0.6$ , and  $0.8$ ) at different temperatures. (a)-(b)  $x = 0.3$ , (c)-(d)  $x = 0.4$ , (e)-(f)  $x = 0.5$ , (g)-(h)  $x = 0.6$ , and (i)-(j)  $x = 0.8$ . The field dependent anomalies are marked with arrows. . . . 142
- 4.31 The SAED pattern for the samples MnFe<sub>1-x</sub>Co<sub>x</sub>Ge with  $x = 0.4$  (a),  $0.5$ (b),  $0.6$ (c), and  $0.8$ (d). . . . . 143

- 4.32 LTEM images of zero field magnetic domains for  $x = 0.4$  sample at a temperature of 100 K. Images are taken in under-focus, in-focus, and over-focus conditions. The small black dots in the images represent small defects on the sample surface. The inset shows the TIE magnetization mapping of the marked region. The color wheel represents the in-plane magnetization directions. . . . . 144
- 4.33 Over-focused LTEM images illustrating the field evolution of magnetic domains for  $x = 0.4$  sample at a temperature of 150 K. The images are recorded at a magnetic field of (a) 0 T, (b) 0.06 T, and (c) 0.16 T. (d) TIE magnetization mapping for the marked region in Figure (b). The color wheel illustrates the direction of in-plane magnetization. . . . . 145
- 4.34 Over-focused LTEM images illustrating magnetic domains evolution with magnetic field for  $x = 0.4$  sample at a temperature of 180 K. The images are recorded at a magnetic field of (a) 0 T and (b) 0.08 T. 145
- 4.35 Over-focused LTEM images illustrating the temperature evolution of zero field magnetic domains for  $x = 0.5$  sample. The images are taken at temperatures of (a) 100 K, (b) 150 K, and (c) 180 K. . . . . 146
- 4.36 Temperature evolution of field-driven magnetic domains for  $x = 0.5$  sample. Over-focused LTEM images at (a)  $T = 100$  K &  $\mu_0 H = 0.43$  T, (b)  $T = 150$  K &  $\mu_0 H = 0.30$  T, & (c)  $T = 180$  K &  $\mu_0 H = 0.15$  T. (d) The TIE magnetization mapping of the skyrmion like domains. The color wheel represents the in-plane magnetization directions. . . . . 146
- 4.37 Field evolution of LTEM images for  $x = 0.6$  sample at 200 K. Images are recorded at a magnetic field of (a) 0 T, (b) 0.1 T, (c) 0.2 T, and (d) 0.3 T. Skyrmions are marked with boxes. . . . . 147



4.38	Temperature evolution of field driven magnetic state for $x = 0.6$ sample. The images are recorded at (a) 100 K and 0.34 T, (b) 130 K and 0.34 T, (c) 180 K and 0.25 T, (d) 200 K and 0.2 T. . . . .	148
4.39	Magnetic field dependent over-focused LTEM images for the sample with $x = 0.8$ at 100 K (a)-(b), 150 K (d)-(e), 220 K (g)-(h). The TIE magnetization mapping corresponding to the marked region in (b), (e), and (h) are shown in (c), (f), and (i), respectively. The color wheels represent the in-plane magnetization components in different directions. . . . .	149
4.40	(a) Average stripe period and skyrmion size of the $x = 0.8$ sample at different temperatures. The stripe periods are calculated at 0 T and the skyrmion size is calculated at 0.2 T. (b) The number of skyrmions and type-II bubbles observed using LTEM at different temperatures for the samples $x = 0.8$ . . . . .	150
4.41	The $x$ vs. $T$ phase diagram for the sample $\text{MnFe}_{1-x}\text{Co}_x\text{Ge}$ . The color bar represents the skyrmion density per $\text{micro-m}^2$ area. PM, SD, IPD, NTB, and SKX represent paramagnetic, stripe domain, in-plane domain, non-topological bubbles, and skyrmions lattice, respectively. Dotted lines are provided as guides to the eye. The asterisk symbols mark experimental data points. The data at the magnetic field where the highest number of skyrmions are observed are considered for a given $(x, T)$ . . . . .	151

- 4.42 The remanent state observed in LTEM for the samples  $x = 0.4$  at 150 K (a),  $x = 0.5$  at 150 K (b),  $x = 0.6$  at 200 K, respectively. The skyrmions are marked with boxes. The TIE magnetization mapping of the marked region in (b). The color wheel represents in-plane magnetization components. The Bloch line orientations are marked with arrows. . . . . 153
- 4.43 The remanent state observed in the LTEM study for the samples  $x = 0.8$  at 220 K (a), 200 K (b), 150 K (c), and 100 K (d), respectively. The remanent states are recorded with increasing field along the zone axis, then making it zero. (e)-(f) TIE magnetization mapping of the marked region in (a) and (d). The color wheel represents the in-plane magnetization components. . . . . 154
- 4.44 The OOMMF simulations of magnetic domains at zero magnetic fields, incorporating tilting the magnetic easy-axis away from the  $c$ -axis by an angle  $\phi$ . The simulations are conducted in the sample dimension of  $1000 \times 1000 \times 100 \text{ nm}^3$ , and cell size of  $4 \times 4 \times 4 \text{ nm}^3$ . The simulation parameters are,  $M_s = 5.8 \times 10^5 \text{ A/m}$ ,  $A = 8 \text{ pJ/m}$ ,  $K_u = 1 \times 10^5 \text{ J/m}^3$ . The color bar represents the  $z(c)$ -axis moment. The black arrows denote the in-plane moment directions. . . . . 155

4.45	The OOMMF simulations of magnetic domains at a magnetic field of 0.2 T along the $c$ -direction, incorporating a tilting of the magnetic easy-axis away from the $c$ -axis by an angle $\phi$ . The simulations are conducted in the sample dimension of $1000 \times 1000 \times 100 \text{ nm}^3$ , and cell size of $4 \times 4 \times 4 \text{ nm}^3$ . The simulation parameters are, $M_S = 5.8 \times 10^5 \text{ A/m}$ , $A = 8 \text{ pJ/m}$ , $K_u = 1 \times 10^5 \text{ J/m}^3$ . The color bar represents the $z(c)$ -axis moment. The arrows denote the in-plane moment directions. A distorted hexagonal skyrmion lattice at $\phi = 0^\circ$ is highlighted with a hexagon, and isolated skyrmions in other cases are marked with solid boxes. . . . .	157
4.46	schematic energy diagram representing the stability of skyrmion and other possible spin textures in $\text{MnFe}_{1-x}\text{Co}_x\text{Ge}$ samples. . . . .	159
5.1	The false colored SEM image of the $c$ -oriented Hall device. . . . .	165
5.2	(a) The field dependent Hall resistivity for the sample $\text{Mn}_4\text{Ga}_2\text{Sn}$ at different temperatures. (b) Extraction of anomalous Hall resistivity ( $\rho_{xy}^A$ ) by linear fitting. (c) Temperature variation of the fitting parameter $R_0$ . (d) Temperature variation of $\rho_{xy}^A$ and longitudinal resistivity ( $\rho_{xx}$ ) for the $c$ -oriented device. . . . .	166
5.3	(a) Temperature dependence of anomalous Hall conductivity ( $\sigma_{xy}^A$ ), (b) Temperature dependence of scaling factor ( $\sigma_{xy}^A/M_s$ ) and anomalous Hall angle (AHA) ( $\sigma_{xy}/\sigma_{xx}$ ). . . . .	167
5.4	(a) Linear fitting between $\rho_{xy}^A$ vs. $\rho_{xx}^2$ , (b) linear fitting between $\sigma_{xy}^A$ vs. $\sigma_{xx}^2$ . . . . .	169
5.5	Magneto-resistance for $c$ -oriented device of the sample $\text{Mn}_4\text{Ga}_2\text{Sn}$ at 250 K, (a) with $H \perp I$ , (b) with $H \parallel I$ . . . . .	170
5.6	Magnetoresistance for the in-plane device of $\text{Mn}_4\text{Ga}_2\text{Sn}$ sample at 250 K. . . . .	171

# Chapter 1

## Introduction

Modern spintronics starts with the groundbreaking discovery of giant magnetoresistance (GMR) [1, 2] and tunneling magnetoresistance (TMR) [3]. In both cases, the electrical resistance of the system depends on the relative orientation of the magnetic moments in the top and bottom ferromagnetic (FM) layers separated by a metallic or insulating layer. The principle of GMR/TMR is primarily being utilized in the reading/writing of data. When it comes to data storage, the most commonly used technologies are magnetic hard disc drives (HDDs) and solid state random access memory (RAM). Although HDDs are less expensive than RAM, the biggest problem is their slower working speed compared to RAM. Hence, the need of the hour is finding a memory device that can be inexpensive, like HDDs, and fast processing like RAMs. In 2008, Parkin et al. proposed a domain wall based racetrack memory (RM) device, where the controlled movement of domain walls with spin polarized current pulses can be employed for realizing low-cost and efficient data storage devices [4]. However, it was found that the motion of the domain wall requires a high current density. In this direction, the recently discovered magnetic skyrmions are proposed to be feasible alternatives to domain walls due to their topological characteristics [5, 6]. Schematics of domain wall and skyrmion based racetrack memory systems are shown in Fig. 1.1.

The magnetic skyrmions are topologically protected localized magnetic objects

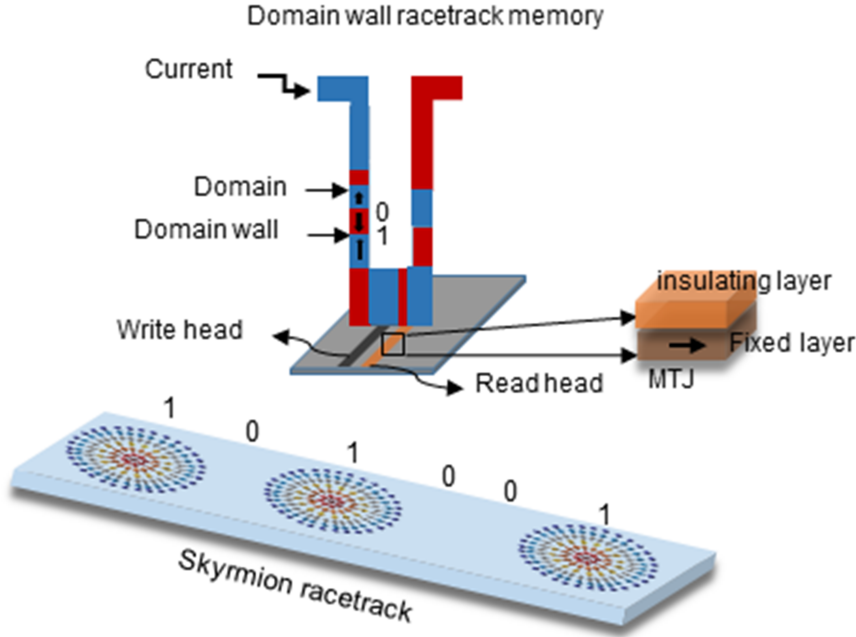


Figure 1.1: Schematic diagrams of domain wall and skyrmion based racetrack memory devices.

with swirling spin configurations. Their topological nature helps them to get depinned in low cut-off current density and avoid defects or pinning centers in their route. Although the stability of skyrmions in chiral magnets is well documented, the simultaneous discovery of several topological spin textures in centrosymmetric systems make these systems more fascinating [7, 8, 9, 10, 11, 12, 13, 14, 15, 16]. The observed spin textures with different topological numbers and helicity may be employed in multi-bit data storage devices where each bit contains more than one state and, hence, more information. This approach has the potential to broaden the concept of skyrmion-based racetrack memory devices. Therefore, finding a new skyrmion hosting centrosymmetric system is a necessary step toward the implementation of skyrmion based racetrack memory devices. The fundamental goal of the present thesis is to find novel skyrmion-hosting centrosymmetric magnetic systems and explore their tunable physical properties in order to grasp their significance toward the application.

The present chapter focuses on the fundamentals of non-collinear magnetism,

including skyrmions, and their topological characteristics. Different energy terms responsible for the stabilization of topological spin textures are briefly discussed.

The principles of different experimental techniques and theoretical methodologies used in this thesis are covered in Chapter 2. The finding of a hexagonal skyrmion lattice in a centrosymmetric kagome ferromagnet  $\text{Mn}_4\text{Ga}_2\text{Sn}$  is discussed in Chapter 3. Chapter 4 covers the observation of skyrmions in a series of noncollinear ferromagnetic compounds  $\text{MnFe}_{1-x}\text{Co}_x\text{Ge}$ . The impact of frustrated exchange interaction induced non-collinearity on the stability of skyrmions has been covered in this chapter. Chapter 5 illustrates the magneto-transport properties of the kagome skyrmion host material  $\text{Mn}_4\text{Ga}_2\text{Sn}$ . The discovery of skyrmion and anomalous Hall effect (AHE) in the same materials may prove to be a crucial step in future spintronics studies. Chapter 6 presents a summary of the present thesis, conclusion, and future prospects.

## 1.1 Noncollinear magnetism

In general, magnetic materials with collinear magnetic states, such as ferromagnetic (FM), antiferromagnetic (AFM), and ferrimagnetic (FIM), dominate the spintronics applications. In recent times, noncollinear magnetic states have received significant research interest due to a better perspective on the direction of current induced manipulation of magnetic states. Magnetic domain walls, spiral magnetic structures, and magnetic vortices are a few examples of non-collinear magnetic states. In a magnetic system, the non-collinear spin ordering can occur as a result of competition between different types of interaction energies. For instance, the presence of geometrical frustration in triangular lattice AFMs [13, 17] and exchange frustration driven by competing nearest neighbor FM and next nearest neighbor AFM interactions [18] are some of the well known sources of non-collinear magnetism. In rare earth based systems, Ruderman–Kittel–Kasuya–Yosida (RKKY) exchange results in a noncollinear magnetic state [19]. In the case of non-centrosymmetric magnets, chiral helimagnetic and cycloidal ground states are obtained due to the competing

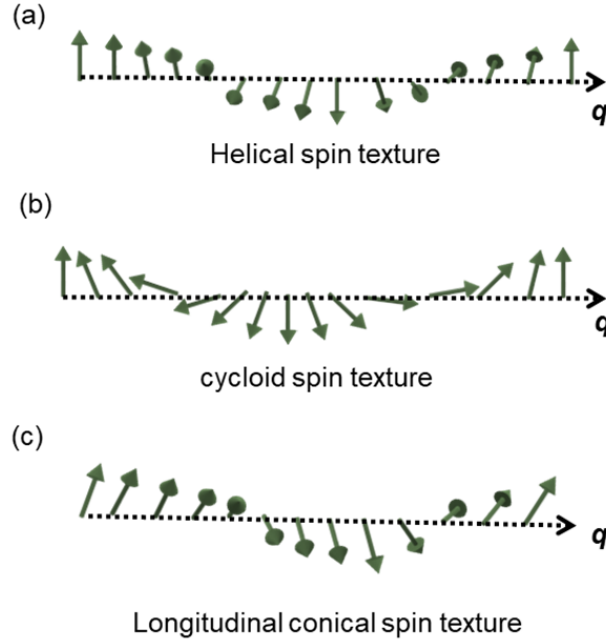


Figure 1.2: Schematic diagrams of different types of non-collinear magnetic states. (a) Helical spin texture, (b) cycloid spin texture, and (c) longitudinal conical spin texture. Green arrows represent the spin direction and  $q$  represents the propagation direction of the spin textures.

Heisenberg exchange and Dzyloshinskii-Moriya (DM) interaction [20, 21, 22]. The chirality of the spin textures is decided by the DM vector direction. In a helical spin texture, the spins rotate in a plane perpendicular to the propagation direction ( $\vec{q}$ ) [see Fig. 1.2(a)]. In contrast, the spins rotate in a plane parallel to the propagation direction in the case of cycloidal texture [shown in Fig. 1.2(b)]. The propagation directions of the spin spirals are typically governed by the crystallographic symmetry of the hosting material. The period of the spiral structures ( $\lambda$ ) depends on the ratio of the exchange constant and DM vector, i.e.,  $\lambda = 4\pi J/D$ , where  $J$  is the exchange constant and  $D$  is the DM vector. The spiral ground state can also be formed in a centrosymmetric system with competing exchange and uniaxial magnetic anisotropy (UMA) energy. In this case, the periodicity of the spiral structure depends on the ratio of the strength of the exchange and UMA energies. In case the spins in the helical structure align slightly towards the propagation direction, the magnetic structure is known as the conical spin texture [shown in Fig. 1.2(c)]. Unlike

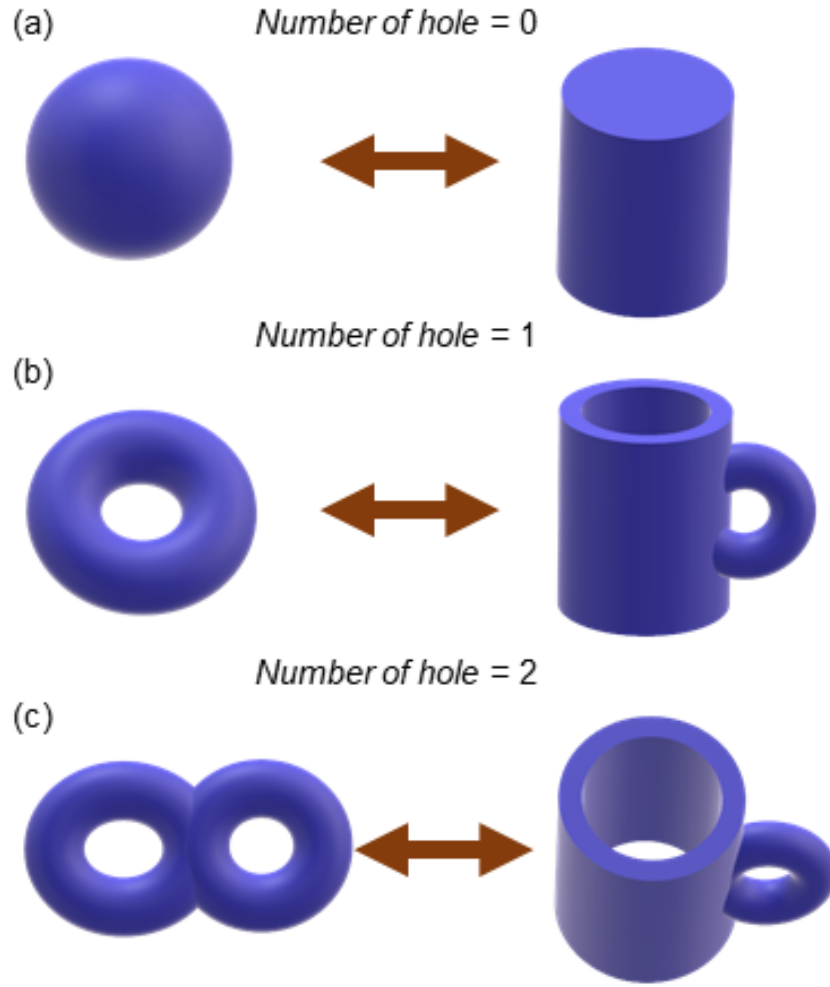


Figure 1.3: Physical objects with different topological properties. The physical objects with different numbers of holes like (a) zero (b) one, and (c) two.

the helical phase, the conical state mostly stabilizes in the direction of the applied magnetic field. Similarly, the stabilization mechanisms of some of the special types of non-collinear magnetic textures with topologically non-trivial features, such as magnetic skyrmions, antiskyrmions, etc, rely on the distinct magnetic interactions inherent in the material system. A brief description of different kinds of magnetic interactions responsible for non-collinear magnetism is discussed in section 1.5.



## 1.2 Topology

Topology deals with the geometry that is conserved in continuous transformation. This transformation permits bending, twisting, stretching, and shrinking but forbids splitting them into separate pieces or joining them together. The properties of a geometric object that stay intact or protected by such continual deformations are the central interest in topology. The following example illustrates how, due to topological equivalence, a doughnut may be continually turned into a coffee mug by first creating a dimple, then gradually widening and enlarging it until the hole forms a handle [see Fig. 1.3(b)]. Similarly, a sphere (a double donut like structure) and a solid cylinder (a coffee mug with an open cylinder) with no hole (two holes) are topologically similar [see Fig. 1.3(a) and (c)]. Many of the key phenomenons in magnetism are connected to topology, such as the anomalous Hall effect [23], topological Hall effect [24], quantum Hall effect [25], de Haas–van Alphen effect [26], stabilization of topological solitons [27], etc.

## 1.3 Topological aspects of noncollinear magnetic textures

Topological magnetic textures are protected in the sense that they can not decay into any other trivial magnetic states by continuous transformation. The topology of such magnetic objects can be explained by an integer winding number. Figure 1.4 shows that the real space planar spin textures can be mapped into an order parameter space, by representing every real space 2D spin angle as a point in order parameter space [28]. The winding number ( $n$ ) denotes the number of times the close circle can be wrapped by the spin texture mapping. Depending on whether the wrapping is clockwise or counter-clockwise,  $n$  might be positive or negative [29]. Due to the topological invariance, a spin texture of winding number  $n$  can't be continuously transformed to other spin textures having winding numbers other than  $n$ . Thus, a

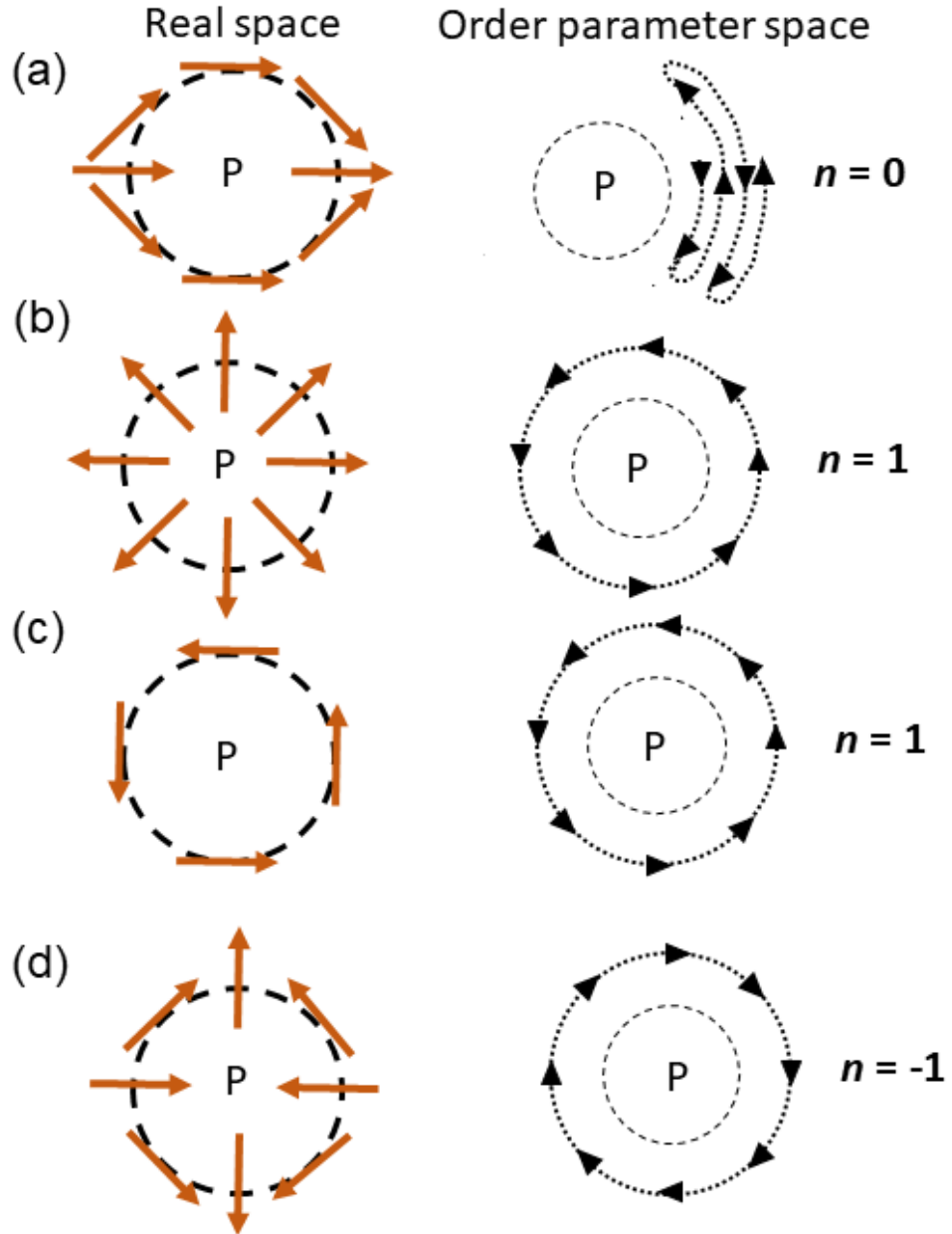


Figure 1.4: 2D real space spin configuration and its mapping on order parameter space.

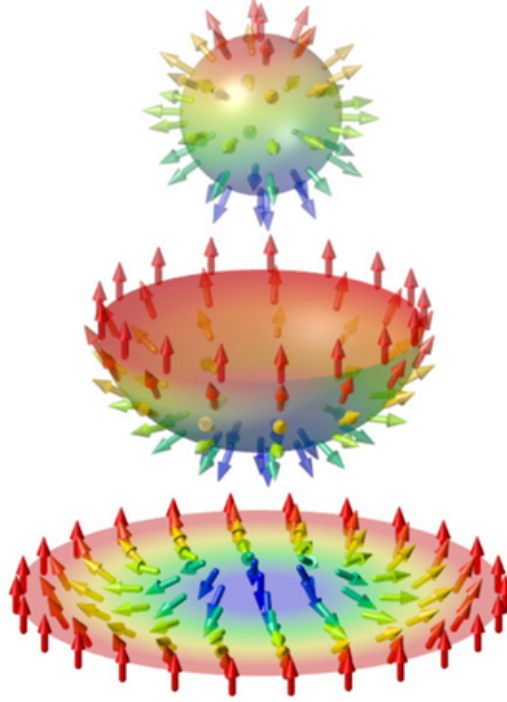


Figure 1.5: A skyrmion and its mapping on a unit sphere. The figure is taken from the reference [30].

spin texture having a non-zero integer winding number is topologically protected.

Now if we replace the 2D spins with 3D spin vectors then the order parameter space will be the surface of a unit sphere rather than a circle. Then, the winding number/topological number/skyrmion number ( $Q$ ) of a spin texture can be explained as,

$$Q = \frac{1}{4\pi} \int \int_{xy} \vec{m} \cdot \left( \frac{\partial \vec{m}}{\partial x} \times \frac{\partial \vec{m}}{\partial y} \right) dx dy \quad (1.1)$$

where  $\vec{m}$  is the unit vector of the magnetization at the  $(x, y)$  point.

A brief overview of magnetic skyrmions with non-zero topology is discussed in the next section.

## 1.4 Magnetic skyrmions

In particle physics, Tony Skyrme first proposes the skyrmion as a particle-like solution to the nonlinear field equation [31, 32]. In 1989, A. N. Bogdanov brought the

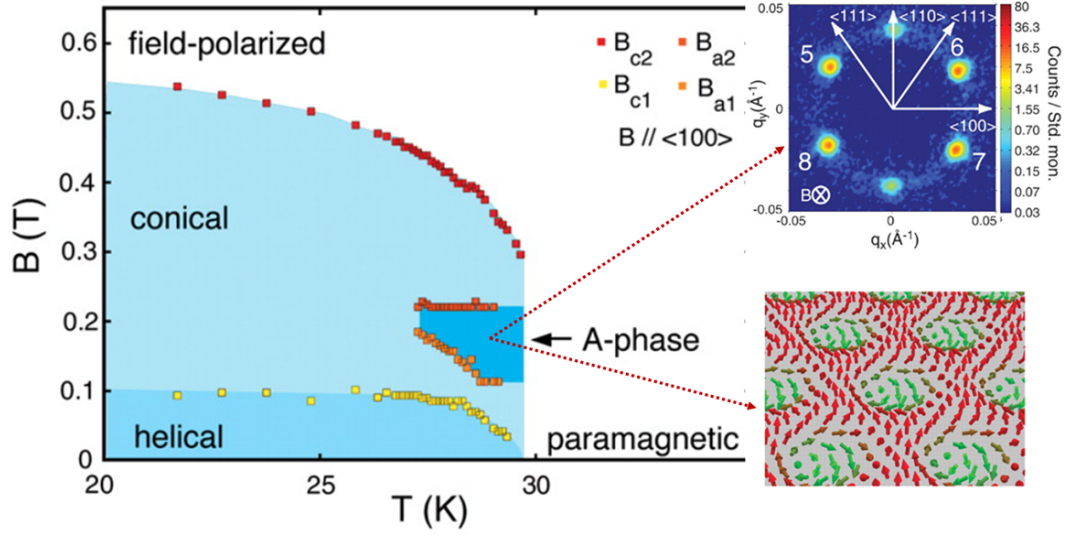


Figure 1.6: First observation of hexagonal skyrmion lattice in MnSi. Magnetic field ( $H$ ) versus temperature ( $T$ ) phase diagram along with six spot small angle neutron scattering pattern in the A-phase and the corresponding hexagonal skyrmion lattice. The figures are taken from reference [20].

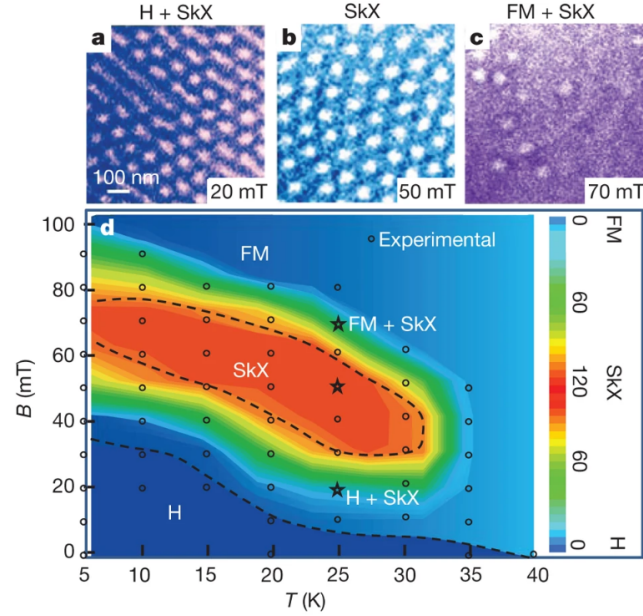


Figure 1.7: First real-space observation of hexagonal skyrmion lattice in FeCoSi. (a)-(c) The Lorentz transmission electron microscopy (LTEM) images of helical (H), skyrmion (SKX), and ferromagnetic phases. (d) Magnetic field ( $H$ ) vs. temperature ( $T$ ) phase diagram. The figures are taken from the reference [21].

concept of magnetic skyrmion in condensed matter physics as thermodynamically stable vortices [33]. It has been theoretically demonstrated that magnetically ordered crystals with particular crystallographic symmetries, such as  $C_{nv}$ ,  $D_{2d}$ ,  $C_n$ ,  $S_4$  ( $n = 3, 4, 6$ ) may host magnetic vortices in a finite field range via the DM interaction [33, 34]. It has also been theoretically demonstrated that the skyrmion state can also emerge spontaneously in the absence of an external magnetic field [35]. The topological protection of the skyrmions provides extra stability to the spin texture. In addition, it helps in avoiding the defects or pinning centers in the crystal, giving a significant benefit for their use in future device applications. The topological number of a skyrmion-like whirling spin pattern, which is the number of times the spins encircle a unit sphere, can be expressed using Equ. 1.1. A skyrmion and its mapping on a unit sphere is shown in Fig. 1.5 [30]. It is also observed that the skyrmions can move with lower cut-off current density ( $10^5$ - $10^6$  A/m<sup>2</sup>) compared to the topological trivial magnetic domain walls [36, 37].

The skyrmion spin texture was first time discovered in 2009 in the cubic heli-magnet MnSi, using a small-angle neutron scattering (SANS) experiment [20]. The helical ground state in this material transforms to a hexagonal skyrmion lattice with the application of a finite magnetic field perpendicular to the sample plate at a very narrow temperature range near the transition point. The skyrmion phase in this sample is shown as A-phase in Fig. 1.6. A hexagonal skyrmion lattice was detected in real space measurements for the first time in 2010 using Lorentz transmission electron microscopy (LTEM) on thin Fe<sub>0.5</sub>Co<sub>0.5</sub>Si lamella [21]. The  $H$ - $T$  phase diagram of Fe<sub>0.5</sub>Co<sub>0.5</sub>Si sample and LTEM images are shown in Fig. 1.7. Different bulk magnetic materials with or without chiral interactions exhibit this type of skyrmions, known as Bloch skyrmions [7, 13, 15, 38, 39].

A Neel skyrmion is another type of skyrmion that, in general, stabilized as a result of interfacial DM interaction in heavy metal/ferromagnetic bilayers or multilayers [40, 41]. Furthermore, the Neel skyrmion is also experimentally observed in bulk magnets, such as polar metallic ferromagnet GaV<sub>4</sub>S<sub>8</sub> [22], PtMnGa [42], van der Waals ferromagnet Fe<sub>3</sub>GeTe<sub>2</sub> [43]. In addition to Bloch and Neel skyrmions,

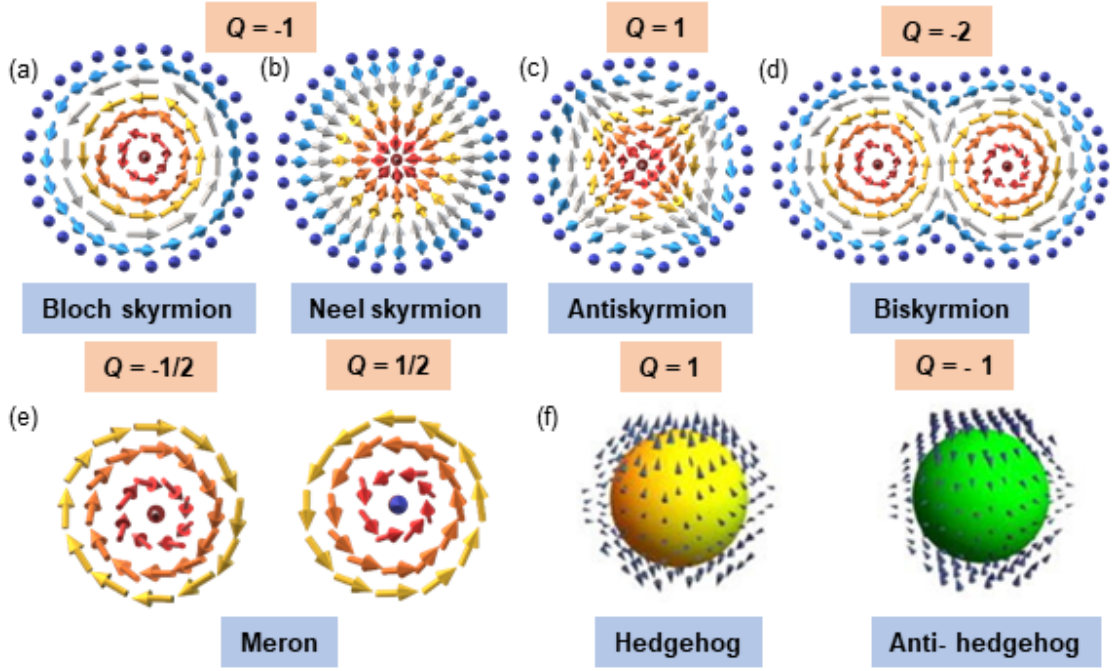


Figure 1.8: (a)-(c) Schematic representation of magnetic spin textures of Bloch skyrmion (a), Neel skyrmion (b), Antiskyrmion (c), biskyrmion (d), merons (e) and hedgehog (f). Figure in (f) is taken from the reference [48]

antiskyrmions are another kind of skyrmion structure that has been experimentally discovered in materials having  $D_{2d}$  and  $S_4$  symmetry [44, 45, 46, 47].

Different kinds of skyrmion-like magnetic structures are schematically shown in Fig. 1.8. In skyrmion spin textures, the spins rotate from a central downward direction to a peripheral upward direction following a particular manner. As depicted in Fig. 1.8 (a) for Bloch skyrmion, spins follow a helicoidal manner while rotating from down to up direction [7, 13, 15, 38, 39]. Whereas, a cycloidal spin rotation is followed for Neel skyrmion [see Fig. 1.8 (b)] by twisting the spins in a plane parallel to the propagation direction [22, 40, 41, 42, 43]. For Antiskyrmions, both Neel and Bloch kinds of spin rotations are observed alternatively, as shown schematically in Fig. 1.8 (c) [44, 45, 46, 47]. The Bloch/Neel skyrmions are represented by the topological number 1, whereas the anti-skyrmions, as shown in Fig. 1.8 (c), are represented by the topological number -1. Other skyrmion-like spin configurations with different topological numbers, such as biskyrmion, merons, and hedgehogs are

demonstrated schematically in Fig. 1.8 (d)-(f). Biskyrmion (Topological Charge 2) can be represented as the addition of two skyrmions with opposing helicity, which is found in some centrosymmetric magnets with uniaxial anisotropy [10, 11, 12]. Meron or half skyrmion (topological number  $\pm 1/2$ ) are experimentally observed in chiral compound CoZnMn,  $\text{Fe}_{0.5}\text{Co}_{0.5}\text{Ge}$ , 2d van der Waals FM compound  $\text{Fe}_5\text{GeTe}_2$  and ferromagnetic GdFeCo [49, 50, 51, 52, 53, 54]. Hedgehog/anti-hedgehog that can be interpreted as a 3q structure with mutually perpendicular arrangement rather than a 120 degree in-plane arrangement like skyrmion lattice is another type of spin texture, experimentally observed in chiral magnet MnGe [48].

In the next section, magnetic interactions responsible for different types of magnetic orderings are discussed.

## 1.5 Magnetic Interactions

The total free energy ( $E_{total}$ ) of a magnetic system can be calculated by adding the energies of different magnetic interactions,

$$E_{total} = E_{dipole} + E_{exchange} + E_{DMI} + E_{anisotropy} + E_{Zeeman} \quad (1.2)$$

where  $E_{dipole}$ ,  $E_{exchange}$ ,  $E_{DMI}$ ,  $E_{anisotropy}$ ,  $E_{Zeeman}$  are the dipole-dipole interaction, exchange interaction, DM interaction, anisotropy, and Zeeman energy, respectively. The magnetic ordering of a system is determined by the free energy minimization. As the thesis is mainly based on the finding of magnetic skyrmions in the centrosymmetric systems, the chiral DM interaction can be discarded here. This section briefly explains several magnetic interactions that are responsible for skyrmion formation in an achiral magnetic system.

### 1.5.1 Exchange interaction

Exchange interaction is one of the key mechanisms for long-range magnetic orderings. Let's consider two electrons having position vectors  $\vec{r}_1, \vec{r}_2$  and single wave function state  $\psi_a(r_1), \psi_b(r_2)$ , respectively. According to the Pauli exclusion principle, the total wave function of the system should be antisymmetric. Now, considering spin states as  $\chi$ , the total wave function can be written as both singlet ( $\psi_S$ ) and triplet state ( $\psi_T$ ),

$$\psi_S = \frac{1}{\sqrt{2}}(\psi_a(\vec{r}_1)\psi_b(\vec{r}_2) + \psi_a(\vec{r}_2)\psi_b(\vec{r}_1)) \cdot \chi_S \quad (1.3)$$

$$\psi_T = \frac{1}{\sqrt{2}}(\psi_a(\vec{r}_1)\psi_b(\vec{r}_2) - \psi_a(\vec{r}_2)\psi_b(\vec{r}_1)) \cdot \chi_T \quad (1.4)$$

The singlet and triplet state energy can be written as,

$$E_S = \int \psi_S^* H \psi_S dV_1 dV_2 \quad (1.5)$$

$$E_T = \int \psi_T^* H \psi_T dV_1 dV_2 \quad (1.6)$$

where  $H$  is the Hamiltonian. Considering,

$$S^2 = (S_1 + S_2)^2 = S_1^2 + S_2^2 + 2 \cdot \vec{S}_1 \cdot \vec{S}_2 \quad (1.7)$$

$$S^2 = S_{total} \cdot (S_{total} + 1) \quad (1.8)$$

we can obtain  $\vec{S}_1 \cdot \vec{S}_2 = -\frac{3}{4}$  for singlet state with  $S_{total} = 0$  and  $\vec{S}_1 \cdot \vec{S}_2 = \frac{1}{4}$  for triplet state with  $S_{total} = 1$ . The effective Hamiltonian can be written as,

$$H = \frac{1}{4}(E_S + E_T) - (E_S - E_T) \vec{S}_1 \cdot \vec{S}_2 \quad (1.9)$$



Spin dependent 2nd term in equation 1.9 refers to the long range ordering of spins. So, the exchange integral ( $J$ ) can be defined as,

$$J = \frac{(E_S - E_T)}{2} = \int \psi_a^*(\vec{r}_1) \psi_b^*(\vec{r}_2) H \psi_a(\vec{r}_2) \psi_b(\vec{r}_1) dV_1 dV_2 \quad (1.10)$$

So, the spin dependent Hamiltonian can be written as,

$$H_{spin} = -2J \vec{S}_1 \cdot \vec{S}_2 \quad (1.11)$$

For many body Heisenberg system, the Hamiltonian can be written as

$$H = -J_{ij} \sum_{ij} \vec{S}_i \cdot \vec{S}_j \quad (1.12)$$

where  $J_{ij}$  is the exchange coupling strength between the  $i^{th}$  and  $j^{th}$  spins [55, 56]. If  $J_{ij}$  is positive, the preferable spin arrangement is parallel (FM), whereas the anti-parallel spin arrangement (AFM) is preferable if  $J_{ij}$  becomes negative. The exchange interaction prefers a single domain arrangement in the FM material, whereas the presence of dipole-dipole and other interactions like magneto-crystalline anisotropy leads to magnetic-domain formation to minimize the energy. The domain wall width depends on the ratio of the exchange interaction and magneto-crystalline anisotropy energy.

When neighboring magnetic atoms interact directly through overlapping of atomic orbitals, it is referred to as direct exchange interaction. However, in real materials, the physical situation is not straightforward. For materials containing rare earths with localized f electrons or even transition metals with d electrons, explaining the magnetic properties through direct exchange becomes challenging. Hence, indirect exchange interactions are crucial for explaining the magnetic behaviors in materials. Various types of indirect exchange interactions exist, including superexchange, RKKY exchange, and double exchange [56]. Superexchange, for instance, is an indirect exchange interaction between non-neighboring magnetic ions, mediated by an

intervening non-magnetic ion. Superexchange predominantly favors AFM configuration when occurring between two occupied magnetic orbitals, owing to the kinetic energy advantage for AFM alignment. However, in certain scenarios, superexchange can be FM type, particularly when the interaction involves one occupied magnetic orbital and one unoccupied magnetic orbital [56]. On the other hand, the RKKY exchange is a conduction electron mediated exchange interaction, named after its inventors Ruderman, Kittel, Kasuya, and Yosida. The interaction is long range and oscillatory, and it can be FM or AFM depending on the distance between the magnetic atoms. Double exchange occurs in materials with mixed valency of magnetic atoms and predominantly favors FM ordering.

### 1.5.2 Magnetic anisotropy

Magnetic anisotropy of a magnetic material refers to the directional preference of the alignment of magnetic moments. In general, there are different kinds of magnetic anisotropies, such as magneto-crystalline anisotropy, shape anisotropy, stress anisotropy, surface and interface anisotropy, etc. The magneto-crystalline anisotropy, which depends on the spin-orbit interaction, is the most important type of anisotropy in a magnetic system. The spin-orbit coupling leads to the preferable orientation of the spins along certain crystallographic directions. The material can be easily magnetized by applying a magnetic field in that particular direction, known as the easy axis of magnetization. The difference between the energy required to magnetize the sample along the easy and hard axis is known as anisotropy energy.

The magneto crystalline anisotropy energy ( $E_{anisotropy}$ ) per unit volume can be explained as power series expansion of magnetization components,

$$E_{anisotropy} = E_0 + \sum_{ij} b_{ij} \alpha_i \alpha_j + \sum_{ijkl} b_{ijkl} \alpha_i \alpha_j \alpha_k \alpha_l + \dots \quad (1.13)$$

where  $\alpha_1$ ,  $\alpha_2$ ,  $\alpha_3$  are the direction cosine of magnetization along  $x$ ,  $y$  and  $z$  directions respectively, as shown in Fig. 1.9. Here, the odd terms are neglected as the

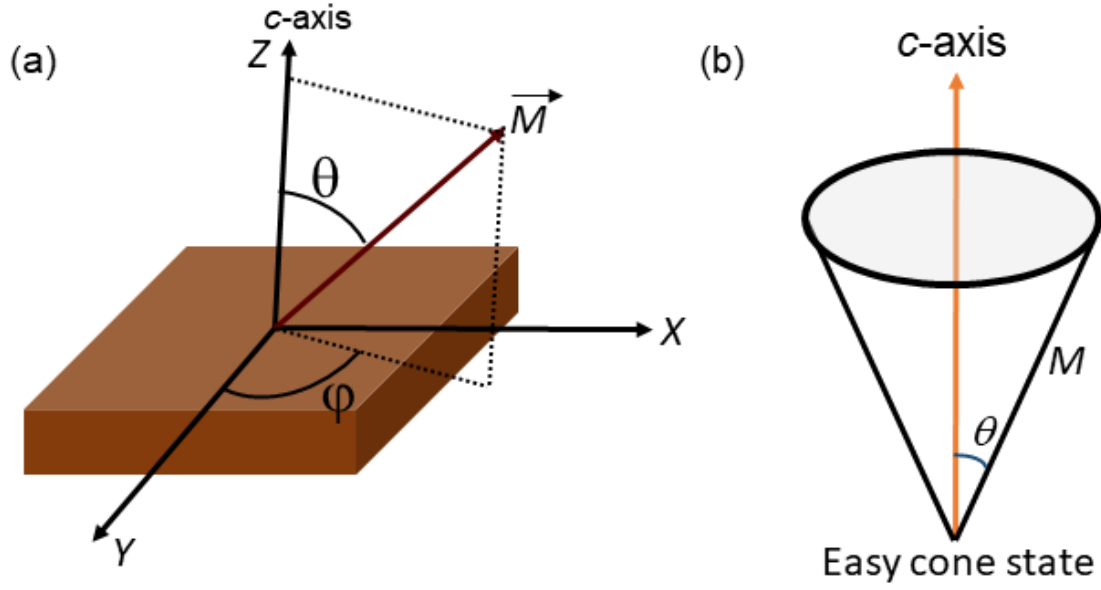


Figure 1.9: Schematic representation of (a) Direction cosine of magnetization of the sample, and (b) easy cone magnetic state.

free energy cannot be negative with the reversing direction of magnetization and the higher order terms are neglected due to their very low contribution. Considering  $\alpha_1 = \sin\theta \cos\phi$ ,  $\alpha_2 = \sin\theta \sin\phi$ ,  $\alpha_3 = \cos\theta$ , and simplifying the expression shown in equ 1.13, one can write the anisotropy energy for systems with different crystallographic structures as,

$$E_{anisotropy}^{cubic} = K_0 + K_1(\alpha_1^2\alpha_2^2 + \alpha_1^2\alpha_3^2 + \alpha_2^2\alpha_3^2) + K_2(\alpha_1^2\alpha_2^2\alpha_3^2) + \dots \quad (1.14)$$

$$E_{anisotropy}^{tetragonal} = K_0 + K_1\alpha_3^2 + K_2\alpha_3^4 + K_3(\alpha_1^4 + \alpha_2^4) + \dots \quad (1.15)$$

$$E_{anisotropy}^{Hexagonal} = K_0 + K_1(\alpha_1^2 + \alpha_2^2) + K_2(\alpha_1^2 + \alpha_2^2)^2 + \dots \quad (1.16)$$

where  $K_i$  is a function of  $b, \dots$ . For uniaxial anisotropy systems like tetragonal and hexagonal, the anisotropy energy can be written in a more simplified way as,

$$E_{anisotropy} = K_0 + K_1\sin^2\theta + K_2\sin^4\theta + \dots \quad (1.17)$$

Where  $K_1$ , and  $K_2$  are the first and second order anisotropy constants, respectively, and  $\theta$  is the angle between the magnetization direction and crystallographic  $c$ -axis [55, 57, 58]. As the strength of  $K_2$  is significantly less compared to that of  $K_1$  in most of the ferromagnets,  $K_1$  can be considered as the most important anisotropy constant. The system having a significant  $K_1$  value only can have a stable solution with  $\theta$  equal to 0 deg or 90 deg [ $\theta$  is the angle between the  $c$ -axis and the magnetic easy axis]. The uniaxial anisotropic nature can be observed for the case when  $K_1 > 0$ , whereas, for the case of  $K_1 < 0$ , the system follows easy-plane anisotropy nature. The presence of significant contribution from  $K_2$  along with  $K_1$  can also give a stable solution with easy axis magnetization in between 0 to 90 deg. This type of magnetic state is called an easy-cone state from the symmetry point of view.

$$E_{anisotropy} = K_1 \sin^2 \theta + K_2 \sin^4 \theta \quad (1.18)$$

$$dE_{anisotropy}/d\theta = 2K_1 \sin \theta \cos \theta + 4K_2 \sin^3 \theta \cos \theta = 2 \sin \theta \cos \theta (K_1 + 2K_2 \sin^2 \theta) \quad (1.19)$$

For a stable solution,

$$dE_{anisotropy}/d\theta = 2 \sin \theta \cos \theta (K_1 + 2K_2 \sin^2 \theta) = 0 \implies \theta = \arcsin(\sqrt[2]{-K_1/2K_2}) \quad (1.20)$$

Therefore to get an easy cone state we need [57, 59, 60],

$$K_2 > -K_1/2 \quad (1.21)$$

In the literature, the leading first order anisotropy term ( $K_1$ ) is considered as an effective term containing the demagnetization factor ( $-\mu_0 M_S^2/2$ ) as shape anisotropy,  $K_1^{eff} = K_1 - \mu_0 M_S^2/2$  [61, 62]. Therefore, the condition for an easy cone state is,

$$K_2 > -K_1^{eff}/2 \quad (1.22)$$

, where  $K_1^{eff}$  is negative.

Another type of magnetic anisotropy, like stress anisotropy is related to magnetostriction. Broken symmetry at the interface or the lower dimension of the system can also modify the anisotropy of the system, which is known as surface or interface anisotropy.

### 1.5.3 Dipole-dipole interaction

The dipole-dipole interaction is one of the most fundamental interactions between two magnetic moments or dipoles. The interaction energy ( $E_{dipole}$ ) between two magnetic dipoles  $\vec{m}_1$  and  $\vec{m}_2$  situated at a distance  $\vec{r}$  will be,

$$E_{dipole} = \frac{\mu_0}{4\pi r^3} [\vec{m}_1 \cdot \vec{m}_2 - \frac{3(\vec{m}_1 \cdot \vec{r})(\vec{m}_2 \cdot \vec{r})}{r^2}] \quad (1.23)$$

The interaction energy basically depends on the magnitude of the dipole moment, orientation and their distances. The energy term will reach its minimum when the magnetic moments  $\vec{m}_1$  and  $\vec{m}_2$  lie in the same plane [55, 56]. So, the dipole-dipole interaction always prefers the in-plane arrangement of the magnetic moments. The dipolar energy can also be written as,

$$E_{dipole} = \frac{\mu_0}{2} \int M(r) H_D(r) dV \quad (1.24)$$

where  $H_D(r)$  is the demagnetizing field,  $M$  is magnetization.  $H_D(r)$  can be expressed as  $-DM$ , where  $D$  is the demagnetizing factor. Therefore the dipolar energy per unit volume can be written as,  $-\mu_0 M_s^2 D/2$ . The demagnetization factor  $D$  depends on the sample's shape and size [58]. In the case of non-cubic magnets, dipole-dipole interactions play a substantial role in contributing to FM anisotropy, often referred to as two-ion anisotropy [57].

### 1.5.4 Zeeman interaction

Quantum mechanically the atomic energy level splits when the atom is placed in an external magnetic field, known as the Zeeman effect. The magnetic moments interact with the applied magnetic fields through Zeeman energy and the energy of a magnetic system with magnetization  $\vec{m}$  and applied magnetic field of  $\vec{H}$  can be written as,

$$E = -\sum(\vec{m} \cdot \vec{H}) \quad (1.25)$$

The static magnetic field applies a net torque on the magnetic dipoles and tries to align the dipole moments along the field direction. The Zeeman energy reaches its minimum when the magnetic moments lie along the field direction. Therefore, due to the dominant Zeeman energy contribution, the magnetic moments get field polarized at high magnetic fields.

## 1.6 Mechanisms of skyrmion stabilization

The most important mechanism of skyrmion stabilization is the competing DM interaction and Heisenberg exchange interaction. The DM interaction is anti-symmetric in nature and can be expressed as,

$$H_{DM} = -\vec{D}_{ij} \cdot (\vec{S}_i \times \vec{S}_j) \quad (1.26)$$

where  $\vec{D}_{ij}$  is the DM vector, and  $\vec{S}_i, \vec{S}_j$  are two nearest-neighbor spins at the  $i$ th and  $j$ th positions, respectively. The Heisenberg exchange with the Hamiltonian discussed in equation 1.12 prefers the collinear arrangement of the spins, whereas the DM interaction prefers the perpendicular spin alignment. Therefore, competition between these two interactions can give rise to helical modulation as a magnetic ground state. When the magnetic field is applied perpendicular to the helical propagation direction, the helical stripes break into skyrmion-like whirling spin textures to minimize the energy. In noncentrosymmetric bulk magnets and ferromagnetic/heavy-metal

bilayer or multilayer systems, the skyrmions are produced with this mechanism [20, 21, 22, 38, 40, 41, 44]. Skyrmions produced with DMI have fixed chirality all over the system depending on the sign and nature of DMI. The skyrmions produced with this mechanism generally have a size between 1 - 100 nm.

Another important mechanism of skyrmion stabilization is the competing dipolar energy and UMA. As discussed earlier, the dipolar energy favors the in-plane spin texture, whereas the out-of-plane UMA favors the spin alignment toward the easy-axis. Hence, competition between these two interactions can also lead to a non-coplanar spin texture like skyrmion. Skyrmions in the uniaxial centrosymmetric system are mainly stabilized through this mechanism [7, 10, 11]. The skyrmions produced with this mechanism can range from 100 nm to a few  $\mu\text{m}$  in size. Due to the absence of DM interaction in the centrosymmetric system, skyrmions exhibit both types of helicity or vector chirality (positive and negative) with equal probability. The skyrmions observed in this case are generally called skyrmionic bubbles due to their larger size.

There are a few alternative approaches for producing skyrmion-like spin textures, such as four spin exchange interactions and frustrated exchange interactions [63, 64]. Skyrmions formed with these mechanisms are of atomistic size. In addition, skyrmions and antiskyrmions exhibit degenerate energy. Skyrmions stabilized by geometrical frustration are found in triangular hexagonal magnets  $\text{Gd}_2\text{PdSi}_3$  [13] and breathing kagome magnet  $\text{Gd}_3\text{Ru}_4\text{Al}_{12}$  [14]. In both of the system's nanometer sized hexagonal skyrmion lattices are formed at a very low temperature. On the other hand, nanometric square skyrmion lattice stabilized by RKKY (Ruderman-Kittel-Kasuya-Yosida) and four spin exchange interactions are found in tetragonal magnets, e.g.  $\text{GdRu}_2\text{Si}_2$  [15] and  $\text{EuAl}_4$  [16].

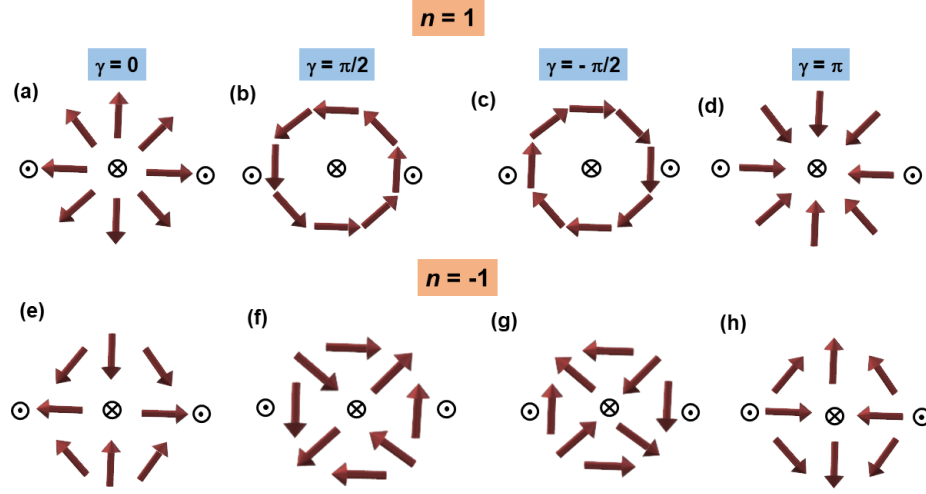


Figure 1.10: Magnetic spin textures with different helicity ( $\gamma$ ) and vorticity ( $n$ ). (a,d) Neel skyrmion, (b,c) Bloch skyrmion, and (e-h) Antiskyrmion. The arrows represent the direction of the in plane magnetization component. The cross and dot sign represent the downward and upward spin direction respectively.

## 1.7 Different degrees of freedom of skyrmion structures

Skyrmion textures can have different degrees of freedom regarding their helicity ( $\gamma$ ) and vorticity ( $n$ ) [65]. The helicity ( $\gamma$ ) or the vector chirality ( $\vec{S}_i \times \vec{S}_j$ ), represents a rotational sense of the in-plane magnetization components of the spin texture. The vorticity ( $n$ ) is related to the topological number and can be explained as  $n = Q$  when the boundary remains fixed at  $r \rightarrow \infty$ . For the Bloch skyrmions with  $n = 1$ , the possible  $\gamma$  will be  $\pm \pi/2$ . Similarly, for Neel skyrmion with  $n = 1$ , the possible  $\gamma$  will be 0 and  $\pi$ . For antiskyrmion with  $n = -1$ , the allowed  $\gamma$  values are 0,  $\pm \pi/2$  and  $\pi$  [ shown in Fig. 1.10]. Due to the presence of DM interaction, the skyrmion helicity in the non-centrosymmetric systems becomes fixed and ceases to act as a degree of freedom. All of the aforementioned structures become degenerate in centrosymmetric magnets due to the absence of the DM interaction. The possibility of observing all kinds of spin textures in the centrosymmetric skyrmion hosting



materials makes them interesting from application perspective.

## 1.8 Skyrmions in centrosymmetric system

Although skyrmions are primarily found in chiral bulk magnets and thin films, centrosymmetric systems with UMA also host skyrmions with a variety of topological spin textures. Bloch-type skyrmions with both clockwise (CW) and counter-clockwise (CCW) helicity, along with non-topological bubbles are found in centrosymmetric kagome ferromagnet  $\text{Fe}_3\text{Sn}_2$  [7], orthorhombic manganite  $\text{La}_{1-x}\text{Sr}_x\text{MnO}_3$  [66], and Sc-doped hexagonal barium ferrite [8]. Apart from Bloch skyrmions, some unique types of magnetic structures, such as biskyrmion with a topological number of 2 are reported in several centrosymmetric materials, such as tetragonal manganite  $\text{La}_{2-2x}\text{Sr}_{1+2x}\text{Mn}_2\text{O}_7$  [9], hexagonal  $\text{MnNiGa}$  [10],  $\text{MnPdGa}$  [11],  $\text{NdCo}_5$  [12]. Skyrmion-like spin textures are stabilized in all the aforementioned systems by combining the effect of the dipole-dipole interaction and anisotropy energy. The size of skyrmions in these systems strongly depends on the sample thickness and magnetic field. Besides all these observations, nanometric skyrmion lattices with hexagonal and square geometry are also experimentally found in rare earth based centrosymmetric magnets, such as  $\text{Gd}_2\text{PdSi}_3$  [13],  $\text{Gd}_3\text{Ru}_4\text{Al}_{12}$  [14],  $\text{GdRu}_2\text{Si}_2$  [15],  $\text{EuAl}_4$  [16]. In these magnets, the skyrmions are stabilized by frustrated or four spin exchange interaction.

The observation of different types of skyrmion like spin textures in the centrosymmetric system makes them more exciting candidates from the application point of view. In the case of non-centrosymmetric systems, the helicity of the skyrmions depends on the nature of the DM interaction. In contrast, the helicity of the skyrmions in centrosymmetric systems can be thought of as an additional degree of freedom. Hence, the presence of different kinds of spin textures with diverse topological features can assist us in preparing data storage with higher reliability [67, 68].

Easily controllable dipolar energy is the fundamental mechanism for skyrmion generation in centrosymmetric materials and it can be used to manipulate different

spin textures. Therefore, the shape, size, and topological numbers of skyrmions in the centrosymmetric system can be simply controlled by altering sample thickness, magnetization, and magnetic field. The ability to easily control different types of spin textures based on our requirement is a huge step forward for realizing skyrmion-based data storage devices.

Although room temperature skyrmion lattice is experimentally observed in a few of the centrosymmetric magnets, the size of these skyrmions is relatively large (about 200 nm) [7, 8]. On the other hand, the nanometric skyrmions in the geometrically frustrated system and/or four spin exchange interaction driven system are only found at very low temperatures [13, 14, 15, 16]. As a result, finding a new centrosymmetric material capable of hosting tiny sized skyrmions at room temperature will be a significant step toward spintronics device implementation.

Existing literature primarily addresses the stabilization of dipolar-stabilized skyrmions in an FM background, none of them discussed the impact of non-collinearity and underlying interactions within the system on skyrmion stabilization. Hence, it is crucial to cognitively comprehend how diverse interactions impact the stability of dipolar stabilized skyrmions before using them in a real-world application. Therefore, the main goal of the present thesis is to realize small size room temperature skyrmions in centrosymmetric magnets and explore their stability and tunability concerning both internal and external parameters.

## 1.9 Anomalous magneto-transport

The Hall effect, named after its discoverer E. H. Hall, refers to the transverse deflection of electrons in a metal relative to the applied current and magnetic field [69]. In addition to the conventional Hall effect, FMs exhibit some additional contributions to the Hall signal, called AHE and topological Hall effects (THE), due to the presence of momentum and real space topological states in the system [11, 12, 70, 71, 72, 73, 74, 75]. Recent studies show that the presence of band topology, e.g., Dirac and Weyl nodes, may affect the dynamics of modulated spin textures like skyrmions

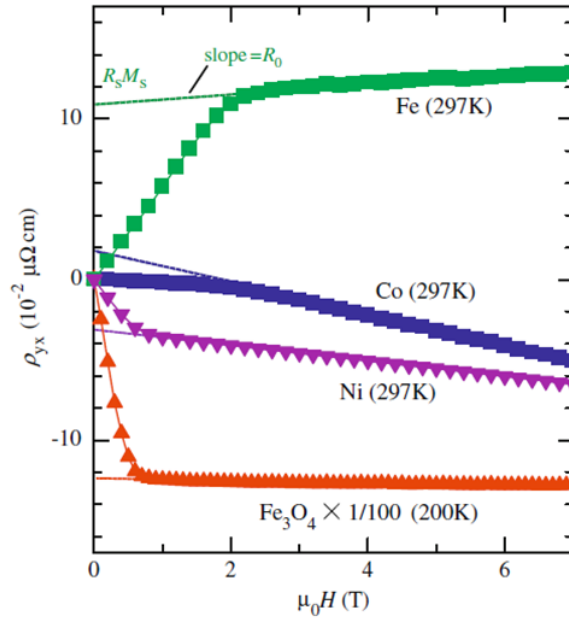


Figure 1.11: Normal and anomalous Hall resistivity. The figure is taken from the reference [81].

in the system by creating a spin orbit torque produced by an axial electromagnetic field [76]. Theoretically, it is also suggested that in the case of anomalous Hall FMs, a charge induced spin orbit torque driven dynamics of spin textures is feasible by providing simply a gate voltage, and the generated torque is proportional to the intrinsic anomalous Hall conductivity (AHC) [77, 78]. Finding a suitable system that can support both the skyrmion and band topology is crucial because the area concerning the interplay between real space magnetic topology and momentum space electronic topology has not been thoroughly explored till now. Additionally, there are very few materials that can have both the skyrmions and band topology [79, 80]. The presence of band topology can be easily detected in the Hall transport, therefore, it is very important to study the Hall effect in the system to clarify the presence of band topology indirectly. The coexistence of band topology and skyrmions in the same material provides a promising platform to explore the impact of band topology on the stability, tunability, and dynamics of skyrmions. The fundamentals of the Berry phase, AHE, and THE are explained in the section.

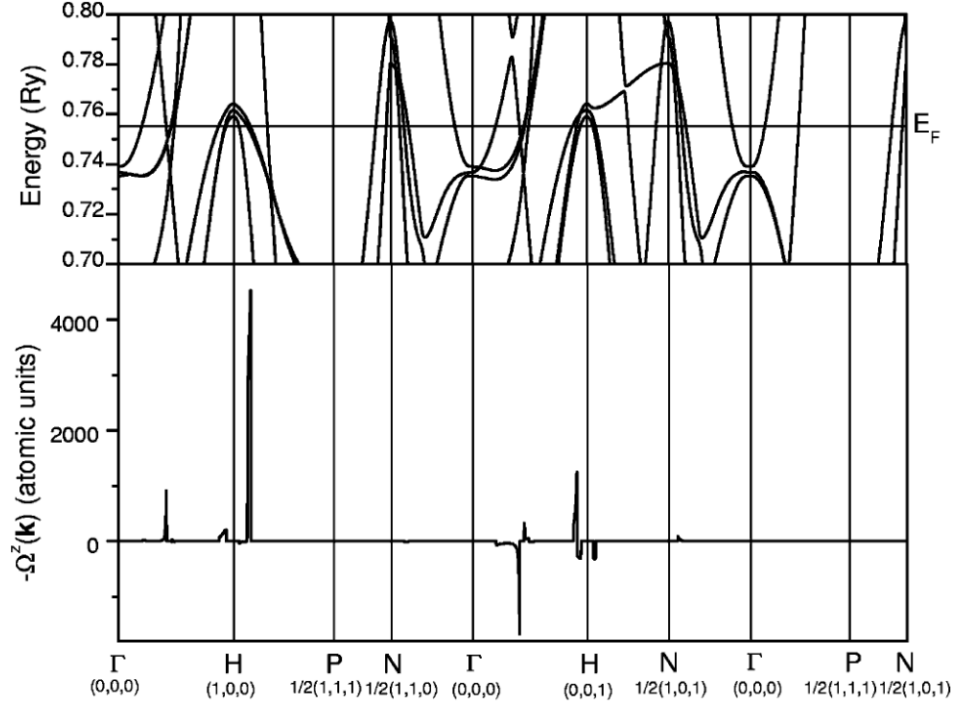


Figure 1.12: (a) Band structure of bulk Fe along with the calculated berry curvature  $[\Omega^z(k)]$  near the Fermi level. The figure is taken from reference [84].

### 1.9.1 Anomalous Hall effect (AHE)

In 1981, E. H. Hall found that the Hall signal is ten times larger in an FM system in comparison to that of a normal metal and named it as anomalous Hall effect (AHE) as it was independent of the magnetic field [82]. An empirical relation for the Hall resistivity ( $\rho_{xy}$ ) in a FM system can be given by,

$$\rho_{xy} = R_0 H_z + R_S M_z \quad (1.27)$$

where  $R_0$  is the normal Hall coefficient and  $R_S$  is the AH coefficient [83].  $R_0$  is determined by carrier density, whereas  $R_S$  is governed by material-specific parameters, such as  $\rho_{xx}$ , longitudinal resistivity. A graphical representation of normal and anomalous Hall resistivity components is shown in Fig. 1.11.

Three different mechanisms are recognized as the origin of AHE.

### Intrinsic mechanism:

The first microscopic theory of AHE by Karplus and Luttinger (KL) establishes that the conduction electrons in ferromagnet acquire an additional group velocity component perpendicular to the applied electric field direction [85]. The transverse component of the anomalous group velocity contributes to the Hall effect, as the sum of that anomalous group velocity component over all the occupied band states is nonzero for ferromagnets. The band structure driven intrinsic (scattering independent) AHE follows the relation  $\rho_{xy} \propto \rho_{xx}^2$ . The anomalous velocity in the KL theory is identified as momentum ( $k$ ) space Berry phase curvature after the discovery of the Berry phase [86]. So, the intrinsic AHE contribution can be explained in terms of the Berry phase curvature of the occupied band,

$$\sigma_{xy}^A = \rho_{xy}^A / \rho_{xx}^2 = -\frac{e^2}{h/2\pi} \sum_n \int \frac{d\vec{k}}{(2\pi)^3} f(\varepsilon_n(\vec{k})) b_n^z(\vec{k}) \quad (1.28)$$

Here, for the state  $|n, \vec{k}\rangle$  the Berry phase connection  $a_n(\vec{k}) = i \langle n, \vec{k} | \nabla | n, \vec{k} \rangle$  and the Berry phase curvature  $b_n(k) = \nabla_k \times a_n(k)$ . The Berry phase connection  $b_n(\vec{k})$  acts as a fictitious magnetic field on the electrons having state  $|n, \vec{k}\rangle$ , and in the presence of an electric field, the electrons acquire an anomalous velocity  $-\frac{e^2}{h/2\pi} \vec{E} \times b_n(\vec{k})$ , which actually contributes to intrinsic AHE [87, 88].

Under the time reversal symmetry, the Berry phase curvature behaves like  $b_n(-k) = -b_n(k)$  and for inversion symmetry, it is  $b_n(-k) = b_n(k)$ . Therefore, for a system with both time reversal and inversion symmetry, the predicted Berry curvature for the whole Brillouin zone is zero [23]. In this context, the breaking of the time reversal symmetry is very crucial for the observation of nonzero berry curvature, hence intrinsic AHE [see Fig. 1.12]. In FM systems, the finite magnetic moment breaks the time reversal symmetry and thereby introduces a finite intrinsic AHE. In addition, the intrinsic AHE can also be greatly influenced by the presence of band crossing points (Dirac point, Weyl point, nodal line, avoided band crossing, etc.), which behave as monopoles and significantly increase intrinsic AHE [23, 84, 89, 90]. The examples of certain ferromagnets whose band topology (avoided band crossing,

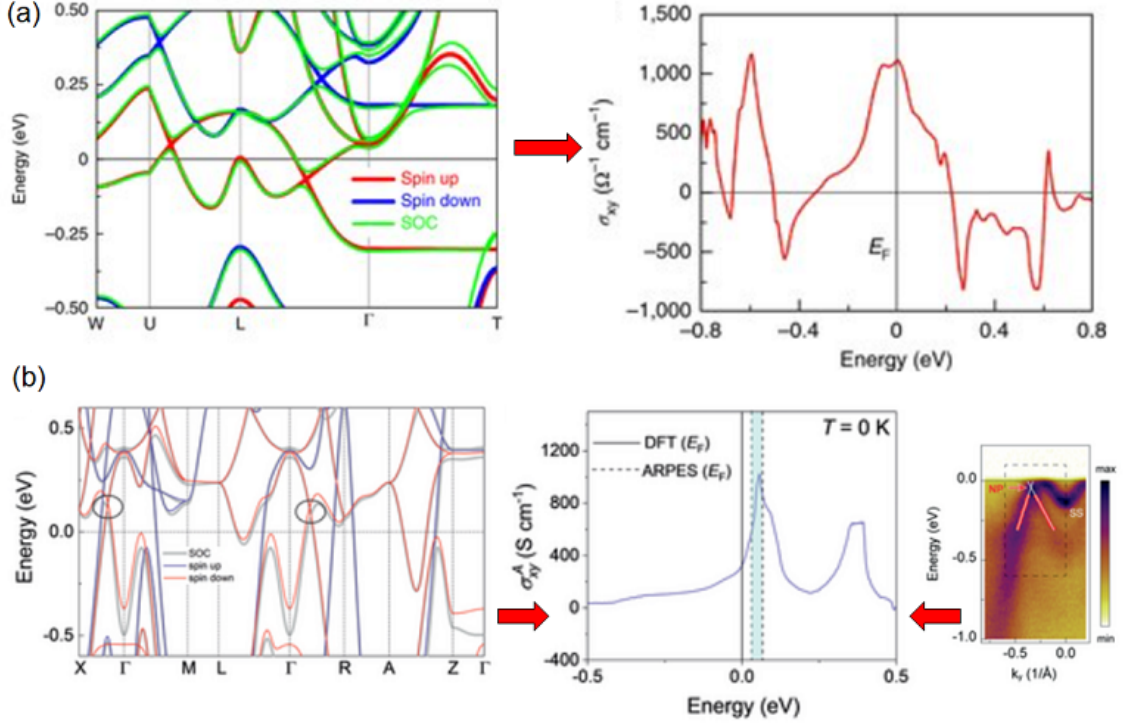


Figure 1.13: (a) The calculated band structure for ferromagnetic Weyl semimetal  $\text{Co}_3\text{Sn}_2\text{S}_2$  along with the corresponding calculated anomalous Hall conductivity  $[\sigma_{xy}]$ . (b) The calculated Band structure of ferromagnetic nodal line semimetal  $\text{MnAlGe}$  along with its calculated anomalous Hall conductivity  $[\sigma_{xy}^A]$ . The right side figure shows the confirmation of band touching using angle resolved photo emission spectroscopy at 14 K. The figures are taken from references [89, 90].

Weyl crossing, and nodal line) gives rise to the AHE are shown in Fig. 1.13. The estimated Berry phase curvature/AHC displays a peak close to the sites of band crossing.

### Extrinsic mechanism:

In the presence of spin-orbit coupling the electrons can be scattered from a scattering potential in two ways known as skew scattering and side jump. The schematics of the skew scattering and side jump scattering mechanism are shown in Fig. 1.14.

Skew scattering is the asymmetric scattering of electrons proposed by Smit [92, 93]. As a result of asymmetric scattering, the electron acquires a finite transverse momentum. The typical deflection angle ( $\delta$ ) is nearly 0.01 rad for skew scattering

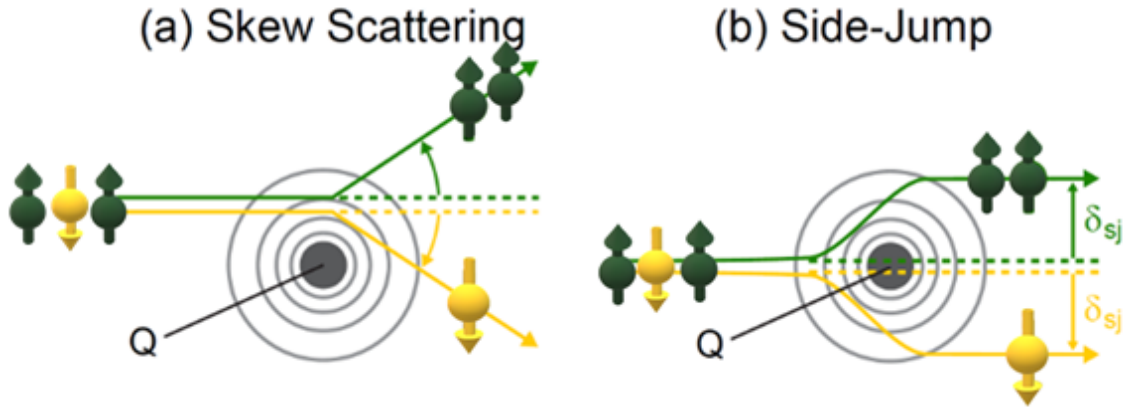


Figure 1.14: Schematic representation of the scattering dependent extrinsic Hall contributions (a) skew scattering, (b) side jump. Here,  $Q$  is the scattering potential. The figure is taken from reference [91]

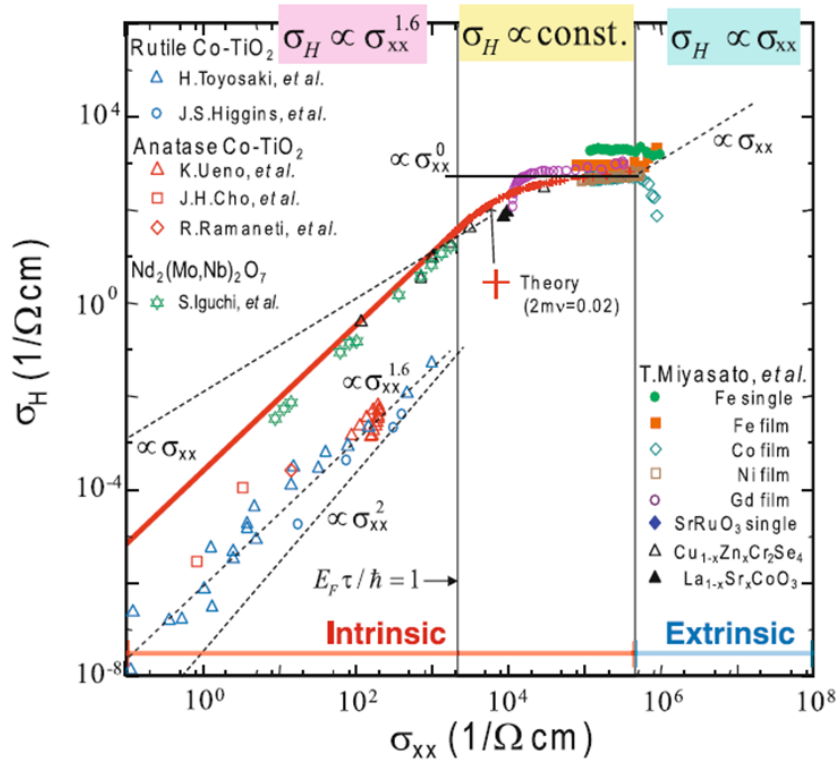


Figure 1.15: Three different regions of AHE with different scaling relation depending on different longitudinal conductivity ( $\sigma_{xx}$ ) of the system. The figure is taken from the reference [81].

[81]. The anomalous Hall resistivity (AHR) arising from skew scattering follows the relation  $\rho_{xy}^{sk} \propto \rho_{xx}$ . The electrons with greater mobility are mostly responsible for skew scattering [81]. The  $s$  electrons with the highest mobility thus contribute the most. However, the contribution of the  $s$  electrons to the skew scattering-induced AHE is minimal as they do not exhibit spin polarization. While  $d$  orbital electrons, because of their moderate mobility and enough spin polarization, play a major role in the skew scattering-induced AHE.

The side jump is the vertical shift of the electron coordinate due to impurity potential in the presence of spin orbit coupling. The estimated value of the vertical shift of electron coordinate ( $\Delta y$ ) is nearly  $10^{-11}$  -  $10^{-12}$  m [81]. The AHE arising from the side jump ( $\rho_{xy}^{sj}$ ) is proportional to  $\rho_{xx}^2$  [94]. It is found that the side jump contribution is not significantly affected by the scattering potential's range, strength, and sign.

The analysis of experimental data as well as theoretical calculations from several systems reveal that there are three major regimes of AHE with different scaling relations as a function of longitudinal conductivity ( $\sigma_{xx}$ ) [see Fig. 1.15]. **High conducting region** ( $\sigma_{xx} > 10^6$ ): A high conducting region with the scaling relation  $\rho_{xy}^A \propto \rho_{xx} \implies \sigma_{xy}^A \propto \sigma_{xx}$ , indicates that the skew scattering contribution predominates. Therefore, anomalous Hall angle (AHA)  $= \sigma_{xy}^A / \sigma_{xx}$  remains constant [23, 81, 95]. **Moderate conducting region** ( $10^4 < \sigma_{xx} < 10^6$ ): The AHE exhibits dominant intrinsic contribution and follows  $\rho_{xy}^A \propto \rho_{xx}^2 \implies \sigma_{xy}^A \propto \sigma_{xx}^0$  scaling in the moderate conducting region. Here the AHE is scattering independent and originates from the band topology or momentum space Berry curvature [23, 73, 81, 96, 97]. **Bad metallic region** ( $\sigma_{xx} < 10^4$ ): In the bad metal region  $\sigma_{xy}^A$  changes more rapidly in comparison to the  $\sigma_{xx}$ . In this region, the materials mostly behave like insulators and exhibit hopping transport. Due to the substantial disorder effect in these regions, the AHE is severely suppressed, and the scaling relation becomes  $\sigma_{xy}^A \propto \sigma_{xx}^\beta$  where  $1.6 < \beta < 2$ . The precise origin of this type of scaling is not understood properly, posing a challenge to the AHE theory [23, 81, 96, 98, 99, 100, 101].

### Scaling of AHE:



It is crucial to distinguish among different components of AHE in order to comprehend the genesis of AHE that is present in a system. Now, the overall anomalous Hall resistivity of a system may be expressed using the equation [23, 81],

$$\rho_{xy}^A = a\rho_{xx} + b\rho_{xx}^2 \quad (1.29)$$

where  $a$  and  $b$  are constants. The first term denotes skew scattering, while the second term is intrinsic contribution and side jump. Later, the equation was further simplified by Tian et al [102],

$$\rho_{xy}^A = a\rho_{xx0} + \beta\rho_{xx0}^2 + b\rho_{xx}^2 \quad (1.30)$$

The skew scattering and side jump contributions at higher temperatures are very small, therefore the extrinsic contribution can be written as  $a\rho_{xx0} + \beta\rho_{xx0}^2$ , where  $a$  and  $\beta$  are constants representing skew scattering, and side jump, respectively. Now by Considering  $\sigma_{xy} = \rho_{xy}/\rho_{xx}^2$  [102],

$$\sigma_{xy}^A = (a\rho_{xx0} + \beta\rho_{xx0}^2)\rho^{-2}xx + b \quad (1.31)$$

$$\sigma_{xy}^A = (a\rho_{xx0} + \beta\rho_{xx0}^2)\sigma^2xx + b \quad (1.32)$$

Hence, it is feasible to determine the dominating origin of AHE in a system using these scaling relations.

### 1.9.2 Chiral anomaly

The chiral anomaly, a violation of classical conservation laws, was discovered in 1968 to elucidate the phenomenon of pion decay [103, 104]. Generally, massless fermions segregate into two independent left-handed (LH) and right-handed (RH) chirality nodes in equal numbers. Intriguingly, chiral symmetry breaks down when these fermions are coupled to an electromagnetic field with a magnetic field parallel to

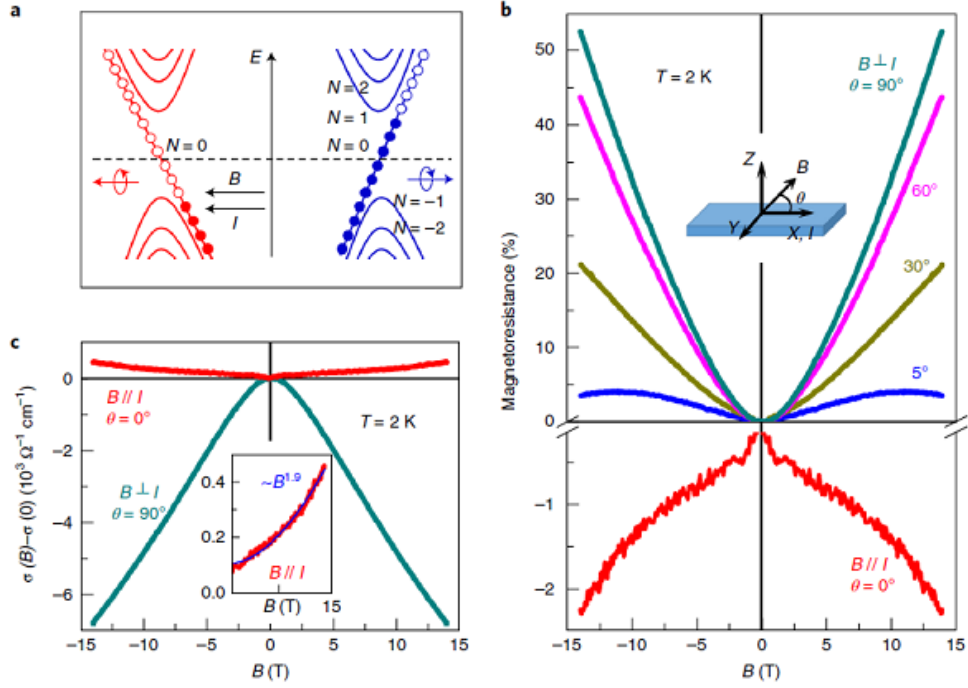


Figure 1.16: Negative MR due to chiral anomaly effect in weyl semimetal  $\text{Co}_3\text{Sn}_2\text{S}_2$ . (a) Schematic representation depicting the Chiral anomaly effect, (b) Angular dependence of MR at 2 K, and (c) Magneto-conductance (MC) at 2 K. The inset shows a quadratic dependence of positive MC with respect to the applied magnetic field ( $B$ ). The figure is taken from the reference [90].

the electric field. This disruption in chiral symmetry results in the emergence of an axial current, generating negative magneto-resistance (MR) in the material [90, 105, 106, 107, 108]. A schematic representation of the Chiral anomaly effect is shown in Fig. 1.16(a). The topological semimetals such as Dirac and Weyl semimetals are expected to show the chiral anomaly effect. Figure 1.16 illustrates an example of chiral anomaly, experimentally observed in Weyl semimetal  $\text{Co}_3\text{Sn}_2\text{S}_2$  [90]. The chiral anomaly is also observed in half Heusler compound  $\text{TbPtBi}$ , which is related to the presence of avoided band crossings [109], as shown in Fig. 1.17. Hence, the chiral anomaly effect serves as an indirect tool for confirming the existence of electronic band topology in a material.

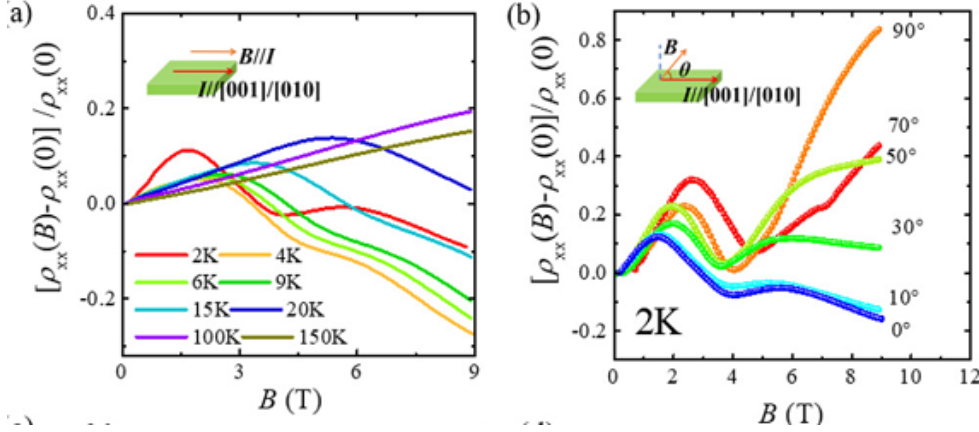


Figure 1.17: Chiral anomaly effect due to avoided band crossing in half-Heusler compound TbPtBi. (a) Field dependent longitudinal MR at different temperatures, (b) Angular dependence of MR at 2 K. The figure is taken from the reference [109].

### 1.9.3 Topological Hall effect (THE)

The topological Hall effect (THE) is an additional contribution to the total Hall signal over the normal and AHE. The fundamental cause of the THE is in fact connected to the real space Berry curvature, which is understandable from the classical example shown in Fig. 1.18(a). When an electron is transported in a close path on the surface of a sphere while keeping the spin direction always toward the tangent of the surface, the electron spin eventually returns to its starting state but acquires an additional geometrical phase, known as the Berry phase [30]. The Berry phase curvature acts as a fictitious magnetic field and arises a large electrical response known as THE. According to the Aharonov-Bohm effect, the electron acquires the quantum mechanical Berry phase as it adiabatically travels through the non-coplanar spin texture with finite scalar spin chirality (SSC) ( $\Omega$ ),  $\Omega = \sum S_i \cdot (S_j \times S_k)$ . Non-coplanar spin textures with trivial topology, in addition to topological spin textures, can also generate THE owing to finite scalar spin chirality [81].

One of the most important topological magnetic textures that can host real space berry curvature induced THE is Skyrmion. The experimentally observed THE and its fitting using  $\rho_{xy}$  vs.  $H$  and  $M$  vs.  $H$  data, for the skyrmion hosting sample  $\text{Gd}_2\text{PdSi}_3$  are shown in Fig. 1.19(a) [13]. For the skyrmion, the THE is inversely

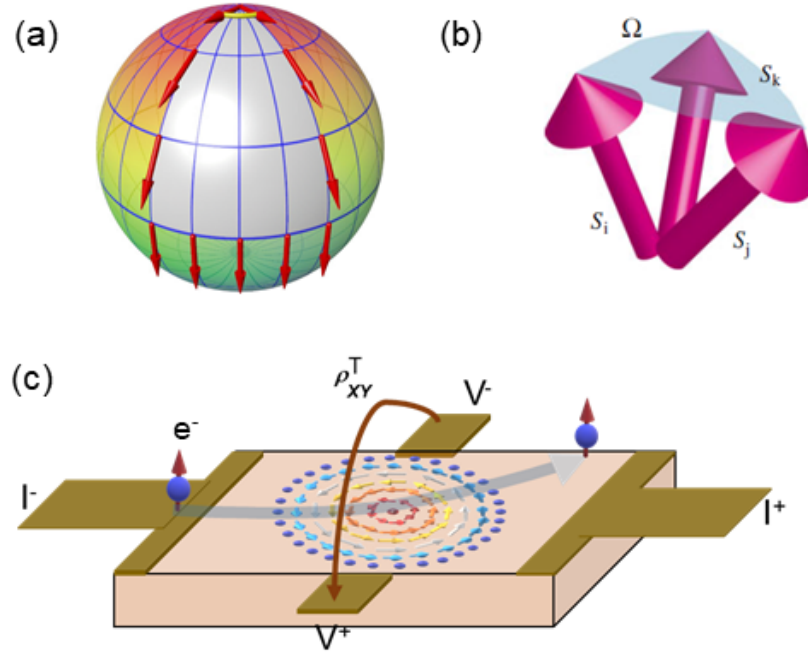


Figure 1.18: Schematic representation of (a) classical example of real space Berry curvature, (b) noncoplanar spin texture with scalar spin chirality ( $\Omega$ ), (c) skyrmion spin texture, while deflecting the conduction electron. Figures (a) and (b) are taken from the references [30, 81]

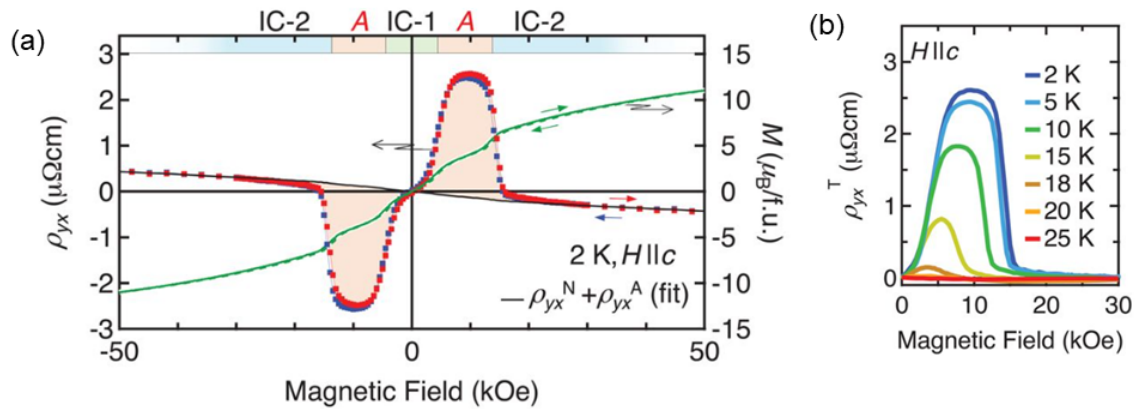


Figure 1.19: (a) The total Hall signal and (b) extracted THE in  $\text{Gd}_2\text{PdSi}_3$ . Figures are taken from the reference [13].

proportional to its size. The expression can be written as,

$$\rho_{xy}^T = PR_0B_{eff} \quad (1.33)$$

where  $B_{eff}$  is the topological magnetic field generated from skyrmion, and  $P$  is the polarization factor which indicates the ratio between majority and minority spins.  $P$  can be calculated simply by dividing the spontaneous magnetization of the skyrmion phase by the saturation magnetization of the system [24]. For the skyrmions with topological charge  $Q$ ,

$$B_{eff} = N_S Q \phi_0 \quad (1.34)$$

where  $N_S$  is skyrmion density and  $\phi_0 = \frac{h}{2e} = 2.06 \times 10^{-15}$  Wb is the flux quanta. Therefore, the expression of  $B_{eff}$  can be written as,

$$B_{eff} = Q\phi_0/a_{sk}^2 \quad (1.35)$$

where  $a_{sk}$  is skyrmion size [24]. According to the above mentioned formula, a skyrmion ( $Q = 1$ ) hosting ferromagnet with  $P \approx 0.8$ , and  $R_0 = 5 \times 10^{-10}$   $\Omega$ -m/T will exhibit the topological Hall resistivity (THR) ( $\rho_{xy}^T$ ) nearly equal to 8 n $\Omega$ -cm for skyrmion size 100 nm. The size of the dipolar stabilized skyrmions in centrosymmetric systems range from 100 nm to a few  $\mu$ m. The estimated topological Hall resistivity for the centrosymmetric skyrmion hosting system is therefore close to a few n $\Omega$ -cm, which is quite a small value.

## 1.10 Important aspects of centrosymmetric hexagonal ferromagnets

The hexagonal ferromagnets with layered structures hold a special place in the spintronics application as they exhibit multiple unique properties, such as large AHE, band topology, and the existence of magnetic skyrmions [7, 70, 71]. The schematic

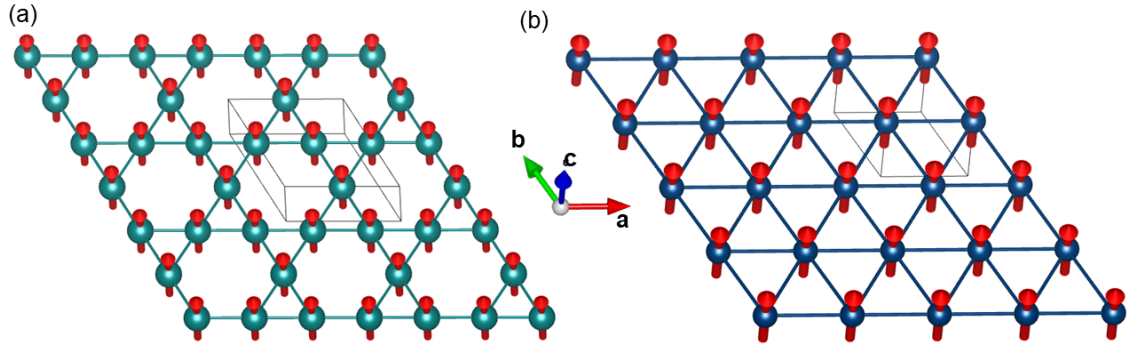


Figure 1.20: Schematic representation of atomic arrangement in hexagonal (a) kagome ferromagnet, and (b) triangular lattice ferromagnet.

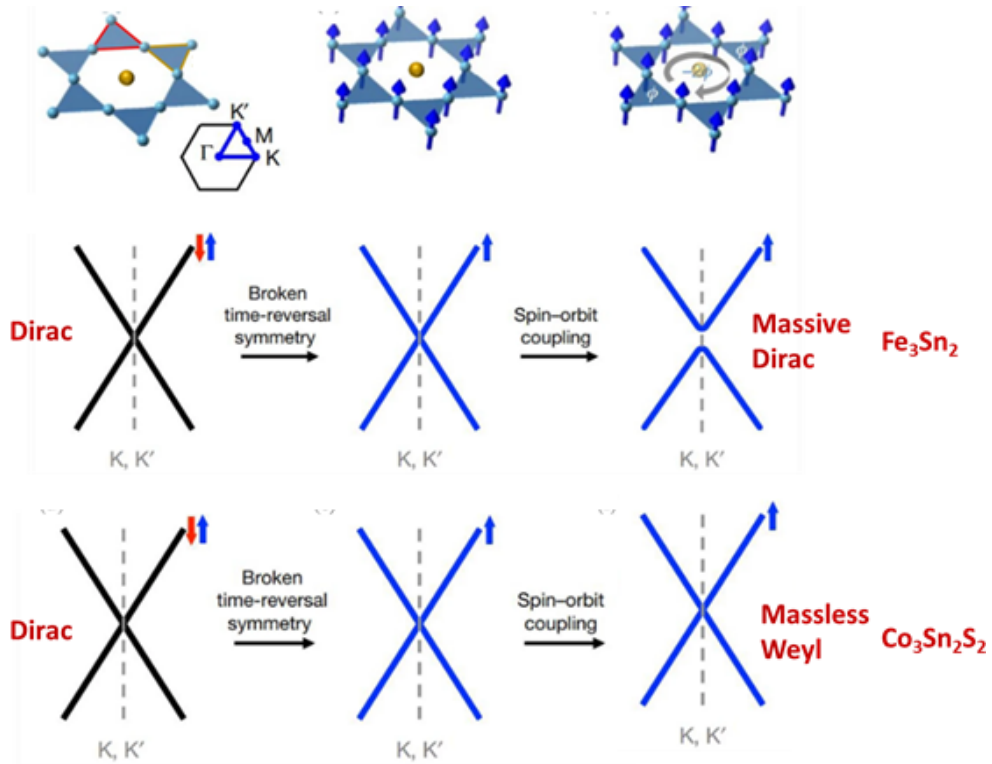


Figure 1.21: Schematic representation of topological band structure present in some of the kagome ferromagnets such as  $\text{Fe}_3\text{Sn}_2$ ,  $\text{Co}_3\text{Sn}_2\text{S}_2$ . The idea of the figure is taken from references [90, 110].

diagrams of hexagonal kagome ferromagnet lattice and triangular lattice ferromagnet are shown in Fig. 1.20. The majority of hexagonal magnets display a temperature dependent transition from in-plane to out-of-plane magnetic anisotropy [7, 12]. This is due to the fact that the magnetic anisotropy of the system switches from a negative (in-plane) to a positive (out-of-plane) value. Since the competition between dipolar energy and magnetic anisotropy energy is an essential mechanism of skyrmion generation in centrosymmetric magnets, hexagonal magnets are extremely important for the realization of room temperature magnetic skyrmions. The skyrmion-like structures with different topologies are experimentally observed in many hexagonal magnets [7, 8]. However, the sizes of the skyrmions at room temperature for all the cases are larger than 200 nm. In addition, the nanometric skyrmions are also found in the hexagonal breathing kagome magnet at a very low temperature (8 K) [14]. So, the observation of nanometric skyrmion at room temperature in new hexagonal magnets might be a significant step for the realization of high density data storage devices.

Although the stabilization mechanism of skyrmion bubbles in centrosymmetric systems is well-explored within a ferromagnetic background [7, 10, 11], the influence of noncollinearity and underlying interactions on skyrmion stabilization is not adequately encased for any of these reports. Before using the dipolar stabilized skyrmions in an application, it is essential to understand the impact of different interactions fundamentally. Hence, it is extremely important to understand the effect of different magnetic backgrounds on the skyrmion stabilization mechanisms as well as their tunability in the hexagonal system.

The dynamics of skyrmion are also crucial for its practical use. As it is well known when the spin polarized current reaches a certain threshold, it can cause a spin transfer torque (STT) that can move skyrmions [36, 37]. However, recent works suggest that driving the skyrmions with spin Hall effect driven spin orbit torque (SOT) is a more effective method [111]. A few recent articles theoretically propose that the skyrmions can be driven by anomalous Hall ferromagnetic systems using charge-induced spin torque without supplying any electric current [77, 78]. In

this case, the spin torque can be generated by applying a gate voltage in the presence of an external magnetic field, and the torque produced will be proportional to the AHC present in the system [77]. A few additional recent theoretical publications also suggest that the existence of band topology, like Weyl and Dirac nodes etc, in the system may affect the dynamics of the skyrmion by introducing an axial electromagnetic field [112]. This axial electromagnetic field causes spin orbit torque-driven magnetization switching when an electric field is introduced to the system, caused by localized spin accumulation at the magnetic texture. Consequently, the motion of skyrmions is still conceivable even in the absence of the conduction electron [76].

In order to successfully implement the above discussed ideas, it is essential to choose a system that can support both the band topology and skyrmion. Practically, there are very few materials that exhibit both properties simultaneously [79, 80]. The potential role of centrosymmetric hexagonal or kagome magnets as a host for skyrmions is well known. Recent studies claim that these materials are equally capable of hosting band topology-driven AHE [70, 71, 72, 73, 74, 90, 110]. A few examples of band topology observed in kagome ferromagnets are schematically shown in Fig. 1.21. Hence, the centrosymmetric hexagonal family of materials are best candidates to identify a system with both skyrmion like spin textures and robust band topology. In order to investigate the band topology as well as the actual real space spin structures, the present thesis includes an anomalous magneto-transport analysis of centrosymmetric hexagonal magnets along with the real space skyrmion observation.





## Chapter 2

# Experimental Techniques and Simulation Details

Different experimental methodologies and their operating principles have been reviewed in this chapter. An arc melting furnace is used to prepare the bulk polycrystalline samples. Scanning electron microscopy (SEM) with energy dispersive X-ray spectroscopy (EDX) and electron back-scattered diffraction (EBSD) are utilized for the compositional analysis and micro-structural study of the samples. The DC and AC magnetic characteristics of the samples are investigated using superconducting quantum interference devices (SQUID) and the AC measurement system option (ACMS) of the physical properties measurement system (PPMS). Different modes of transmission electron microscopy (TEM), such as Lorentz transmission electron microscopy (LTEM), high resolution transmission electron microscopy (HRTEM), and selected area electron diffraction (SAED), are used to directly visualize magnetic textures and structural properties of the sample. Powder neutron diffraction (PND) is carried out to study the magnetic ground state of the samples. A  $\text{Ga}^+$  ion-based focused ion beam (FIB) instrument is employed to prepare thin TEM lamellae from polycrystalline bulk samples.

The simulations of magnetic domains under various circumstances that are comparable to the experiment are performed based on the object oriented micromagnetic

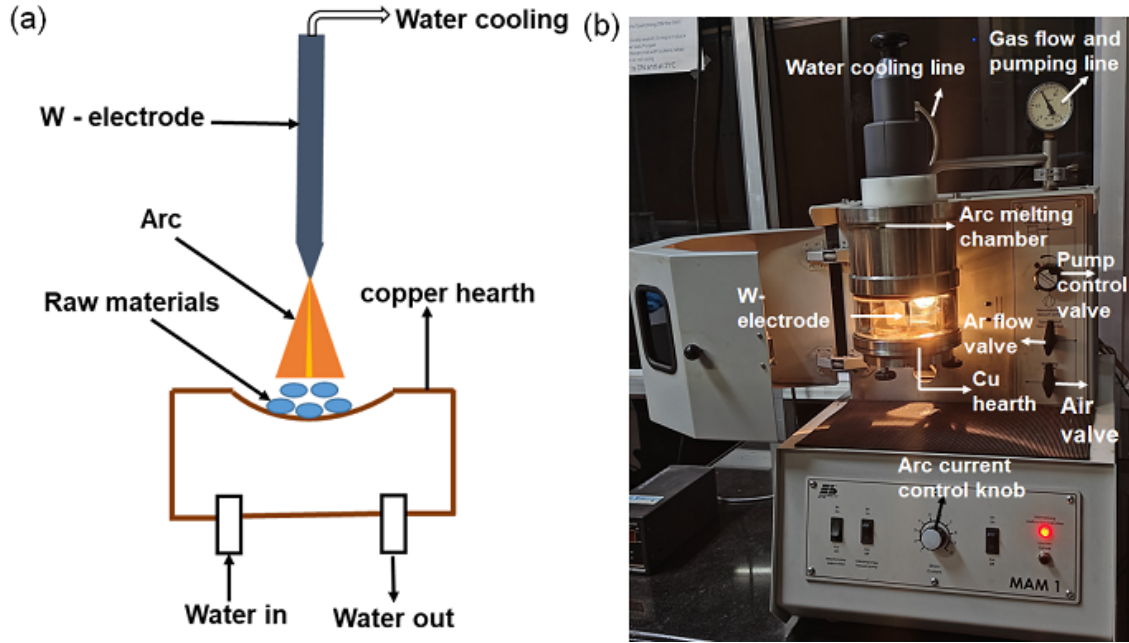


Figure 2.1: (a) Schematic representation of an Arc melting furnace. (b) Physical view of an Arc melting furnace.

framework (OOMMF). In the following, a brief discussion of the above mentioned techniques is presented.

## 2.1 Arc melting furnace

For the purpose of melting and mixing metals to create alloys, arc melting furnaces are often utilized. Melting is performed by heating the metals (up to  $3000^{\circ}\text{C}$ ) in a copper hearth by applying an electric arc between the tungsten (W) electrode and the metal to be melted, as shown schematically in Fig. 2.1. The copper hearth and W-electrode are cooled by continuous circulation of water from a chiller. The arc melting chamber was evacuated (up to  $10^{-3}$  mbar) and purged with Ar gas to remove oxygen. Subsequently, the arc-melt chamber was filled with inert Ar gas for arc generation. The melted alloy ingots are flipped and remelted multiple times to get the homogeneous mixing of the constituent elements.

The polycrystalline bulk samples are prepared by taking high-pure constituent elements in a stoichiometric ratio and melting them together multiple times in an

Ar atmosphere to get material with homogeneous compositional characteristics. For Mn based samples, raw Mn pieces are vacuum sealed in a quartz tube and annealed at 1000 °C for 12 hrs to remove the oxidation layer and achieve pure Mn. Due to high vapor pressure of Mn, 3 % extra Mn is taken to compensate for Mn loss during arc melting. The ingots are vacuum sealed in a quartz tube and subsequently annealed at required temperatures (550 °C for  $\text{Mn}_4\text{Ga}_2\text{Sn}$ , 850 °C for  $\text{MnFe}_{1-x}\text{Co}_x\text{Ge}$ ) for several weeks to ensure the homogeneous crystal structure of samples. The annealed samples are then quenched in the ice-water mixture to get the desired structural phase.

## 2.2 Scanning electron microscopy (SEM) and Energy dispersive X-ray spectroscopy (EDX)

In scanning electron microscopy (SEM), a focused high energy electron beam of 5 - 30 keV is used to reveal the sample's structural/microstructural details, including external morphology and chemical composition [113]. As schematically shown in Fig. 2.2, an SEM column contains an electron beam source, a set of electromagnetic lenses to control the electron beam path, and electron detectors that detect electrons coming from the sample. The scanning coil above the objective lens controls the electron beam position on the sample. When the high energy electrons with sufficient kinetic energies fall on the sample, they interact with the sample in various ways, and the produced signal is detected by appropriate detectors. Various possible interactions of the primary electron beam with the specimen are shown schematically in Fig. 2.3. When the electron beam penetrates the sample, secondary electrons (SE), backscattered electrons (BSE), and characteristic X-rays are generated from the sample. Electrons coming out from different depths of the sample provide distinct information about the sample. SE originates from the inelastic interaction between the primary electron beam and the sample atoms. The SE comes out from the surface and gives the topographical information of the sample. The SE,

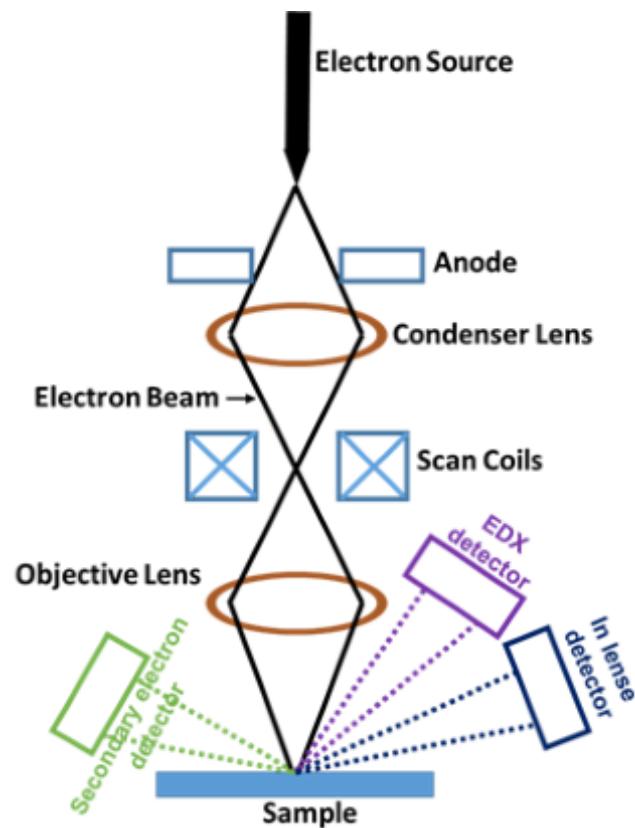


Figure 2.2: Schematic representation of SEM column.

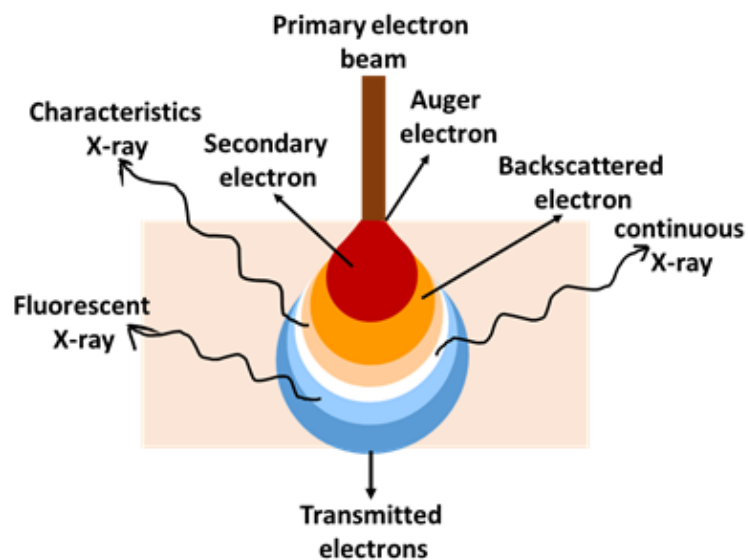


Figure 2.3: Schematic representation of various interactions, possible between sample and primary electron beam.

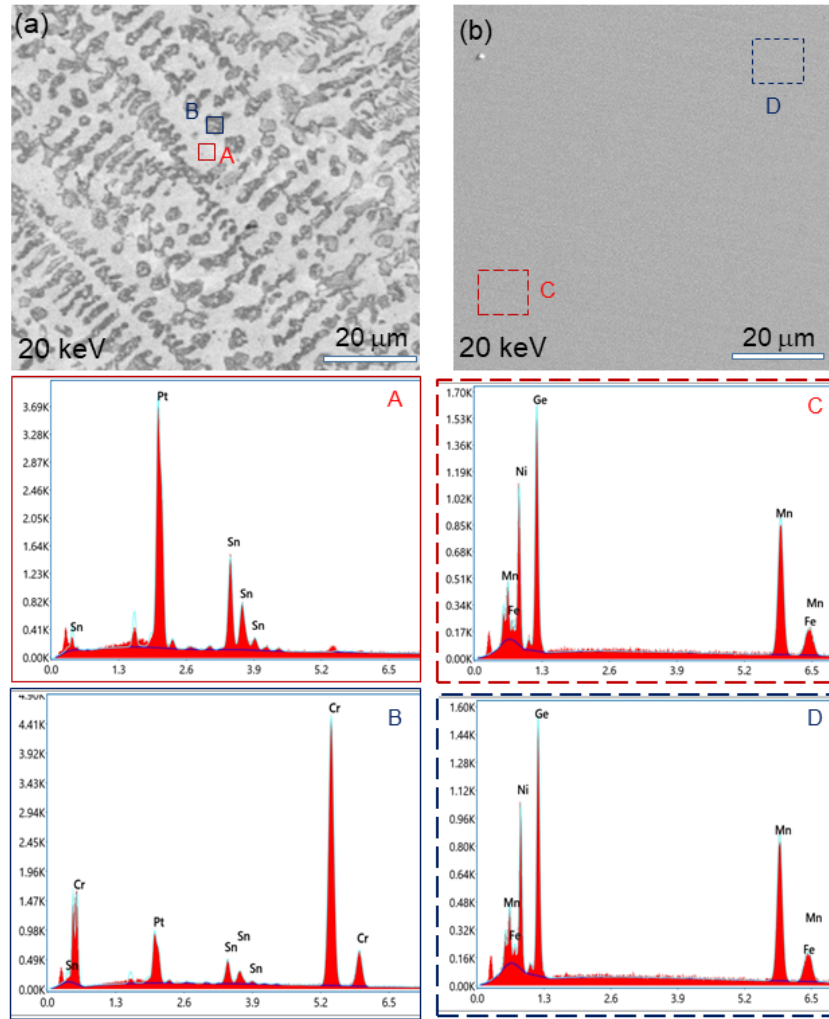


Figure 2.4: Comparison between the SEM images and corresponding EDX patterns of two different samples having compositional double phase (a) and single phase (b). The images are taken with an SE detector at 20 keV energy.

generated from higher penetration depth, and the BSE, originating from the atom's elastic scattering, give information about the compositional inhomogeneity in the sample under observation. The energy of the SE depends on the atomic weight of the constituent elements. As a result, the samples with compositional inhomogeneity show distinct contrast at different places of the sample, as shown in Fig. 2.4.

The energy dispersive X-ray spectroscopy (EDX) is the scientific technique to perform the sample's elemental characterization and chemical composition analysis.

When the focused electron beam with sufficient energy can knock out the inner cell electrons from an atom, the outer cell electron comes to fill the empty place in the inner cell, originating characteristic X-rays. The energy of the generated X-ray is a unique and characteristic feature of an atom, as it depends on the energy difference between two electron energy cells. These features make the characteristic X-ray able to detect the sample's chemical composition. The EDX spectra of two separate samples with compositionally double-phase or single-phase nature are compared in Fig. 2.4.

In the present thesis, a field emission SEM along with an EDX detector from the ZEISS (Sigma), with a maximum accelerating voltage of 20 kV is used to analyze the compositional characteristics of the sample.

## 2.3 Electron backscatter diffraction (EBSD)

Electron backscatter diffraction is an SEM-based technique in which a backscattered electron beam is diffracted by the atomic planes of the samples, resulting in a black and white contrasted band pattern on the phosphor detector screen. The pattern is known as the Kikuchi pattern. When the primary electrons pass through the sample, they are scattered diffusely and deflected by the atomic planes according to Bragg's law. The central line of each Kikuchi band represents the gnomonic projection of the crystal plane. The Kikuchi patterns effectively provide information about the crystalline orientation from which they are generated. When the pattern is used in conjunction with a database and software that includes crystallographic structural information of interest, the pattern can be indexed, and the data can be used to identify the local grain orientations at different places of the polycrystalline sample. Therefore, the EBSD pattern is useful for identifying the local grain orientation, phases, and strain in the polycrystalline sample [114, 115, 116].

The schematic of the EBSD experiment is shown in Fig. 2.5. An EBSD detector with a phosphor screen is placed in the perpendicular direction to the electron beam gun. The width of each Kikuchi band is equal to  $2\theta$ , where  $\theta$  is the Bragg angle.

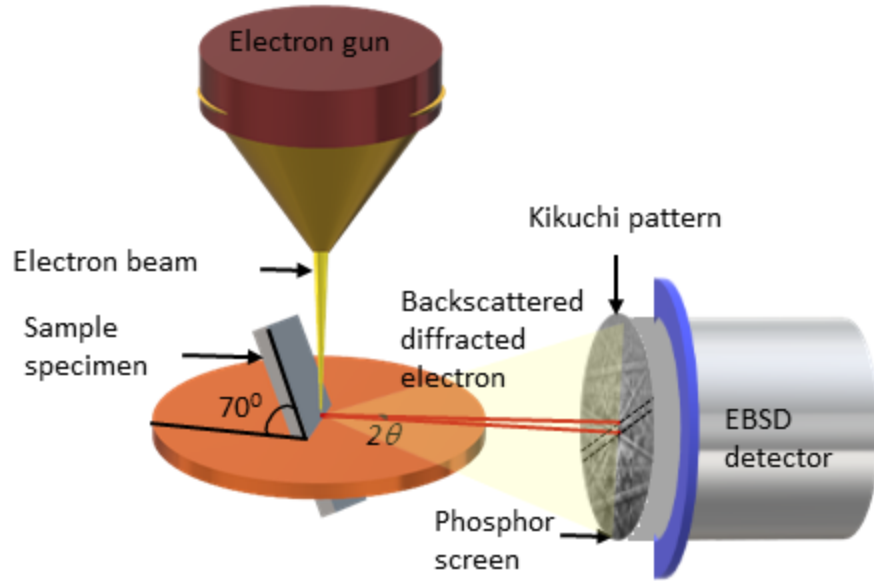


Figure 2.5: Schematic representation of EBSD experiment.

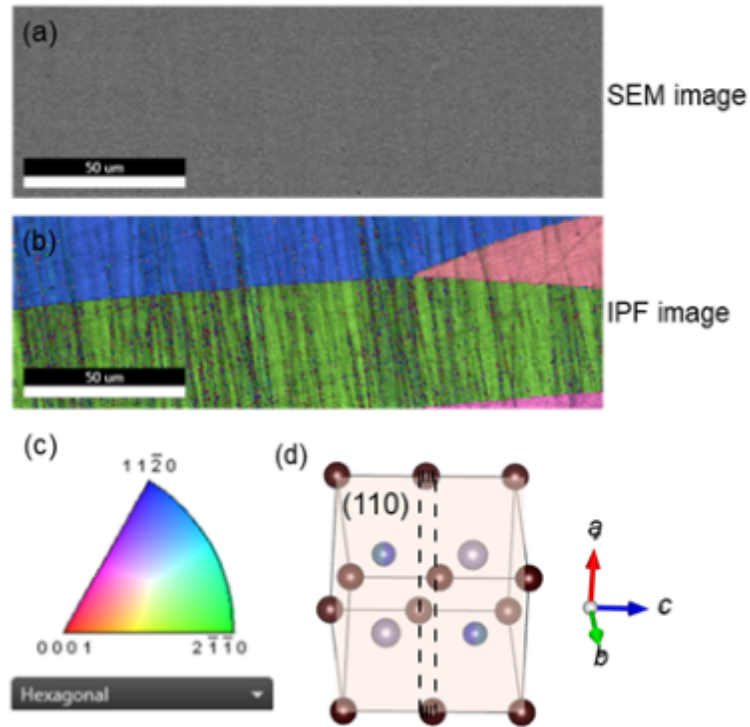


Figure 2.6: Model orientation map for the MnFeCoGe sample. (a) SEM image, (b) inverse pole figure (IPF) EBSD mapping of the sample which shows different grains in different colors. (c) IPF color bar to evaluate the crystal orientation of the sample. (d) The crystal structure, the corresponding (110) plane, and the cutting direction are marked with a black rectangle.



For the EBSD experiment, a finely polished sample surface without damage and oxidation coating is required, as the backscattered electrons diffracted from a few tens of nanometers of the sample. Since mechanical polishing leaves scratches on the sample surface, chemical polishing is necessary for a clean and smooth sample surface. In the EBSD experiment, the highly polished samples are tilted by 70 degrees from their horizontal axis to improve the signal to noise ratio of diffraction intensity. The working distance (distance between the sample surface and the SEM column's final lens) is kept between 18 to 22 mm to adjust the pattern center and decrease the noise in the Kikuchi pattern. The SEM image and the corresponding EBSD mapping are shown in Fig. 2.6.

## 2.4 X-ray diffraction (XRD)

W. C. Röntgen, a German physicist, first identified X-rays as electromagnetic radiation with few angstrom wavelength and particle-like properties [117]. Different characteristics of X-ray can be used to explain various phenomena related to X-ray radiation. The continuous X-ray spectrum can be produced in an X-ray tube, with an electron source and two electrodes with tens of kilovolt voltage differences. Here, the anode, or the target, acts as the source of X-ray radiation. When the electrons with sufficient kinetic energy rapidly decelerate, the radiations with different wavelengths are produced, known as continuous X-rays. When the voltage between the metal electrodes increases above a certain critical value, a sharp intensity spectrum with a particular wavelength related to the target characteristics is produced, along with the continuous spectrum. The continuous X-ray provides the background, whereas the characteristic X-ray with monochromatic radiation plays the leading role in the diffraction experiment. Production of characteristic X-rays can be explained in Fig. 2.7(a). When one of the  $K$ -shell electrons is knocked out by high energy electrons, the electrons from the higher energy shell fall to the vacant position of the  $K$ -shell to minimize the energy of the atom, and  $K_\alpha$  or  $K_\beta$  characteristic lines are formed. Due to the higher intensity of  $K_\alpha$  radiation, it is mainly

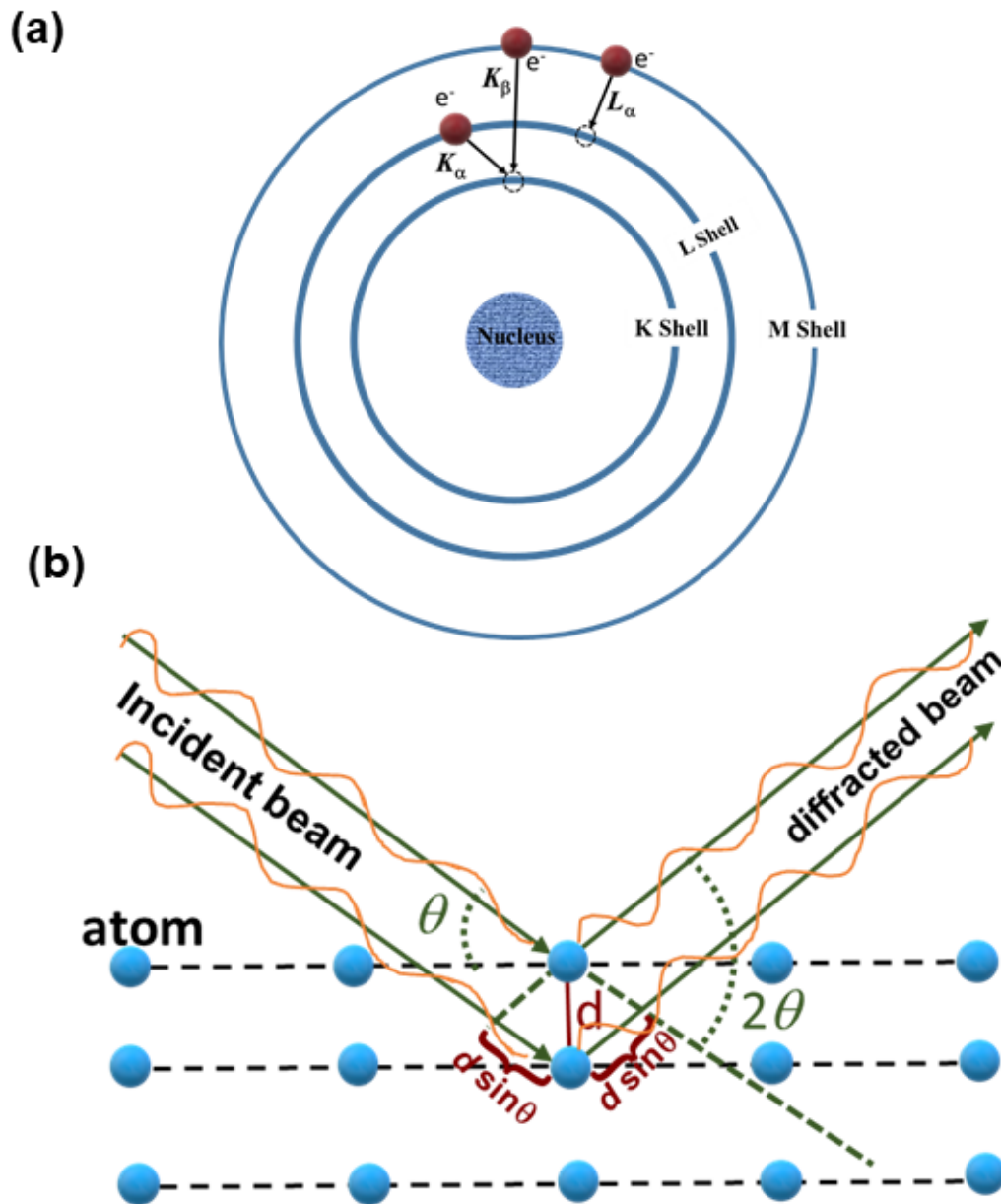


Figure 2.7: Schematic of (a) characteristic X-ray production in an atom and (b) x-ray diffraction and Bragg's law.

used for X-ray diffraction experiments.

In 1912, another German physicist M. von Laue experimentally demonstrated that a periodic crystal can scatter an X-ray, with a periodicity nearly equal to the X-ray wavelength [117]. Later, the necessary condition of X-ray diffraction was analyzed by two English physicists, W. H. Bragg and W. L. Bragg. They found that constructive interference can happen when the path difference between the incident and diffracted beam equals to an integer multiple of the X-ray wavelength, known as Bragg's law. As shown in Fig. 2.7(b), for the atomic planes with lattice spacing  $d$  and diffraction angle  $2\theta$ , Bragg's law can be written as,

$$2d\sin\theta = n\lambda \quad (2.1)$$

where  $\lambda$  is the x-ray wavelength. The lattice plane spacing is proportional to the lattice parameter of the crystal but can vary depending on different lattice planes with various Miller indices.

In this thesis, the X-ray diffraction of our material is carried out using a Rigaku smart lab X-ray diffractometer. The crystal structure of the samples are determined using Bragg's law and the peak position in the intensity vs.  $2\theta$  data. The XRD data in this investigation are fitted using the Fullprof program.

## 2.5 Superconducting quantum interference device (SQUID)-Vibrating sample magnetometer (VSM)

The superconducting quantum interference device (SQUID), made up of a Josephson junction (a thin insulating junction between two superconductors) is the most sensitive tool to measure tiny magnetic moments. The sample vibrates sinusoidally inside the pickup coil set in the SQUID-Vibrating sample magnetometer (VSM). The pickup coils are inductively coupled to the direct current (DC) SQUID through

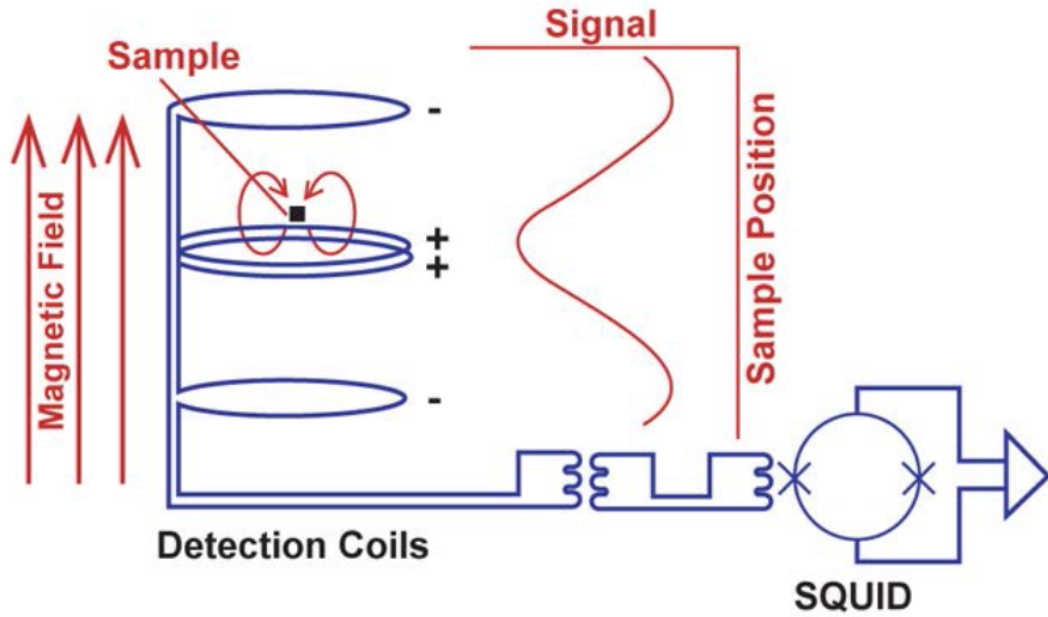


Figure 2.8: Schematic diagram of SQUID detection technique. The picture is taken from Quantum Design MPMS3 user manual. For further references see <https://qd-india.com>.

a transformer to measure the magnetic moment with high sensitivity. As shown in Fig. 2.8, the superconducting detection coil is made as a second-order gradiometer or counter wound loop geometry. This coil arrangement makes the detection coil non-responsive to the uniform magnetic field or linear magnetic field gradient. To generate the magnetic moment in the sample, a vertical magnetic field of a superconducting NbTi solenoid is used. When the sample vibrates inside the pickup coil, it induces a voltage in the pickup coil due to a change in magnetic flux according to Faraday's law.

$$E = -\frac{d\phi}{dt} \quad (2.2)$$

Now, current is generated in the coil because of the induced voltage. Due to the smaller sample size (recommended sample size < 5 mm ) compared to the dimension of the detection coil, the current induced in the detection coil is a function of sample position, as shown in Fig. 2.8. The induced current again converted to the voltage, as the detection coil is inductively coupled to the SQUID. Then, the SQUID voltage is multiplied and digitalized using the electronic parts of the instrument. The

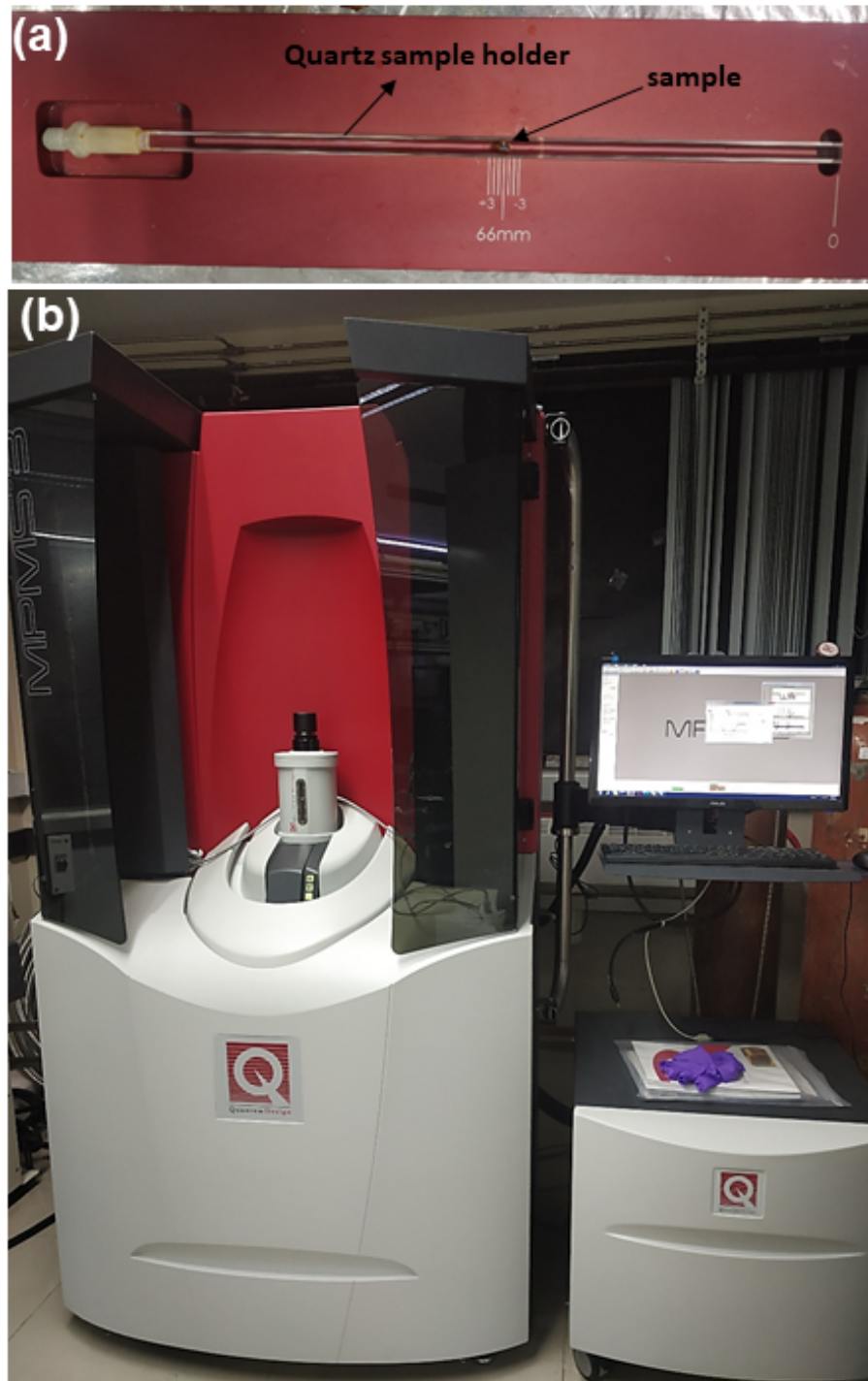


Figure 2.9: (a) Sample mounting station for SQUID-VSM. (b) Physical view of Quantum Design SQUID-VSM.

generated signal is used to calculate the magnetic moment of the sample.

For the present thesis, SQUID-VSM from Quantum Design is used for temperature/magnetic field vs. magnetic moment measurements. Figure 2.9 shows a physical view of a Quantum Design SQUID-VSM [Fig. 2.9 (b)] with sample mounting station [Fig. 2.9 (a)]. A maximum field of 7 Tesla and temperature ranging from 1.8 K- 400 K can be achieved in the present system. The magnetic moment calibration for the SQUID-VSM is done by measuring a standard palladium sample (a circular cylinder of 3 mm diameter and 3 mm height) over a range of magnetic fields. A magnetic moment of the order of  $10^{-8}$  emu to 3 emu can be measured accurately in the instrument. Magnetization ( $M$ ) vs temperature ( $T$ ) measurements are performed in both field cooled (FC) and zero field cooled (ZFC) modes. In ZFC mode, the sample is cooled to a low temperature without applying a magnetic field. Then the data are taken by applying a magnetic field while heating the sample. For the FC mode, the data are taken while cooling the sample with a magnetic field application.

## 2.6 Powder neutron diffraction (PND)

Although the mechanism of neutron diffraction (ND) and X-ray diffraction are similar, the neutron beam interacts with the material differently. The neutron beam mostly interacts with the atom's nuclei, whereas the X-rays primarily interact with the electron cloud that surrounds the nucleus. The neutron wavelength should be equivalent to the lattice spacing for the purpose of diffraction. Thus, thermal neutrons are employed to produce a wavelength of 1 - 2 Å. Since the neutron beam's scattering strength is independent of atomic weight, it may be used to identify light elements very effectively. Other than that, a neutron may be used as a probe to discover the system's microscopic magnetic moment since it carries a very small moment ( $-1.913 \mu_N$ , 1000 times less than an electron's).

The neutron diffraction exhibits different results depending on the magnetic ground states, as illustrated in Fig. 2.10. As shown in Fig. 2.10(a), only nuclear

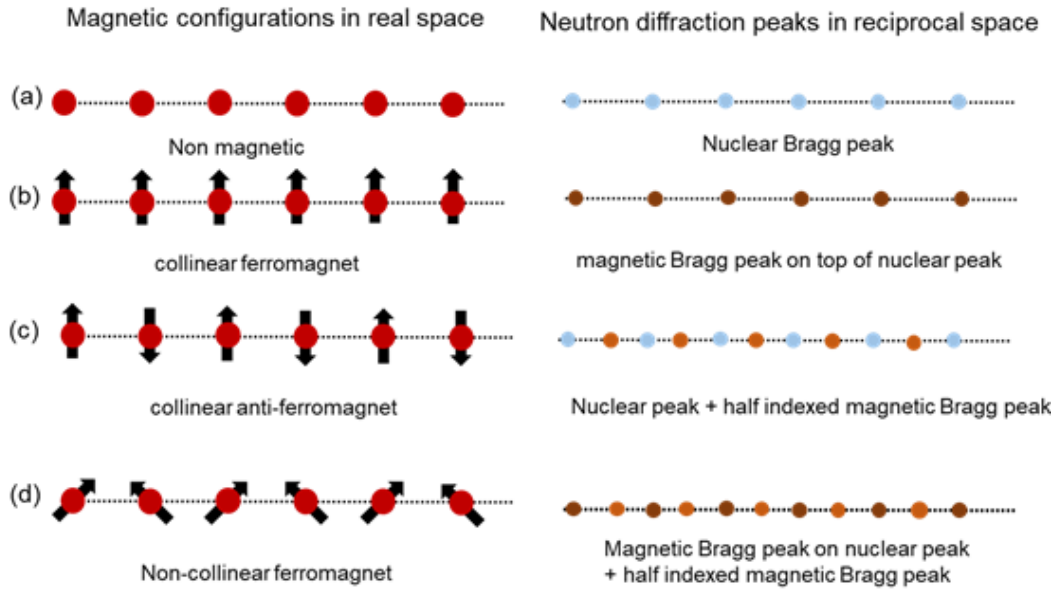


Figure 2.10: Schematic representation of different magnetic states along with their corresponding possible neutron diffraction. The idea of the schematic is taken from the reference [118].

peaks can be observed for the nonmagnetic samples however, for collinear ferromagnet, the magnetic Bragg peaks will emerge on top of the nuclear peaks [Fig. 2.10(b)]. In the case of a collinear antiferromagnet, the magnetic unit cell gets the periodicity double of the structural lattice parameter. As a result, half-indexed magnetic reflections are seen together with nuclear Bragg peaks [Fig. 2.10(c)]. For the non-collinear ferromagnet, as shown in Fig. 2.10(d), the magnetic reflections due to the existing ferromagnetic component appear on top of the nuclear reflections. In addition, half-indexed magnetic reflections also emerge simultaneously because of the antiferromagnetic component that coexists with the magnetic cell double of the lattice unit cell. Therefore, using these concepts make it possible to determine the sample's real magnetic ground state.

Here for the thesis work, the ND data are taken using the PD1 neutron diffractometer with  $\lambda = 1.094 \text{ \AA}$  at the Dhruva reactor in Bhabha Atomic Research Center, Mumbai.

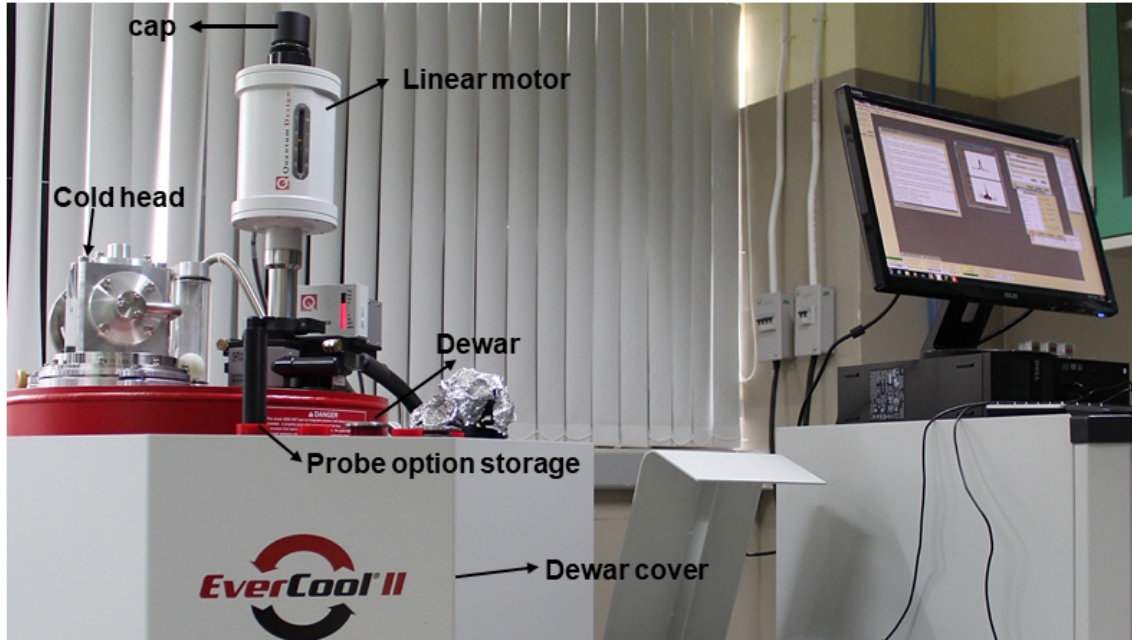


Figure 2.11: Physical view of physical property measurement system (PPMS).

## 2.7 Physical property measurement system (PPMS)

Physical property measurement system (PPMS) is a multipurpose instrument that can be used for a variety of measurements such as ac/dc transport, ac/dc magnetization, specific heat, thermal transport, etc. Here, Quantum Designed PPMS with Evercool II option is used. In Evercool II, the helium gas from a cylinder is directly transferred to the dewar with an integrated cryocooler (Cold head and the compressor) system as a liquefier. Also, the re-condensation of cold helium gas before it escapes helps to minimize the liquid helium loss effectively, making the Evercool II option more efficient for PPMS. The Evercool option is fully automated with the Multiview software. Dewar pressure is always maintained higher than atmospheric pressure to avoid air leaking in dewar. The physical View of PPMS is illustrated in Fig. 2.11.



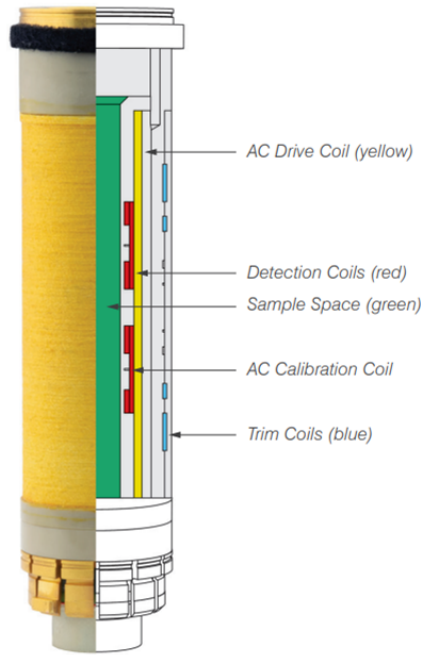


Figure 2.12: Schematic representation of ac measurement system (ACMS) coil. The picture is taken from the Quantum design website. For further references see <https://qd-india.com>.

### 2.7.1 Ac measurement system

Ac measurement system (ACMS II) option in PPMS can be utilized to measure both ac and dc magnetic properties using an ACMS coil set. The physical view of the ACMS II coil is shown in Fig. 2.12. The coil set contains one ac drive coil for applying an ac magnetic field up to 17 Oe with frequencies ranging from 10 to 10000 Hz. The detection coil is made of first-order gradiometer geometry (two opposite wound copper coils connected in series) to eliminate the effect of a uniform background field. All the ac drive and detection coils are concentric with the superconducting magnet of PPMS. For the dc measurement, the sample vibrates at the center of the gradiometer, and dc moment measurements are performed based on the voltage generation by Faraday's law as a result of magnetic flux change caused by sample vibration.

For ac measurements, the sample is positioned at the center of each detection coil, and the alternative field is applied in superposition with the dc field. Therefore,

the change in magnetization by the ac drive field generates the signal in the detection coil. During the ac measurement, the detection coil, along with the calibration coil (a low inductance coil situated inside the detection coil), helps to identify the phase and amplitude accurately. ACMS coil can differentiate between the in-phase and out-of-phase components of ac susceptibility. The ac susceptibility can be calculated by dividing the change in magnetic field amplitude ( $dH$ ) from a change in the moment ( $dM$ ),

$$\chi = dM/dH \quad (2.3)$$

Due to the high frequency of the ac magnetic field, the sample moment cannot follow the drive field frequency. As a result, a phase lag between the ac drive field and the measured signal is introduced. Thus, the susceptibility can have two components, one is the in-phase or real component and the other is the out-of-phase or imaginary component. The real and imaginary parts of the waveform are extracted by comparing the waveform to the drive signal. If the amplitude of the susceptibility is  $\chi$  and the phase lag is  $\phi$ , we can write the real ac susceptibility ( $\chi'$ ) and the imaginary ac susceptibility ( $\chi''$ ) as,

$$\chi' = \chi \cos \phi \implies \chi = \sqrt{\chi'^2 + \chi''^2} \quad (2.4)$$

$$\chi'' = \chi \sin \phi \implies \phi = \arctan\left(\frac{\chi''}{\chi'}\right) \quad (2.5)$$

$\chi'$  is mainly related to the change of slope of  $M$  vs.  $H$  measurement ( $dM/dH$ ), whereas  $\chi''$  is mainly related to the dissipation in the system. Both  $\chi'$  and  $\chi''$  are sensitive to thermodynamic changes like first-order phase transition. These features make the ac susceptibility measurement very efficient to indirectly verify the existence of magnetic phase transitions in the samples, as observed in the case of helical to the skyrmion phase transition. In this study, the isothermal magnetic field-dependent ac susceptibility is measured at various temperatures with a frequency of 331 Hz and an ac field amplitude of 10 Oe.

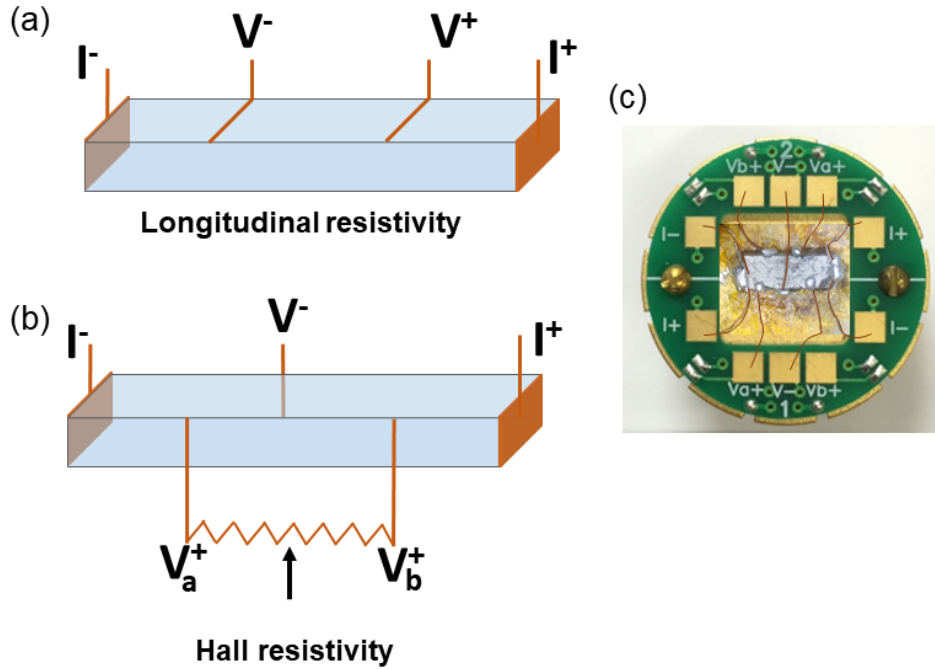


Figure 2.13: Schematic diagram of (a) longitudinal and (b) Hall resistivity measurement setup. (c) The physical view of an ACT sample puck along with the sample. The connections are made using copper wire and indium soldering.

### 2.7.2 Ac magneto-transport measurement

The ac transport (ACT) option in the PPMS with a precision current source and voltage detector is the approach used to assess the electronic resistivity of the sample. The precision current source has a resolution of  $0.02 \mu\text{A}$  and the possible maximum current amplitude is 2 A. Typically, the measurements are taken by putting the sample in a puck and the connections are then made in the manner as illustrated in Fig. 2.13. The rectangular bar shaped samples are subjected to a continuous current along their long axis. The current connections are created with uniform contact across the edges to ensure a uniform flow of current throughout the sample. To eliminate the influence of contact resistance, a four probe design with two voltage and two current contacts is employed for the longitudinal resistivity measurement

[Fig. 2.13 (a)]. The resistivity can be calculated based on the formula,

$$\rho = \frac{VA}{Il} \quad (2.6)$$

where  $V$  is the measured voltage drop,  $I$  is the applied current through the sample,  $A$  is the cross sectional area through which the current flows, and  $l$  is the voltage lead separation.

For the Hall voltage measurement, the voltage contacts must be placed in a perfect perpendicular manner to the current contact. However, making the connection perfectly in the same line is quite difficult to implement. Practically, there is always a misalignment that produces a non-zero magneto-resistance (MR) component with the Hall resistance. As a result, to avoid the MR contribution, the five probe Hall measurement approach is employed [Fig 2.13 (b)]. In the five-probe geometry, there are three voltage contacts, where balancing with zero resistance at zero magnetic fields can be accomplished by a potentiometer in between two of the voltage contacts.

The ACT option can supply ac current with frequencies ranging from 1 Hz to 1 kHz, and it provides an advantage over dc measurement via signal filtering. In the filtering process, the output signal is collected with a known specific driving frequency, whereas other contributions with different frequencies, dc offset, and instrumental drift noise are removed.

Here, the Hall transport measurements of the samples in between 2 K to 300 K are performed using the ACT option of Quantum design PPMS where the ac current of 20-30 mA with a frequency of 131 Hz is used.

## 2.8 Transmission electron microscopy (TEM)

In TEM, the high energy electron beam is transmitted through a thinned sample specimen of thickness  $< 200$  nm, and an image is produced due to the scattering of the electron beam while passing through the sample. The electrons can be produced

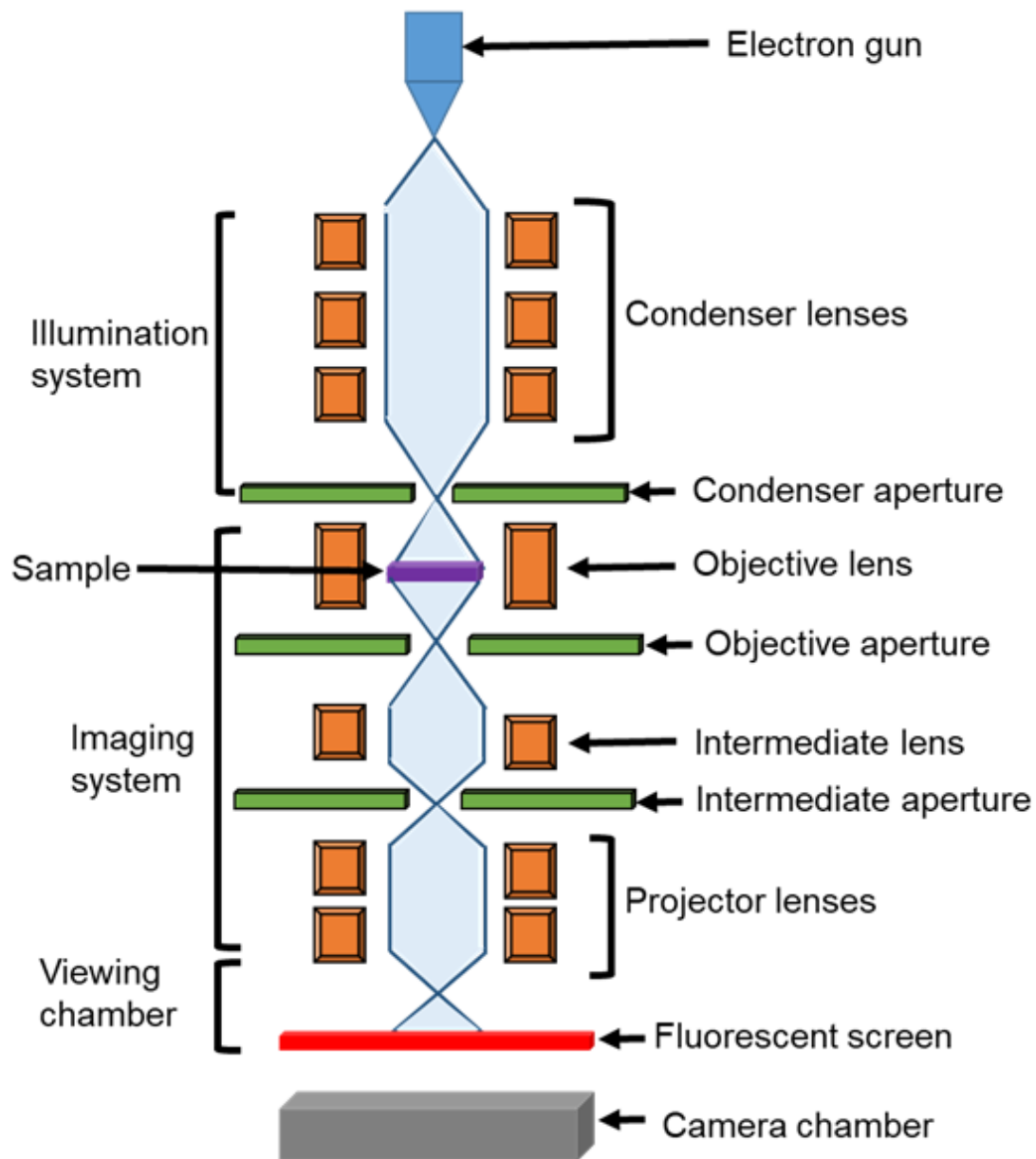


Figure 2.14: Schematic diagram of different parts of transmission electron microscopy (TEM). The idea of the image is taken from <https://bitesizebio.com/29197/electron-microscopy-techniques>

by an electron gun with a thermionic or field emission mechanism. Recently, field emission electron guns have achieved high preference due to their coherent characteristics. The emitted electrons are then accelerated to a high voltage of 100-200 kV to achieve the experimental goal. The electrons travel with relativistic velocity in the TEM and its wavelength ( $\lambda$ ) can be calculated by using the formula,

$$\lambda = \frac{h}{\sqrt{2m_0eV(1 + \frac{eV}{2m_0c^2})}} \quad (2.7)$$

where  $h$  is Planck's constant,  $m_0$  is the rest mass of an electron,  $e$  is the electron charge,  $V$  is accelerating voltage and  $c$  is the speed of light. This highly accelerated electron beam path is controlled by a series of electromagnetic lenses and apertures, as schematically shown in Fig. 2.14. The condenser lens and apertures above the sample specimen, control the illumination area and intensity of the electron beam on the sample. The objective lens near the sample specimen plays the leading role in producing the sample's image, which is further magnified by intermediate and projector lenses. The resolution of a 200 keV TEM can be a few angstroms to sub-angstroms.

### 2.8.1 Selected area electron diffraction (SAED)

Electron diffraction, considering the wave nature of electrons can be helpful for the characterization of the sample's crystal structure. Electron diffraction can also be described with Bragg's law similar to that of XRD, as explained in equation 2.1. Both the diffraction and image pattern of the sample can be achieved using different modes of TEM operation. As schematically shown in Fig.2.15, the intermediate lens acts as the selector between image mode and diffraction mode in the TEM. The diffraction pattern forms when the intermediate lens is focused on the back focal plane [Fig. 2.15 (b)]. If the intermediate lens is focused on the first image plane, a sample image can be formed [Fig. 2.15 (a)], which is further magnified by the projector lens. The diffraction pattern from the particular selected area of the

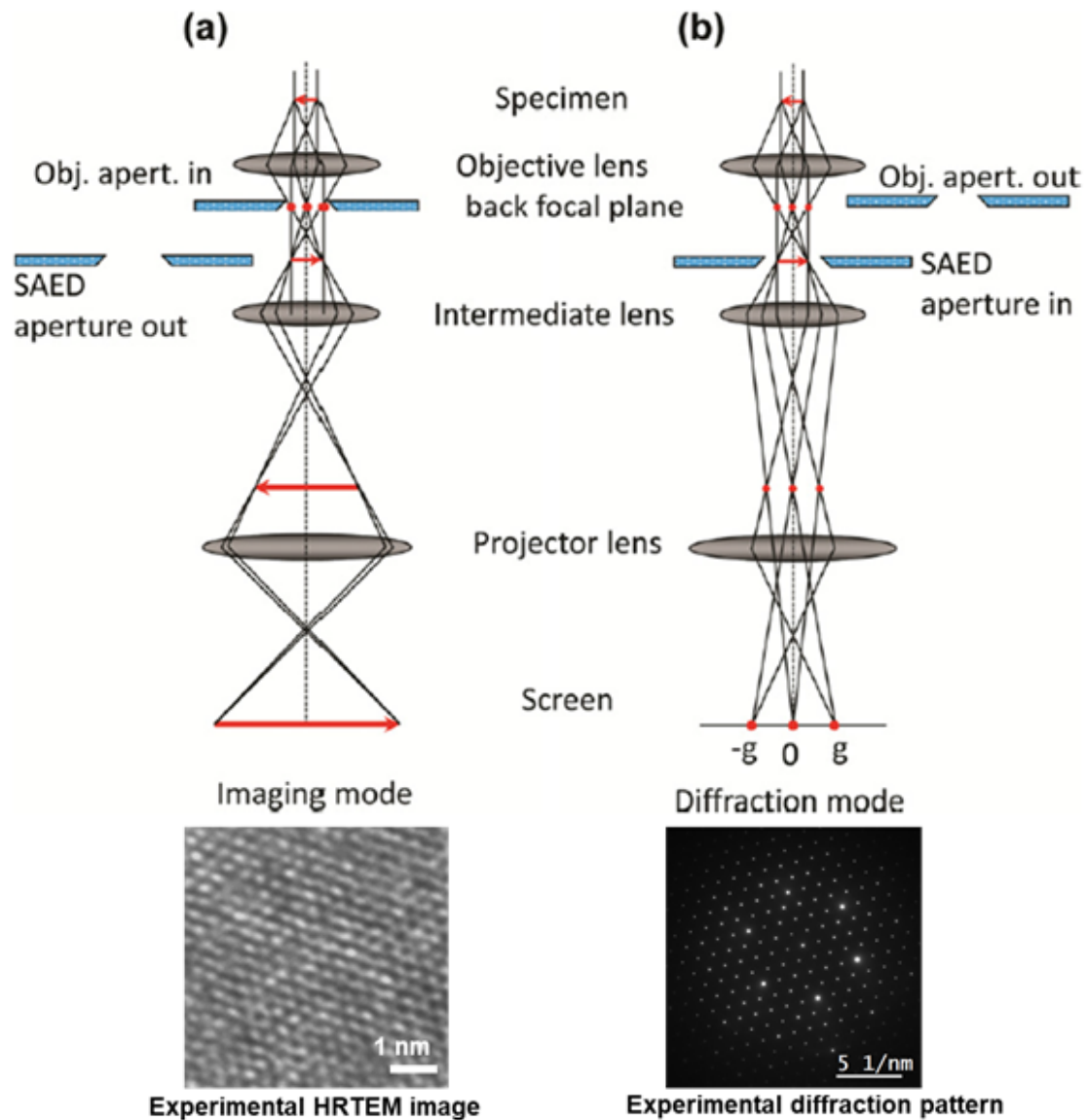


Figure 2.15: Schematic representation as well as real experimental images of two different measurement modes possible in TEM. (a) Imaging mode, (b) Diffraction mode. The idea of the schematic is taken from the reference [119].

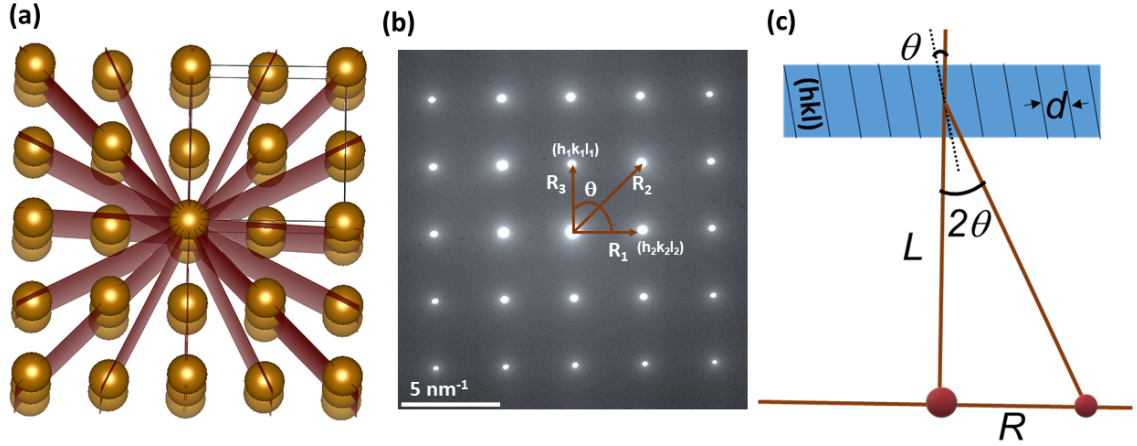


Figure 2.16: (a) A crystal lattice with lattice planes and (b) corresponding possible SAED pattern. (c) Schematic representation of the relation between different parameters for the indexing of diffraction spots.

sample can be achieved by using a selected area aperture, as schematically shown in Fig. 2.15 (b).

Figure 2.16 (a) shows a crystalline atomic structure with different lattice planes, and Fig. 2.16 (b) shows the corresponding SAED diffraction pattern. The diffraction spot for each of the  $(hkl)$  reflections can be identified by measuring its distance from the central spot and the angle between the consecutive spots. As shown in Fig. 2.16 (c), we have  $2\theta = \frac{R}{L}$ , where  $L$  is the camera length, and  $R$  is the distance of the diffraction spot from the central diffraction spot (000). From Bragg's law in equation 2.1,  $2\sin\theta = \frac{\lambda}{d}$ . If  $\theta$  is considered very small, the relation can be written as,

$$\frac{R}{L} = \frac{\lambda}{d} \implies Rd = L\lambda \quad (2.8)$$

Then by knowing the camera length and measuring the distance  $R$ , one can calculate the lattice spacing  $d = \frac{L\lambda}{R}$ . By comparing the calculated  $d$  value with the reported JCPDS database  $d$  values of the same sample, one can decide the  $(hkl)$  family corresponding to the diffraction spot. The different diffraction spots belonging to the same  $(hkl)$  family can be identified by calculating the angle  $(\theta)$



between  $R$  vectors of different spots using the relation,

$$\cos \theta = \frac{\vec{R}_1 \cdot \vec{R}_3}{|\vec{R}_1| |\vec{R}_3|} = \frac{h_1 h_2 + k_1 k_2 + l_1 l_2}{\sqrt{h_1^2 + k_1^2 + l_1^2} \sqrt{h_2^2 + k_2^2 + l_2^2}} \quad (2.9)$$

### 2.8.2 Lorentz transmission electron microscopy (LTEM)

Lorentz transmission electron microscopy (LTEM) works based on Lorentz force, and it can only detect the in-plane components of magnetic moments. As explained schematically (Fig. 2.17), when an electron beam passes through the magnetic sample, the magnetic moments act as a magnetic field on the electron beam. As a result, the electron beam deviates from its straight-line path due to the Lorentz force,

$$F_L = -e(\vec{v} \times \vec{B}) \quad (2.10)$$

, where  $e$  is the electron charge,  $\vec{v}$  is the electron velocity, and  $\vec{B}$  is the magnetic field. It gives detailed information about the magnetic domain walls with a few tens of nm resolutions. Although LTEM cannot detect the out-of-plane component of the magnetic moment, it is advantageous to study the nanometric spin texture with varying magnetic moment orientation and nonzero in-plane components.

To explain the experimental condition, in the schematic (Fig. 2.17), a specimen with a 180-degree domain wall is considered. When the parallel electron beam passes through the magnetic sample, the electrons are deflected in the opposite way for opposite magnetizations in the 180-degree domains. These deflected electron beams contain information about the deflecting magnetic domains. In the Fresnel mode, no magnetic contrast is observed for the in-focus condition, whereas the domain wall is observed as a white or black line in the defocus condition, as shown in Fig. 2.17 (a)-(c). In the under-focus (UF) condition, the domain wall is observed as a white line due to the enhancement of electron beam intensity near the domain wall (Fig. 2.17 (b)). Similarly in the over-focus (OF) condition, the domain walls show dark contrast due to a decrease in electron intensity (Fig. 2.17 (c)). Although the

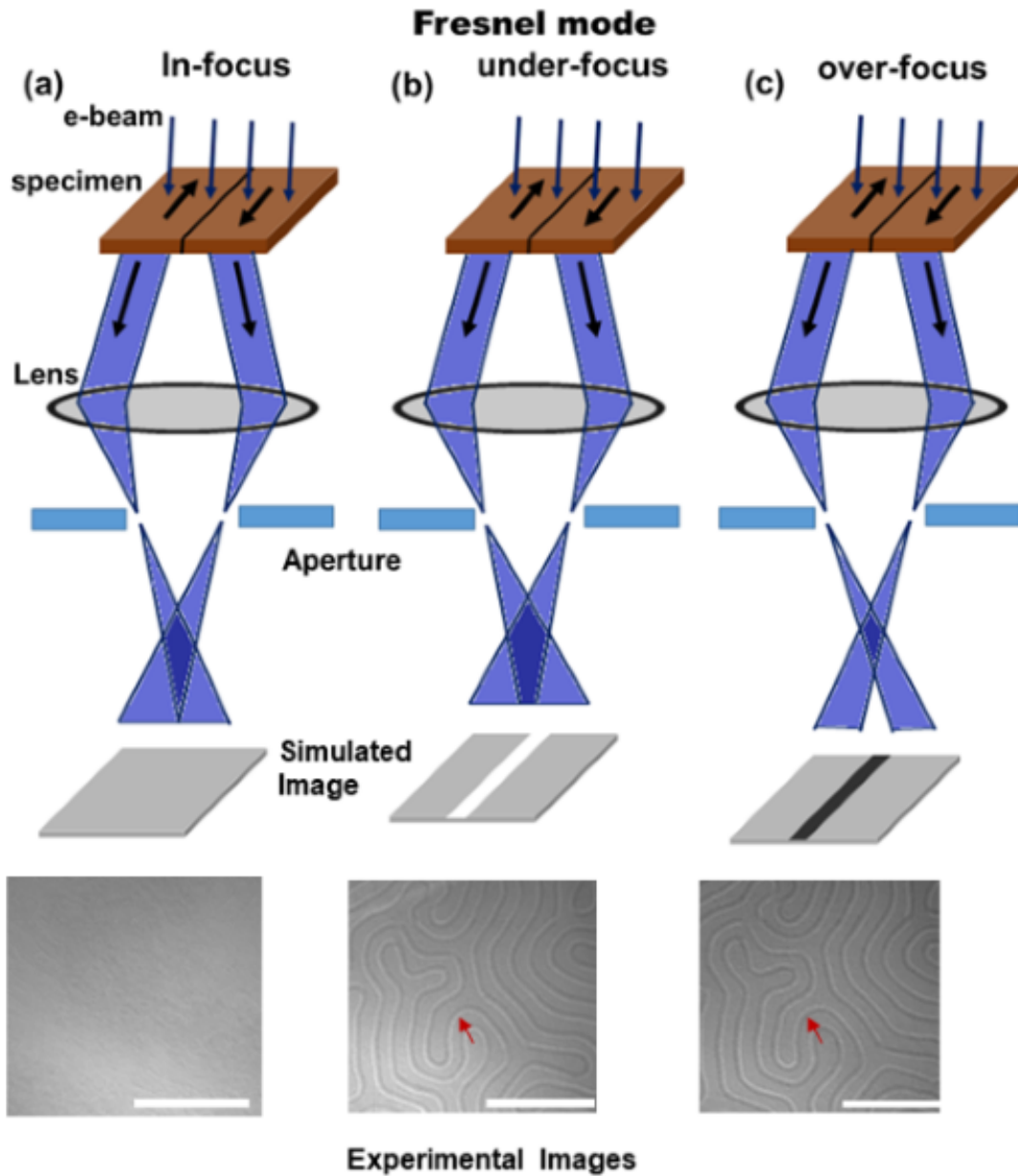


Figure 2.17: Schematic ray diagram representation of electron beam and the images for LTEM in Fresnel mode. Black arrows in the sample specimen represent the moment direction in different magnetic domains. The arrows in the real experimental images point to the white line in under focused condition that turns to the black contrast in over-focused condition. The scale bars in experimental images represent 500 nm. The idea of the image is taken from [120]

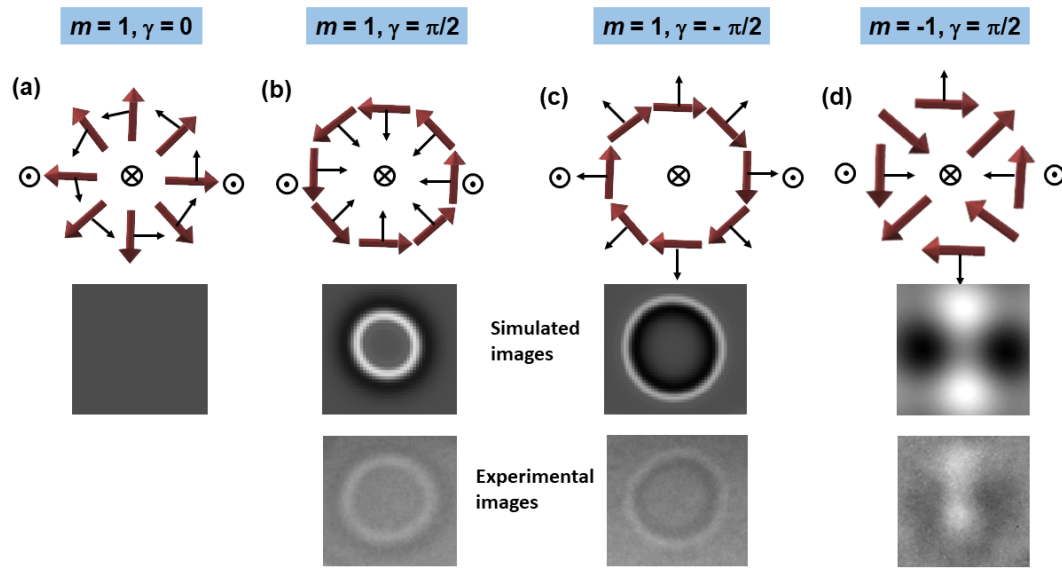


Figure 2.18: Schematic representation of electron beam deflection in LTEM by different types of skyrmions and the corresponding simulated as well as experimental real space LTEM images. (a) Neel skyrmion, (b-c) Bloch skyrmion, and (d) Antiskyrmion. The maroon arrows represent the in plane component of spin texture and the black arrows represent the direction of electron deflection. The cross and dot sign represent the downward and upward spin direction. The picture of anti-skyrmion are taken from the reference [44].

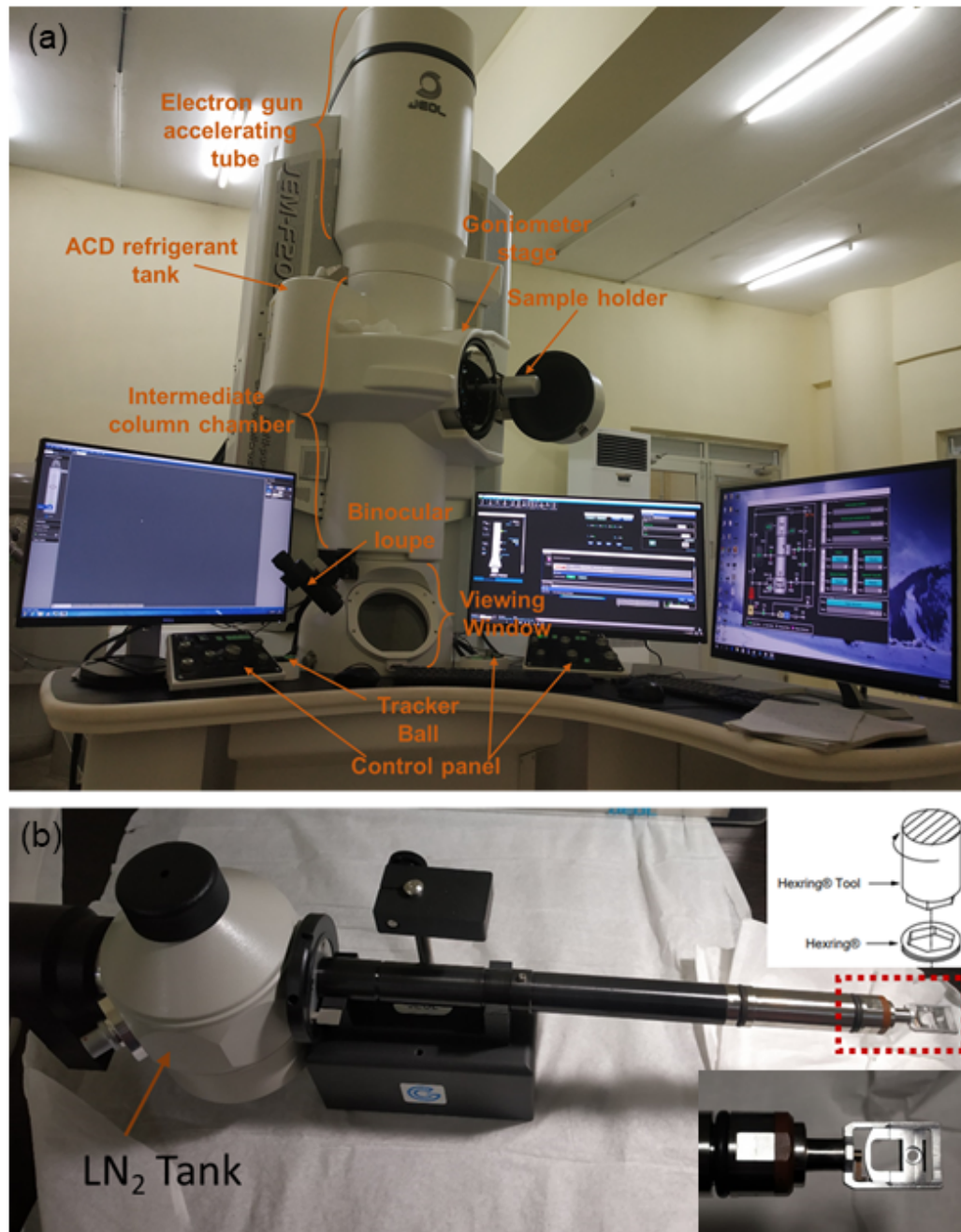


Figure 2.19: External view of (a) TEM with model JEMF200, (b) double tilt beryllium cooling holder.

spatial resolution of LTEM in Fresnel mode is less compared to the other mode due to the observation in defocused conditions, it is beneficial for extensive study of domain walls and spatially varying spin structures. For this study, Fresnel mode is used to observe the topological spatially varying spin textures like skyrmion. The electron deflection in LTEM, for different types of skyrmion and the corresponding simulated as well as real space LTEM images are shown in Fig. 2.18. As shown in Fig. 2.18(b)-(c), the electron beam either diverges or converges towards the center depending on the chirality of the Bloch skyrmion. As a result, circular dark and bright rings are formed in the LTEM images of Bloch skyrmion. Whereas for the Neel skyrmion shown in Fig. 2.18(a), no magnetic contrast can be observed due to the constant phase difference between the deflected electron beams. Figure 2.18(d) shows the antiskyrmion, with two Bloch walls having opposite chirality and 90 degrees apart, which gives four alternative bright and dark spots kind of contrasts in the LTEM image.

Generally, The TEM samples are examined under the high current objective lens (OL) (MAG mode) for regular TEM operation. In these conditions, around 3 T magnetic field is present near the sample space, which may lead to the saturated magnetic state, thereby destroying any magnetic contrast. The magnetic domain states are observed in the LOW MAG mode with OL turned off. To apply any magnetic field to the sample, the OL current can be applied in a controlled manner using the "lens-free control option." The residual magnetic field on the sample while keeping OL turned off remains around 200 Oe for this system.

The physical view of the TEM instrument is shown in Fig. 2.19(a), here a 200 keV TEM with model JEMF200 is used for the experiment. The sample is inserted into the column chamber with a specimen holder. For the HRTEM, SAED pattern observation, and low temperature LTEM imaging, a double tilt beryllium TEM holder with a liquid nitrogen chamber is utilized [Fig. 2.19(b)].

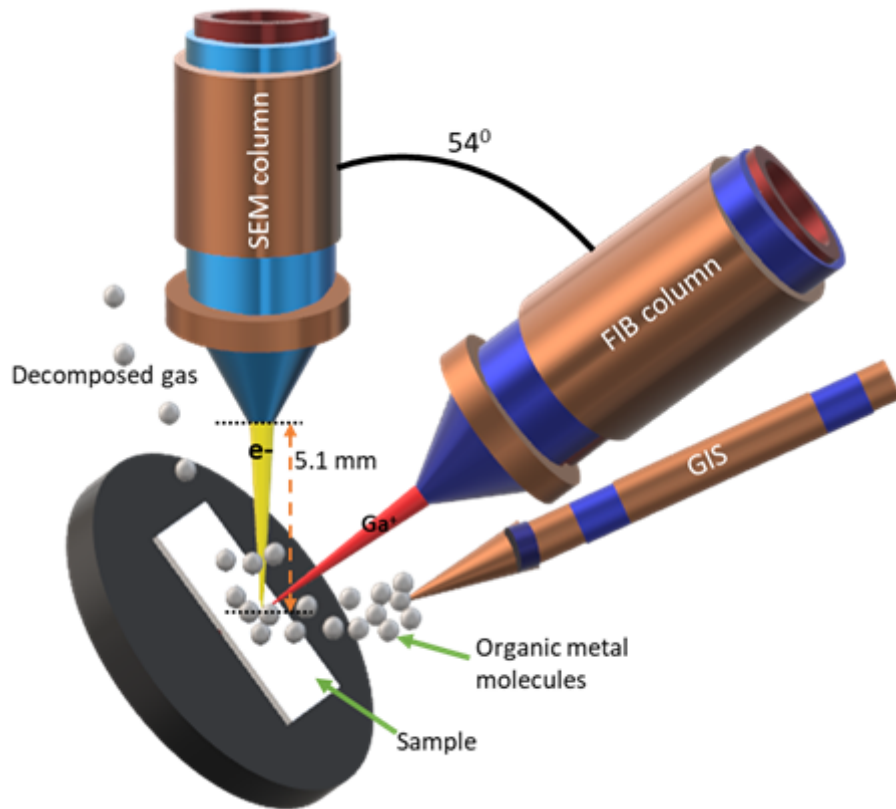


Figure 2.20: Schematic representation of FIB experiment.

## 2.9 TEM sample preparation technique

The main drawback of the TEM instrument is its laborious sample preparation techniques. Here, the  $\text{Ga}^+$  ion-based focused ion beam (FIB) technique is used for thin lamella preparation. In order to determine the necessary grain in polycrystalline materials, an SEM based electron backscatter diffraction (EBSD) unit is used [already discussed in section 2.3].

### 2.9.1 Focused ion beam (FIB)

After selecting the required grain area, thin lamella is cut using the  $\text{Ga}^+$  ion-based focused ion beam (FIB) technique. The schematic of the FIB experimental setup is shown in Fig. 2.20. Here, a dual column system (Zeiss Gemini SEM/FIB) comprising an SEM and ion beam column is used for this study [Fig. 2.21]. The  $\text{Ga}^+$  ion beam



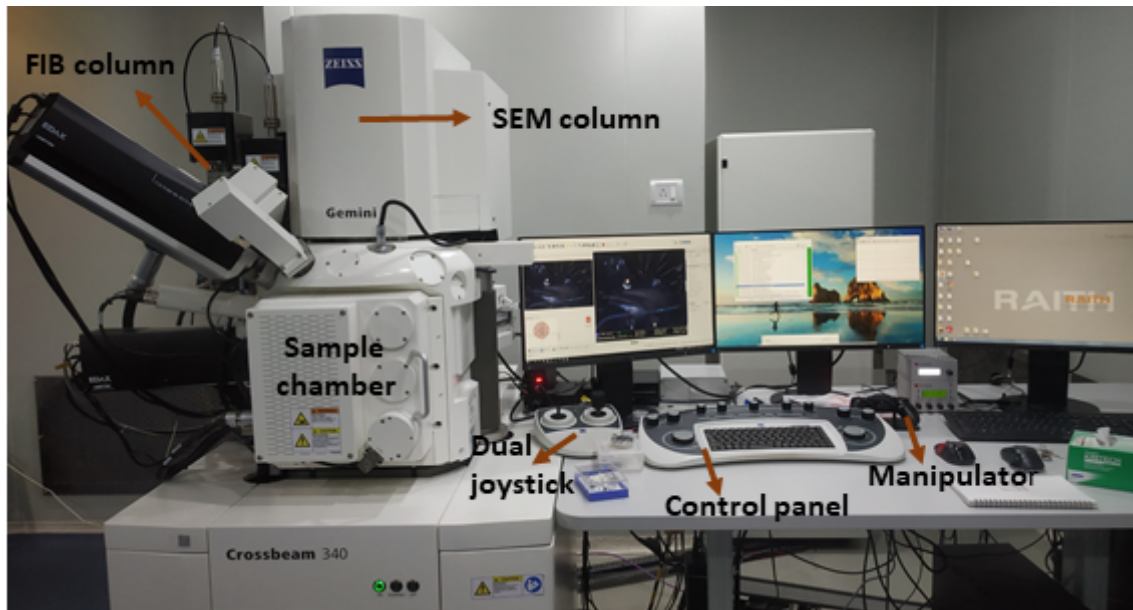


Figure 2.21: Picture of a crossbeam duel column FIB/SEM system used for the TEM sample preparation.

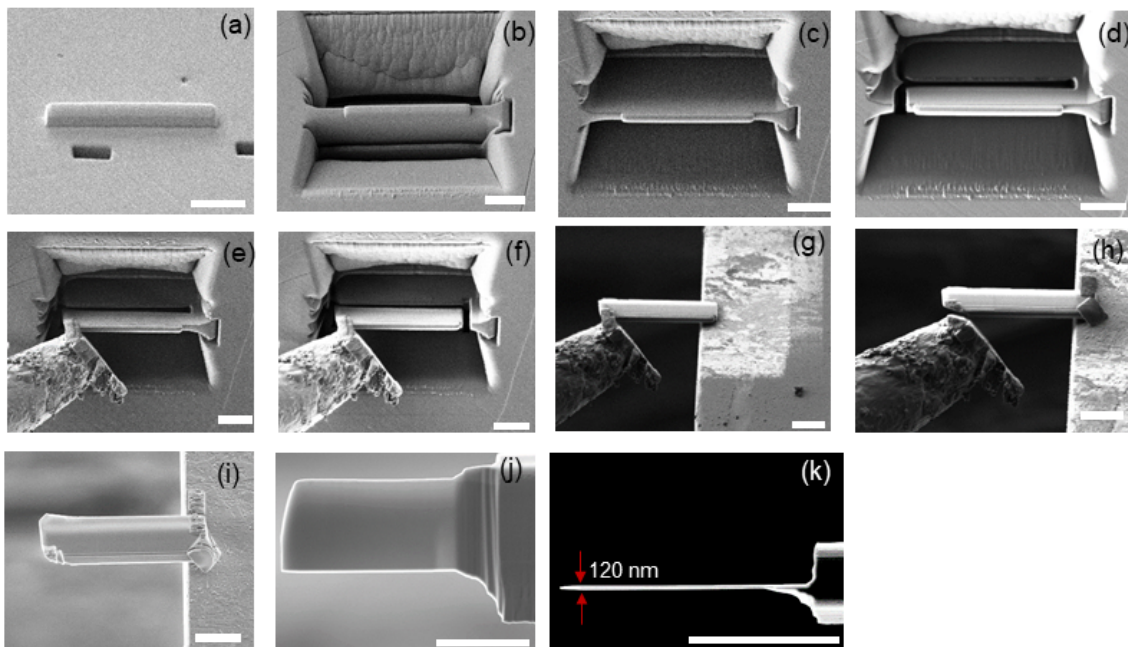


Figure 2.22: Different steps of Lamella preparation for the sample  $\text{Mn}_4\text{Ga}_2\text{Sn}$  using a FIB. The scale bars in each figure correspond to  $5\text{ }\mu\text{m}$ .

column is situated at a 54 degree angle with respect to the vertical SEM column. Here, the FIB column contains a liquid metal ion source (LMIS) suitable to focus ions in a few nanometer spots on the sample. Ga has a low melting point ( $< 30^{\circ}\text{C}$ ) and lower vapor pressure. As a result, Ga LMIS can be easily operated at room temperature. Therefore, Ga is preferred over other metals for LMIS applications. FIB can be operated in the energy range 2-30 keV. This high energy ion beam is typically used to remove materials from a sample. Materials deposition can be achieved in the FIB when it is simultaneously used with a gas injection system (GIS). GIS basically used to supply the organometallic gases on the sample surface locally. The precursor molecules are absorbed by the sample surface due to the Van der Waals forces. The secondary electrons produced due to collision between the primary ion beam and surface atoms help to dissociate the hydrocarbon precursor molecules, resulting in the local deposition of metals (Pt, W, Au) on the sample surface. Masks of different shapes are employed in the FIB system at various stages of thin lamella preparation for material deposition, cutting, and polishing. A manipulator was utilized to take the lamella from the bulk sample and place it on the five-handed copper grid with a half-moon geometry.

In this study, cross sectional lamellas are made using the steps mentioned below. **Step 1:** After selecting the necessary sample region, the stage is tilted to a 54 degrees angle with respect to the electron beam column. Then, a protective layer of almost 1-micron thick platinum is deposited, using GIS and a  $\text{Ga}^{+}$  ion beam [SEM view at  $0^{\circ}$  is shown in Fig. 2.22(a)]. The protection layer helps to minimize the damage of the lamella during ion milling. **Step 2:** In the following stage, a rough cutting with a high current (30 kV, 7 nA) is performed around the Pt deposited area. The cross sectional cutting view using the FIB probe is shown in Fig. 2.22(b). Further milling is conducted on both sides of the Pt deposited region to reduce thickness gradients in the lamella by tilting the stage to  $\pm 2$  degrees (56 degrees for front-side polishing and 52 degrees for backside polishing). In this case, beam currents of 700 pA and 300 pA are employed to polish both sides of the lamella. **Step 3:** The stage was then tilted back to 20 degrees, and an L cut was conducted on the micron-size



sample using the ion beam. The lamella's appearance in the FIB probe before and after the L cut is depicted in Fig. 2.22(c)-(d). **Step 4:** The micrometer-sized sample is lifted off using a nano-manipulator. The manipulator is properly positioned and attached to the lamella via Pt soldering [Fig. 2.22(e)]. Then, the other side of the lamella is separated from the bulk sample, and the lamella is taken off using the manipulator [Fig. 2.22(f)]. **Step 5:** After lift off, the micrometer-sized sample is placed on a five-armed half-moon grid [Fig. 2.22(g)] and fixed to the grid using Pt plating. The manipulator is then separated from the sample lamella [Fig. 2.22(h)]. **Step 6:** The stage is again tilted back to 54 degrees, and the up and down sides of the lamella are polished with a low current (30 kV, 50 pA) ion beam to achieve the required electron beam transparent lamella thickness. The SEM and FIB view of the lamella about 120 nm thick are shown in Fig. 2.22(i)-(k), respectively.

## 2.10 Theoretical analysis

To understand the effect of different energy terms on the stability of topological skyrmion-like spin textures, micromagnetic simulations are performed.

### 2.10.1 Micromagnetic simulations

Micromagnetics deals with the magnetic behavior at the micron or sub-micron level. Here, using the continuum approximation, the length scales are considered in micron size. Micromagnetics was introduced theoretically in 1963 by William Fuller Brown Jr. Static micromagnetics deals with energy minimization and relaxes the system based on the time dependent LLG (Landau–Lifshitz–Gilbert) equation. LLG equation describes the magnetization dynamics around an effective field with an additional damping term. The Landau–Lifshitz ordinary differential equation can be written as,

$$\frac{d\vec{m}}{dt} = -\frac{|\gamma|}{1+\alpha^2}\vec{m} \times \vec{H}_{eff} - \frac{\alpha|\gamma|}{1+\alpha^2}\vec{m} \times (\vec{m} \times \vec{H}_{eff}) \quad (2.11)$$

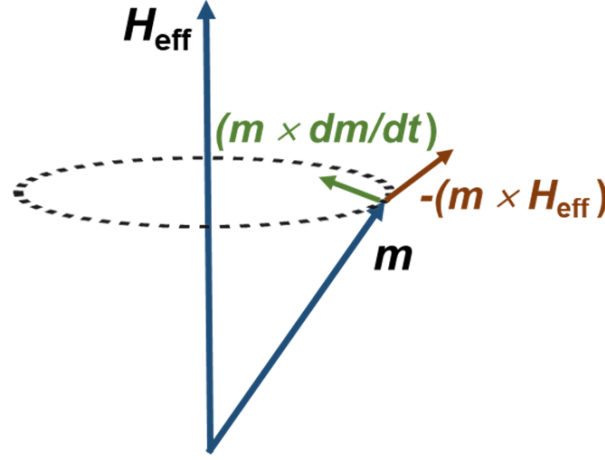


Figure 2.23: Schematic diagram of damping precession of magnetization according to the LLG equation.

where  $\vec{m}$  is system moment,  $H_{eff}$  is the effective magnetic field,  $\gamma$  is the electron gyromagnetic ratio and  $\alpha$  is the Gilbert damping constant. In Gilbert form, the equation can be written as,

$$\frac{d\vec{m}}{dt} = -|\gamma| \vec{m} \times H_{eff} + \frac{\alpha}{m_s} (\vec{m} \times \frac{d\vec{m}}{dt}) \quad (2.12)$$

where  $m_s$  is the saturation magnetization. The schematic representation of the damping process is shown in Fig. 2.23.

The simulation involves magnetic Gibbs free energy derived by Brown in 1963,

$$E = \int (e_{ex} + e_Z + e_a + e_d) dv \quad (2.13)$$

where  $e_{ex}$  is the exchange energy which indicates interaction between two spins,  $e_Z$  is the Zeeman energy,  $e_a$  is the volume anisotropy energy depending on the system properties, and  $e_d$  is the demagnetization energy mimics the dipolar nature of the system under consideration. In continuum expression, we can write the exchange energy as,

$$e_{ex} = A \int_v ((\nabla m_x)^2 + (\nabla m_y)^2 + (\nabla m_z)^2) dv \quad (2.14)$$

where  $A$  is the exchange stiffness constant and  $m_x$ ,  $m_y$ , and  $m_z$  are magnetization in the  $x$ ,  $y$ , and  $z$  directions respectively. Uniaxial anisotropy energy in (001) direction can be written as,

$$e_a = \int_v -K_z(m_z)^2 dv \quad (2.15)$$

where  $K_z$  is the anisotropy constant in the (001) direction. The Zeeman energy can be written as,

$$e_Z = -\frac{\mu_0}{2} \int_v m \cdot H dv \quad (2.16)$$

where  $H$  is the applied field and  $m$  is magnetization. The demagnetization energy can be written as,

$$e_d = -\frac{\mu_0}{2} \int_v m \cdot H_d dv \quad (2.17)$$

where  $H_d$  is the demagnetization field and can be expressed as,

$$H_d = -\frac{1}{4\pi} \int_v (\nabla \cdot m) \frac{\vec{r}}{r^3} dv \quad (2.18)$$

where  $\vec{r}$  is a vector pointing from the current integration point to the point where  $H_d$  is calculated.

Here for this study, OOMMF (Object Oriented Micromagnetic Framework) code [check OOMMF user guide] is used to simulate the spin textures with varying system parameters like exchange stiffness constant ( $A$  in J/m), magnetization ( $M$  in A/m), anisotropy constant ( $K$  in J/m<sup>3</sup>) and magnetic field ( $H$  in tesla). Mike Donahue and Don Porter developed the OOMMF code in the Information Technology Laboratory (ITL) at the National Institute of Standards and Technology (NIST). The magnetic states are achieved by fully relaxing the system starting from the random magnetic state with different parameters at 0 K temperature. A grid size of 4 nm  $\times$  4 nm  $\times$  4 nm geometry is used for the present study.

### 2.10.2 Lorentz-TEM simulations

The LTEM images corresponding to the OOMMF simulated spin textures are reconstructed using Pylorentz master code [available online], integrated with Python workflows. The .ovf and .omf files produced by the OOMMF simulations can be utilized as input in this case. The phase image of the provided magnetization is then produced using the Mansuripur algorithm or the linear superposition approach. After that, the phase picture is employed to generate the expected LTEM image.

### 2.10.3 Transport of intensity equation (TIE) analysis

The transport of intensity equation (TIE) is the differential equation that relates the intensity  $[I(xyz)]$  and phase  $[\phi(xyz)]$  of an object wave,

$$\frac{\pi}{\lambda} \frac{\delta I(xyz)}{\delta z} = -\nabla_{xy} \cdot (I(xyz) \nabla_{xy} \phi(xyz)) \quad (2.19)$$

$\nabla_{xy}$  is 2D gradient operator, i.e.,

$$\nabla_{xy} \phi(xyz) = \left( \frac{\delta \phi}{\delta x}, \frac{\delta \phi}{\delta y} \right) \quad (2.20)$$

Here, the TIE analysis of the LTEM pictures is performed using quantum phase technology (QPT), a plug-in for Gatan's DigitalMicrograph of GMS (Gatan Microscopy Suite). For the TIE analysis, a series of three LTEM pictures are captured in focus, as well as at the identical negative and positive defocus conditions. The photos are then aligned manually or through affine alignment, which selects the same region on each image to adjust the rotation angle and scale. After accurate alignment, a high pass filter is used to generate the QPT phase image, attenuating low-frequency noise. The phase image comprises information on the electrons' refractive index, which might vary depending on the sample's electric and magnetic fields. The data from the phase images may then be used to recreate the magnetic field mapping of the LTEM image.



## Chapter 3

# Tunable magnetic skyrmions in a centrosymmetric kagome magnet $\text{Mn}_4\text{Ga}_2\text{Sn}$

The presence of additional degrees of freedom related to the helicity and vorticity of magnetic skyrmions in centrosymmetric magnets makes them interesting candidates for different applications. In this direction, the present chapter discusses about the finding of tunable skyrmion lattice up to room temperature in a novel skyrmion hosting kagome ferromagnet  $\text{Mn}_4\text{Ga}_2\text{Sn}$ . It is already discussed in Chapter 1 that the uniaxial hexagonal / kagome centrosymmetric ferromagnets are potential candidates to host skyrmion-like spin textures. This is due to the fact that in centrosymmetric magnets, the competition between the uniaxial magnetocrystalline anisotropy (UMA) and dipolar energy gives rise to the stabilization of magnetic skyrmions. This is possible when the magnitude of UMA and dipolar energy are comparable to each other. One signature of such criteria is the observation of a spin reorientation transition from the easy-axis to easy-plane magnetization alignment. In this context, the compound  $\text{Mn}_4\text{Ga}_2\text{Sn}$ , which exhibits a hexagonal crystal structure with a spin-reorientation transition at low temperature, holds promise for hosting magnetic skyrmions. Additionally, this sample has an above room temperature

magnetic ordering temperature of 320 K. These unique features in  $\text{Mn}_4\text{Ga}_2\text{Sn}$  made us to believe that this is a potential candidate to explore skyrmions.

Polycrystalline samples of  $\text{Mn}_4\text{Ga}_2\text{Sn}$  are prepared using an arc melting furnace by melting and mixing the stoichiometric amount of high purity constituent elements, as discussed in section 2.1.  $\text{Mn}_4\text{Ga}_2\text{Sn}$  sample shows a hexagonal crystal structure with space group  $P6_3/mmc$ . In the crystal structure, Mn atoms occupy the Wyckoff positions 6g (0.5, 0, 0) and 6h ( $x$ ,  $2x$ , 0.25) ( $x = 0.1526$ ), Ga atoms occupy the Wyckoff position 6h ( $x$ ,  $2x$ , 0.75) ( $x = 0.1989$ ), and Sn atoms preferentially sit in the Wyckoff positions 2a (0, 0, 0) and 2c (0.6667, 0.3333, 0.75). The crystal structure of the  $\text{Mn}_4\text{Ga}_2\text{Sn}$  sample is shown in Fig. 3.1(a). The sample contains alternative repeating atomic layers of Mn-Sn and Mn-Ga-Sn along the  $c$ -axis. The Mn-Sn and Mn-Ga-Sn layers viewed from the  $c$ -axis are shown in Fig. 3.1(b) and (c), respectively. The Mn atoms in the Mn-Sn layer form an ideal kagome lattice, with the Sn atoms at the center position. On the other hand, the Mn atoms occupying the Mn-Ga-Sn layer form a breathing kagome lattice. In an ideal Kagome lattice, all bond lengths are equal. In contrast, variable bond length are found in the case of a breathing Kagome geometry.

### 3.1 Compositional homogeneity characterization of $\text{Mn}_4\text{Ga}_2\text{Sn}$

As discussed in section 2.2, the SEM with EDX is used for the compositional homogeneity characterization for  $\text{Mn}_4\text{Ga}_2\text{Sn}$ . The SEM image of the sample is shown in Fig. 3.2. Uniform contrast all over the sample suggests a single compositional phase of the sample. The small dot like features in the SEM image represent the presence of small holes on the sample surface. A comparison between the experimental as well as the exact atomic percentage of the constituent elements is shown in Table 3.1. The atomic percentage obtained from the EDX study nearly matches the exact atomic percentage for the  $\text{Mn}_4\text{Ga}_2\text{Sn}$  sample.

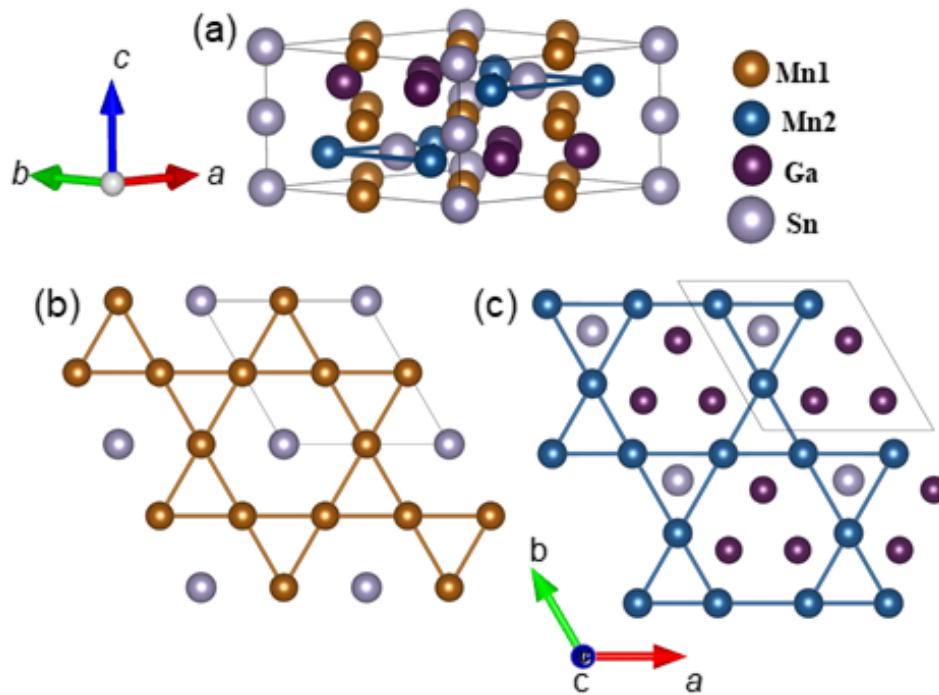


Figure 3.1: Crystal structure of  $\text{Mn}_4\text{Ga}_2\text{Sn}$ . (a) Unit cell, (b) Mn-Sn kagome layer, (c) Mn-Ga-Sn kagome layer.

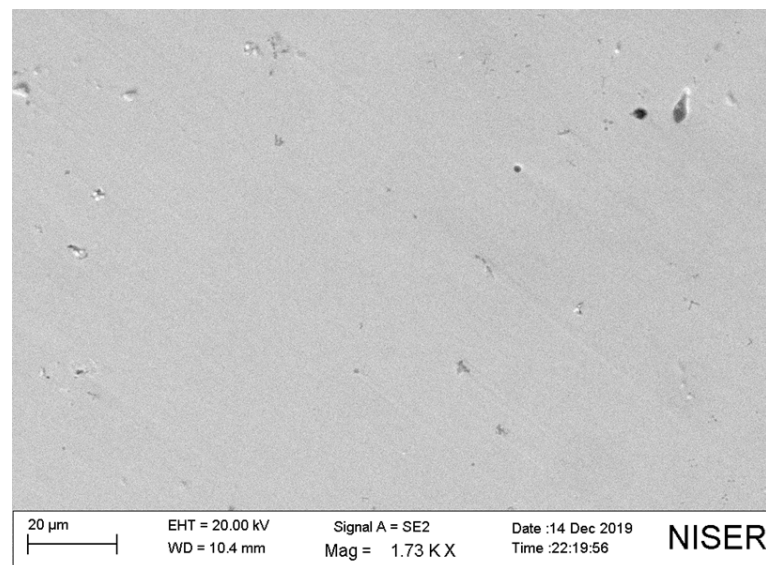


Figure 3.2: SEM image of polycrystalline  $\text{Mn}_4\text{Ga}_2\text{Sn}$  sample.



Element	Exact atomic percentage	Obtained atomic percentage
SnL	14.3	$14.0 \pm 0.7$
MnK	57.1	$58.7 \pm 2.3$
GaK	28.5	$25.6 \pm 1.3$

Table 3.1: Comparison between experimentally obtained atomic percentage and exact atomic percentage.

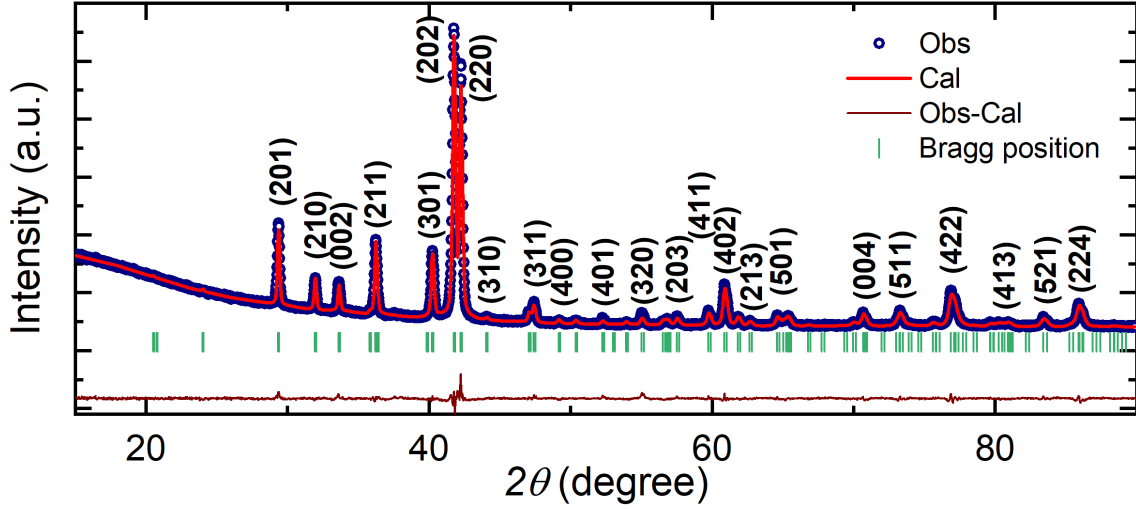


Figure 3.3: Fullprof fitted room temperature powder XRD pattern for  $\text{Mn}_4\text{Ga}_2\text{Sn}$  sample.

### 3.2 Structural characterization of $\text{Mn}_4\text{Ga}_2\text{Sn}$

Room temperature powder XRD pattern with Rietveld analysis using fullprof suit for the  $\text{Mn}_4\text{Ga}_2\text{Sn}$  sample is shown in Fig. 3.3. The XRD pattern indicates that the sample crystallizes in a single phase hexagonal crystal structure with space group  $P6_3/mmc$  and lattice parameters  $a = b = 8.5527 \pm 0.0002 \text{ \AA}$  and  $c = 5.3264 \pm 0.0001 \text{ \AA}$ .

For further verification of crystal structure, high-resolution transmission electron microscopy imaging (HRTEM) and SAED measurements are performed. For this purpose, a 120 nm thin plate of  $\text{Mn}_4\text{Ga}_2\text{Sn}$  sample is prepared using the Ga ion based FIB technique following the procedure, as explained in Chapter 2. The real space view of the kagome structure formed by the Mn-Sn atoms, as expected from the

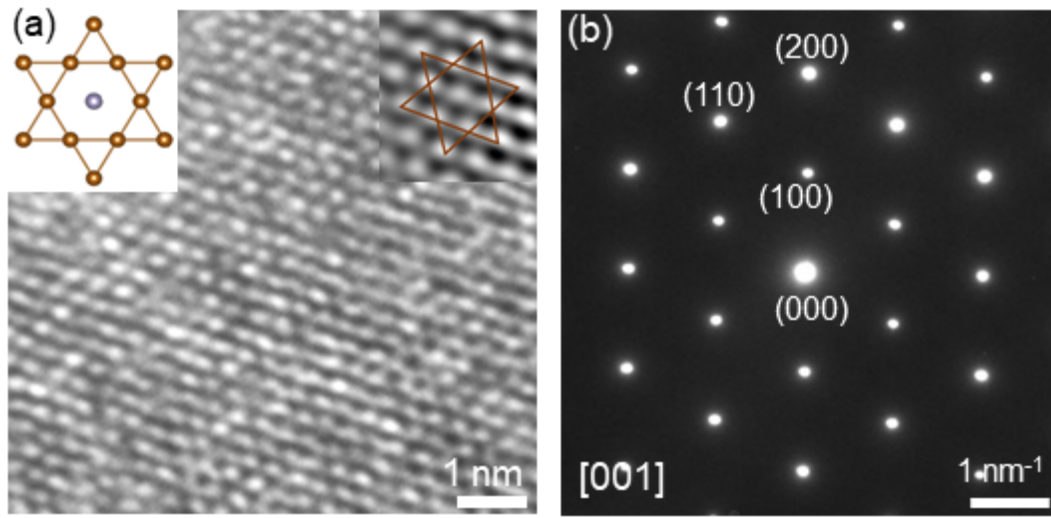


Figure 3.4: (a) HRTEM image of the FIB lamella with  $[001]$  orientation. The right inset shows the enlarged view of the reconstructed atomic arrangement after the inverse fast Fourier transformation (FFT) of the FFT of the actual image. The kagome structure formed with Mn atoms in the top Mn-Sn layer is marked with deep orange colored lines. The corresponding Mn-Sn kagome structure is shown in the left inset. The dark yellow balls represent the Mn atoms and the grey balls appear for the Sn atoms. (b) The SAED pattern of the FIB lamella with  $[001]$  orientation.

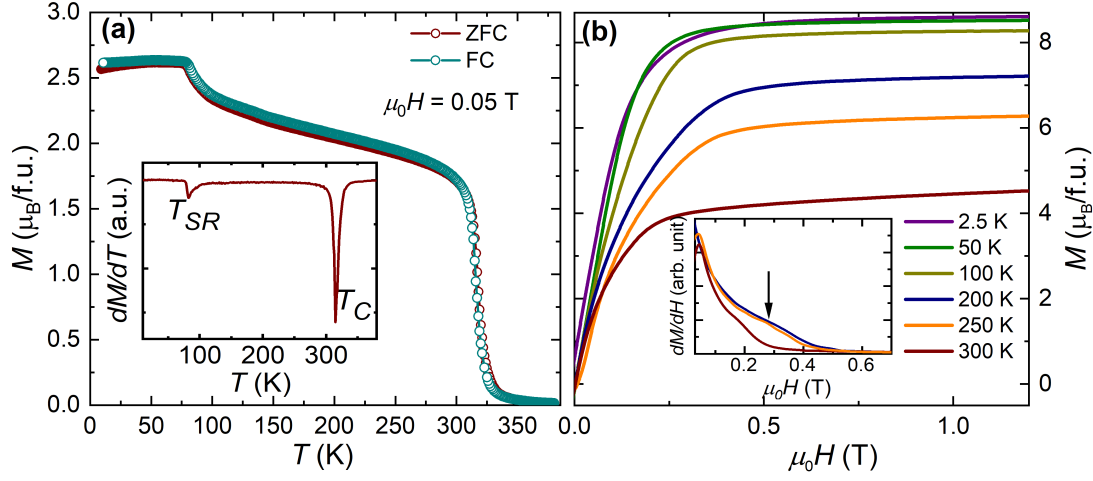


Figure 3.5: Magnetic properties of  $\text{Mn}_4\text{Ga}_2\text{Sn}$  sample. (a) Temperature dependent ZFC and FC data taken at a magnetic field of 0.5 kOe. The inset shows the temperature dependent first derivative ( $\frac{dM}{dT}$ ) of the FC  $M$  vs  $T$  curve. (b) Isothermal field dependent magnetization at various temperatures from 2.5 K to 300 K. The inset shows the first derivative of  $M$  vs.  $H$  data at selected temperatures with anomaly pointed by black arrows.

unit cell is shown in Fig. 3.4(a). The indexed six-spot SAED pattern also represents the hexagonal structure [shown in Fig. 3.4(b)] of the atomic plane and confirms the  $c$ -orientation of the thin sample plate.

### 3.3 Magnetic Properties of $\text{Mn}_4\text{Ga}_2\text{Sn}$

As mentioned earlier in Chapter 2, the dc magnetization measurement with ZFC and FC protocols is performed using a SQUID magnetometer in the presence of a 0.05 T magnetic field. From the  $M$  vs.  $T$  measurement as shown in Fig. 3.5(a), the Curie temperature ( $T_C$ ) is found to be around 320 K. In addition, a second transition is also observed at a temperature close to 90 K. This additional transition can be seen more clearly in the first derivative of the  $M$  vs.  $T$  plot [shown in the inset of Fig. 3.5(a)]. It has been suggested that this transition can be accounted for a spin-reorientation transition ( $T_{SR}$ ) from a high-temperature easy axis configuration to a low-temperature easy plane arrangement at  $T_{SR}$  [121]. This kind of spin reorientation transition can be explained by the competition between mag-

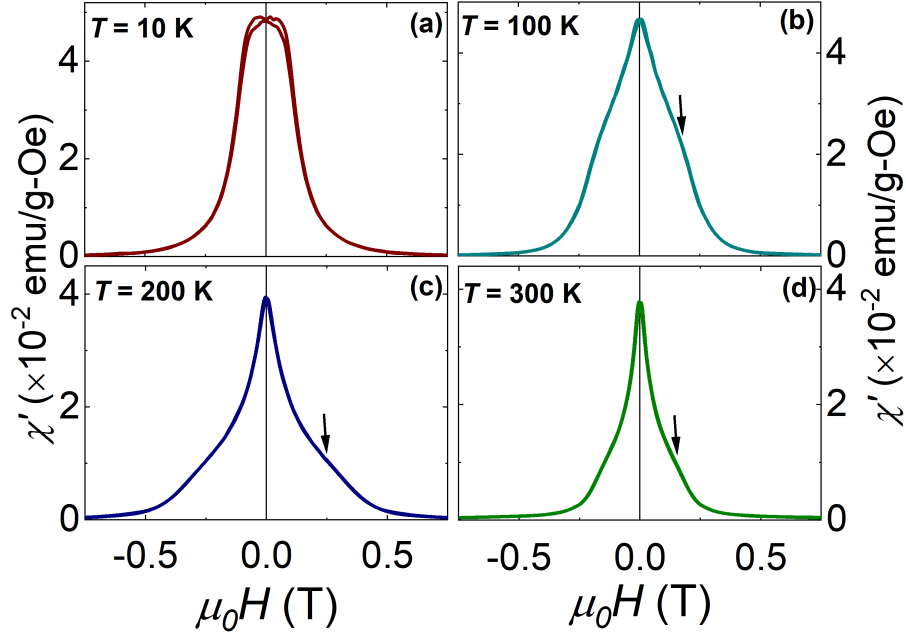


Figure 3.6: Magnetic field dependent ac susceptibility measurement of  $\text{Mn}_4\text{Ga}_2\text{Sn}$  sample at different temperatures from 10 K to 300 K. (a) 10 K, (b) 100 K, (c) 200 K (d) 300 K. The black arrows mark the hump like anomalies.

netocrystalline anisotropy energy and dipolar interaction energy [122]. Competing dipolar and magnetic anisotropy energies play a critical role in creating spin patterns resembling skyrmions in the centrosymmetric samples, as previously mentioned in Chapter 1. Hence, the present material is a potential candidate to host skyrmions, as its effective anisotropy changes with temperature from a positive (uniaxial) value to a negative value (in-plane).

Figure 3.5(b) shows the isothermal dc magnetic field ( $H$ ) dependent magnetization ( $M$ ) measurements at different temperatures ranging from 2.5 K to 300 K. The sample shows a magnetic moment of  $8.41 \mu_B/\text{f.u}$  at 2.5 K. At temperatures exceeding  $T_{SR}$ , the low field area of the  $M$ - $H$  plots exhibit hump-like characteristics that are more pronounced in the first derivative of the  $M$ - $H$  plots [see the inset of Fig. 3.5(b)]. This type of anomaly in the  $M$  vs.  $H$  plot has been observed in many previously reported skyrmion hosting materials as a result of the transition from the helical to the skyrmion state [13, 22, 44, 45].

The ac magnetization measurements are often used to indirectly verify the exis-

tence of the skyrmion phase [45, 123]. The field dependent ac susceptibility [ $\chi'(H)$ ] data for our sample measured at different temperatures ranging from 10 K to 300 K are shown in Fig. 3.6. The  $\chi'(H)$  data at 10 K exhibits typical ferromagnetic like behavior [Fig. 3.6(a)]. In contrast,  $\chi'(H)$  data above 100 K exhibit some additional hump-like behavior [marked with black arrows in Fig. 3.6(b)-(d)]. The majority of the Skyrmion hosting materials are well known for showing these kinds of anomalies in the  $\chi'(H)$  data [45, 123]. The anomaly in  $\chi'(H)$  represents a 1st order phase transition between two magnetic phases with distinct characteristics. Therefore, it suggests the presence of a possible skyrmion phase in the material above the  $T_{SR}$ .

### 3.4 Real space observation of magnetic domains in $\text{Mn}_4\text{Ga}_2\text{Sn}$

Motivated by the ac and dc magnetization measurements, further real-space observation of the magnetic textures is carried out utilizing LTEM measurements. Room temperature LTEM images for the lamella with [001] orientation are shown in Fig. 3.7. Stripe domains with an average periodicity of around 100 nm are observed as the magnetic ground state. As expected, no magnetic contrast is found in the in-focus condition [see Fig. 3.7(b)]. Very poor magnetic contrast is recorded at room temperature as the  $T_C$  is around 320 K. With an increase in the magnetic field by increasing OL current, the stripe domains break into small circular magnetic domains, as shown in Fig. 3.7(d). However, the poor magnetic contrast of the sample at room temperature restricts the identification of the actual nature and properties of the magnetic textures. In order to learn more about the true nature of the exhibited spin patterns, the sample is cooled down to 100 K using a liquid  $\text{N}_2$  TEM holder, as shown in Fig. 2.19(b).

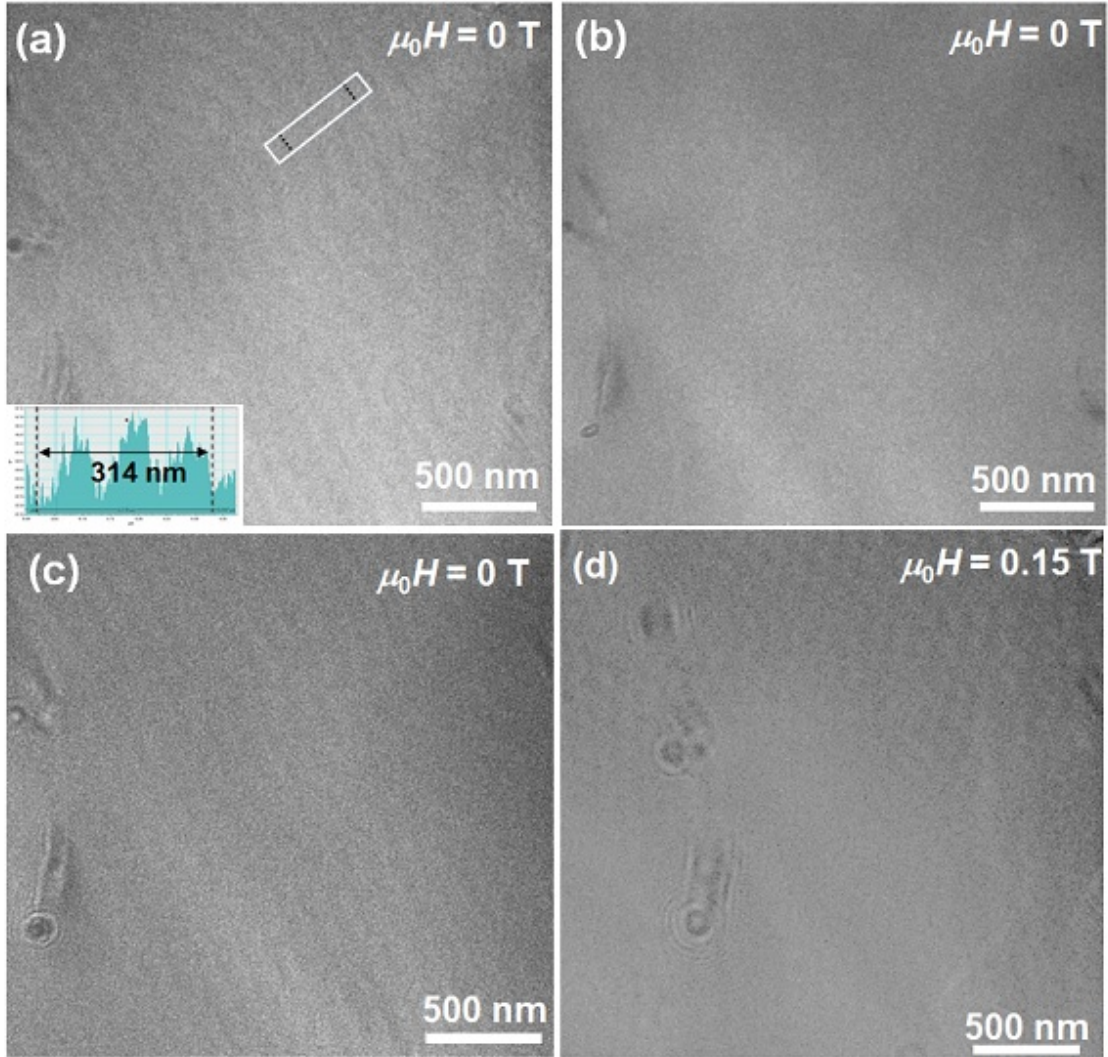


Figure 3.7: Real space observation of magnetic domains for  $\text{Mn}_4\text{Ga}_2\text{Sn}$  sample at room temperature. Zero field magnetic ground state in (a) under-focused, (b) in-focus, and (c) over-focused condition. The inset in Fig. (a) shows the intensity profile of the marked region. (d) Under-focused LTEM image for the sample at a magnetic field of 0.15 T.



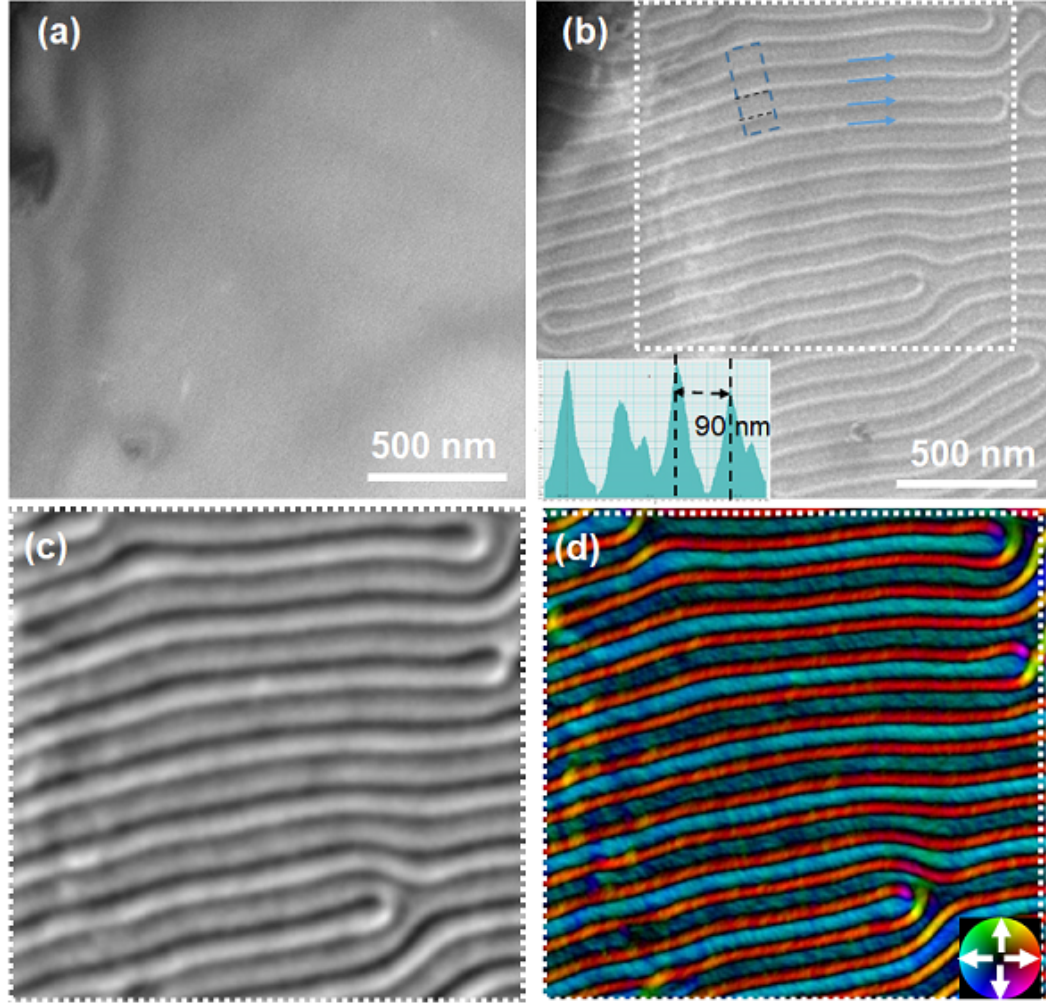


Figure 3.8: Real space observation of magnetic ground states at 100 K for  $\text{Mn}_4\text{Ga}_2\text{Sn}$  sample at (a) in-focus, and (b) over-focused, condition. The inset shows the intensity profile. (c) The TIE reconstructed phase image of the magnetic domains. (d) The in-plane magnetization mapping of the domains constructed using the phase image. The color wheel in the inset of (d) represents the magnetization components at each point.

### 3.4.1 Field evolution of magnetic domains at different temperatures

Stripe domains with an average periodicity of 90 nm are observed as the spontaneous magnetic state at 100 K [Fig. 3.8(b)]. The TIE-constructed magnetization mapping for the stripe domains is shown in Fig. 3.8(d). With an increase in the magnetic field to 0.3 T the stripe domains break into hexagonal lattices of small bubble domains of nearly 100 nm size [Fig. 3.9(a)]. Figure 3.9(b) shows the TIE constructed magnetization mapping of the LTEM image. The zoomed view of the observed bubble structure shows alternative half-circles of black and white contrasts. The zoomed view of the TIE reconstructed phase image and the magnetization mapping of the bubble is shown in Fig. 3.9(c). Although these kinds of magnetic contrasts are already observed experimentally, there exist some contradicting reports about the topology of these magnetic textures. In some literature, this kind of magnetic structure is explained as biskyrmion (topological number 2) [9, 10, 11]. Some reports describe it as a type-II bubble with topological number zero [8, 124]. So, the observed spin texture in the present system can be a non-topological type II bubble or topological biskyrmion, as the LTEM simulated images of both the spin textures are expected to have similar contrast [125]. The magnetization mapping and simulated LTEM image corresponding to the simulated type-II bubble are shown in Fig. 3.9(d). The TIE magnetization mapping of the observed bubble image matches well with the single core type-II bubble rather than the dual core biskyrmions. Therefore, the observed spin texture can be concluded as type-II bubbles with zero topological number.

For a better understanding of the magnetic textures in the present system, LTEM measurements are performed at different temperatures ranging from 100 K to 300 K. With an increase in temperature to 200 K the stripe domain size decreases to 80 nm. With a further increase in magnetic field to 0.3 T, the stripe domains break into magnetic bubbles. The temperature evolution of field driven magnetic domains is shown in Fig. 3.10. An additional magnetic contrast with white and black circular



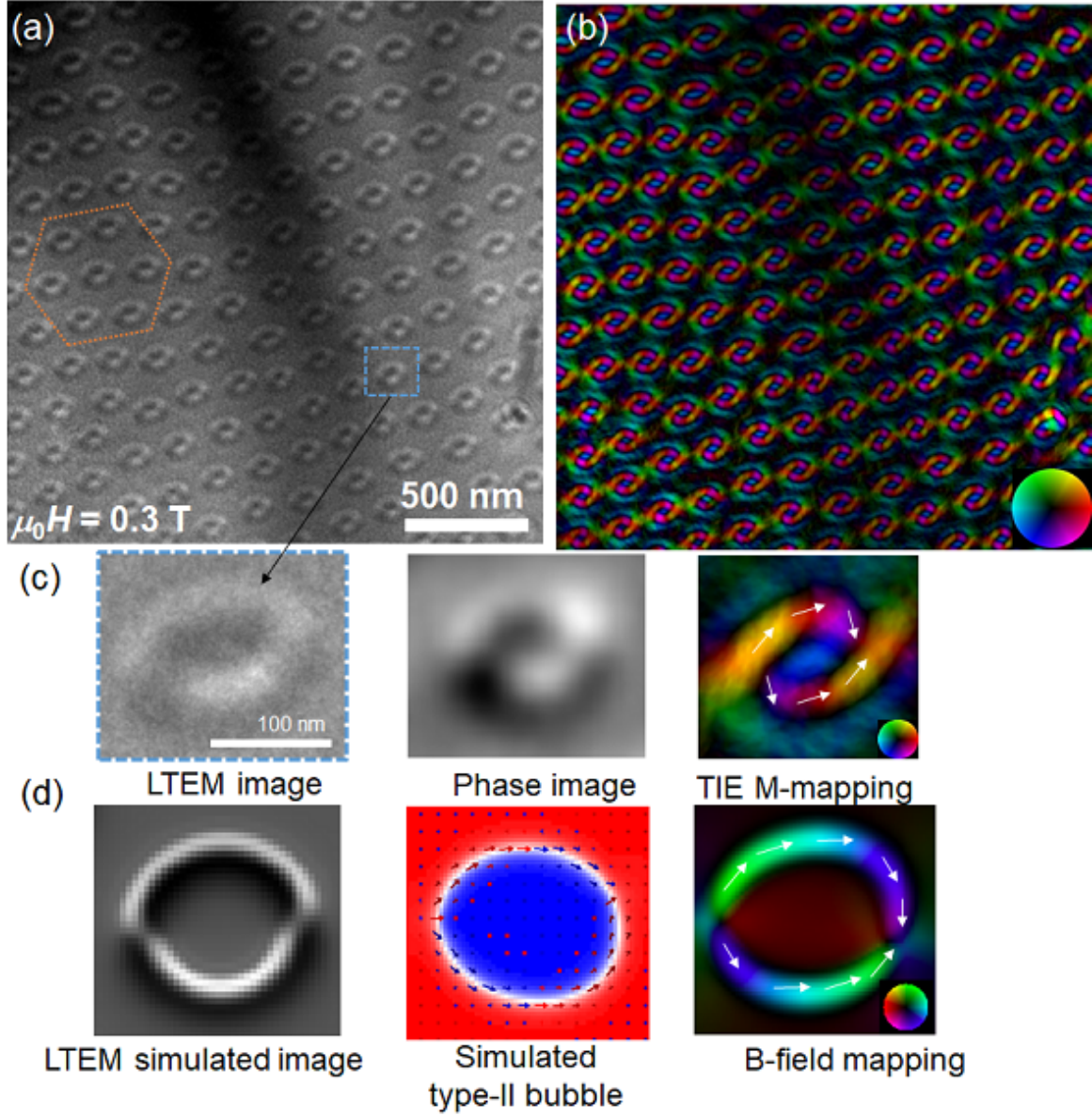


Figure 3.9: (a) Over-focused LTEM images for the  $\text{Mn}_4\text{Ga}_2\text{Sn}$  sample taken at  $T = 100$  K and field of 0.3 T. (b) The TIE field mapping of corresponding LTEM image. (c) Zoomed view of the LTEM images of the magnetic bubble structure, the TIE reconstructed phase image, and its magnetization mapping using TIE. (d) The LTEM simulated image corresponding to the type-II bubble constructed using PyLorentz code and its field mapping. The color wheel corresponds to the images shown in the insets.

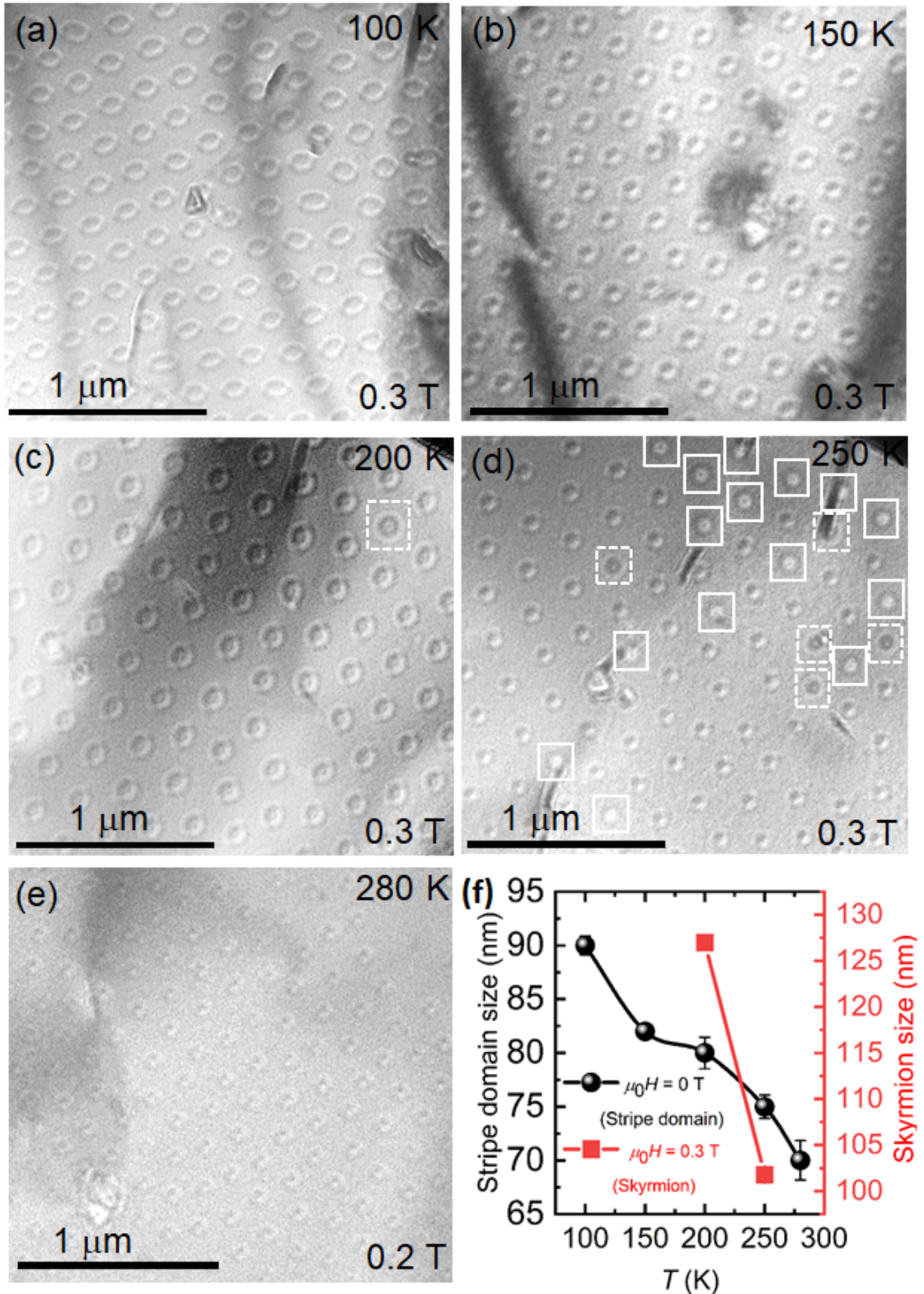


Figure 3.10: Over-focused LTEM images of magnetic domains with varying temperatures for  $\text{Mn}_4\text{Ga}_2\text{Sn}$  sample. The images are taken at a magnetic field of 0.3 T for temperatures (a) 100 K, (b) 150 K, (c) 200 K, (d) 250 K, and at a magnetic field of 0.2 T for (e) 280 K. Observed skyrmions with clockwise (CW) and counter clockwise (CCW) helicity are marked with dashed and solid boxes, respectively. (f) Temperature variation of observed stripe domain size and skyrmion size.



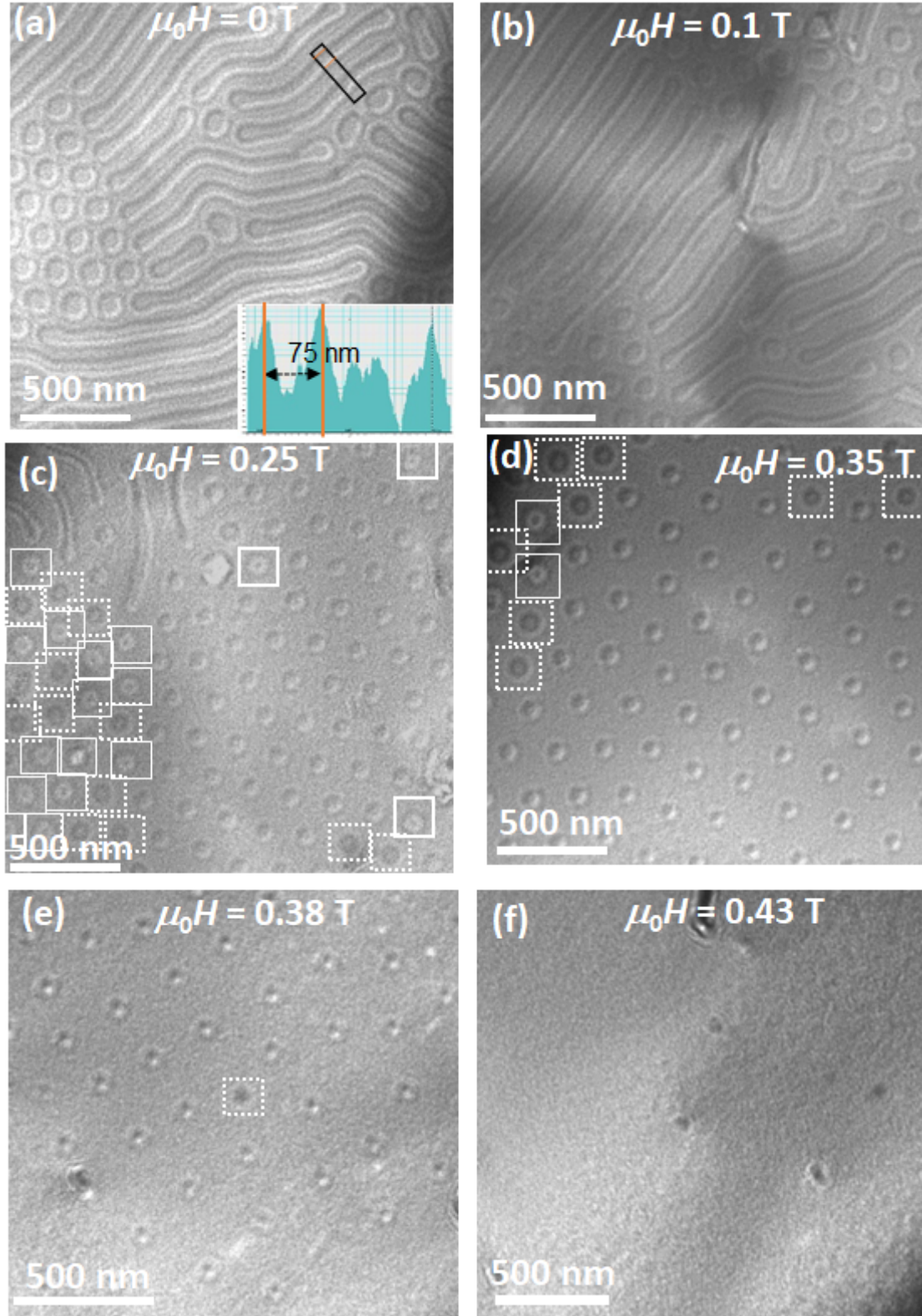


Figure 3.11: Real space LTEM images of field dependent magnetic domains for  $\text{Mn}_4\text{Ga}_2\text{Sn}$  sample in over-focused mode at 250 K. The images are taken at magnetic field of (a) 0 T, (b) 0.1 T, (c) 0.25 T, (d) 0.35 T, (e) 0.38 T, and (f) 0.43 T. The inset in Fig.(a) shows the intensity profile corresponding to stripe domains marked in box. The additional skyrmion like structures are marked with solid/dotted boxes.

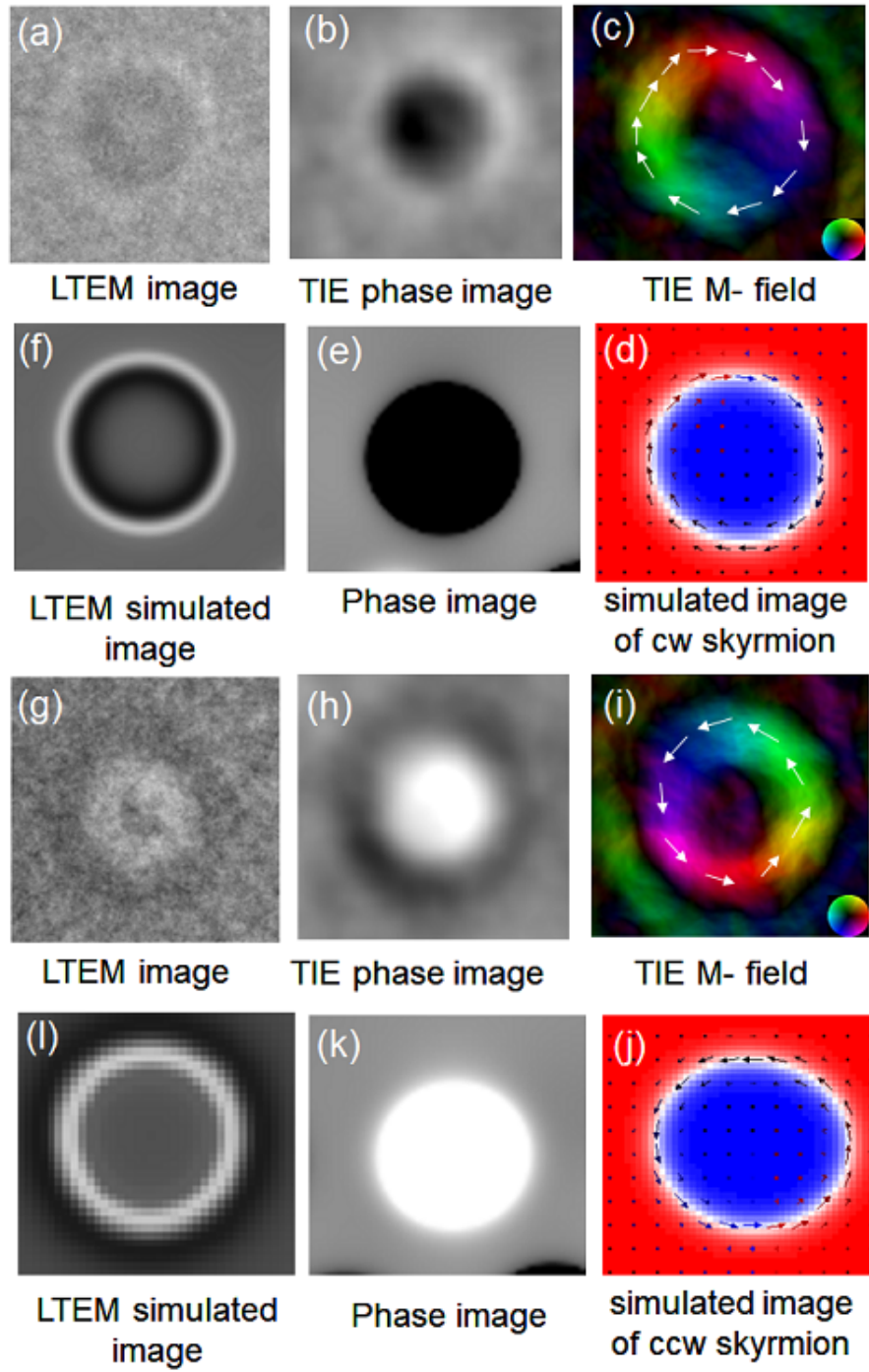


Figure 3.12: (a)-(c) and (g)-(i) The LTEM images, the associated TIE phase image, and magnetization mapping of the additional contrast marked with dashed/solid boxes in Fig. 3.10 . The simulated spin texture of the CW/ CCW skyrmion along with the corresponding phase image and the LTEM simulated image using pylorntz-master code (d)-(f)/ (j)-(l).

rings [marked with dashed boxes in Fig. 3.10(c)] is also observed at 200 K, along with the magnetic states observed at 100 K. With a further increase in temperature to 250 K, the stripe domain size further decreases to 75 nm [see Fig. 3.11(a)]. The field dependent magnetic contrasts for the sample at 250 K are shown in Fig. 3.11. Another additional magnetic state [marked with solid boxes] along with the magnetic states observed at 200 K is observed at 250 K for a field of about 0.2 T [Fig. 3.10(d), 3.11(c)].

The zoomed view of the observed additional magnetic contrasts at 200 K/250 K and their TIE analysis are shown in Fig. 3.12. The in-plane magnetization mapping of the observed circular magnetic contrasts constructed using TIE analysis reveals a magnetic structure of skyrmions [see Fig. 3.12(c), (i)]. The LTEM contrasts for the simulated skyrmions created with the Pylorentz algorithm [Fig. 3.12(f),(i)] closely resemble the observed LTEM images shown in Fig. 3.12(a),(g). When the temperature is raised to 280 K, the ground state stripe domains shrink even further to 70 nm [see Fig. 3.10(f)], and when the magnetic field increases, the stripe domains separate into bubble-like domains, as shown in the case of 100 K [Fig. 3.10(e)]. The temperature variation of the size of the zero field stripe domain and skyrmions (at 0.3 T) are plotted in Fig. 3.10(f). Hence, the simultaneous observation of different kinds of spin textures in the present system deserves further study to explore the actual mechanism.

The over-focused LTEM images taken at different temperatures and with a magnetic field of 0.3 T clearly show that the number of nucleated skyrmions are more at 250 K [Fig. 3.10(d)]. Near the  $T_{SR}$  ( $\approx 90$  K), no skyrmion nucleation is observed [see Fig. 3.10(a)]. Nonetheless, the probability of skyrmion nucleation increases with increasing temperature above  $T_{SR}$  and peaks at 250K. Near the  $T_C$ , the skyrmions formation probability again decreases [Fig. 3.10(e)]. This observation indirectly signifies the role of temperature varying parameters, such as the effective UMA on the skyrmion nucleation. The variation of stripe domain size, as well as the skyrmion size with temperature also signifies the importance of dipolar energy in the present system.

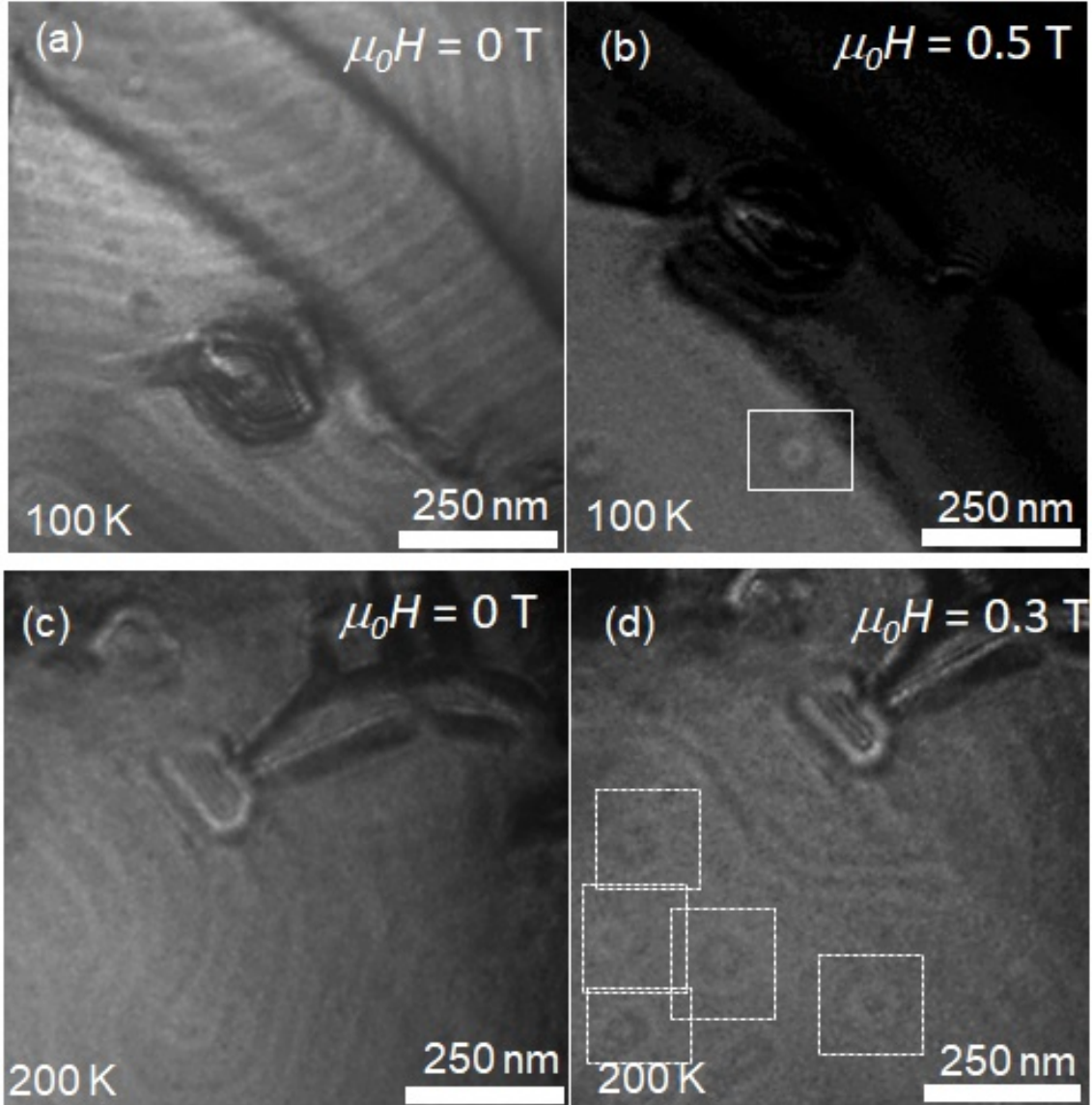


Figure 3.13: Over-focused LTEM images of field dependent magnetic domains at 100 K, 200 K for  $\text{Mn}_4\text{Ga}_2\text{Sn}$  sample taken at zero degree sample tilting condition. (a-b) The images at 100 K are taken at magnetic fields of 0 T (a), 0.5 T (b). (c-d) The images at 200 K are taken at magnetic fields of 0 T (c), 0.3 T (d). The skyrmions are marked with boxes. The observed magnetic contrast is very poor due to presence of strong bending contour.

### 3.4.2 Magnetic states with zero sample tilting condition

It is important to mention here that it is extremely difficult to get a good LTEM contrast along the zone axis for most of the samples due to the bending contour effect. Bending contour effect is a shadow kind of pattern that originates from the diffraction related contrast and appears on top of the image. This effect typically arises from the slight elastic bending of thin TEM lamellae and may also be influenced by factors such as strain, impurities, and lattice defects within the lamella. Even with bending less than  $0.1^\circ$ , the bending contour effect can be significant in real thin specimens, making it challenging to circumvent entirely [126]. Moreover, the bending contour effect is more pronounced and complicated near the zone axis. However, that can be avoided by slight tilting of the samples away from the zone axis. So, all the images shown in Fig. 3.8, 3.9, 3.10, and 3.11 are taken by slightly tilting (nearly 3 degrees) the sample with respect to its zone axis to avoid the bending contour effect. When the sample is tilted with respect to the zone axis, there is a finite in-plane component of the applied magnetic field along with the out-of-plane component. To check the effect of the in-plane magnetic field on the LTEM measurements, it is necessary to know the magnetic states at zero in-plane magnetic field. Few isolated skyrmions are observed at 100 K/200 K, but the presence of a strong bending contours effect affects the LTEM data [see Fig. 3.13]. Whereas, at 250 K the bending contour effect improves substantially.

The magnetic field dependent LTEM measurements at 250 K with nearly zero tilting condition i.e., with zero in-plane magnetic field are shown in Fig. 3.14. With zero tilting condition, the stripe domains are observed as the magnetic ground state. Whereas, with increase in the magnetic field the stripe domains break into skyrmions with both clockwise (CW) and counter-clockwise (CCW) helicity. A distorted hexagonal skyrmion lattice [marked with a hexagon in Fig. 3.14(c)] is observed at a magnetic field of 0.3 T. With further increase in the magnetic field, the skyrmions start to shrink and disappear at a magnetic field of 0.4 T. When the magnetic field is decreased after reaching the saturated magnetic state, the hexagonal skyrmion



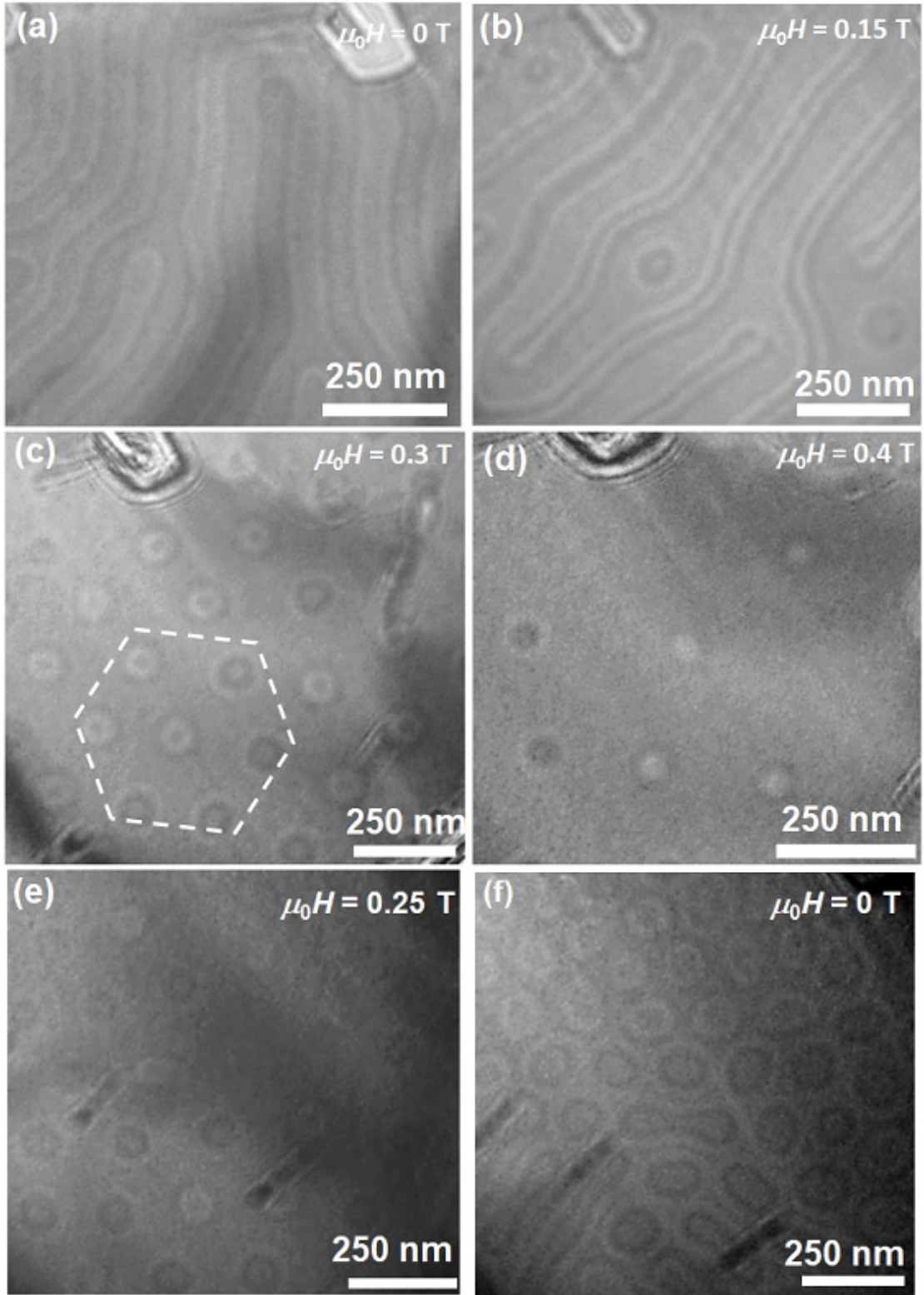


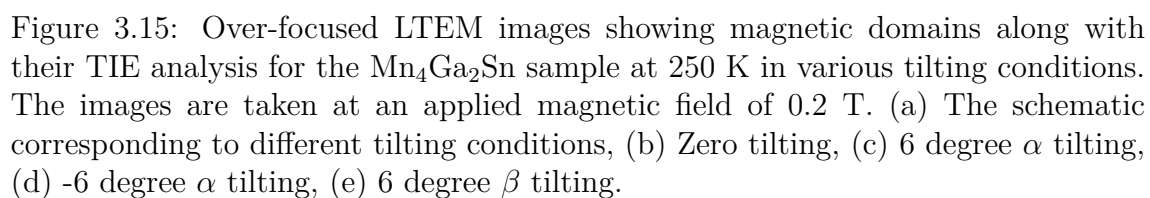
Figure 3.14: Over-focused LTEM images of field dependent magnetic domains at 250 K for  $\text{Mn}_4\text{Ga}_2\text{Sn}$  sample in zero degree sample tilting condition. The images are taken at magnetic fields of (a) 0 T, (b) 0.15 T, (c) 0.3 T, (d) 0.4 T, (e) 0.25 T, and (f) 0 T. The hexagonal skyrmion lattice is marked with a hexagon in Figure (c).



lattice again appears at a magnetic field of 0.25 T. With a further decrease in the magnetic field, a mixed state of skyrmion and dumbbell like stripe domain structure [topologically equivalent to skyrmions] is obtained. The mixed state further persists up to zero field as a remanent magnetic state. This observation suggests that the skyrmion state is the stable magnetic state at zero tilting condition instead of the magnetic bubble state that is observed at a finite sample tilting.

### 3.4.3 Controlled tuning/switching of magnetic spin textures at 250 K

To understand the in-plane magnetic field effect more clearly, the tilting experiment is performed in a controlled way. The tilting conditions are schematically depicted in Fig. 3.15(a). The in-plane magnetic field in the  $x$  and  $y$  direction is regulated by tilting the sample along  $y$ -( $\beta$ ) and  $x$ -axes ( $\alpha$ ), respectively. At a magnetic field of 0.2 T and zero tilting angle, i.e. zero in-plane magnetic field, the hexagonal skyrmion lattice is observed as a stable magnetic state [Fig. 3.15(b)]. The skyrmion state changes to a magnetic bubble-like structure when the sample is tilted to 6 degrees  $\alpha$  or  $\beta$  angle [Fig. 3.15(c)-(e)]. Whereas, the skyrmion state comes back again with zero  $\alpha$  and  $\beta$  tilting [Fig. 3.16(c)]. These observations clearly suggest that the skyrmion state is the stable magnetic state at zero sample tilting condition, whereas the type-II bubble can be achieved as a metastable state with a finite in-plane magnetic field [see Fig. 3.16(d)]. From the zoomed view of the magnetic domains at 6 degrees  $\beta$  tilting it is observed that the Bloch-line in the magnetic bubble structure aligns in the in-plane magnetic field direction ( $x$ -direction) [Fig. 3.15(e)]. Similarly, when the sample is tilted at  $\pm 6$  degrees  $\alpha$  angle, the domain pattern aligns in the  $y$ -direction, as expected [Fig. 3.15(c)-(d)]. Also, the LTEM intensity contrast becomes opposite with changing the in-plane field direction, which is clearly shown in Fig. 3.15(c)-(d) and its zoomed view. Similarly, the LTEM magnetic contrast in the case of  $\beta$  tilting is changed by 90 degrees as shown in the zoomed view of Fig. 3.15(e). The results of the TIE analysis of the spin textures demonstrate that the in-plane arrangement



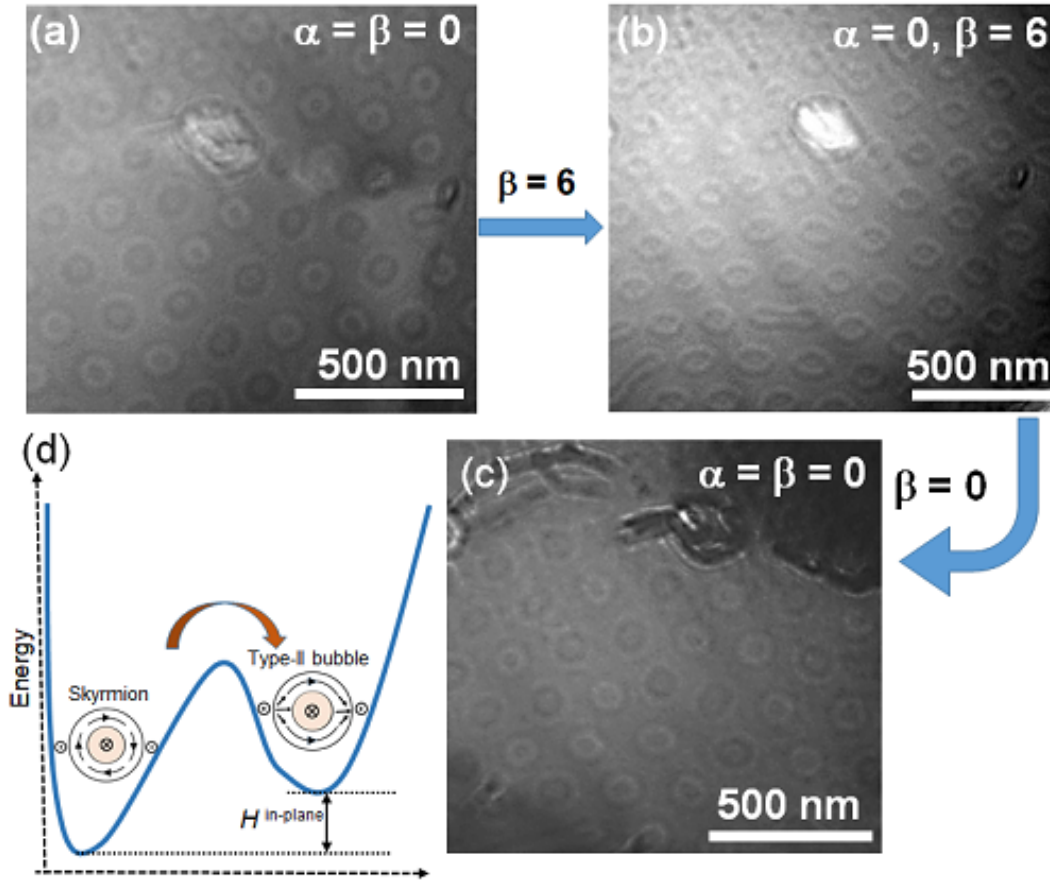


Figure 3.16: Over-focused LTEM images showing magnetic domains at 250 K for  $\text{Mn}_4\text{Ga}_2\text{Sn}$  sample in 6 degree  $\beta$  tilting condition. The images are taken at an applied magnetic field of 0.2 T. (a) Zero tilting, (b) 6 degree  $\beta$  tilting, (c) zero tilting angle after decreasing  $\beta$  to zero. (d) The energy diagram for skyrmion and type-II bubble in the system.

of the spin textures appears in the direction of the in-plane external magnetic field. These observations demonstrate that the in-plane magnetic field direction plays a significant role in deciding the configuration of the type-II bubble spin texture.

### 3.4.4 Phase diagram

A  $H$ - $T$  phase diagram is constructed based on the LTEM experiments performed at nearly 3 degree sample tilting conditions [shown in Fig. 3.17]. The magnetic bubble state is observed as the stable magnetic state up to 200 K. Whereas, at the same tilting condition few magnetic skyrmions are stabilized along with magnetic bubble state above 200 K. The skyrmion number considerably increased with increasing temperature to 250 K. To find out the origin behind this observation, effective uniaxial magnetocrystalline anisotropy of the sample is calculated for the temperature range 100 K to 300 K, as anisotropy plays a key role in producing skyrmion texture in the centrosymmetric system.

## 3.5 Magnetocrystalline anisotropy in $\text{Mn}_4\text{Ga}_2\text{Sn}$

The effective uniaxial magnetocrystalline anisotropy ( $K_{eff}$ ) of the polycrystalline sample  $\text{Mn}_4\text{Ga}_2\text{Sn}$  is calculated over a temperature range starting from  $T_{SR}$  to  $T_C$  using the law of approach to saturation. The magnetization ( $M$ ) near the saturation ( $\frac{M}{M_S} \geq 0.9$ , where  $M_S$  is saturation magnetization) can be written as,

$$M = M_S(1 - \frac{a_2}{H^2}) \quad (3.1)$$

where

$$a_2 = \frac{4K_{eff}^2}{15M_S^2} \quad (3.2)$$

is the fitting parameter [127]. Here

$$K_{eff}^2 = K_1^2 + \frac{16}{7}(K_1 + \frac{2}{3}K_2)K_2 \quad (3.3)$$

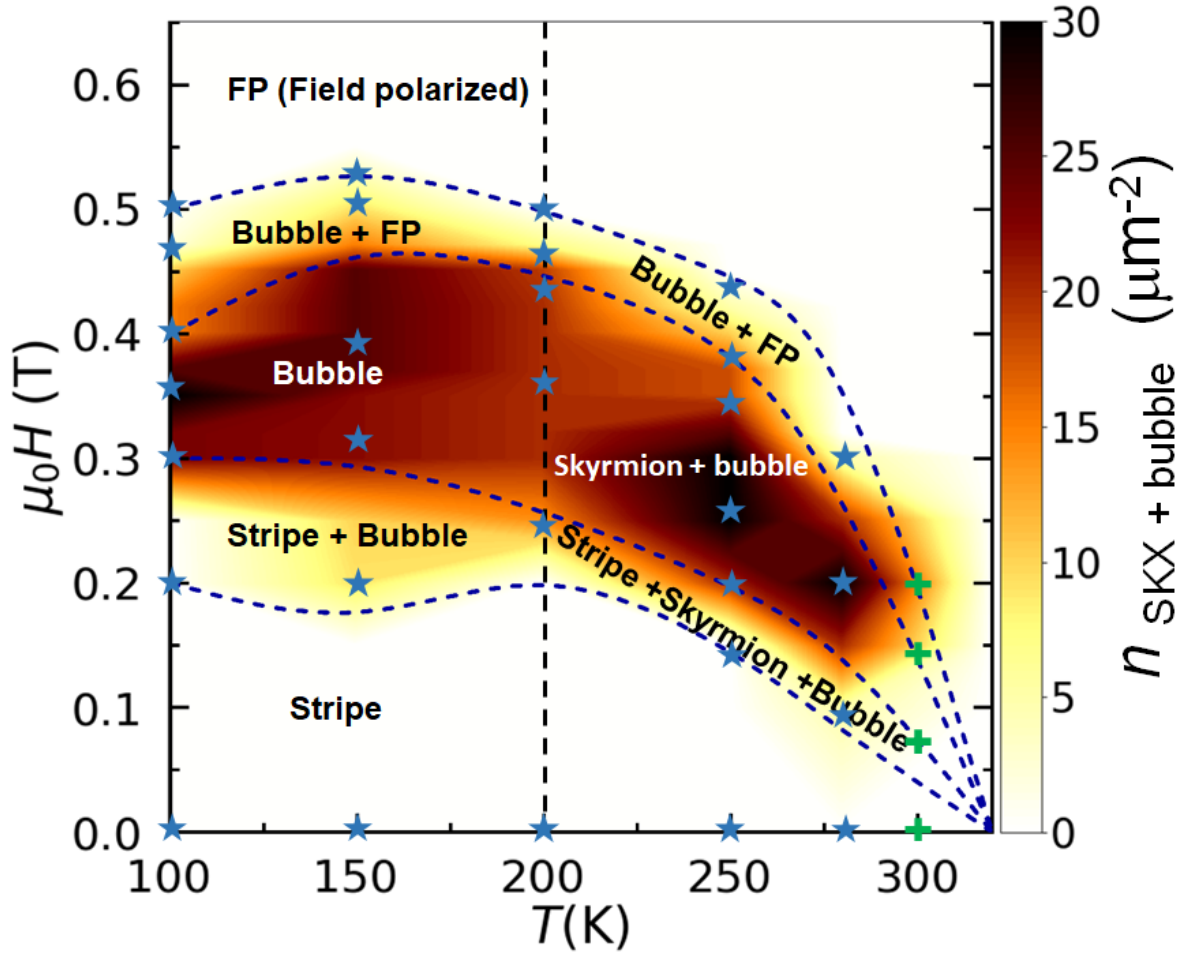


Figure 3.17:  $H$ - $T$  phase diagram constructed using LTEM experiment performed with nearly 3 degree sample tilting. Star symbols represent the data points where the LTEM measurements are performed. The plus symbols represent the data points taken from ac susceptibility measurement at room temperature.  $n_{SKX+bubble}$  represents the density of skyrmions and bubbles per micrometer square area of the TEM lammela of the sample.

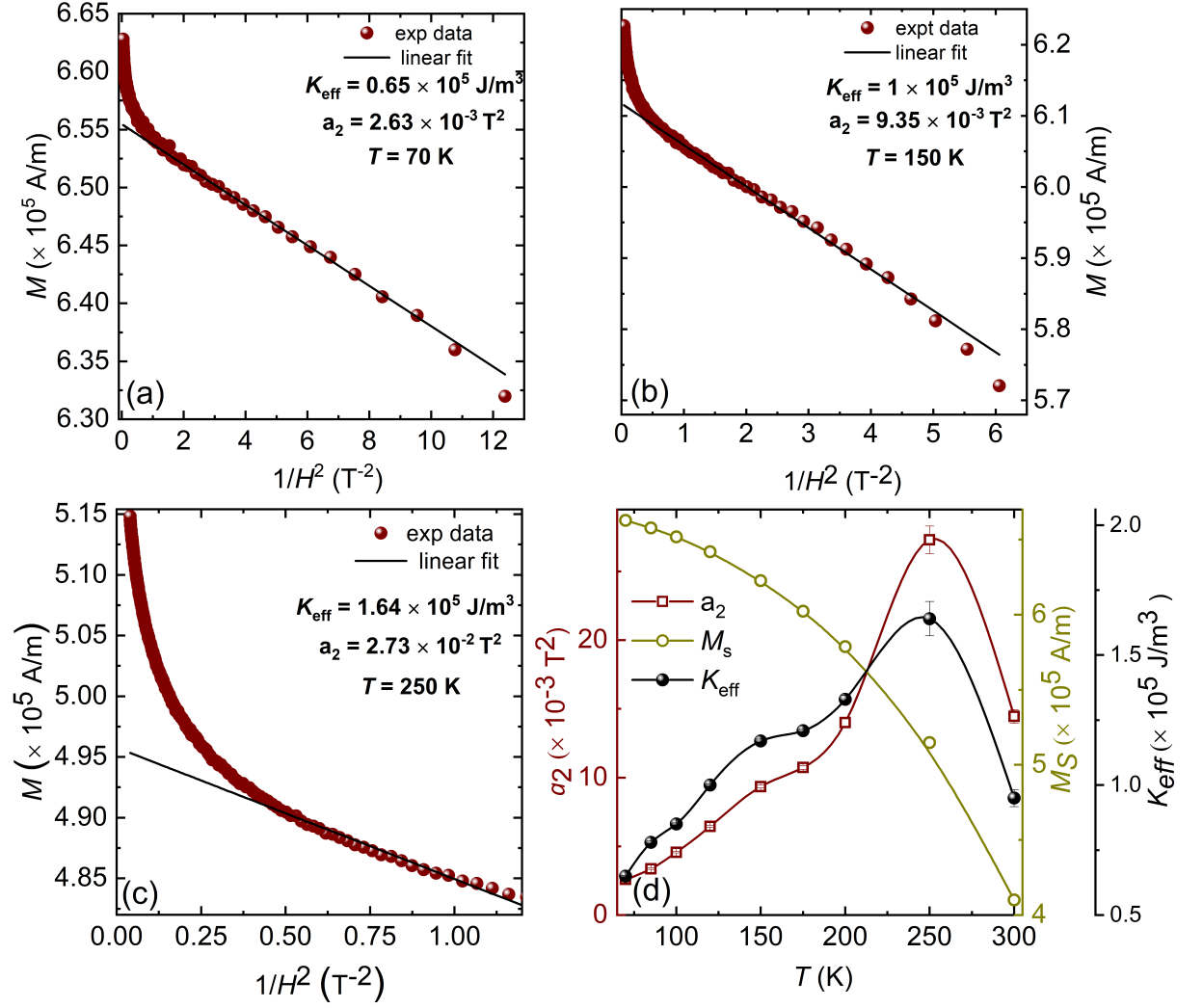


Figure 3.18: Fitting of  $M$  vs  $H^{-2}$  plots using the law of approach to saturation at different temperatures (a-c). Measured  $M_s$ , calculated  $a_2$ ,  $K_{\text{eff}}$  values at different temperatures (d).

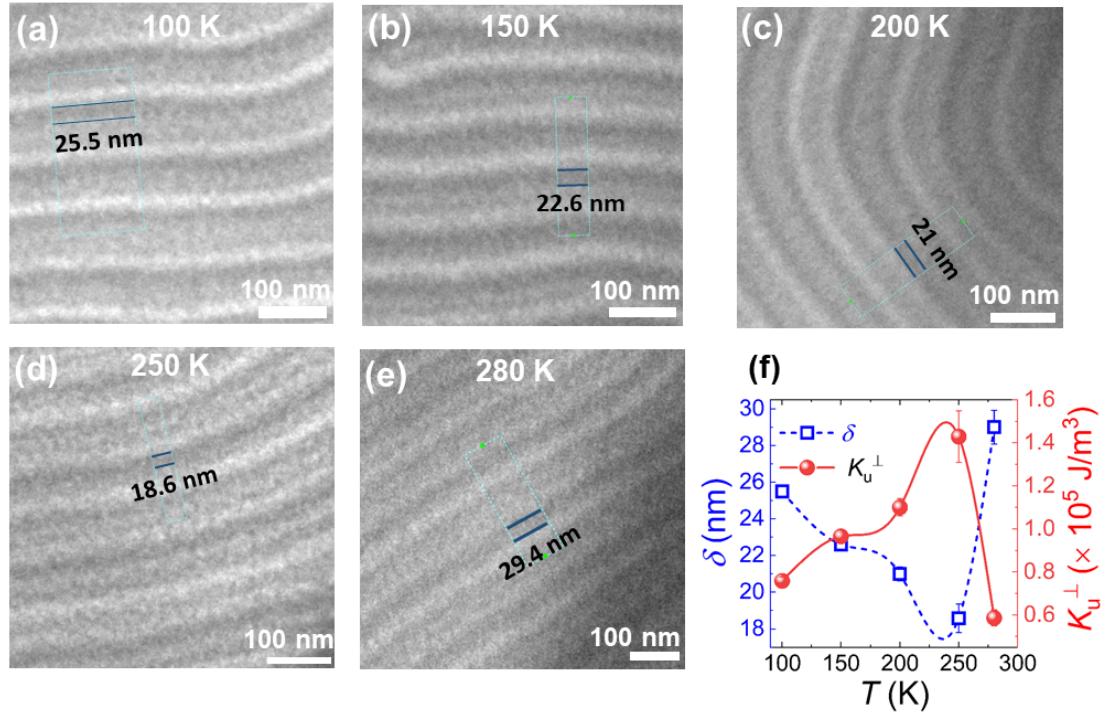


Figure 3.19: Over-focused LTEM images of stripe domains at different temperatures and the calculated uniaxial magnetocrystalline anisotropy ( $K_u^\perp$ ).

where  $K_1$ , and  $K_2$  are the first and second order uniaxial anisotropy, respectively. For the material having negligible  $K_2$  value,  $K_{eff}$  is nearly equal to  $K_1$ . From the straight line fitting of  $M$  vs  $H^{-2}$  data near the saturation ( $\frac{M}{M_S} \geq 0.95$ ),  $a_2$  values are calculated and then the possible  $K_{eff}$  values are estimated using equation 3.2. Fitting for temperatures 70 K, 150 K, and 250 K are shown in Fig. 3.18 (a)-(c), respectively. The temperature variation of  $a_2$ ,  $M_S$  and  $K_{eff}$  are plotted in Fig. 3.18 (d). Effective magneto-crystalline anisotropy of the system is minimum near  $T_{SR}$ , whereas it increases with increasing temperature up to 250 K. The maximum effective uniaxial anisotropy is observed around 250 K. Above 250 K the anisotropy again decreases as the sample  $T_C$  is near 300 K.

Out-of-plane magneto-crystalline anisotropy ( $K_u^\perp$ ) of the system is also calculated based on the observed domain wall width ( $\delta$ ) calculated from the image taken using LTEM. The width is calculated using the formula  $\delta = \pi \sqrt{\frac{A}{K_u^\perp}}$ , where  $A$  is the exchange stiffness constant.  $A$  is calculated using the formula,  $A = \frac{K_B T_C}{a}$ , where  $K_B$

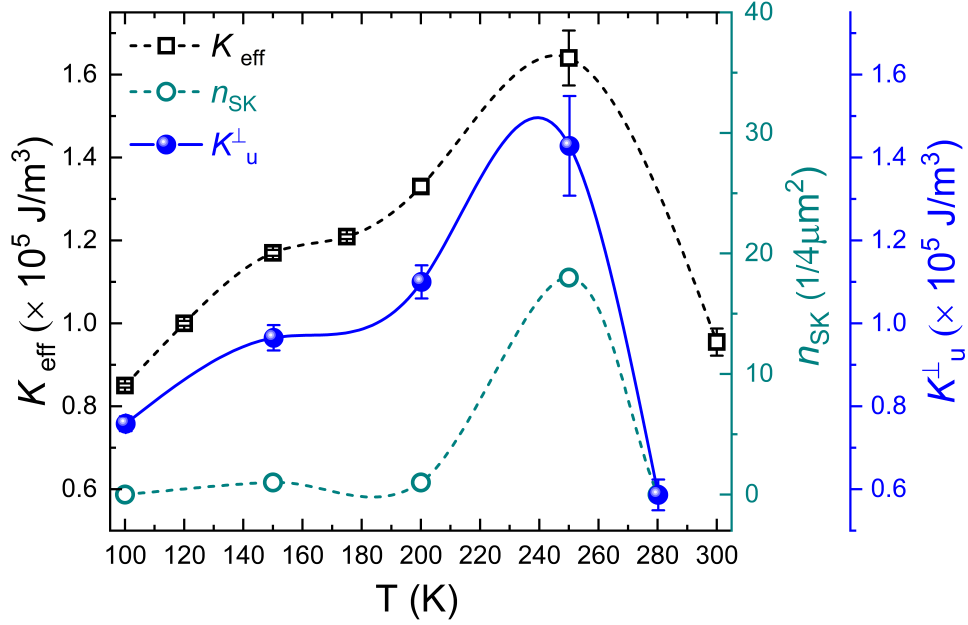


Figure 3.20: The calculated uniaxial magnetocrystalline anisotropy ( $K_{\text{eff}}$ ) from approach to saturation method and domain wall width observation from LTEM ( $K_u^\perp$ ), and the number of observed isolated skyrmions ( $n_{\text{SK}}$ ) at 3 degree sample tilting condition at different temperatures.

is the Boltzmann constant,  $T_C$  is the curie temperature,  $a$  is the lattice constant of the sample  $\text{Mn}_4\text{Ga}_2\text{Sn}$ . The domain wall width of the sample (001) plane at different temperatures are shown in Fig. 3.19. The estimated value of the exchange stiffness constant ( $A$ ) of the sample appears to be  $5 \times 10^{-12}$  J/m. The observed domain wall width and calculated UMA at various temperatures are plotted in Fig. 3.19(f). The variation of UMA calculated using domain wall width nearly matches the effective UMA calculated using  $M - H$  data of the polycrystalline sample. The number of observed isolated skyrmions ( $n_{\text{SK}}$ ) at different temperatures with nearly 3 degree sample tilting conditions are plotted in Fig. 3.20. A direct correlation between  $K_{\text{eff}}$  ( $K_u^\perp$ ) and  $n_{\text{SK}}$  is observed in Fig. 3.20. This observation proves that the skyrmion nucleation probability at a finite tilting condition is higher for higher anisotropy. The higher anisotropy at 250 K aids in the nucleation of a greater number of isolated skyrmions at that temperature compared to lower temperatures under the same tilting condition, as illustrated in Fig. 3.10.



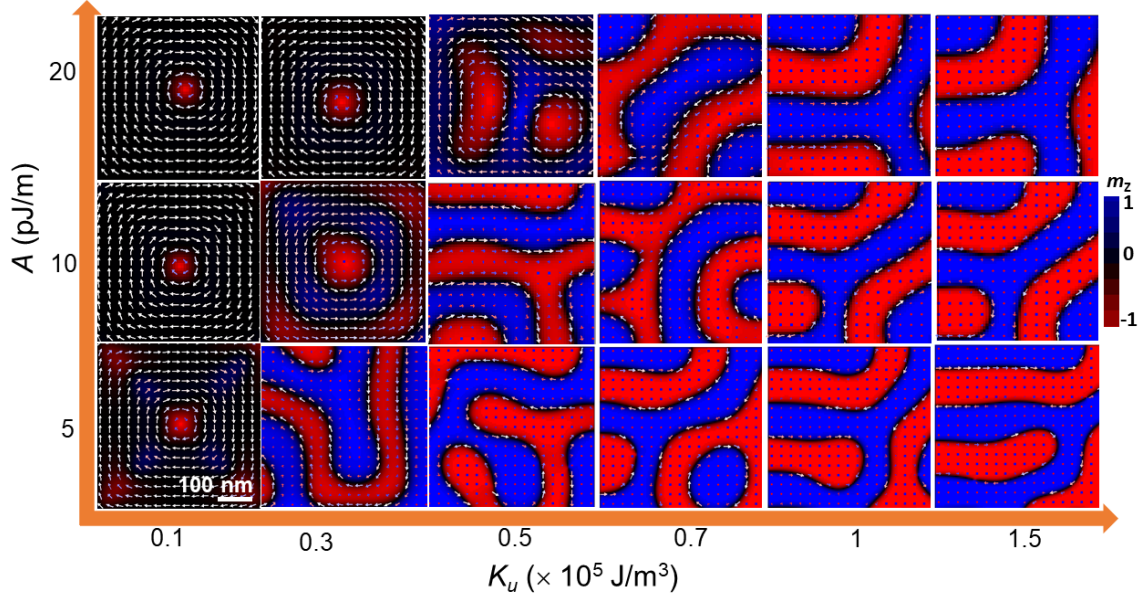


Figure 3.21: Micromagnetic simulated images with varying exchange stiffness constant ( $A$ ) and uniaxial anisotropy ( $K_u$ ) at zero magnetic field. other parameters like,  $M_S$  is taken  $5.35 \times 10^5$  A/m, Gilbert damping constant ( $\alpha$ ) 0.5. The color contrast represents the  $Z$ -direction magnetic moment. The white arrows represent the in plane spin direction.

### 3.6 Micromagnetic simulation

The micromagnetic simulations are performed to further support the experimental result. The cell size for the simulation is taken as  $1 \mu\text{m} \times 1 \mu\text{m} \times 100 \text{ nm}$ . The magnetic ground states of the centrosymmetric system with varying  $A$  and  $K_u$  values are shown in Fig. 3.21. It is observed that the lower anisotropy prefers the vortex state as the ground state, whereas higher anisotropy prefers the stripe domain as the magnetic ground state. It is also observed that the stripe domain formation happens at higher anisotropy for a higher  $A$  value. These observations suggest that the competition between  $A$  and  $K_u$  plays an important role in forming the stripe domain as the magnetic ground state in the system. The exchange stiffness constant ( $A$ ) of the system is calculated based on the equation,  $A = \frac{K_B T_C}{a}$ , where  $K_B$ ,  $T_C$ ,  $a$  are the Boltzmann constant, Curie constant, and lattice parameter, respectively. The calculated value of  $A$  appears  $5 \times 10^{-12}$  J/m. The saturation magnetization

( $M_S$ ) is taken  $5.35 \times 10^5$  A/m, similar to the experimentally observed moment at 250 K. The  $K_u$  is taken as  $1 \times 10^5$  J/m<sup>3</sup>, which roughly corresponds to the order of the computed anisotropy shown in Fig. 3.20. The stripe domain is observed as a magnetic ground state at zero magnetic field. The simulations are performed by considering the random domain state as the initial state. At the same time, the simulations with increasing field are performed by considering the stripe domain as an initial magnetic state. The stripe domains break into skyrmions at a field of 0.2 T, and a distorted hexagonal skyrmion lattice is formed at 0.3 T [Fig 3.22]. The system becomes field polarized at 0.4 T magnetic field. The simulated results readily confirm the skyrmion state as a stable magnetic state for centrosymmetric systems with uniaxial anisotropy.

Now, to accumulate more knowledge about the tilting effect on the system, micromagnetic simulations are performed with a finite in-plane field in different directions. The present in-plane fields actually mimic the tilting of the sample, as tilting basically introduces an in-plane magnetic field. We have taken the simulation parameters similar to those in Fig 3.22. The spin textures are simulated with out of plane magnetic field of 0.2 T ( $\approx 0.2 \cos 6^\circ$ ) along with an extra in-plane field of 0.02 T ( $\approx 0.2 \sin 6^\circ$ ) in different directions. All the spin textures are simulated by completely relaxing the random magnetic state. As shown in Fig. 3.23(a), the skyrmions with both clockwise and counter-clockwise helicity stabilized at zero in-plane magnetic field and 0.2 T out-of-plane magnetic field. The skyrmions transformed into Type-II bubbles with the application of an additional in-plane magnetic field of 0.02 T. For the in-plane magnetic field along  $\pm x$  ( $\pm y$ )-direction, the in-plane magnetization components of the spin textures are organized along  $\pm x$  ( $\pm y$ )-direction. The inset of Fig. 3.23 shows the LTEM simulated images of the micromagnetic simulated spin textures. The LTEM simulated images match well with the experimentally observed images at various sample tilting conditions as shown in Fig. 3.15. These simulations prove that the in-plane magnetic field is the deciding factor for the internal structure of type-II bubbles. The simulations are also performed considering the skyrmion state as the initial state and it is observed that a higher in-plane field

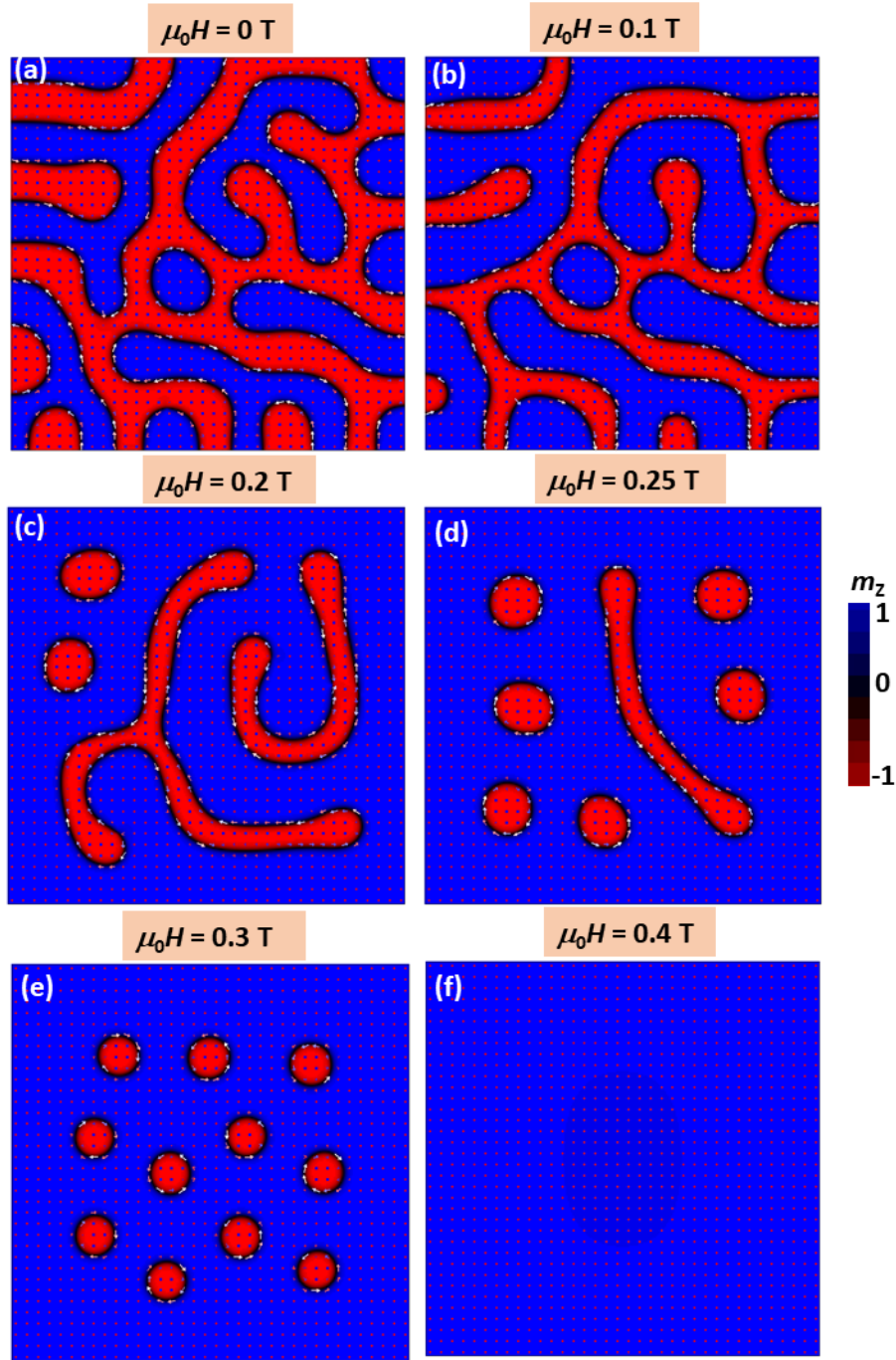


Figure 3.22: Micromagnetic simulated images with varying magnetic field by considering the stripe domain as an initial magnetic state. All the simulations are performed by completely relaxing the initial state. The parameters like  $A$ ,  $K_u$ ,  $M_S$ ,  $\alpha$  are taken as,  $5 \text{ pJ/m}$ ,  $1 \times 10^5 \text{ J/m}^3$ ,  $5.35 \times 10^5 \text{ A/m}$ , and  $0.5$ , respectively. The color contrast represents the Z-direction magnetic moment. The white arrows represent the in-plane spin direction.

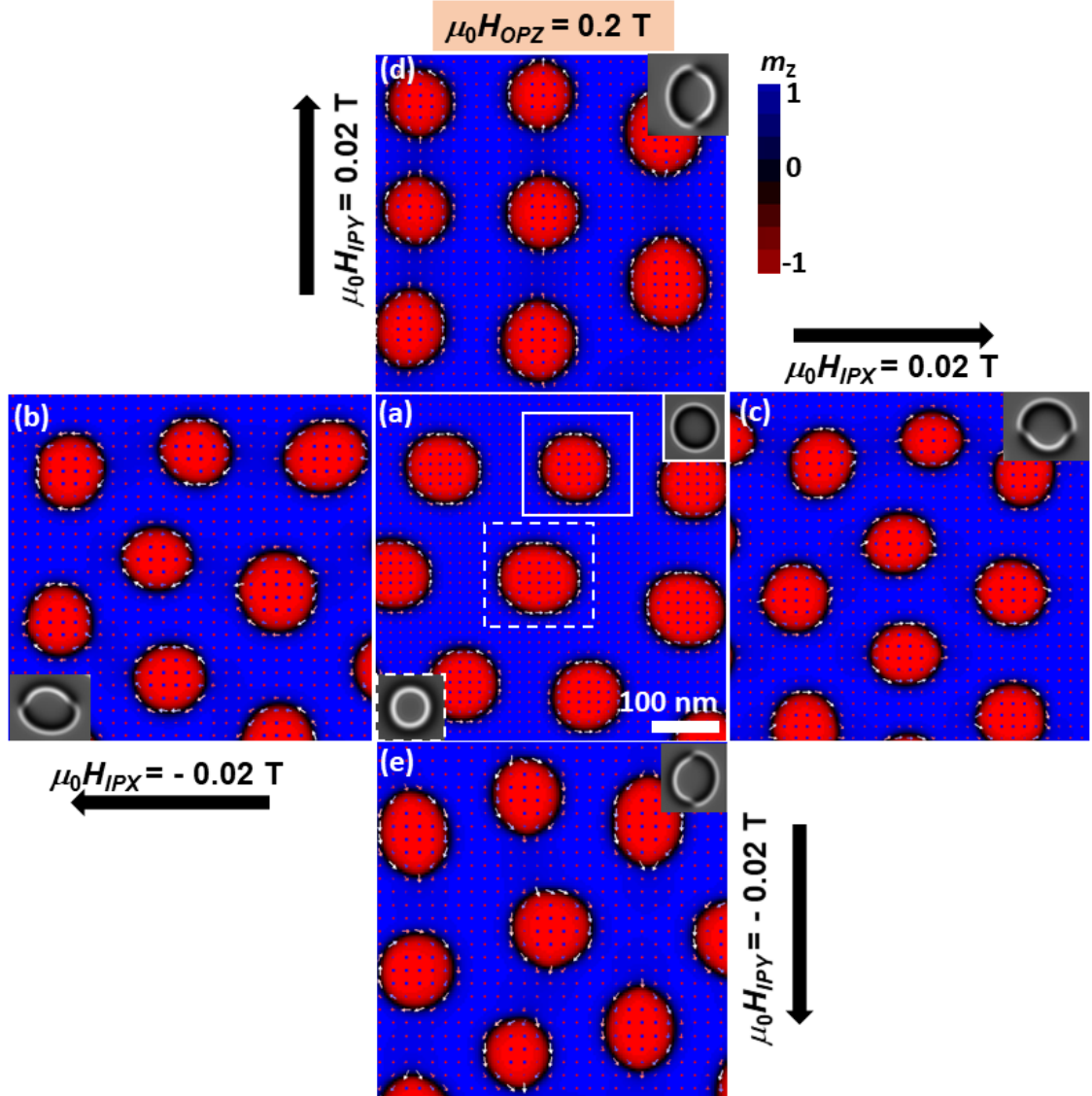


Figure 3.23: Micromagnetic simulated images at 0.2 T out-of-plane magnetic field along with (a) 0 in-plane magnetic field, (b) 0.02 T in-plane magnetic field in negative  $x$ -direction, (c) 0.02 T in-plane magnetic field in positive  $x$ -direction, (d) 0.02 T in-plane magnetic field in positive  $y$ -direction, (e) 0.02 T in-plane magnetic field in negative  $y$ -direction. All the simulations are performed by completely relaxing the random magnetic domain as an initial state. The parameters like  $A$ ,  $K_u$ ,  $M_S$ ,  $\alpha$  are taken as, 5 pJ/m,  $1 \times 10^5 \text{ J/m}^3$ ,  $5.35 \times 10^5 \text{ A/m}$ , and 0.5, respectively. The color contrast represents the  $z$ -direction magnetic moment. The white arrows represent the in-plane spin direction. The index shows the LTEM simulated images of the simulated spin textures. The solid and dashed boxes in Figure (a) mark clockwise and counter-clockwise skyrmions, respectively.



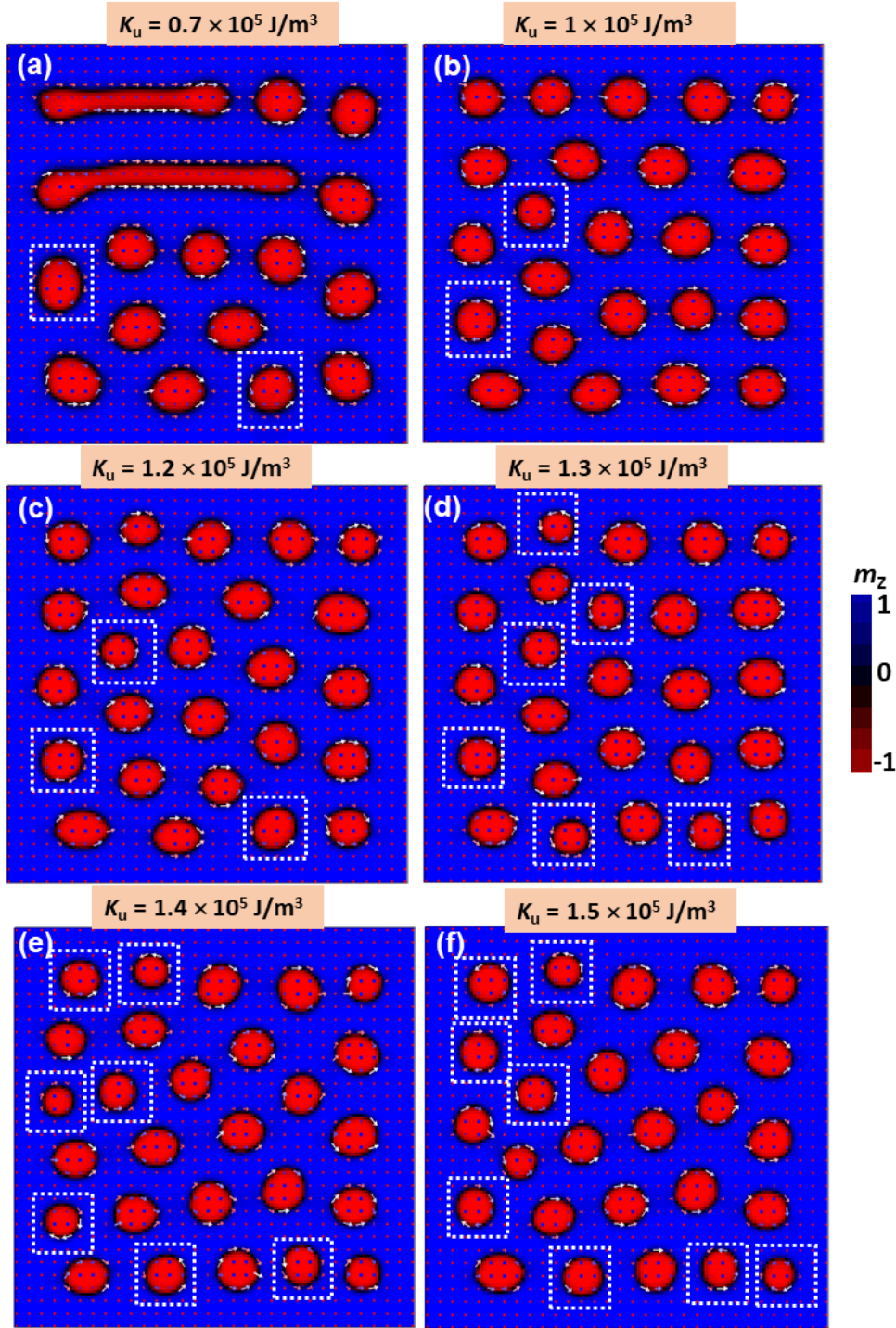


Figure 3.24: The simulated magnetic textures for different uniaxial anisotropy constant values with out of plane magnetic field of 0.3 T and in-plane magnetic field of 0.02 T. The used parameters are,  $A = 5 \times 10^{-12} \text{ J/m}$ ,  $M_s = 6.68 \times 10^5 \text{ A/m}$  (saturation magnetization corresponding to 100 K). The white arrows represent the in-plane magnetization components. The simulations are performed considering a sample area of  $1 \mu\text{m} \times 1 \mu\text{m}$  and thickness of 100 nm. The skyrmion spin textures are marked with white dashed boxes.

( $\approx 0.06$  T for out-of-plane field of 0.2 T) is required to transform the skyrmion into a type -II bubble. The simulations performed considering the random state as the initial state match better with the experimental result, as all the simulations are performed at 0 K i.e., without the finite temperature effect. All the experimental and simulation results categorically establish that controlled switching between topological skyrmion and non-topological type-II bubble is possible by application of a finite in-plane magnetic field.

The simulations are also performed with different UMA while keeping the other parameters constant [Fig 3.24]. It is observed that at a particular in-plane magnetic field, the skyrmion number increases with increasing the strength of UMA. Therefore, the simulation demonstrates that the transformation barrier between topological skyrmion and non-topological type-II bubble depends on the strength of the UMA of the system. The probability of skyrmion formation is higher at higher UMA i.e., the transformation probability is lesser for higher anisotropy case. Figure 3.25 shows the experimentally observed isolated skyrmion number in each  $4 \mu\text{m}^2$  sample area with changing anisotropy, as calculated using the LTEM domain wall observation. The inset shows the simulated isolated skyrmion number with changing anisotropy while keeping the parameters as mentioned in Fig. 3.24. As expected the simulated data match well with the experimentally observed relation between isolated skyrmion numbers at 3 degree sample tilting condition and UMA.

### 3.7 Discussion and conclusion

In this chapter, a new skyrmion hosting centrosymmetric ferromagnet  $\text{Mn}_4\text{Ga}_2\text{Sn}$  is explored, where near room temperature skyrmions with a size of nearly 100 nm are observed. Recently, skyrmions with few nanometer sizes are found in some of the centrosymmetric systems like  $\text{Gd}_2\text{PdSi}_3$ ,  $\text{GdRu}_3\text{Al}_{12}$ ,  $\text{GdRu}_2\text{Si}_2$  due to four spin exchange interaction or geometrical frustration [13, 14, 15]. For all the above mentioned systems the skyrmions are stabilized at very low temperatures of below 20 K. On the other hand, the reported room temperature skyrmions stabilized by

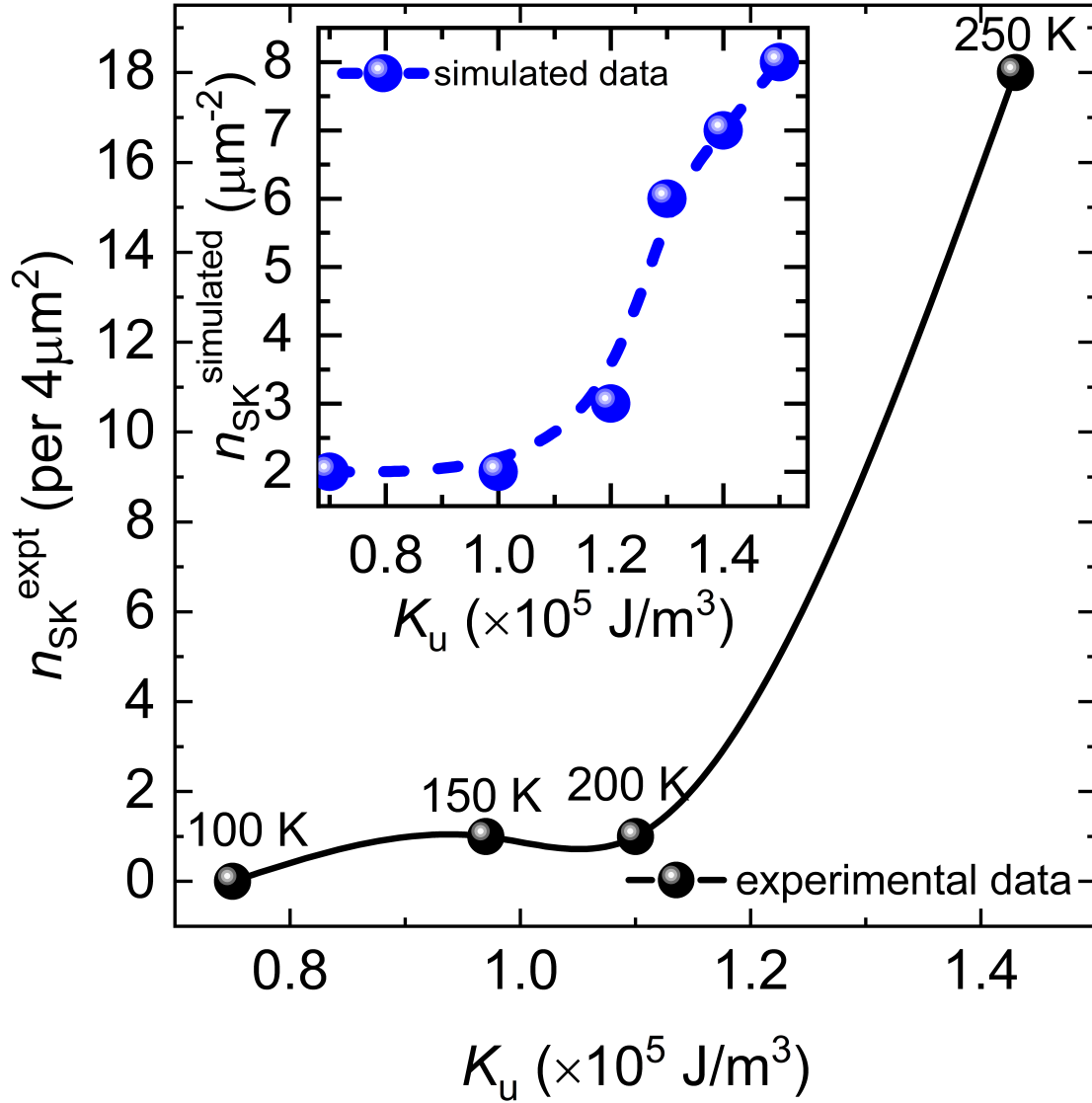


Figure 3.25: Variation of experimentally observed isolated skyrmion numbers at 3 degree sample tilting condition with changing anisotropy. The inset shows the simulated number of isolated skyrmions with changing anisotropy as observed in Fig. 3.24.

dipolar and anisotropy interaction exhibit a size of about 200 nm [7, 8]. Therefore, the observed near room temperature skyrmion with a lower size ( $\approx 100$  nm at 250 K) is important from the practical application point of view.

Topological skyrmion to non-topological type II bubble transformation is recently observed in a few of the centrosymmetric systems [128, 129]. In this study a detailed discussion about the transformation mechanism between skyrmion and type-II bubble in achiral system is provided. Here, it is proved that the skyrmion state is the stable magnetic state when the magnetic field is applied along the out-of-plane ( $c$ ) direction only. In contrast, the type-II bubbles are formed as a metastable state when a finite in-plane magnetic field is present along with the out-of-plane magnetic field. The in-plane magnetic field value and direction are controlled by tilting the sample at various angles in different directions. By the systematic study of the spin textures at different tilting directions, both with the help of experiment and simulation, it is observed that the in-plane magnetic field direction plays a crucial role in deciding the configuration of type-II bubble spin texture. The in-plane moment of the type-II bubble follows the in-plane magnetic field direction in the present system. This kind of transformation is also reported in the non-centrosymmetric  $D_{2d}$  system having anisotropic Dzyloshinskii Moriya interaction (DMI), such as  $D_X = -D_y$  [130]. In these systems, the transformation between the antiskyrmion and the non-topological bubble is related to the magnetic anisotropy of the skyrmion provided by  $D_{2d}$  symmetry. Whereas, the presence of mirror symmetry in centrosymmetric systems make the transformation properties same for all directions of the in-plane magnetic field. In this system, the transformation is observed due to nearly degenerate energy state of the skyrmion and bubble. The applied in-plane magnetic field produces the Bloch wall and leads to the type II bubble formation by crossing the energy barrier. When the in-plane field is withdrawn the Bloch wall disappears and the skyrmion again comes back in a stable state. All centrosymmetric systems with ferromagnetic characteristics are expected to show similar transformation characteristics with different in-plane magnetic field amplitude depending on the system parameters.



The calculated effective UMA of the present system shows a noticeable correlation with the observed isolated skyrmion number at different temperatures with finite sample tilting condition. These observations readily prove that the higher anisotropy hinders the transformation between skyrmion and type-II bubble, thereby supporting the formation of a large number of isolated skyrmions in the presence of the same magnitude of in-plane magnetic field at a higher temperature (250 K) with higher anisotropy. These observations are also theoretically validated by micromagnetic simulations with a finite in-plane magnetic field and different anisotropies.

In conclusion, the presence of a skyrmionic state has been established as a stable magnetic state in a new centrosymmetric system  $\text{Mn}_4\text{Ga}_2\text{Sn}$ . The skyrmions can be transformed into type-II bubbles with a finite in-plane magnetic field. It is also shown that the in-plane magnetic field acts as a deciding factor for the spin texture arrangements of type-II bubbles. Most importantly, the role of anisotropy in the above explained transformation is understood systematically with the help of experimental studies and micromagnetic simulations. It is observed that the higher anisotropy actually opposes the transformation between skyrmions and magnetic bubbles, whereas easy transformation can be possible for lower anisotropy. Therefore, the strength of UMA decides the energy barrier between the skyrmion and type-II bubble.

## Chapter 4

# Magnetic-order dependent skyrmion stabilization in MnFeCoGe centrosymmetric hexagonal magnets

Chapter 3 of the present thesis introduces a centrosymmetric kagome ferromagnet  $\text{Mn}_4\text{Ga}_2\text{Sn}$  as a novel host for skyrmions. The tunability of the skyrmions in  $\text{Mn}_4\text{Ga}_2\text{Sn}$  was studied in terms of external magnetic field strength. Although recent literature extensively explores the tunable characteristics of skyrmions in such systems with external factors like magnetic fields [43, 125, 131] and electric currents [128, 129, 132], there exists limited research on skyrmion tunability considering internal energy parameters or material-specific properties. As a result, the primary focus of this chapter is to investigate how the magnetic orderings and underlying interactions impact the stability of skyrmions in a centrosymmetric system. In this direction, a centrosymmetric hexagonal magnet with UMA and tunable magnetic ground state can serve the purpose.

It has been reported theoretically and experimentally that the hexagonal Mn-

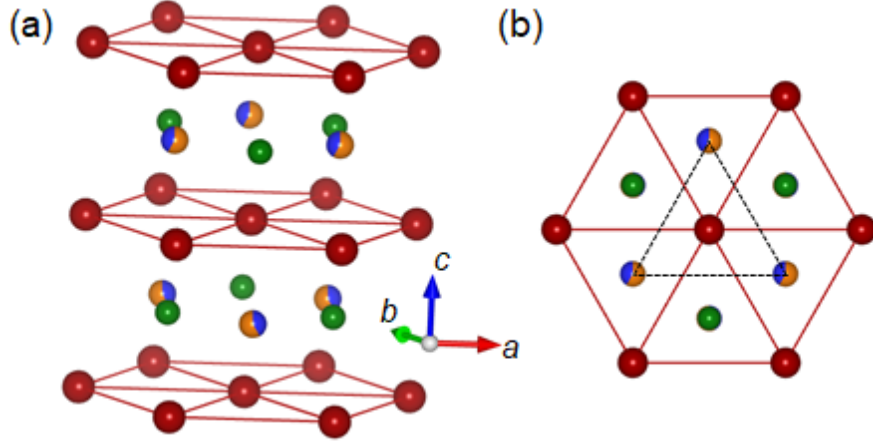


Figure 4.1: (a) Crystal structure of MnFe<sub>1-x</sub>Co<sub>x</sub>Ge samples. The red, blue, orange, and green balls represent Mn, Co, Fe, and Ge atoms, respectively. (b) Top (*c*-axis) view of the triangular lattice arrangement of Mn atoms.

FeGe system exhibits a non-collinear magnetic ground state due to exchange frustration, characterized by an FM component along the *c*-axis and an AFM component in the basal plane [133, 134]. In contrast, the hexagonal magnet MnCoGe displays a collinear ferromagnetic structure [133]. Consequently, substituting Fe with Co can tailor the magnetic ground state ordering from a non-collinear to a collinear ferromagnet. Additionally, some reports suggest MnFeGe as a potential skyrmion hosting system based on the *Q* factor calculation, which is the ratio between anisotropy energy and demagnetization energy [134]. As a result, the MnFe<sub>1-x</sub>Co<sub>x</sub>Ge series of compounds present a promising option for investigating the impact of magnetic ground state ordering and underlying interactions on the stability of skyrmions in centrosymmetric systems. The MnFe<sub>1-x</sub>Co<sub>x</sub>Ge samples feature alternating layers of Mn atoms and Fe (Co)-Ge atoms along the *c*-axis, as depicted in Fig. 4.1(a). In each layer, the Mn atoms form a triangular lattice arrangement, as illustrated in Fig. 4.1(b).

To improve our understanding of potential magnetic ground states and the underlying interaction mechanisms, collaborative density functional theory (DFT) calculations are conducted [For detailed techniques of the theoretical calculations, please refer to the theoretical calculation section in arXiv:2311.15823]. The follow-

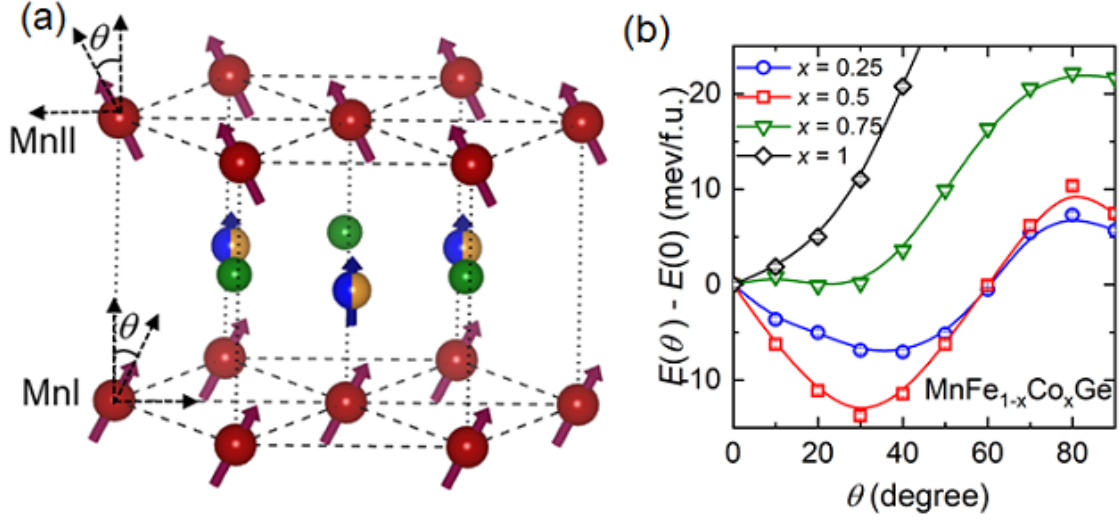


Figure 4.2: (a) Potential Magnetic Ground States for  $\text{MnFe}_{1-x}\text{Co}_x\text{Ge}$  Samples. The red, blue, orange, and green colored atoms represent Mn, Co, Fe, and Ge, respectively. (b) The Variation in Energy with Non-Collinear Canting Angle in  $\text{MnFe}_{1-x}\text{Co}_x\text{Ge}$  Sample.

ing section summarizes the outcomes of the DFT calculations, contributing to a comprehensive understanding of our experimental observations.

## 4.1 Theoretical understanding

Figure 4.2(a) illustrates the schematic representation of a non-collinear magnetic state with a  $c$ -axis FM component and an  $ab$ -plane AFM component. The energy variation concerning the change in non-collinear canting angle ( $\theta$ ) for  $\text{MnFe}_{1-x}\text{Co}_x\text{Ge}$  samples is depicted in Fig. 4.2(b). The compound with  $x = 0.25$  exhibits a local energy minimum at  $\theta = 40^\circ$ , which is in good agreement with the previously calculated  $\theta$  value for  $\text{MnFeGe}$  [134]. As the Co concentration increases to  $x = 0.5$ , the energy minimum position shifts to  $30^\circ$ . With a subsequent increase in Co concentration to  $x = 0.75$  and  $x = 1$ , the energy minimum state transitions into a collinear ferromagnetic configuration with  $\theta = 0^\circ$ . In summary, the theoretical calculations indicate that the sample with  $x = 0.25, 0.5$  exhibits a non-collinear magnetic ground state, whereas the magnetic ground state changes to a collinear FM configuration

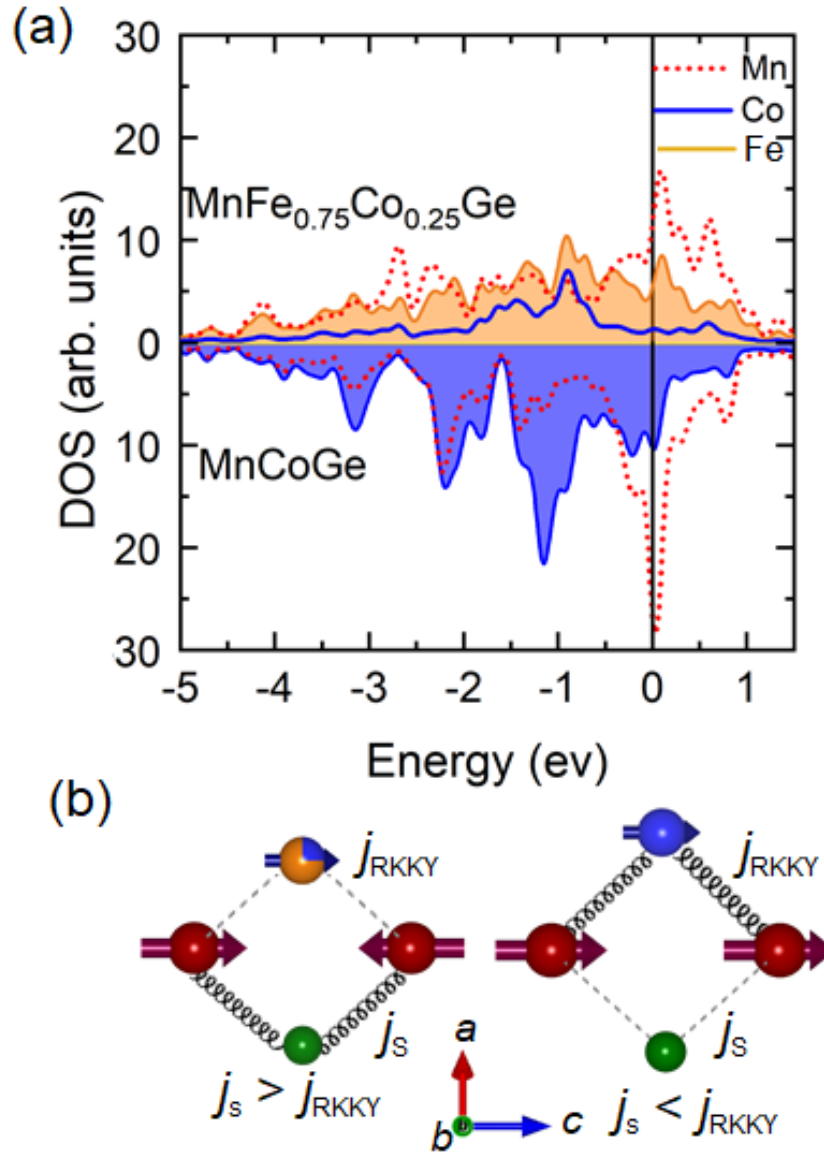


Figure 4.3: (a) The d state projected density of state (DOS) of Mn, Fe, and Co for non-magnetic MnCoGe and MnFe<sub>0.75</sub>Co<sub>0.25</sub>Ge systems. (b) The schematic illustration of probable indirect exchange interactions between Mn-Mn localized moments with change in Co concentration.

with a further increase in Co concentration ( $x \geq 0.75$ ).

Since the distribution and density of states (DOS) close to the Fermi level are crucial for determining the exchange parameters, a comprehensive investigation of the projected DOS for the d states of Mn, Fe, and Co atoms in the samples is performed to understand the mechanisms leading to the modification of magnetic ground states with an increase in Co concentration. Figure 4.3(a) illustrates the projected DOS for d-states of Mn, Fe, and Co atoms in non-magnetic  $\text{MnFe}_{0.75}\text{Co}_{0.25}\text{Ge}$  and  $\text{MnCoGe}$  systems. A noticeable variation in DOS is seen close to the Fermi level for both materials, especially in the Fe-d and/or Co-d states. The indirect exchange model of magnetic ordering, which includes a competition between carrier-mediated (RKKY-like) exchange and superexchange can be used to explain the observed changes in Fermi-level DOS [135]. The transition energy from the d-states to the Fermi level determines the parameters of these exchange interactions inversely [135, 136, 137]. In Fe-rich samples, the availability of Fe-d states is higher above the Fermi level than just below it.  $\text{MnCoGe}$ , on the other hand, exhibits more Co-d states just below the Fermi level. In this context, the change in DOS between Fe and Co resembles the rigid-band model, wherein introducing an additional electron leads to an upward shift in the Fermi level. By employing a perturbative approach, the RKKY coupling constant ( $j_{\text{RKKY}}$ ) and super exchange coupling constant ( $j_s$ ) can be expressed in  $q \rightarrow 0$  limit as follows,

$$j_{\text{RKKY}}(0) = V^4 D(\epsilon_F) / E_h^2 \quad (4.1)$$

$$j_s(0) = V^4 \sum_{nk}^{\epsilon_{nk} \geq \epsilon_F} (\epsilon_{nk} - \epsilon_F - E_h)^{-3} \quad (4.2)$$

Here,  $V$  represents the electron mixing parameter, and  $D(\epsilon_F)$  denotes the DOS at the Fermi level.  $\epsilon_{nk}$  signifies the energy at the  $k$ -point of the  $n$ th band, while  $E_h$  corresponds to the energy involved in electron transfer from d-states to the Fermi level. The Fe and Co-rich samples show a large DOS near the Fermi level, whereas a fall in DOS near the Fermi level in the Fe-rich case ( $\text{MnFe}_{0.75}\text{Co}_{0.25}\text{Ge}$ ) indicates

a decrease in  $j_{RKKY}$  in Fe-rich samples. The superexchange coupling constant can be constrained as follows [135, 136, 137],

$$j_s(0) \leq V^4 N / E_h^3 \quad (4.3)$$

As the number of unoccupied states ( $N$ ) near the Fermi level is considerably smaller for MnCoGe compared to the Fe-rich case (MnFe<sub>0.75</sub>Co<sub>0.25</sub>Ge),  $j_s$  should be greater for the Fe-rich sample. Conversely,  $D(\epsilon_F)$  is larger for the Co-rich sample (MnCoGe) than the Fe-rich sample (MnFe<sub>0.75</sub>Co<sub>0.25</sub>Ge); therefore,  $j_{RKKY}$  should be higher for the Co-rich sample. Hence, AFM ordering is preferable for the Fe-rich sample with  $j_s > j_{RKKY}$ , whereas the Co-rich samples with  $j_{RKKY} > j_s$  favor FM ordering. Figure 4.3(b) illustrates a schematic representation of Co conduction electron-mediated dominant RKKY exchange between two localized Mn moments in MnCoGe, resulting in FM ordering rather than AFM ordering. The calculations clearly indicate the existence of competing FM and AFM interactions among localized Mn moments in the MnFe<sub>1-x</sub>Co<sub>x</sub>Ge systems. Consequently, the observed exchange frustration in the systems can be attributed to non-collinear magnetic states. The strength of exchange frustration can be tuned by adjusting the Co concentration, offering the flexibility to modify the magnetic ground state from non-collinear to collinear ferromagnetic ordering in the MnFe<sub>1-x</sub>Co<sub>x</sub>Ge sample.

## 4.2 Experimental results

Theoretical calculations highlight the MnFe<sub>1-x</sub>Co<sub>x</sub>Ge compound as a promising candidate for investigating the impact of both magnetic ground states and exchange frustrations on skyrmion stabilization. To explore this, polycrystalline samples of MnFe<sub>1-x</sub>Co<sub>x</sub>Ge with varying Co concentrations (from  $x = 0.2$  to  $0.8$ ) are prepared using an arc melting furnace. A combination of powder Neutron diffraction (PND) and Lorentz transmission electron microscopy (LTEM) measurements are used to experimentally evaluate the skyrmion tunability resulting from different magnetic

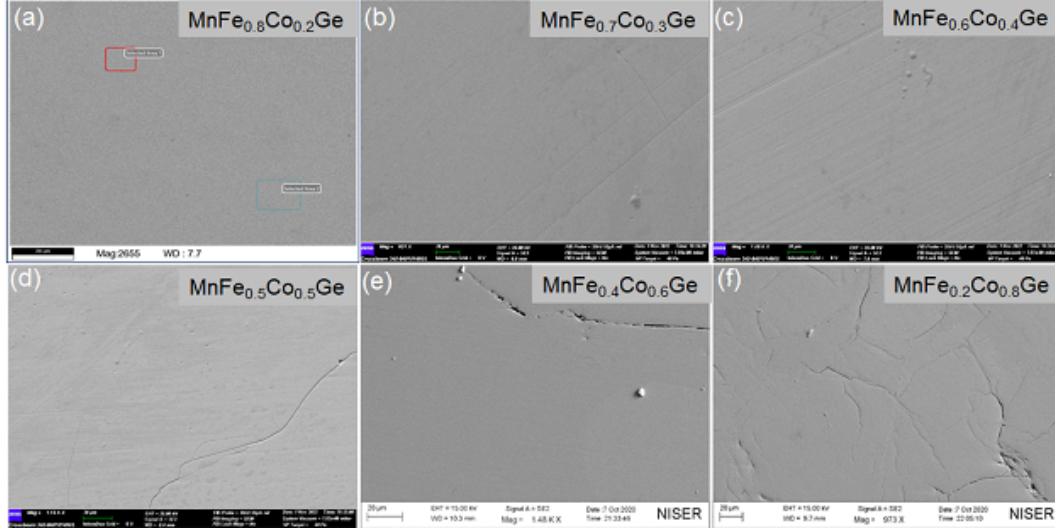


Figure 4.4: SEM images of the samples  $\text{MnFe}_{1-x}\text{Co}_x\text{Ge}$  ( $x = 0.2$  to  $0.8$ ). The boxed areas in Figure 4.4a denote various locations on the sample from which the EDX spectra were collected.

configurations.

#### 4.2.1 Compositional homogeneity characterization

The FESEM images, along with the EDX study, reveal that the samples are compositionally single phase. The SEM images of the samples with uniform contrast are shown in Fig. 4.4. A comparison between EDX observed atomic percentages and exact atomic percentages of the constituent elements is shown in Table 4.1. The obtained atomic percentages nearly match the expected atomic percentage of constituent elements. The EDX spectra calculated at different places in the samples, as shown in Fig. 4.4(a).

#### 4.2.2 Structural characterization

The Rietveld refined room temperature powder XRD patterns for the samples  $\text{MnFe}_{1-x}\text{Co}_x\text{Ge}$  ( $x = 0.2$  to  $0.8$ ) are shown in Fig. 4.5. All the samples crystallize in hexagonal crystal structure with space group  $P6_3/mmc$ . In the crystal structure, the Mn and Fe atoms preferentially occupy the Wyckoff positions 2a (0,0,0)



Sample composition	Exact atomic percentage	Obtained atomic percentage
MnFe <sub>0.8</sub> Co <sub>0.2</sub> Ge	MnK - 33.33 FeK - 26.67 CoK - 6.67 GeK - 33.33	MnK - 35.85 ± 0.91 FeK - 27.86 ± 0.76 CoK - 6.76 ± 0.46 GeK - 29.60 ± 1.24
MnFe <sub>0.7</sub> Co <sub>0.3</sub> Ge	MnK - 33.33 FeK - 23.33 CoK - 10 GeK - 33.33	MnK - 35.71 ± 0.87 FeK - 24.18 ± 0.67 CoK - 9.72 ± 0.47 GeK - 30.39 ± 1.20
MnFe <sub>0.6</sub> Co <sub>0.4</sub> Ge	MnK - 33.33 FeK - 20 CoK - 13.33 GeK - 33.33	MnK - 35.90 ± 0.82 FeK - 20.80 ± 0.57 CoK - 13.34 ± 0.52 GeK - 29.96 ± 1.11
MnFe <sub>0.5</sub> Co <sub>0.5</sub> Ge	MnK - 33.33 FeK - 16.67 CoK - 16.67 GeK - 33.33	MnK - 35.04 ± 0.82 FeK - 18.19 ± 0.5 CoK - 17.43 ± 0.61 GeK - 29.35 ± 1.03
MnFe <sub>0.4</sub> Co <sub>0.6</sub> Ge	MnK - 33.33 FeK - 13.33 CoK - 20 GeK - 33.33	MnK - 33.80 ± 1.86 FeK - 12.60 ± 1.50 CoK - 18.10 ± 1.85 GeK - 35.80 ± 2.51
MnFe <sub>0.2</sub> Co <sub>0.8</sub> Ge	MnK - 33.33 FeK - 6.67 CoK - 26.66 GeK - 33.33	MnK - 32.60 ± 1.70 FeK - 6.70 ± 1.21 CoK - 24.80 ± 1.84 GeK - 35.90 ± 2.48

Table 4.1: Comparison between experimentally obtained atomic percentages and exact atomic percentages.

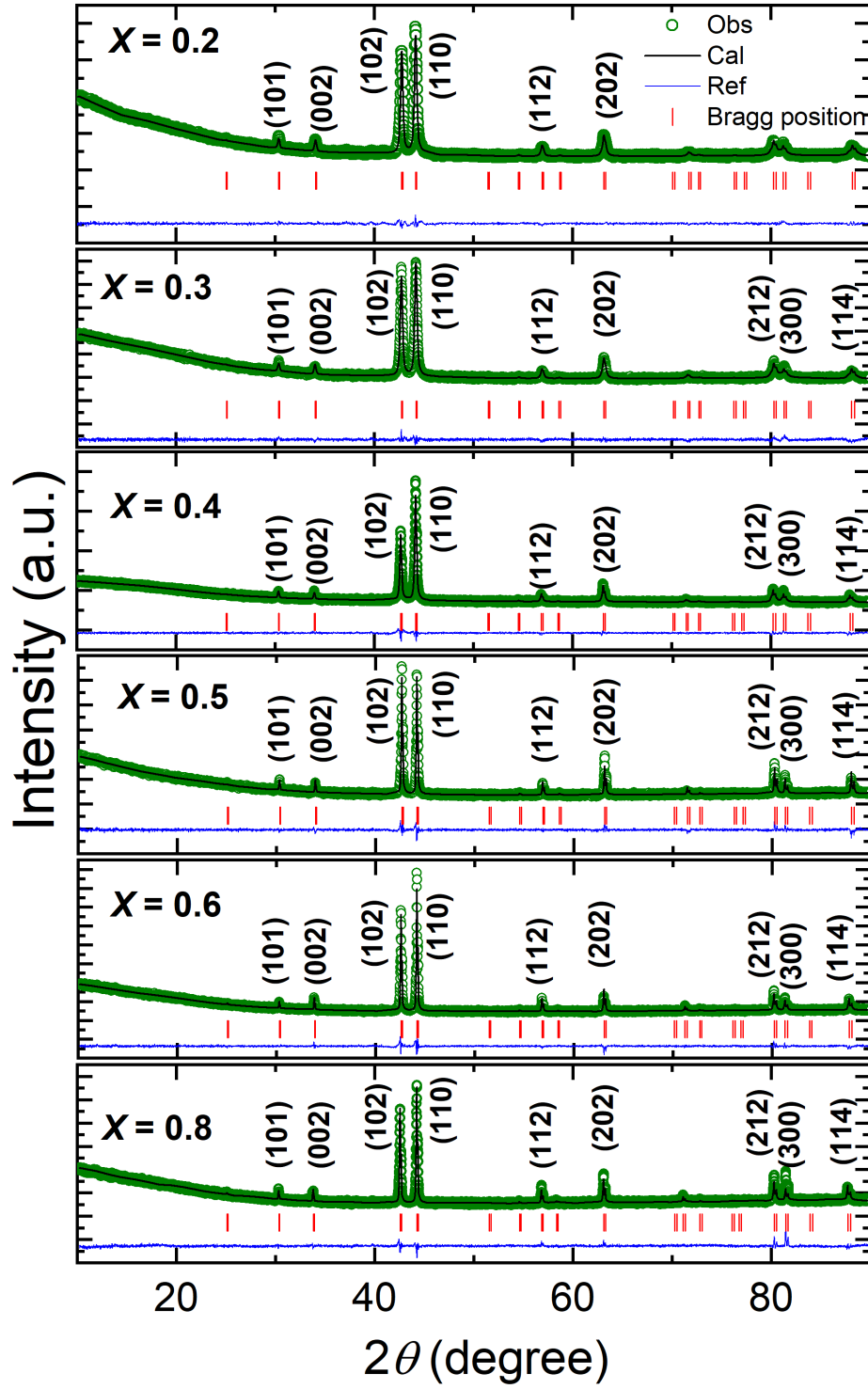


Figure 4.5: Rietveld refined room temperature powder XRD patterns of the samples  $\text{MnFe}_{1-x}\text{Co}_x\text{Ge}$  ( $x = 0.2$  to  $0.8$ ).

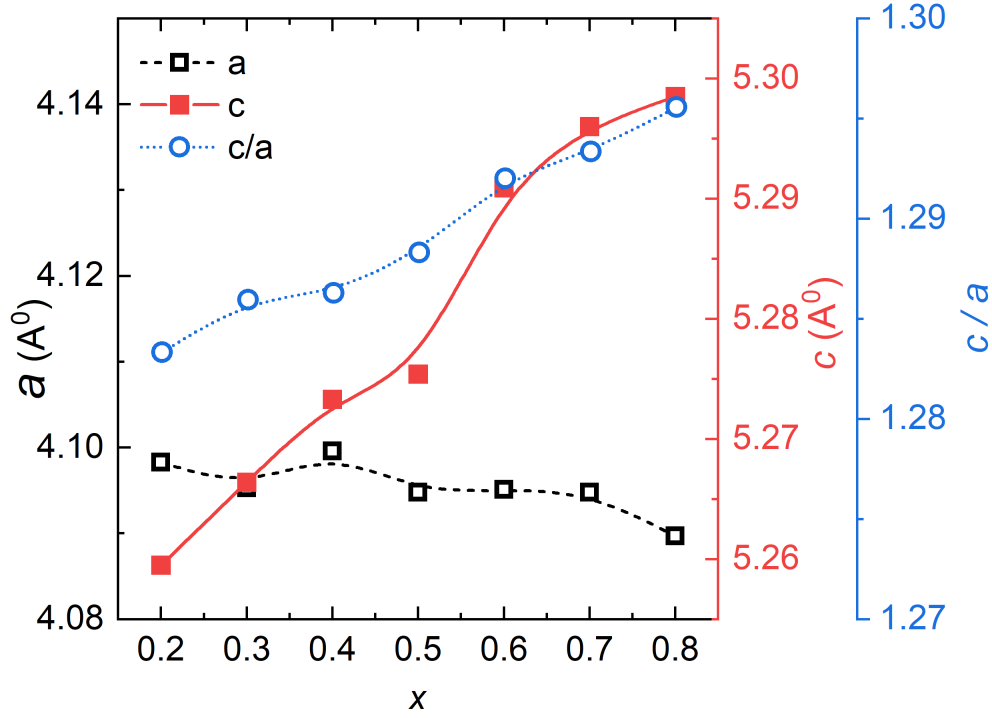


Figure 4.6: Rietveld refined room temperature lattice parameters for the samples  $\text{MnFe}_{1-x}\text{Co}_x\text{Ge}$  ( $x = 0.2$  to  $0.8$ ).

and 2d (0.3333, 0.6667, 0.75), respectively, whereas Ge atoms occupy position 2c (0.3333, 0.6667, 0.25). The refined room temperature lattice parameters are shown in Fig. 4.6. A little increase in the  $c$  value and the  $c/a$  ratio of the samples is observed with increasing the Co concentration ( $x$ ). It is expected that the system exhibits a competing exchange interaction that can be altered when the  $c$  value changes [134]. Hence, it is feasible to tune the magnetic ground state between non-collinear to collinear magnetic structures in the  $\text{MnFe}(\text{Co})\text{Ge}$  system.

### 4.2.3 Magnetic characterization

The magnetization ( $M$ ) vs. temperature ( $T$ ) plots for the samples  $\text{MnFe}_{1-x}\text{Co}_x\text{Ge}$  ( $x = 0.2$  to  $0.8$ ) at a magnetic field of 1 kOe are presented in Fig. 4.7. The ordering temperature ( $T_C$ ) of the samples increases from 170 K to 265 K with increasing the Co concentration from  $x = 0.2$  to  $0.8$  [shown in Fig. 4.9]. The  $M$  vs  $T$  curves exhibit a similar behavior to that of the parent compound  $\text{MnFeGe}$  for Co doping

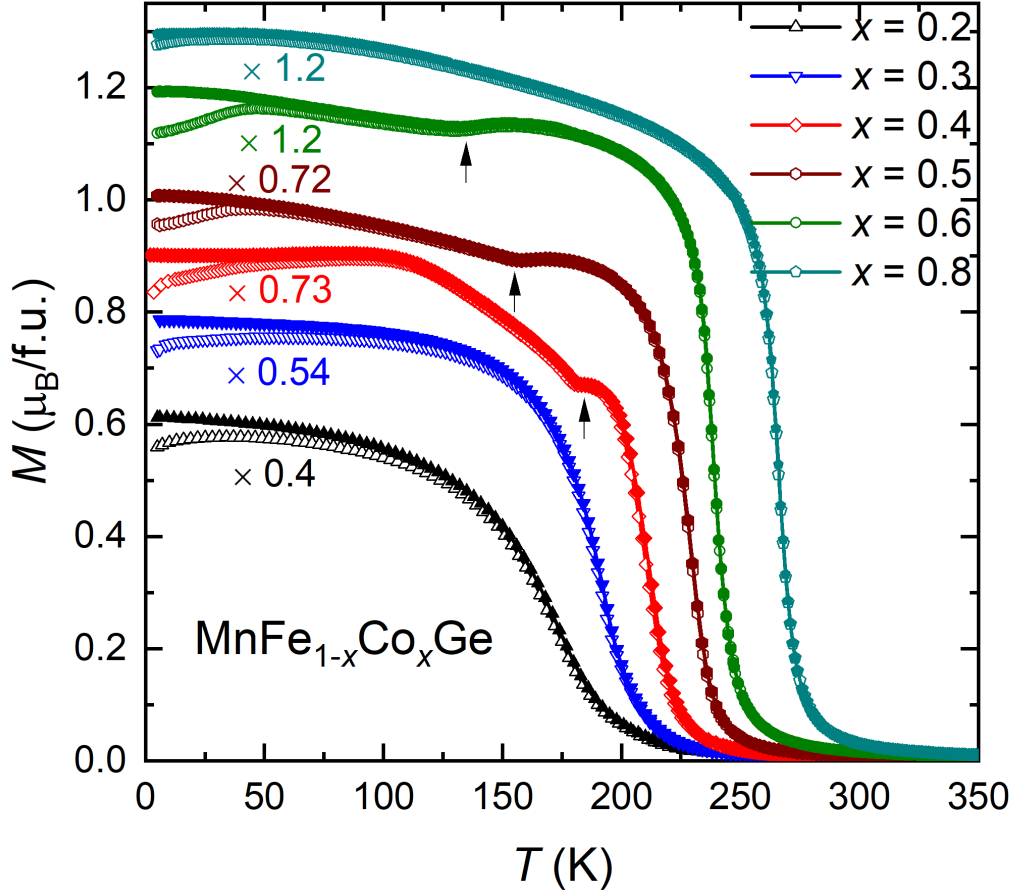


Figure 4.7: Magnetization( $M$ ) vs. temperature( $T$ ) plots for the samples  $\text{MnFe}_{1-x}\text{Co}_x\text{Ge}$  ( $x = 0.2$  to  $0.8$ ) at a magnetic field of 1 kOe. The additional transitions are marked with arrows. The factors written beside the curves represent that the data shown in the Figure is actual data multiplied the factors.

up to  $x = 0.3$ [133, 134]. Hence, the samples up to  $x = 0.3$  are expected to possess magnetic ground states similar to the parent compound. However, in addition to  $T_C$ , the samples with higher Co concentrations exhibit an additional transition ( $T_t$ ), as shown with arrows in Fig. 4.7. The transition is quite sharp for the sample with  $x = 0.4$  and gradually fades for  $x \geq 0.5$ . This additional transition in the sample with  $x = 0.8$  is evident in the  $M$  vs.  $T$  plot at a lower magnetic field of 0.1 kOe [see Fig. 4.8(a)]. The transition is also observed in temperature dependent ac susceptibility [ $\chi'(T)$ ] data [see Fig. 4.8(b)]. The graph in Fig. 4.9 displays the  $T_t$  and  $T_C$  for samples with varying Co concentrations. Isothermal field ( $\mu_0 H$ ) dependent magnetization ( $M$ ) curves for the samples  $\text{MnFe}_{1-x}\text{Co}_x\text{Ge}$  ( $x = 0.2$  to  $0.8$ ) at 5 K

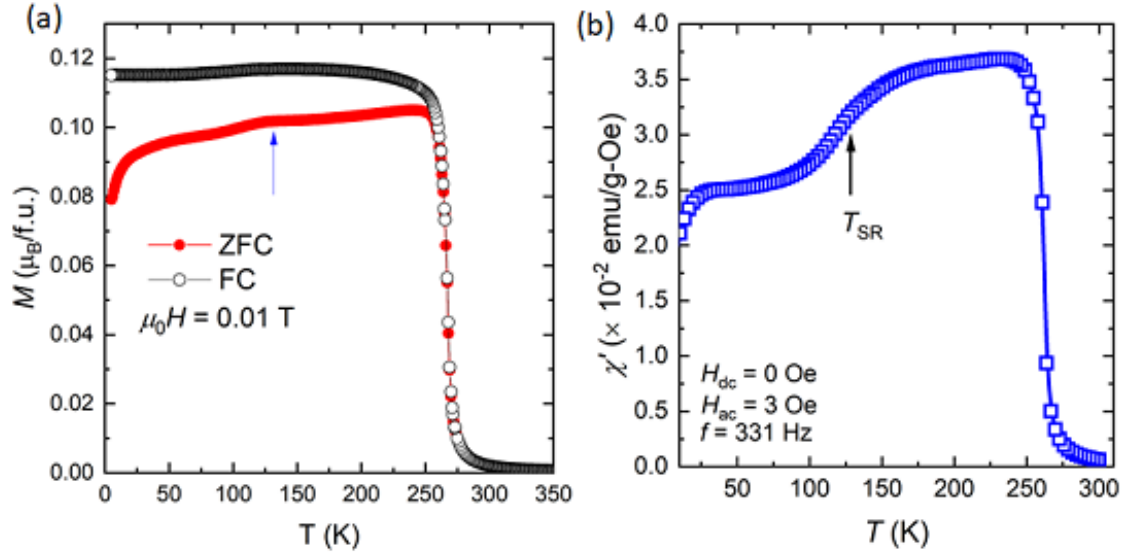


Figure 4.8: (a) Magnetization ( $M$ ) vs. temperature ( $T$ ) plot for  $\text{MnFe}_{0.2}\text{Co}_{0.8}\text{Ge}$  ( $x = 0.8$ ) at a magnetic field of 0.1 kOe. The additional transition is marked with an arrow. (b) Temperature dependent ac susceptibility [ $\chi'(T)$ ] for  $\text{MnFe}_{0.2}\text{Co}_{0.8}\text{Ge}$ .

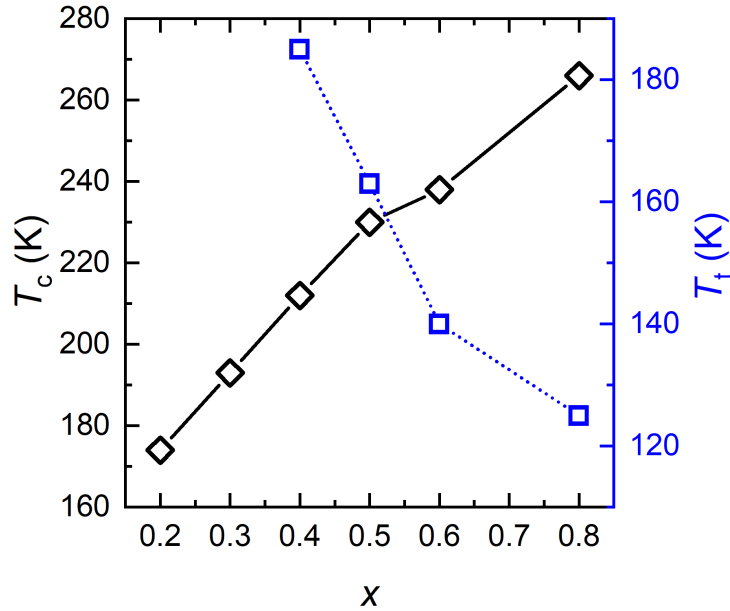


Figure 4.9: Curie temperature ( $T_C$ ) and additional magnetic transition temperature ( $T_t$ ) for different compositions of  $\text{MnFe}_{1-x}\text{Co}_x\text{Ge}$  ( $x = 0.2$  to  $0.8$ ).

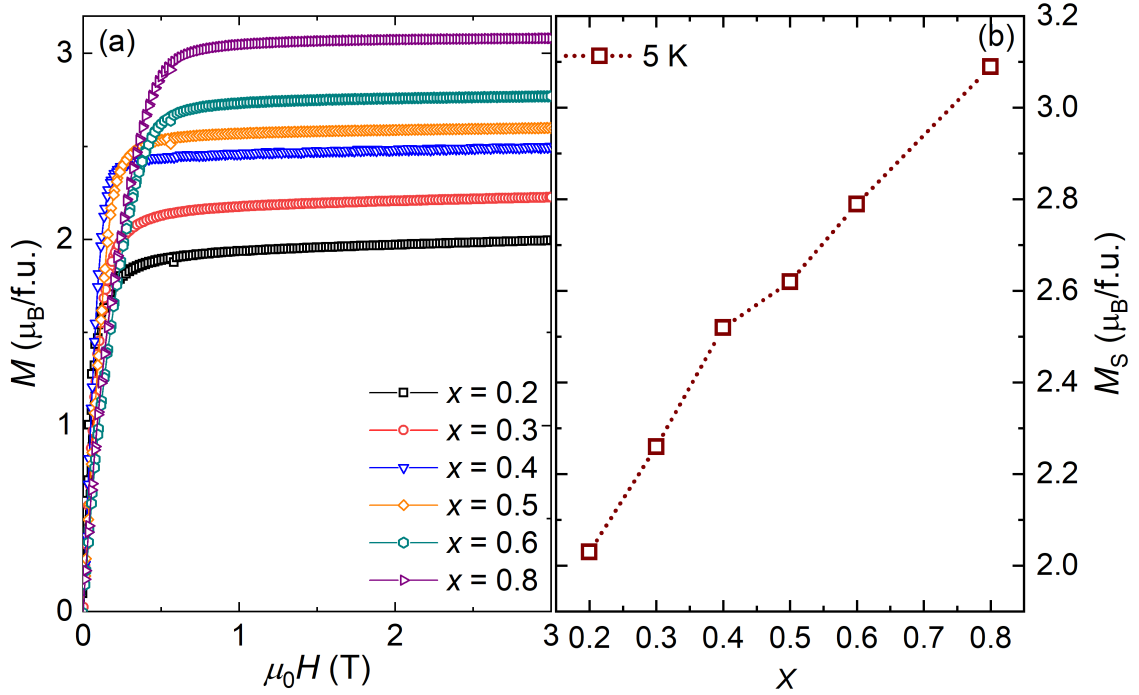


Figure 4.10: (a) Magnetic moment ( $M$ ) vs. magnetic field ( $\mu_0 H$ ) plots for the samples  $\text{MnFe}_{1-x}\text{Co}_x\text{Ge}$  ( $x = 0.2$  to  $0.8$ ) at temperature of 5 K. (b) The variation of saturation magnetization ( $M_S$ ) of the samples with varying Co concentration ( $x$ ).

are shown in Fig. 4.10. The saturation magnetization of the samples at 5 K increases from  $2 \mu_B/\text{f.u.}$  to  $3.1 \mu_B/\text{f.u.}$ , while increasing Co concentration ( $x$ ) from 0.2 to 0.8. The increase in both the ordering temperature ( $T_C$ ) and saturation magnetization ( $M_S$ ) indirectly indicates an enhancement in the strength of ferromagnetic exchange with the increasing concentration of Co ( $x$ ) concentration. Figure 4.11 illustrates a comparison between the experimental  $M_S$  and the net moment calculated using DFT for various possible magnetic configurations for the samples  $\text{MnFe}_{1-x}\text{Co}_x\text{Ge}$ . The  $M_S$  value for the samples  $x = 0.75$  and 1 closely matches the DFT calculated moment for the collinear ferromagnetic (CFM) configuration. In agreement with the calculations, the  $M_S$  values for  $x = 0.25$  and  $0.5$  match more closely with the DFT calculated net moment for the non-collinear ferromagnetic (NCFM) configuration rather than the CFM configuration.

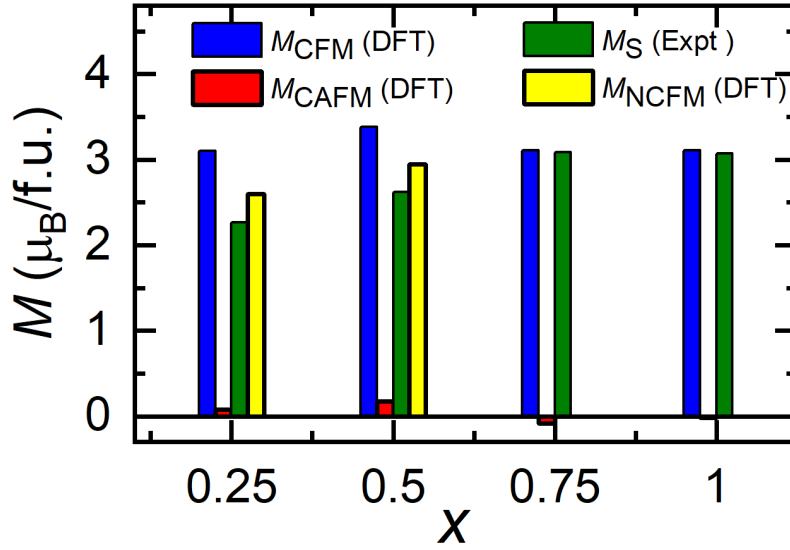


Figure 4.11: A comparison between the experimental saturation moment ( $M_S$ ) and the net moment calculated through DFT for samples with different potential magnetic ground states. The acronyms CFM, NCFM, and CAFM represent collinear ferromagnet, non-collinear ferromagnet, and collinear antiferromagnet, respectively. The  $M_s$  values of nearby compositions (i.e,  $x = 0.3, 0.5, 0.8$ ) are used for comparison, and the  $M_s$  value for  $x = 1$  is obtained from reference [133].

#### 4.2.4 Magnetic ground states using powder neutron diffraction (PND) experiment

To throw more light into the magnetic interaction in the sample, powder neutron diffraction (PND) studies are carried out on materials with  $x = 0.4$  (Fe rich) and 0.8 (Co rich). The PND data are collected using a neutron beam of wavelength  $1.094 \text{ \AA}$ . The structural parameters of the samples are refined above the ordering temperature only. The magnetic phase is included at lower temperatures, where the lattice parameters and moment components are refined. Both samples confirm their hexagonal crystal structure with space group  $P6_3/\text{mmc}$  (No. 194).

##### Magnetic ground state for $\text{MnFe}_{0.6}\text{Co}_{0.4}\text{Ge}$ ( $x = 0.4$ ):

In addition to the nuclear Bragg reflections, the  $\text{MnFe}_{0.6}\text{Co}_{0.4}\text{Ge}$  sample ( $x = 0.4$ ) exhibits a pronounced (001) magnetic reflection below the ordering temperature, as depicted in Fig. 4.12. This observation signifies the presence of an in-plane

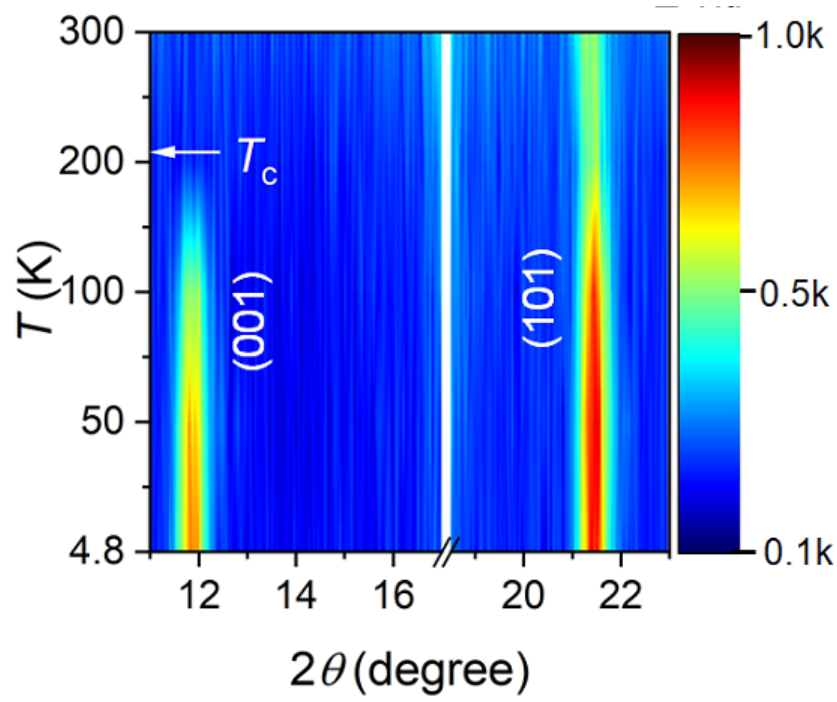


Figure 4.12: The zoomed-in contour plot of (001) and (101) PND reflections for the  $\text{MnFe}_{0.6}\text{Co}_{0.4}\text{Ge}$  ( $x = 0.4$ ) sample at different temperatures. The color bar represents the intensity profile of the PND data in arbitrary units.

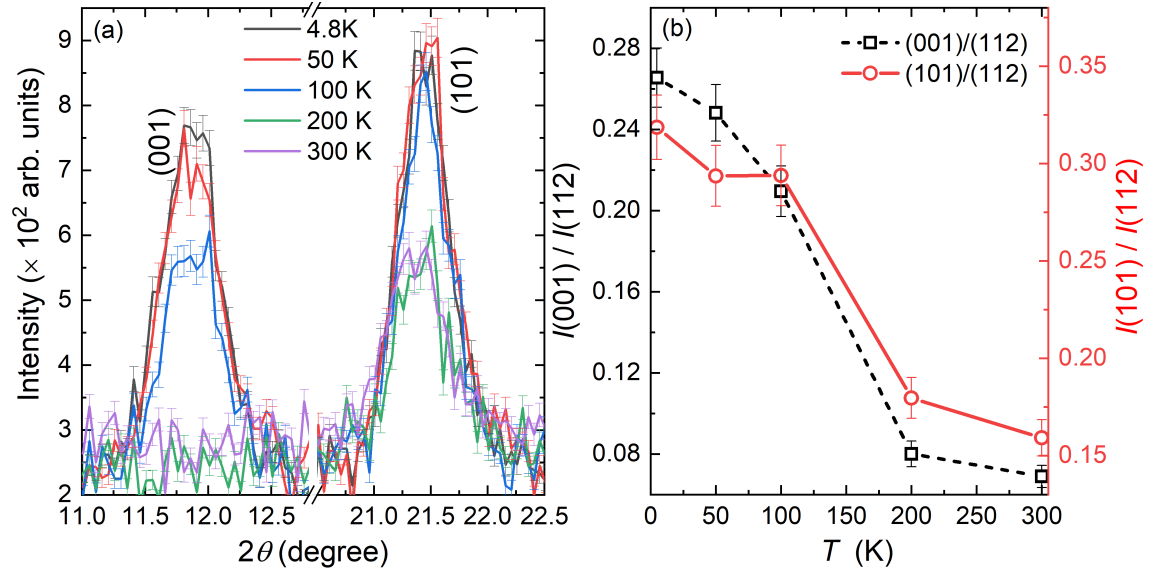


Figure 4.13: (a) The zoomed view of (001) and (101) raw PND data with error bars for  $\text{MnFe}_{0.6}\text{Co}_{0.4}\text{Ge}$  ( $x = 0.4$ ) sample at different temperatures. (b) Temperature variation of the relative intensity of (001) and (101) reflections with respect to (112) reflection.



AFM component in the system [133, 138, 139]. Moreover, the PND data for the sample reveals a significant increase in the intensity of (101) and (001) reflections at temperatures below 200 K (near  $T_c \cong 212$  K) [see Fig. 4.12]. Figure 4.13 provides an enlarged view of the (001) and (101) reflections, along with their relative intensities concerning the (112) reflection. Figure 4.14 compares the refined PND data employing a collinear and non-collinear spin configuration at different temperatures. The non-collinear structure (Fig. 4.14) with a  $c$ -axis FM and a basal plane AFM component fits the data better compared to the collinear arrangement along the  $c$ -axis. The schematic representation of collinear and non-collinear magnetic ground states are shown in Fig. 4.15. The Rietveld refined PND data for the sample at 200 K and 50 K are depicted in Figure 4.16. The temperature-dependent analysis reveals a gradual reduction in the basal plane AFM component with increasing temperature, as evidenced by the decreasing canting angle of Mn moments concerning the  $c$ -axis ( $\theta$ ). This angle decreases from 33.4 deg to nearly 0 deg with increasing temperature to 200 K (near  $T_c$ ) [See Fig. 4.17(b)]. Figure 4.17(a) illustrates the components of site-specific magnetic moments for Mn (2a) and Co/Fe (2d) atoms. The experimental moment of  $2.52 \mu_B/\text{f.u}$  obtained from the magnetization measurement at 5 K agrees well with  $2.67 \pm 0.1 \mu_B$  of net refined moment realized from the PND study for the sample along the  $c$ -direction at 4.8 K. The refined lattice parameters for the sample at different temperatures are illustrated in Fig. 4.18. The lattice parameters ( $a$ ,  $c$ ), as well as the cell volume of the sample, naturally decrease with decreasing temperature. Concurrently, the sample exhibits a slight increase in its  $c/a$  ratio below the ordering temperature, where it develops a basal plane AFM component in addition to an out-of-plane FM component [see Fig. 4.18]. These kinds of anomalous changes in the  $c/a$  ratio indicate a strong dependence of magnetic interaction on the crystal lattice spacing [140, 141]. Consequently, the PND measurements for the MnFe<sub>0.6</sub>Co<sub>0.4</sub>Ge sample affirm its non-collinear magnetic ground state, featuring both FM and AFM components along the  $c$ -axis and basal plane.

#### **Magnetic ground state for MnFe<sub>0.2</sub>Co<sub>0.8</sub>Ge ( $x = 0.8$ ):**

For the MnFe<sub>0.2</sub>Co<sub>0.8</sub>Ge sample, no super-lattice or satellite reflections corre-

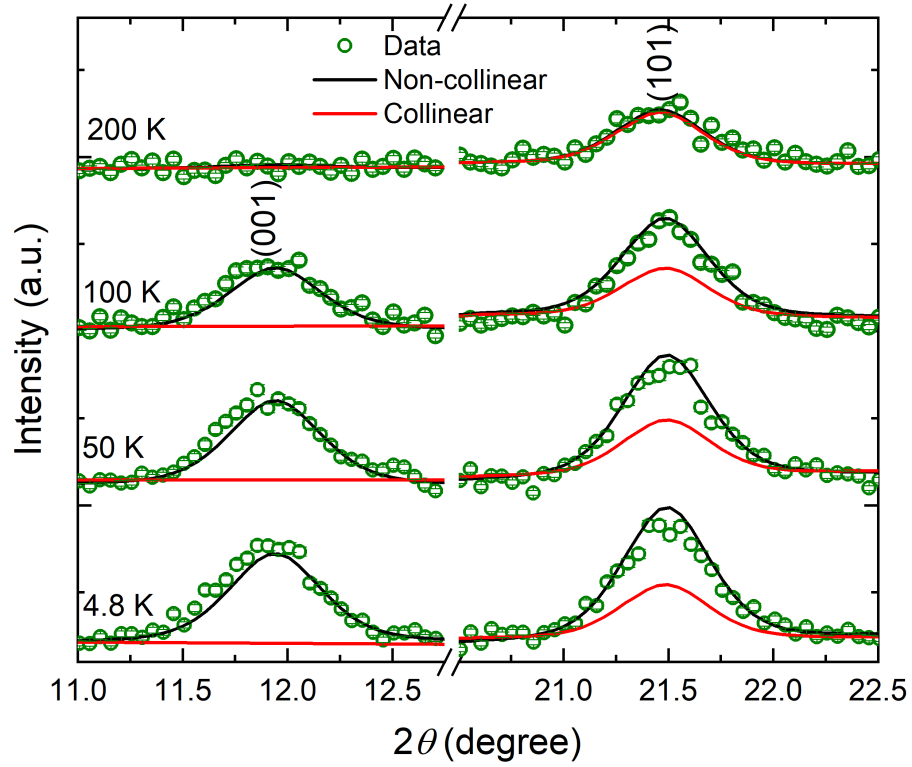


Figure 4.14: Zoomed view of Rietveld refined PND patterns for  $\text{MnFe}_{0.6}\text{Co}_{0.4}\text{Ge}$  ( $x = 0.4$ ) sample, considering both collinear and non-collinear spin arrangement.

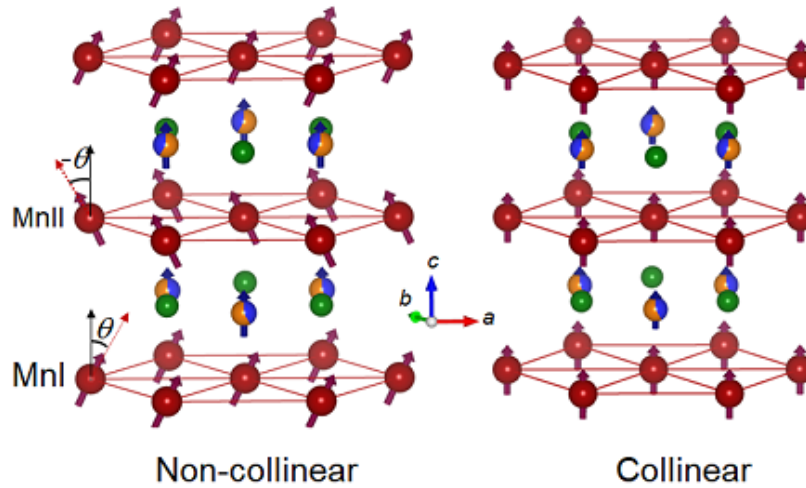


Figure 4.15: Schematic representation of collinear and noncollinear Magnetic ground states for the sample  $\text{MnFe}_{0.6}\text{Co}_{0.4}\text{Ge}$  ( $x = 0.4$ ). The red, blue, orange, and green balls represent Mn, Co, Fe, and Ge atoms, respectively.

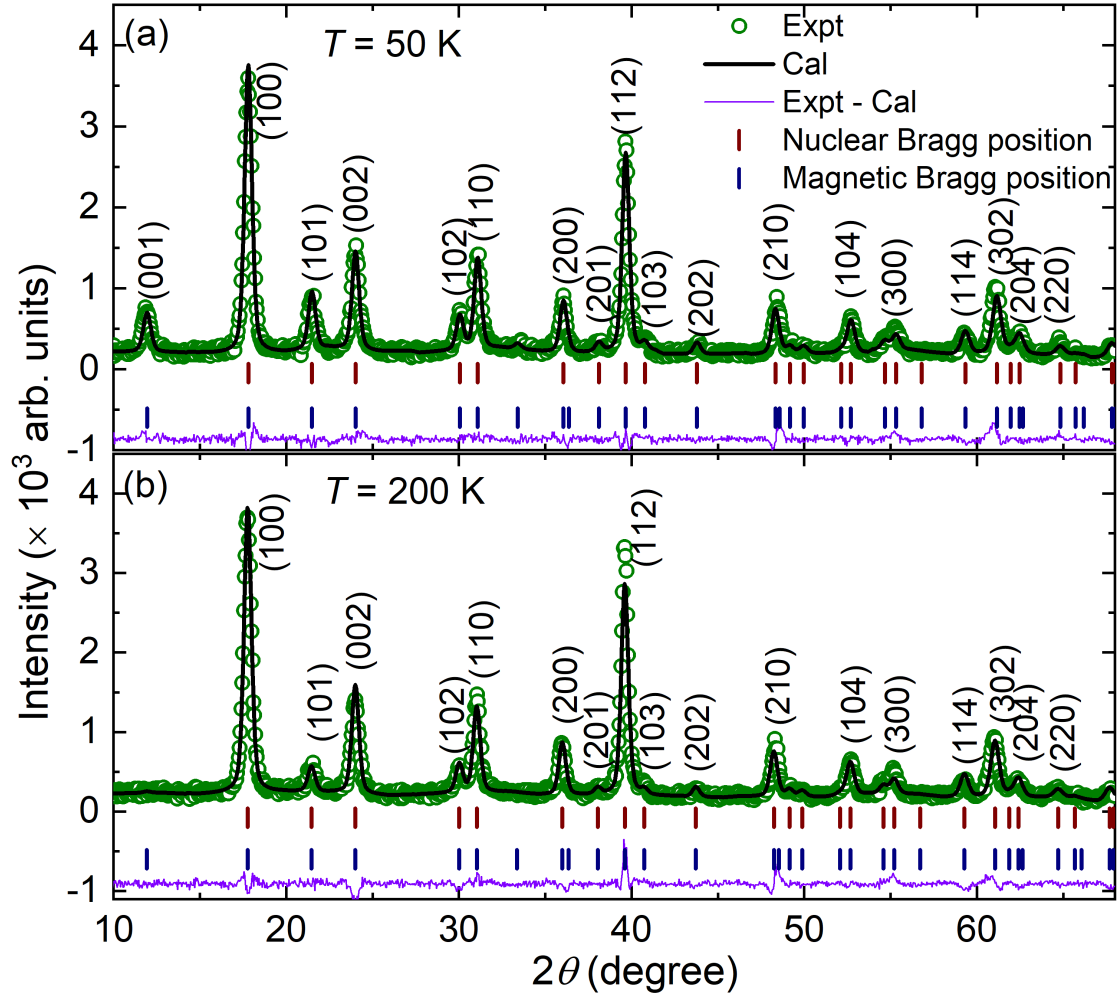


Figure 4.16: Rietveld refined PND patterns for MnFe<sub>0.6</sub>Co<sub>0.4</sub>Ge ( $x = 0.4$ ) sample at (a) 50 K, (b) 200 K.

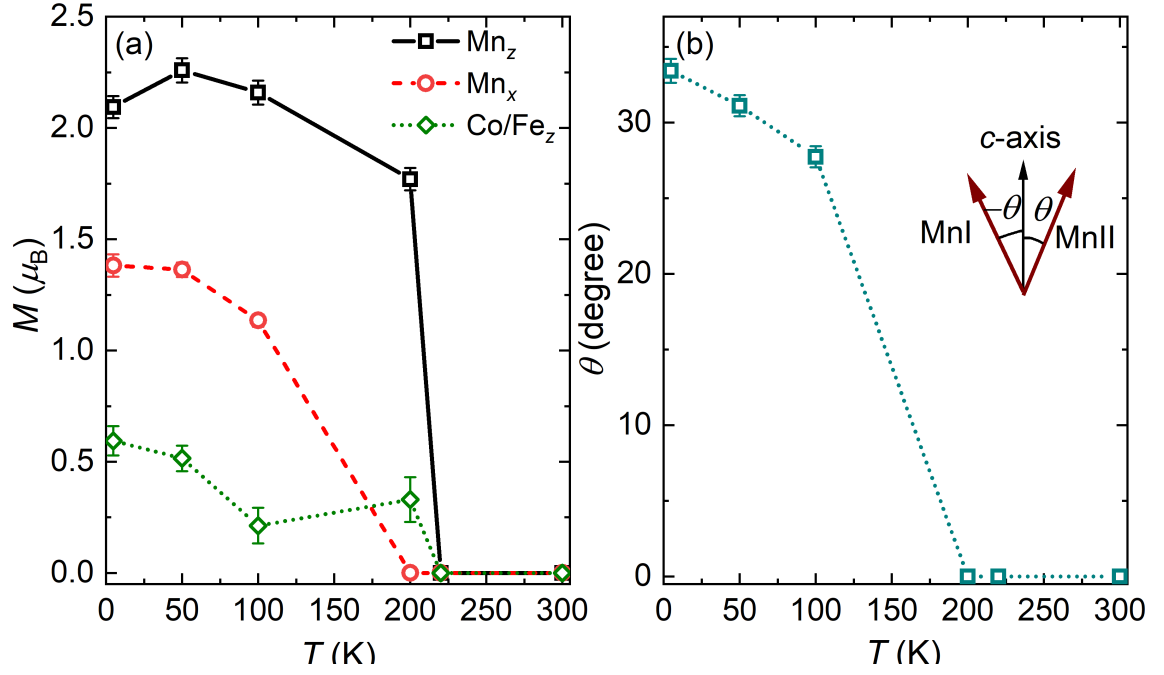


Figure 4.17: (a) The Rietveld refined site specific moments of Mn (2a) and Co/Fe (2d) atoms in  $\text{MnFe}_{0.6}\text{Co}_{0.4}\text{Ge}$  ( $x = 0.4$ ) sample at different temperatures. (b) The canting angles of MnI and MnII moments concerning the  $c$ -axis at different temperatures.

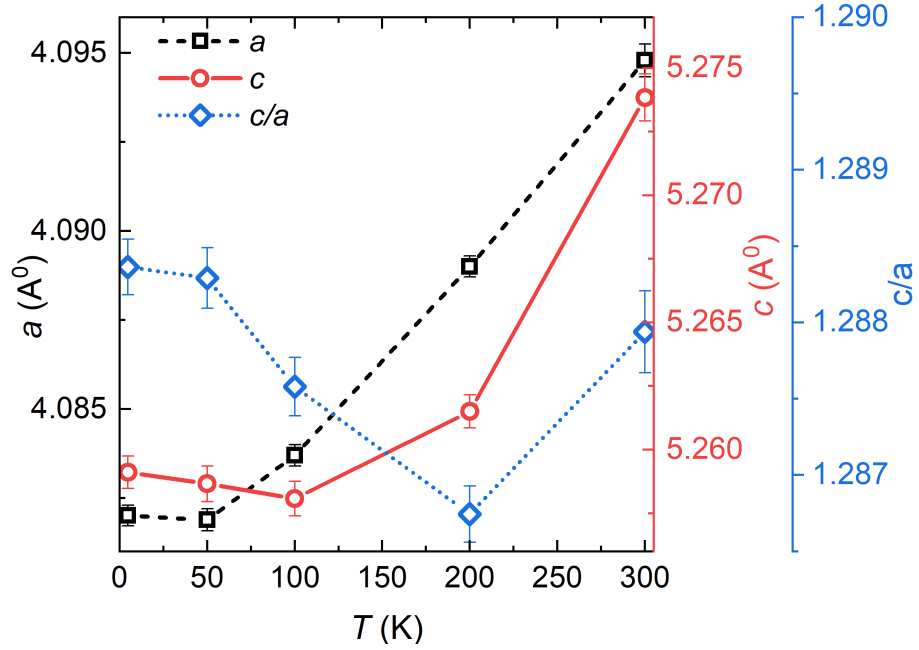


Figure 4.18: Temperature dependence of the refined lattice parameters for  $\text{MnFe}_{0.6}\text{Co}_{0.4}\text{Ge}$  ( $x = 0.4$ ) sample.

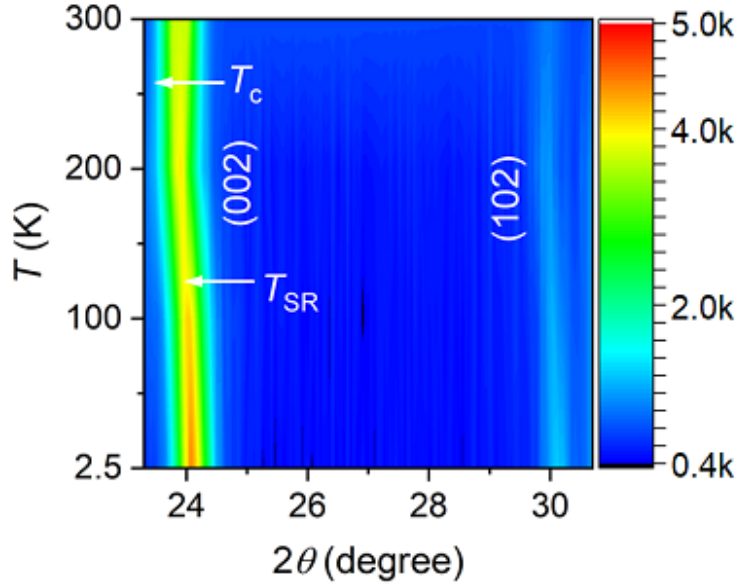


Figure 4.19: The zoomed-in contour plot of (002) and (102) PND reflections for the  $\text{MnFe}_{0.2}\text{Co}_{0.8}\text{Ge}$  ( $x = 0.8$ ) sample at different temperatures. The color bar represents the intensity profile of the PND data in arbitrary units.

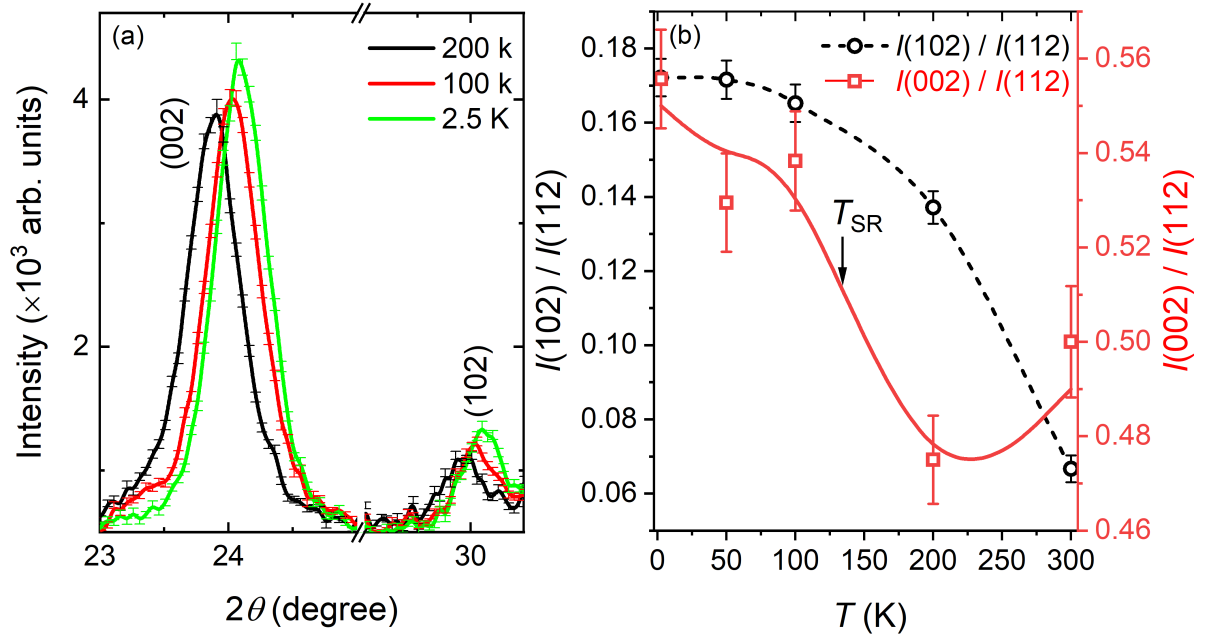


Figure 4.20: (a) The zoomed view of (002) and (102) raw PND data with error bars for  $\text{MnFe}_{0.2}\text{Co}_{0.8}\text{Ge}$  ( $x = 0.8$ ) sample at different temperatures. (b) Temperature variation of the relative intensity of (002) and (102) reflections with respect to (112) reflection.

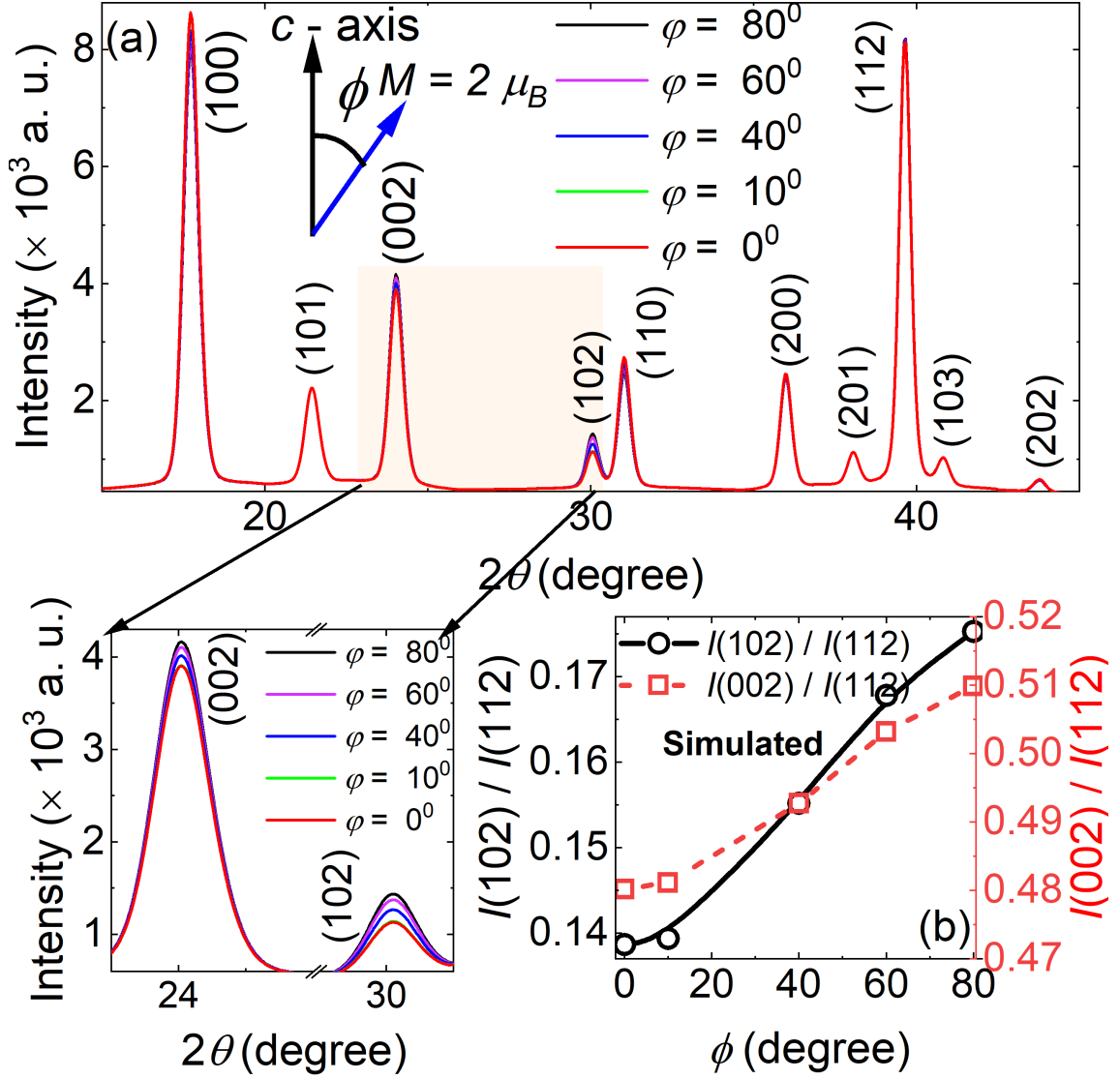


Figure 4.21: The Zoomed view of the simulated (002), (102) ND reflections with different tilting ( $\phi$ ) of the magnetic easy axis with respect to the  $c$ -axis (a) and the corresponding relative intensity of the reflections with respect to (112) reflection (b). The moment is set to  $2 \mu_B$  during the simulation.

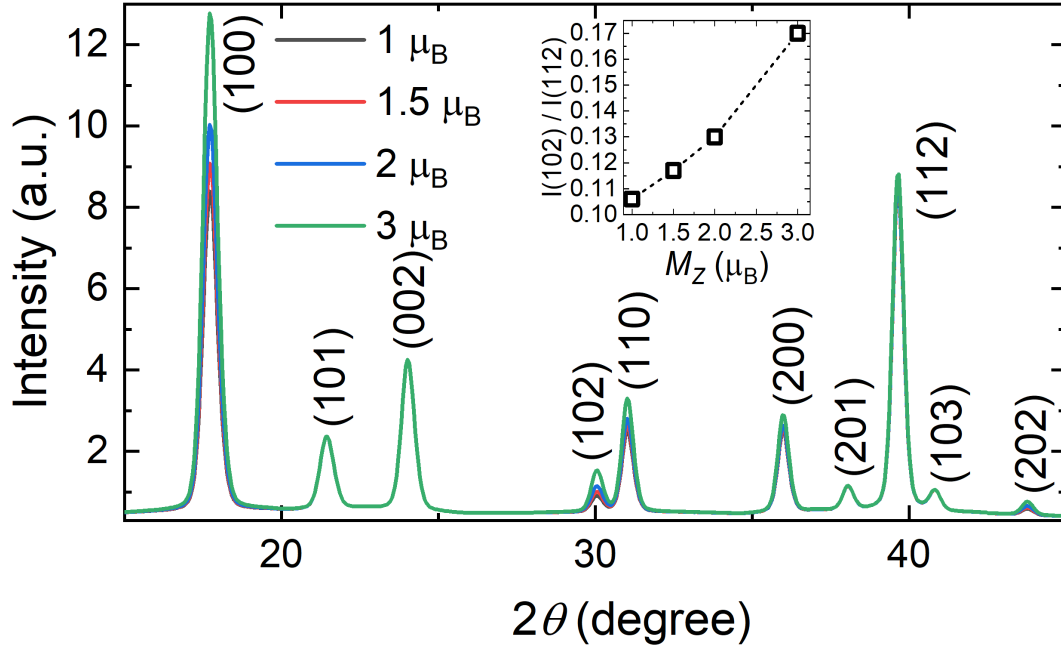


Figure 4.22: The simulated ND pattern with increasing moment along the  $c$ -axis and the corresponding relative intensity value of (102) reflection with respect to (112).

sponding to any AFM ordering are detected at temperatures below the ordering temperature ( $T_C \cong 265$  K). As a result, it can be inferred that the sample with the larger Co concentration (MnFe<sub>0.2</sub>Co<sub>0.8</sub>Ge) exhibits a collinear ferromagnet in its ground state. Moreover, a careful analysis of the PND data for the sample shows that the (002) and (102) reflections significantly intensify when temperature decreases, especially below  $T_{SR}$  [See Fig. 4.19]. Figure 4.20 shows a magnified view of the (002) and (102) reflections for the sample, as well as their relative intensities with respect to the (112) reflection at different temperatures. To explore potential magnetic ground states in the case of  $x=0.8$  sample, PND patterns are simulated using a wavelength  $\lambda = 1.049$  Å. The ND patterns are simulated by tilting the magnetic easy axis away from the  $c$ -axis by an angle  $\phi$ . Figure 4.21 depicts simulated ND patterns with varying  $\phi$ . The intensity of the simulated (002) and (102) reflections increase with increasing the angle  $\phi$  [see Fig. 4.21]. While the increasing moment along the  $c$ -axis can partially enhance the intensity of (102) reflections,

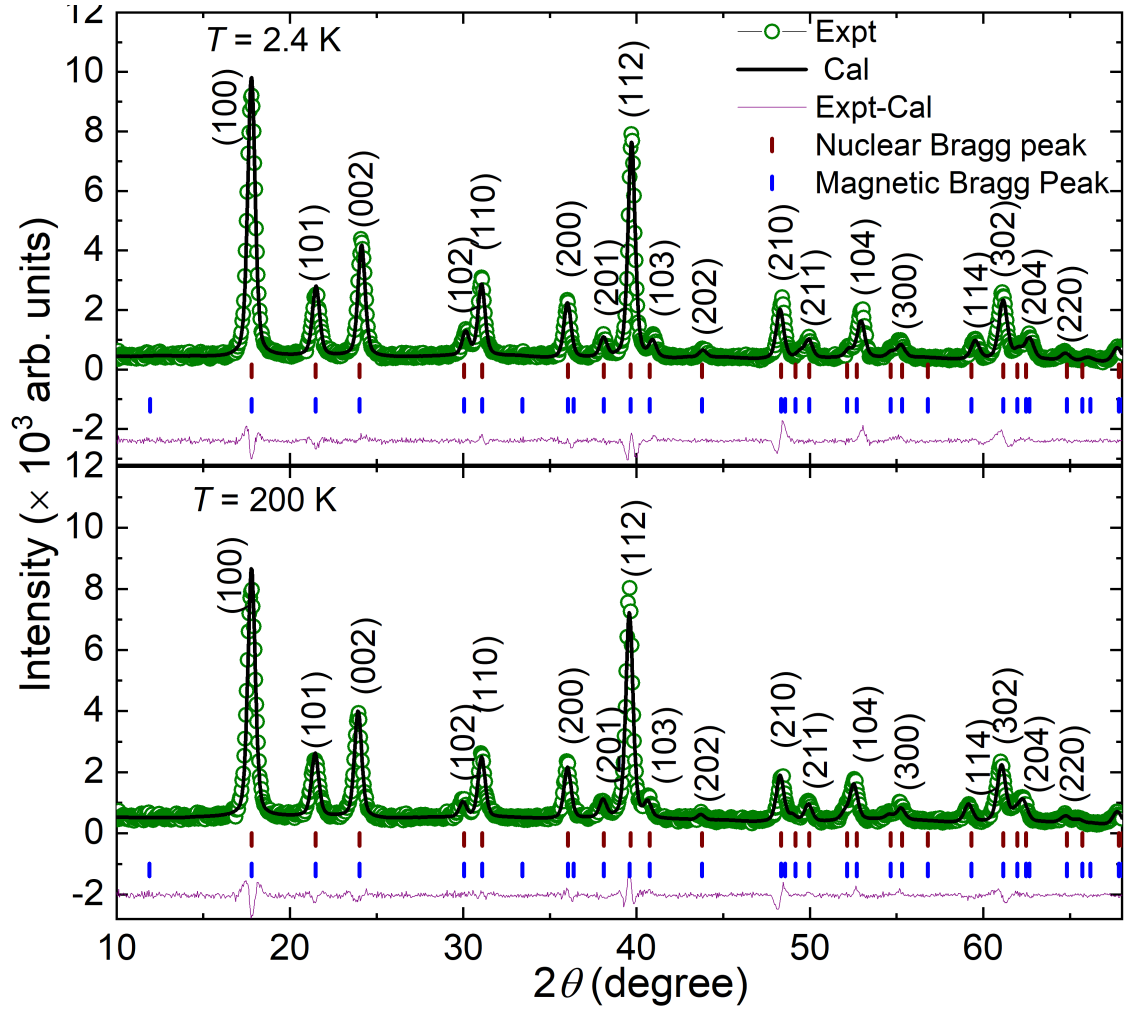


Figure 4.23: The Rietveld refined PND patterns for  $\text{MnFe}_{0.2}\text{Co}_{0.8}\text{Ge}$  ( $x = 0.8$ ) at temperature 2.4 K, and 200 K.



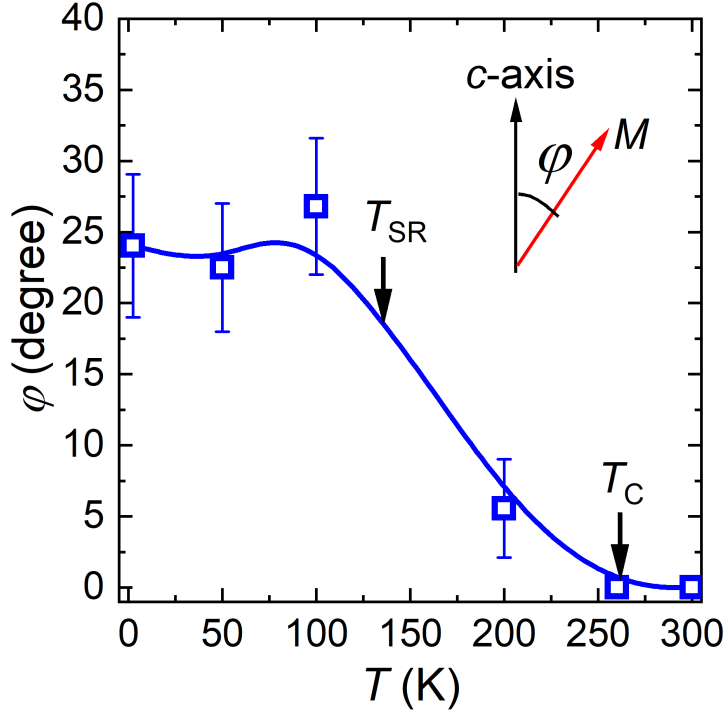


Figure 4.24: The temperature dependence of the easy cone angle ( $\phi$ ) i.e., the angle by which the easy axis tilted away from  $c$ -axis for  $\text{MnFe}_{0.2}\text{Co}_{0.8}\text{Ge}$  ( $x = 0.8$ ).

it has no influence on (002) reflections, as depicted in Fig. 4.22. Hence, in the  $\text{MnFe}_{0.2}\text{Co}_{0.8}\text{Ge}$  system, the increasing intensity of both (002) and (102) reflections with decreasing temperature below  $T_{SR}$  indicates the generation of a finite in-plane moment with a slanted magnetic easy axis [142, 143, 144]. Therefore, the PND data for the sample are refined using an easy-cone model. The refined PND data for the  $\text{MnFe}_{0.2}\text{Co}_{0.8}\text{Ge}$  sample at 2.4 K and 200 K are shown in Fig. 4.23. The refined tilting angles between the magnetic easy axis and the  $c$ -axis ( $\phi$ ) at different temperatures are presented in Fig. 4.24. At 100K and below ( $< T_{SR}$ ), the easy-cone angle is found to be around  $\approx 25^\circ \pm 5^\circ$ , whereas the refined easy cone angle at 200K ( $> T_{SR}$ ) is almost  $0^\circ$ . Figure 4.25 schematically represents the magnetic structures corresponding to temperatures of 2.4 K and 200 K. These observations indicate that the sample transforms from an easy-axis magnetic anisotropy to an easy-cone phase below  $T_{SR}$ .

The temperature-dependent site-specific refined moments for different atoms

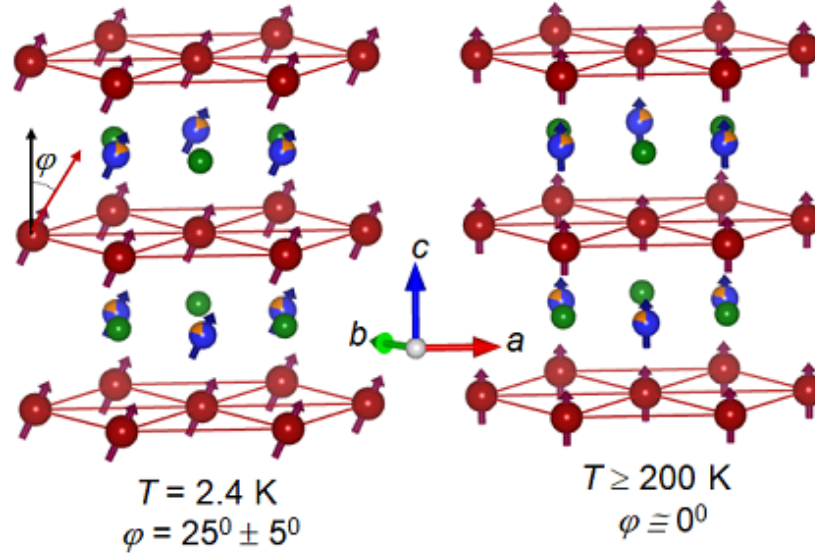


Figure 4.25: The Rietveld refined magnetic structures for sample  $\text{MnFe}_{0.2}\text{Co}_{0.8}\text{Ge}$  ( $x = 0.8$ ) at temperature 2.4 K, and 200 K. The red, blue, orange, and green balls represent the Mn, Co, Fe, and Ge atoms, respectively.

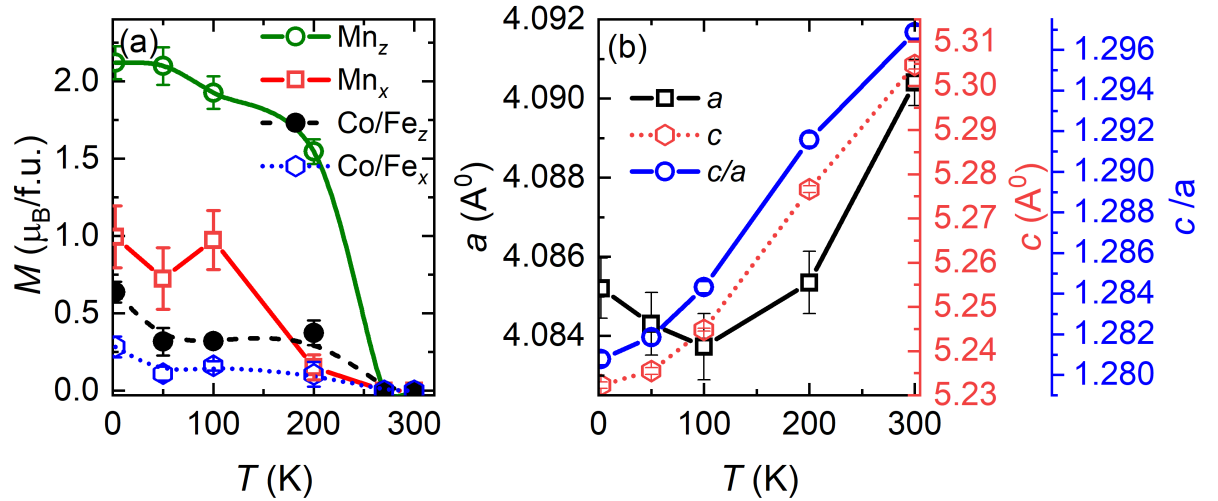


Figure 4.26: (a) The refined site-specific moment of Mn and Co in the sample  $\text{MnFe}_{0.2}\text{Co}_{0.8}\text{Ge}$  ( $x = 0.8$ ) at different temperatures. (b) The temperature dependent refined lattice parameters for the sample.

in MnFe<sub>0.2</sub>Co<sub>0.8</sub>Ge along different directions are illustrated in Fig. 4.26(a). At 2.4 K, the refined absolute moments are as follows: for Mn(2a),  $2.55 \pm 0.12 \mu_B$ , and for Co/Fe(2d),  $0.725 \pm 0.071 \mu_B$ . Hence, the resultant magnetic moment  $3.278 \pm 0.19 \mu_B/\text{f.u.}$  closely matches with the experimentally observed moment of  $3.14 \mu_B/\text{f.u.}$  at 5 K. The refined lattice parameters evaluated using PND data with varying temperatures are plotted in Fig. 4.26(b). As expected, the lattice parameters and the volume of the sample shrinks with decreasing temperature. Although the  $a$  value displays an upturn at low temperatures ( $<100$  K), it is still within the error bar range. The  $c/a$  ratio of the sample also decreases with decreasing temperature. In most of the uniaxial anisotropic collinear ferromagnets, the  $c/a$  ratio is closely related to the magnetic anisotropy of the sample. The tilting of the magnetic easy axis away from the  $c$ -axis that affects the uniaxial anisotropy component can be assigned to the decreasing  $c/a$  ratio with lowering temperature. The  $c/a$  ratio often get influenced by the chemical doping due to the induced chemical pressure. In magnetic samples, change in the  $c/a$  ratio is often closely linked to the magneto-elastic coupling. The  $x = 0.8$  sample exhibits a collinear ferromagnetic state with uniaxial magnetic anisotropy, where magnetic moments are aligned in the  $c$ -direction. Therefore, we observe a monotonic kind of increase in the  $c/a$  ratio with increasing temperature for  $x = 0.8$ . In contrast,  $x = 0.4$  exhibits a non-collinear antiferromagnetic state with in-plane magnetic anisotropy below the magnetic ordering temperature of about 210 K. Therefore, the  $c/a$  ratio exhibits an opposite trend, i.e. increases with decreasing temperature, below the magnetic ordering temperature. Above the magnetic ordering temperature, the  $c/a$  ratio again increases with increasing temperature. Therefore, the overall increase in the  $c/a$  ratio for  $x=0.4$  is almost negligible in comparison to that of  $x = 0.8$ .

Hence, the PND studies indicate that samples with lower Co concentration exhibit a non-collinear magnetic ground state, whereas a collinear ferromagnetic state is expected for the samples with higher Co concentration. Additionally, the sample with a higher Co concentration ( $x = 0.8$ ) reveals the presence of an easy cone phase at temperatures below 100 K. The change in the magnetic ground state for

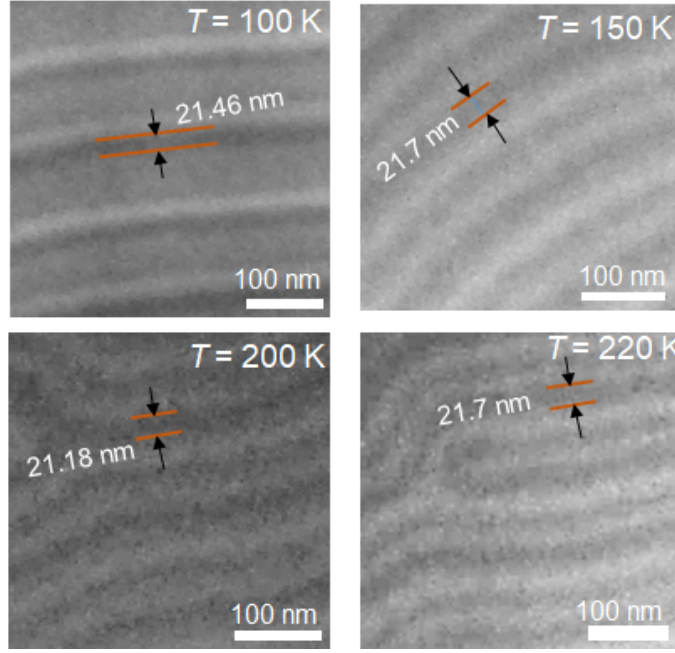


Figure 4.27: LTEM observed zero field stripe domains for  $\text{MnFe}_{0.2}\text{Co}_{0.8}\text{Ge}$  at various temperatures. The corresponding domain wall width( $\delta$ ) marked with black arrows.

the sample is also reflected in the magnetization data as shown in Fig. 4.8.

#### 4.2.5 Origin of easy-cone magnetic anisotropy for $\text{MnFe}_{0.2}\text{Co}_{0.8}\text{Ge}$ ( $x = 0.8$ )

Easy-cone magnetic ground states have been experimentally observed in bulk and thin film systems [61, 62, 145, 146]. The formation of easy-cone magnetic ground state in the hexagonal magnets can be explained by considering the effect of strong second-order magnetic anisotropy constant ( $K_2$ ) along with the negative leading first-order anisotropy constant ( $K_1$ ) [57, 58, 59, 60, 145]. Detailed analysis is provided in section 1.5.2. The condition for easy cone magnetic state is given by,

$$K_2 > -K_1^{eff}/2 \quad (4.4)$$

with  $K_1^{eff} < 0$ ,  $K_2 > 0$ , where,  $K_1^{eff} = K_1 - \mu_0 M_S^2/2$  [61, 62]. Here the polycrystalline nature of the samples makes it challenging to distinguish between the true  $K_1$  and

$K_2$  values. Hence, the LTEM observed stripe domain wall width ( $\delta$ ) in a 100 nm thick (001) lamella is used to calculate the perpendicular magnetic anisotropy ( $K_u^\perp$ ) of the system at different temperatures, using the formula,  $\delta = \pi\sqrt{A/K_u^\perp}$ , where  $A$  is exchange stiffness constant [7, 57]. The magnetic ground state and the observed domain wall width at different temperatures from 100 K to 220 K for the sample  $x = 0.8$  are shown in Fig. 4.27. The calculated  $K_1^{eff} = K_u^\perp - \mu_0 M_S^2/2$  shows a negative value, nearly below the temperature  $T \approx 150$  K [see Fig. 4.28]. Generally, the easy-axis magnetic ground state stabilizes when the leading anisotropy energy term dominates over the dipolar effect induced two ion anisotropy energy [57, 122]. In the present case, the dipolar energy prevails over the UMA for  $T \lesssim 150$  K. Consequently, the presence of a non-zero in-plane anisotropy component or in-plane magnetic moment for the sample is expected at temperatures below 150 K ( $\approx T_{SR}$ ). Moreover, a notable number of hexagonal magnets show a significant increase in their positive  $K_2$  value, primarily influenced by the presence of non-zero Co concentration, ultimately leads to the stabilization of an easy-cone magnetic state [147, 148, 149, 150, 151, 152, 153, 154, 155]. In this context, the current MnFe<sub>0.2</sub>Co<sub>0.8</sub>Ge sample, marked by predominant dipolar energy at low temperatures, holds the potential to exhibit easy-cone magnetic anisotropy. Additionally, the downfall in temperature dependent ac susceptibility [ $\chi'(T)$ ] data in the vicinity of  $T_{SR}$  [see Fig. 4.8(b)] bears resemblance to the reported  $\chi'(T)$  for the sample undergoing a transition from easy-axis to easy-cone ferromagnet [145]. Furthermore, the micromagnetic simulations with varying  $K_2$  values, while maintaining the  $K_1$  fixed to  $-0.5 \times 10^5$  J/m<sup>3</sup>, show that the stripe domain formation is only feasible with negative  $K_1$  when  $K_2 \geq -2K_1$  [see Fig. 4.29]. Thus, the condition for forming an easy-cone state with  $K_2 \geq -K_1/2$  is satisfied. The formation of a stripe domain in an easy-cone magnet requires the easy-cone angle  $\phi$  ( $\sin^{-1}\sqrt{\frac{-K_1}{2K_2}} \leq \sin^{-1}\frac{1}{2}$  i.e.,  $30^\circ$ ). Hence, the simulations validate our experimental results show stripe domains in an easy-cone state with  $\phi = 25^\circ \pm 5^\circ$ .

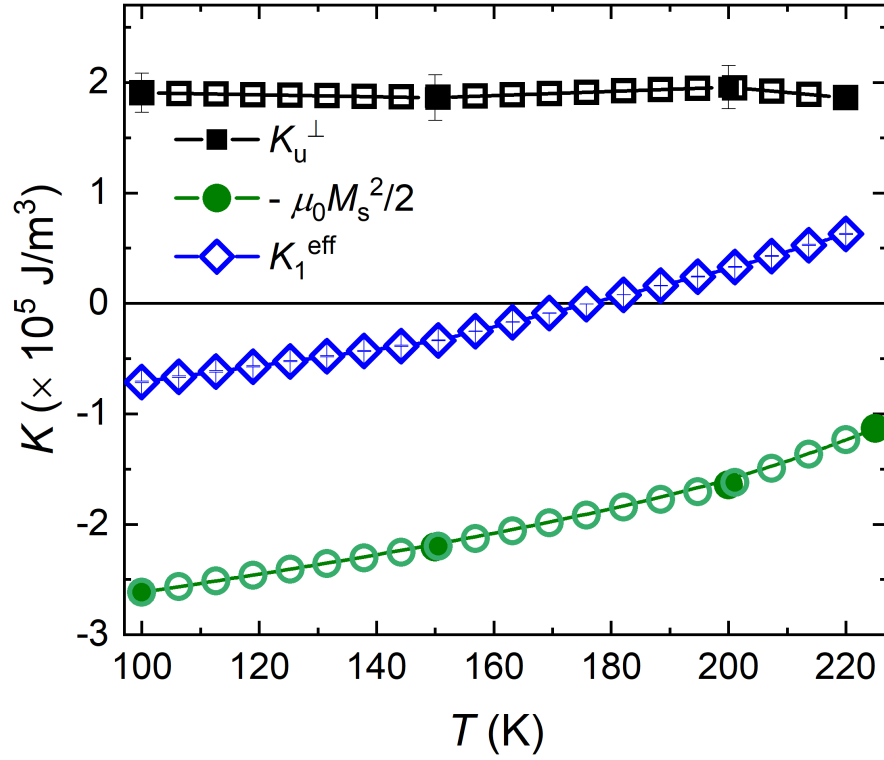


Figure 4.28: Temperature dependent perpendicular magnetic anisotropy ( $K_u^\perp$ ) calculated using the average domain wall width ( $\delta$ ) of the zero field stripe domain observed in LTEM measurements. The anisotropy energy related to the dipolar effect is calculated using the saturation magnetization  $M_S$ . The effective leading anisotropy constant,  $K_1^{\text{eff}} = K_u^\perp - \mu_0 M_S^2/2$ . The solid symbols represent the experimental data points, and the open symbols in between show the interpolated points.

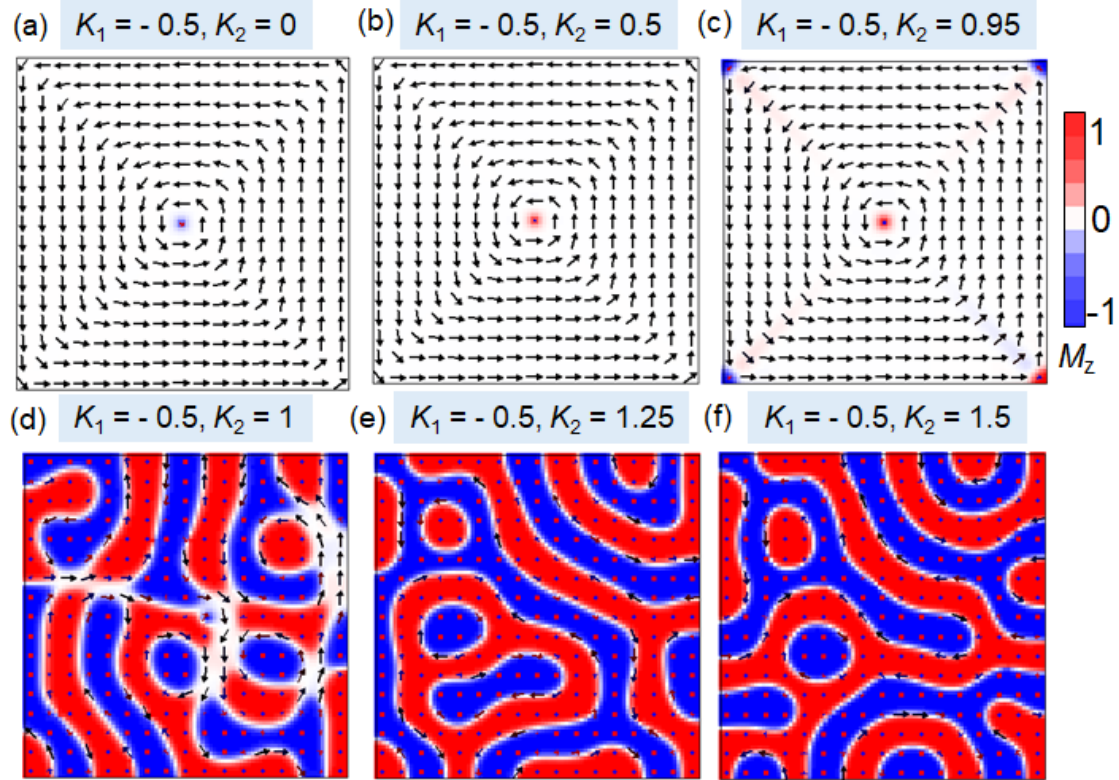


Figure 4.29: The MUMAX simulated magnetic ground states for the sample  $x = 0.8$  with varying 2nd order anisotropy constant  $K_2$ , while fixing the  $K_1$  value to  $-0.5 \times 10^5 \text{ J/m}^3$ . The simulations are conducted in the sample dimension of  $1000 \times 1000 \times 100 \text{ nm}^3$ , and cell size of  $4 \times 4 \times 4 \text{ nm}^3$ . The parameters include exchange stiffness  $A$  of  $8 \text{ pJ/m}$ , saturation magnetization  $M_S$  of  $5.8 \times 10^5 \text{ A/m}$ , damping constant  $\alpha$  of  $0.9$ , and external field  $H$  of  $0 \text{ T}$ . The color bar represents the out-of-plane moment. The arrows represent the direction of in plane moments.

### 4.2.6 Magnetic field dependent ac susceptibility measurements for $\text{MnFe}_{1-x}\text{Co}_x\text{Ge}$

The field dependent ac susceptibility  $[\chi' (H)]$  measurements are performed on the samples  $\text{MnFe}_{1-x}\text{Co}_x\text{Ge}$ , to explore the potential skyrmion phase in the system. This method is frequently employed as a quick and simple indirect tool to infer the existence of skyrmions in a system [45, 123]. The results of ac susceptibility for the  $\text{MnFe}_{(1-x)}\text{Co}_x\text{Ge}$  samples (with  $x = 0.3, 0.4, 0.5, 0.6$ , and  $0.8$ ) are presented in Fig. 4.30. No abnormalities are seen in the samples up to  $x = 0.4$ ; however, as the Co concentration increased to  $x \geq 0.5$ , the samples exhibit field-dependent anomalies in the ac-susceptibility curve, indicated by arrows in Fig. 4.30. These anomalies suggest a field-dependent magnetic phase transition in the samples, indicating the possibility of the presence of skyrmion-like spin textures. The sample with  $x = 0.8$ , characterized by a collinear ferromagnetic ground state, exhibits the anomaly most prominently. These observations indirectly suggest that the skyrmion phase might be more stable for the  $x = 0.8$  sample rather than a non-collinear magnet with  $x = 0.4$ .

### 4.2.7 Real space observation of magnetic domains in $\text{MnFe}_{1-x}\text{Co}_x\text{Ge}$ system

To directly visualize the stability of any magnetic structures in the present system, real-space LTEM measurements are performed on the FIB-thinned lamellae of the samples  $\text{MnFe}_{1-x}\text{Co}_x\text{Ge}$  with  $x = 0.4, 0.5, 0.6, 0.8$ . The SAED patterns of the sample lamellae confirm the  $[001]$  orientation of the lamellae [see Fig. 4.31]. The existence of a finite in-plane magnetic field can cause skyrmions to transform into type-II bubbles in a centrosymmetric system, and that can be accomplished by simply tilting the sample away from the  $c$ -axis, as explained in Chapter 3. Therefore, to avoid that impact, the magnetic field is applied approximately along the zone-axis ( $< 1^\circ$ ) for all of the LTEM experiments presented in this chapter.



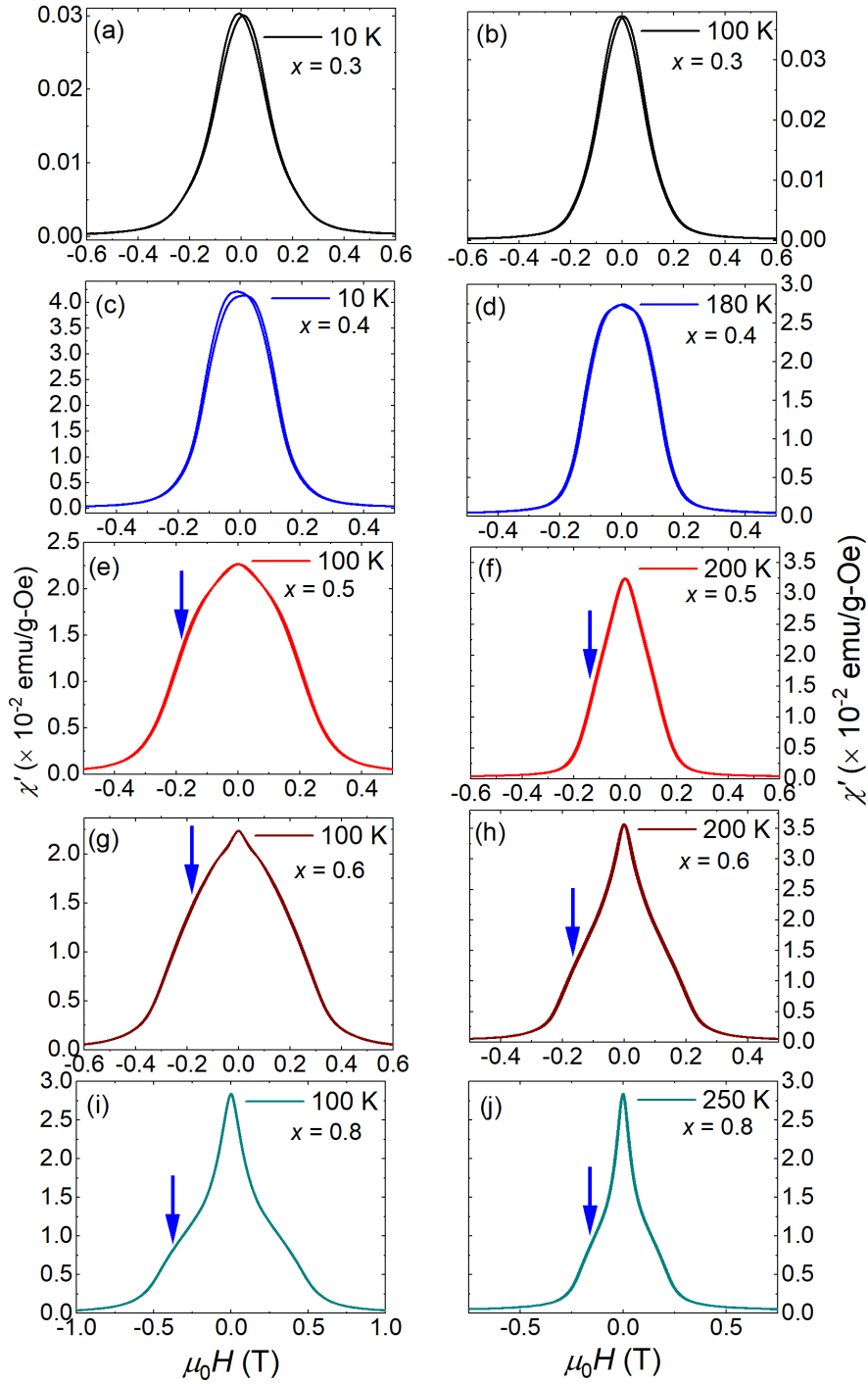


Figure 4.30: Field dependent ac susceptibility measurements  $[\chi' (H)]$  for MnFe<sub>(1-x)</sub>Co<sub>x</sub>Ge ( $x = 0.3, 0.4, 0.5, 0.6$ , and  $0.8$ ) at different temperatures. (a)-(b)  $x = 0.3$ , (c)-(d)  $x = 0.4$ , (e)-(f)  $x = 0.5$ , (g)-(h)  $x = 0.6$ , and (i)-(j)  $x = 0.8$ . The field dependent anomalies are marked with arrows.

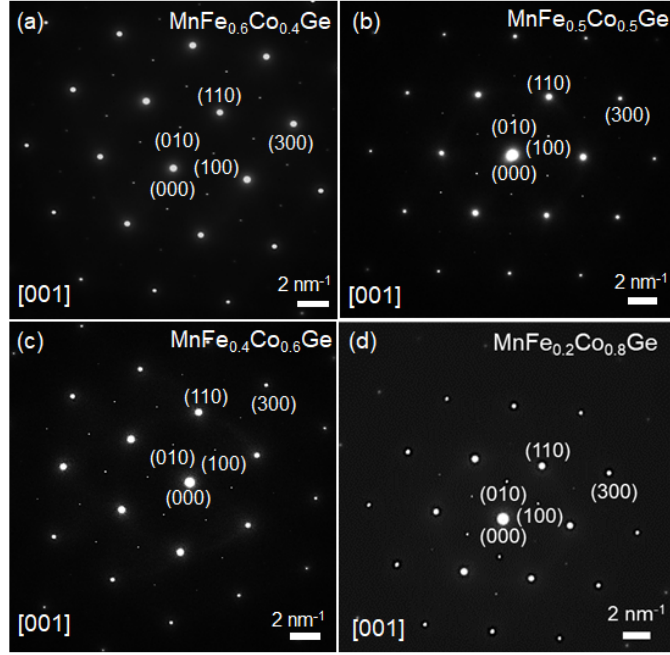


Figure 4.31: The SAED pattern for the samples  $\text{MnFe}_{1-x}\text{Co}_x\text{Ge}$  with  $x = 0.4$  (a),  $0.5$ (b),  $0.6$ (c), and  $0.8$ (d).

#### LTEM study in $\text{MnFe}_{0.6}\text{Co}_{0.4}\text{Ge}$ :

The sample with  $x = 0.4$ , i.e.  $\text{MnFe}_{0.6}\text{Co}_{0.4}\text{Ge}$  exhibits in-plane domain walls as zero field magnetic state at 100 K, as illustrated in Fig. 4.32. According to the PND study, the sample with  $x = 0.4$  exhibits a non-collinear ferromagnetic ground state having a  $c$ -axis FM component as well as an in-plane AFM component, as schematically shown in Fig. 4.15. Therefore, the presence of a sufficiently strong in-plane anisotropy component ( $K_u^{\parallel}$ ) associated with the in-plane AFM components at 100 K can be attributed to the stabilization of in-plane domains. Furthermore, the PND data for the sample demonstrates a decrease in the noncollinear canting angle ( $\theta$ ) with increasing temperature [see Figure 4.17(b)]. Consequently, due to the reduction in the in-plane anisotropy component ( $K_u^{\parallel}$ ), out-of-plane stripe domains with very weak contrast are detected at 150 K, along with in-plane domain wall, as shown in Figure 4.33. However, as the magnetic field strength increases, the stripe domains begin to disappear, and eventually, the sample becomes field-polarized [see Figure 4.33]. The magnetic domains of the samples exhibit a similar behavior at

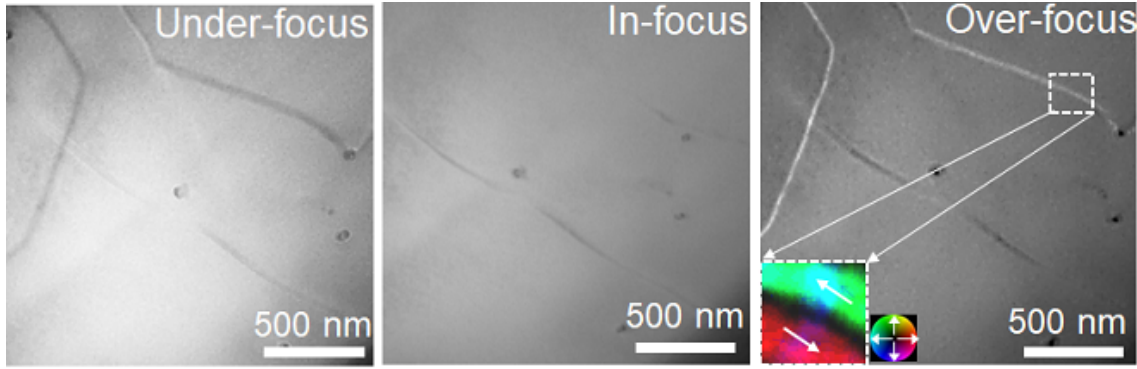


Figure 4.32: LTEM images of zero field magnetic domains for  $x = 0.4$  sample at a temperature of 100 K. Images are taken in under-focus, in-focus, and over-focus conditions. The small black dots in the images represent small defects on the sample surface. The inset shows the TIE magnetization mapping of the marked region. The color wheel represents the in-plane magnetization directions.

180 K as well [see Fig. 4.34]. Skyrmion-like spin textures are absent in the sample all over the temperature range. Consequently, the stripe domains vanish with increasing magnetic field strength, and the sample reaches saturation without the emergence of skyrmions or type-II bubbles.

#### LTEM study in MnFe<sub>0.5</sub>Co<sub>0.5</sub>Ge:

The behavior of the  $x = 0.5$  sample differs slightly from that of the  $x = 0.4$  sample. The sample with  $x = 0.5$  exhibits stripe domains of periodicity  $\approx 125$  nm as zero field state over the entire temperature range. Figure. 4.35 depicts the temperature evolution of the zero field magnetic state for the sample with  $x = 0.5$ . As the magnetic field increases, the stripe domains transform into bubble-like domains. The field-driven states for the sample at different temperatures are presented in Fig. 4.36. The TIE analysis of the observed bubble domains is shown in Fig.4.36(d). At 100 K, type-II bubbles containing Bloch lines are mainly stabilized as field driven states. As temperatures rise to 150 K and 180 K, a few skyrmions are observed with clockwise (CW) and counterclockwise (CCW) helicity. Furthermore, the greater number of type-II bubbles at all temperatures indicates the higher stability of type-II bubbles for the sample compared to that of skyrmions, implying a lower energy state for type-II bubbles.

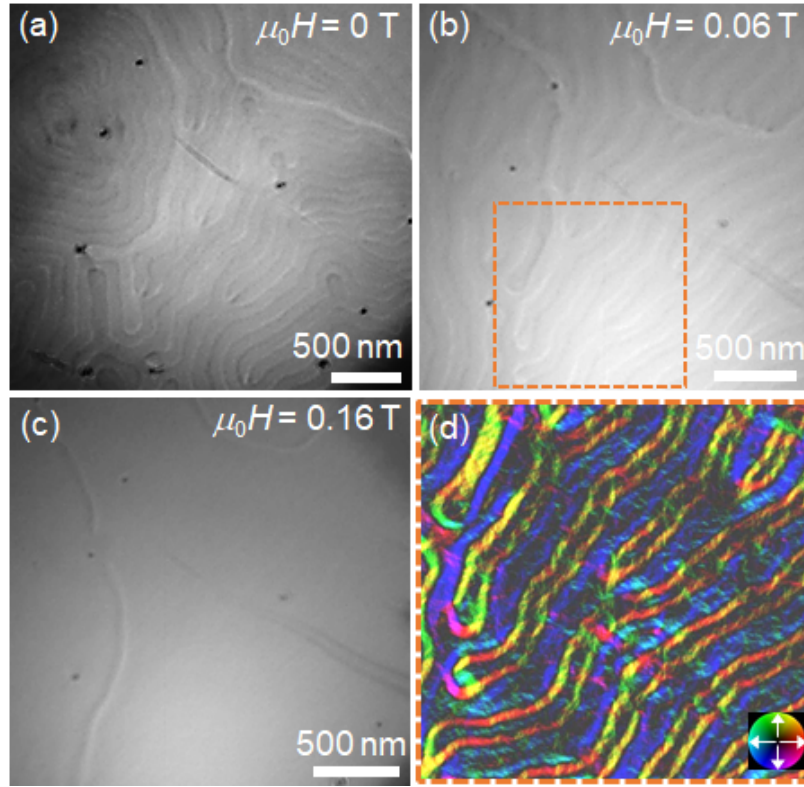


Figure 4.33: Over-focused LTEM images illustrating the field evolution of magnetic domains for  $x = 0.4$  sample at a temperature of 150 K. The images are recorded at a magnetic field of (a) 0 T, (b) 0.06 T, and (c) 0.16 T. (d) TIE magnetization mapping for the marked region in Figure (b). The color wheel illustrates the direction of in-plane magnetization.

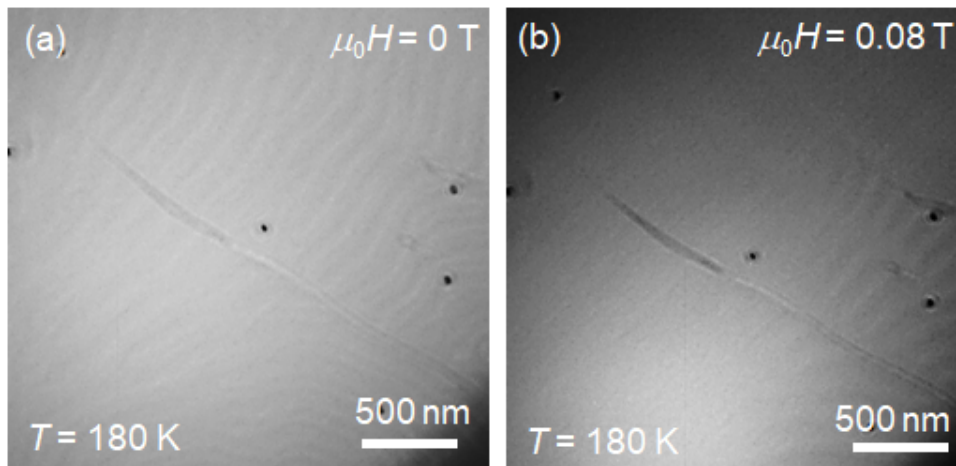


Figure 4.34: Over-focused LTEM images illustrating magnetic domains evolution with magnetic field for  $x = 0.4$  sample at a temperature of 180 K. The images are recorded at a magnetic field of (a) 0 T and (b) 0.08 T.

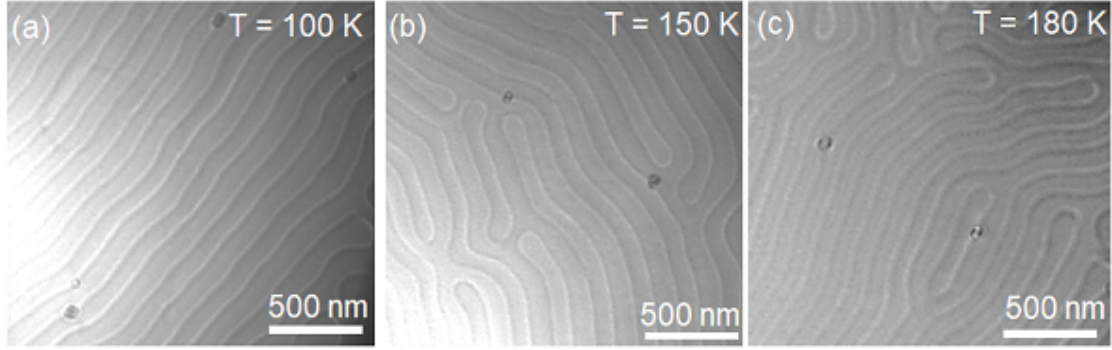


Figure 4.35: Over-focused LTEM images illustrating the temperature evolution of zero field magnetic domains for  $x = 0.5$  sample. The images are taken at temperatures of (a) 100 K, (b) 150 K, and (c) 180 K.

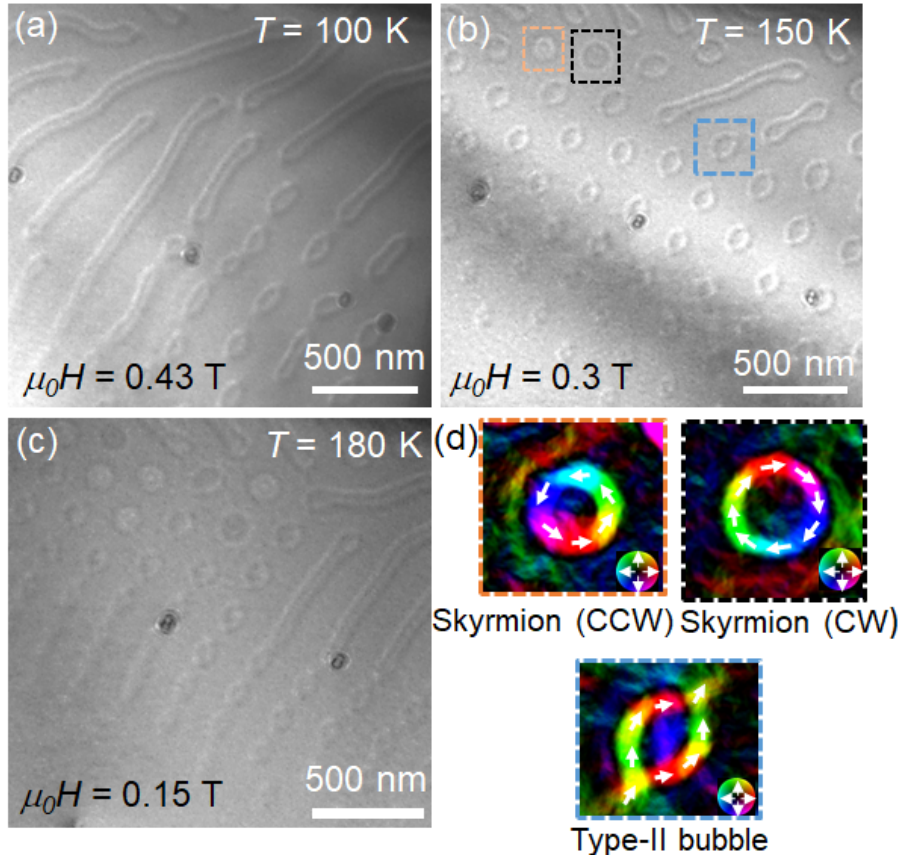


Figure 4.36: Temperature evolution of field-driven magnetic domains for  $x = 0.5$  sample. Over-focused LTEM images at (a)  $T = 100$  K &  $\mu_0 H = 0.43$  T, (b)  $T = 150$  K &  $\mu_0 H = 0.30$  T, & (c)  $T = 180$  K &  $\mu_0 H = 0.15$  T. (d) The TIE magnetization mapping of the skyrmion like domains. The color wheel represents the in-plane magnetization directions.

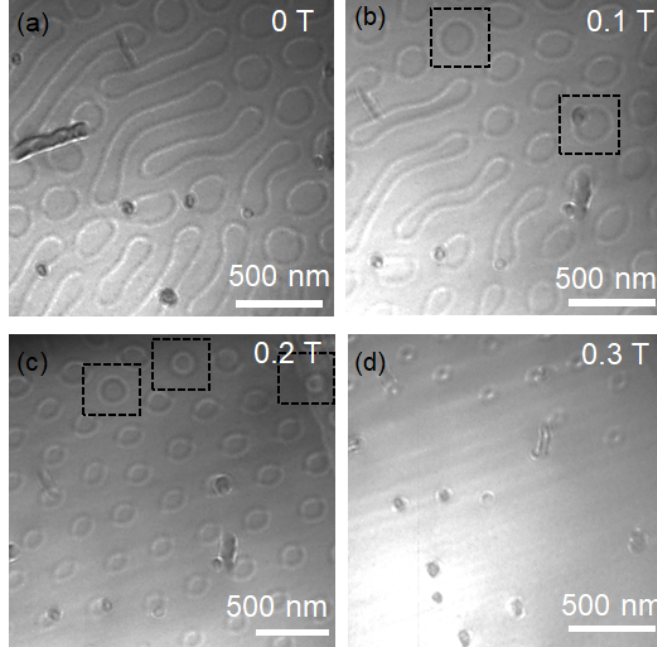


Figure 4.37: Field evolution of LTEM images for  $x = 0.6$  sample at 200 K. Images are recorded at a magnetic field of (a) 0 T, (b) 0.1 T, (c) 0.2 T, and (d) 0.3 T. Skyrmions are marked with boxes.

#### LTEM study in $\text{MnFe}_{0.4}\text{Co}_{0.6}\text{Ge}$ :

The  $x = 0.6$  sample exhibits similar characteristics to that of the  $x = 0.5$  sample, displaying stripe domains as the zero-field magnetic state. In Fig. 4.37, the field evolution of magnetic domains for the  $x = 0.6$  sample at 200 K is presented. As the magnetic field increases, the stripe domains predominantly transform into type-II bubbles, accompanied by very few numbers of skyrmions. The temperature variation in field-driven magnetic domains for the  $x = 0.6$  sample is illustrated in Fig. 4.38. Across the temperature range, the prevailing field-driven state for this sample comprises type-II bubbles rather than skyrmions, resembling the behavior observed for the  $x = 0.5$  sample.

#### LTEM study in $\text{MnFe}_{0.2}\text{Co}_{0.8}\text{Ge}$ :

The sample with  $x=0.8$  exhibits stripe domains as a zero-field state across the temperature range, as illustrated in Fig. 4.39(a), (d), (g). The periodicity of these stripe domains diminishes from 76 nm to  $\approx 60$  nm when the temperature rises from 100 K to 220 K, as depicted in Fig. 4.40(a). Notably, at 100 K, the stripe



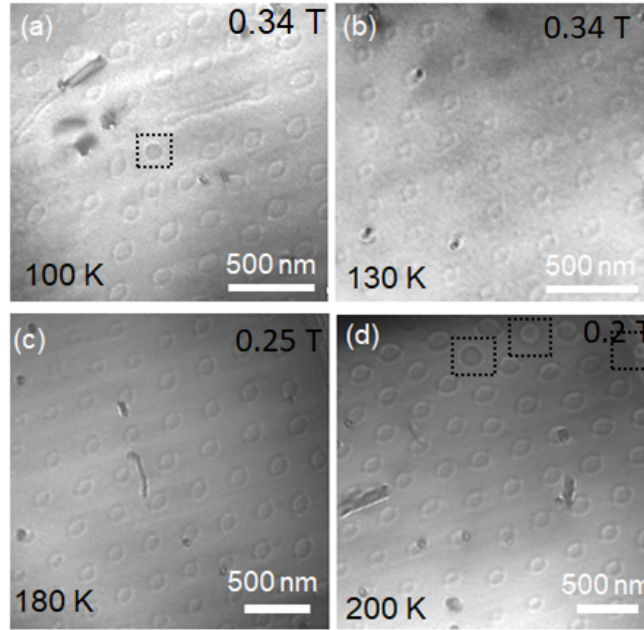


Figure 4.38: Temperature evolution of field driven magnetic state for  $x = 0.6$  sample. The images are recorded at (a) 100 K and 0.34 T, (b) 130 K and 0.34 T, (c) 180 K and 0.25 T, (d) 200 K and 0.2 T.

domains appear more organized compared to other temperatures, which may be related to the effect of an in-plane magnetic field or a specific directional in-plane anisotropy component. Here, the in-plane field effect is expected to be negligible as the experiments are conducted near the pole position. The evolution of field-driven magnetic states for the sample at different temperatures present a notably distinct scenario compared to the other samples with  $x = 0.4$ ,  $0.5$ , and  $0.6$ . At  $T = 220$  K, the sample exhibits a hexagonal skyrmion lattice as a field-driven state with an estimated skyrmion size of 95 nm, as illustrated in Fig. 4.39(h). A transitional state emerges after reducing the temperature to 150 K, consisting of a mixed configuration of skyrmions and type-II bubbles, as observed in Fig. 4.39(e). Subsequently, further cooling of the sample (at 100 K) below  $T_{SR}$  results in the formation of a hexagonal lattice composed of Type-II bubbles, as depicted in Fig. 4.39(b). The nature of the magnetic spin textures is verified through TIE analysis conducted on the LTEM images, as shown in Fig. 4.39(c), (f), and (g). Figure 4.40(b) visually represents the average density of skyrmions and type-II bubbles per square micrometer across

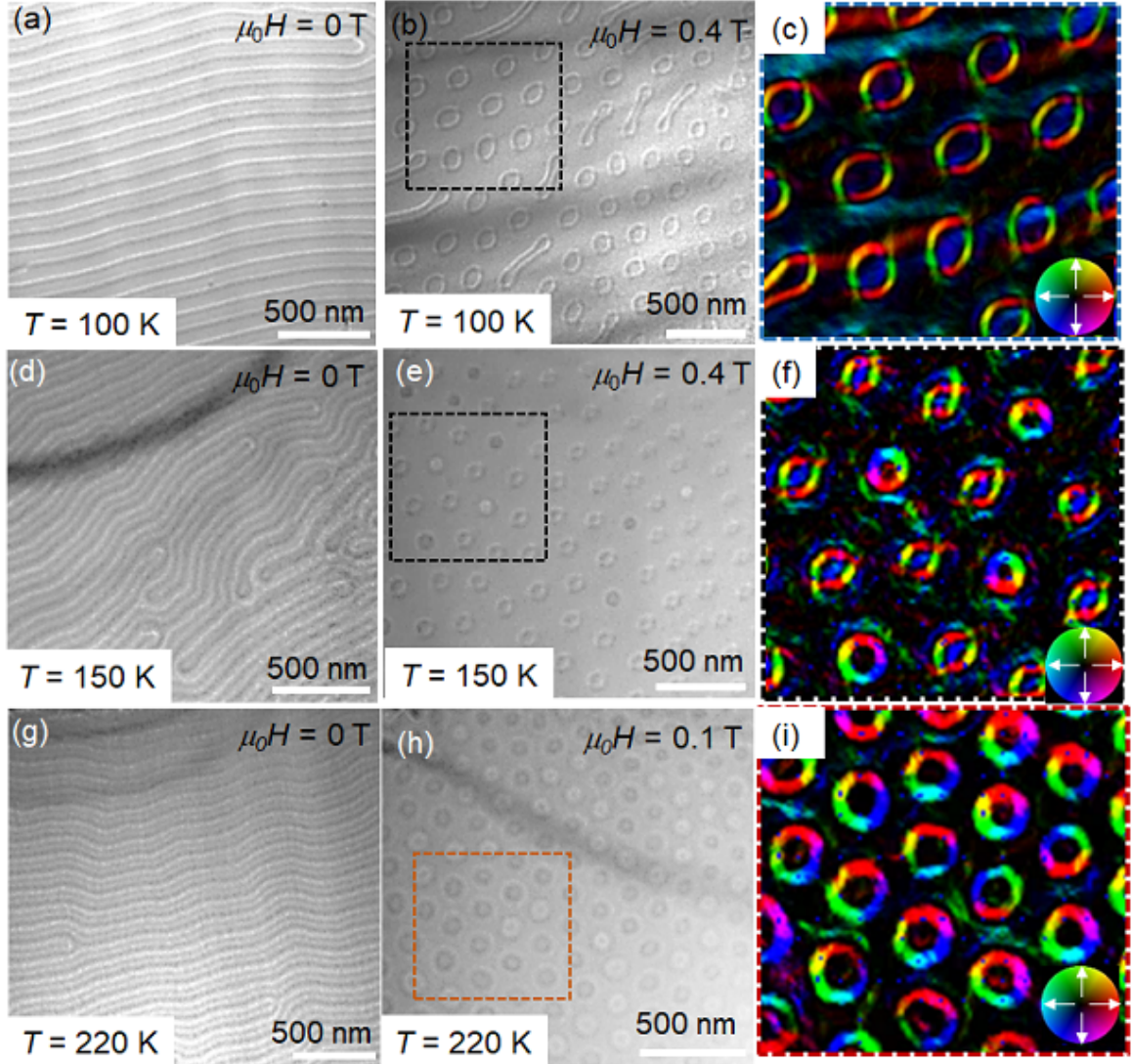


Figure 4.39: Magnetic field dependent over-focused LTEM images for the sample with  $x = 0.8$  at 100 K (a)-(b), 150 K (d)-(e), 220 K (g)-(h). The TIE magnetization mapping corresponding to the marked region in (b), (e), and (h) are shown in (c), (f), and (i), respectively. The color wheels represent the in-plane magnetization components in different directions.



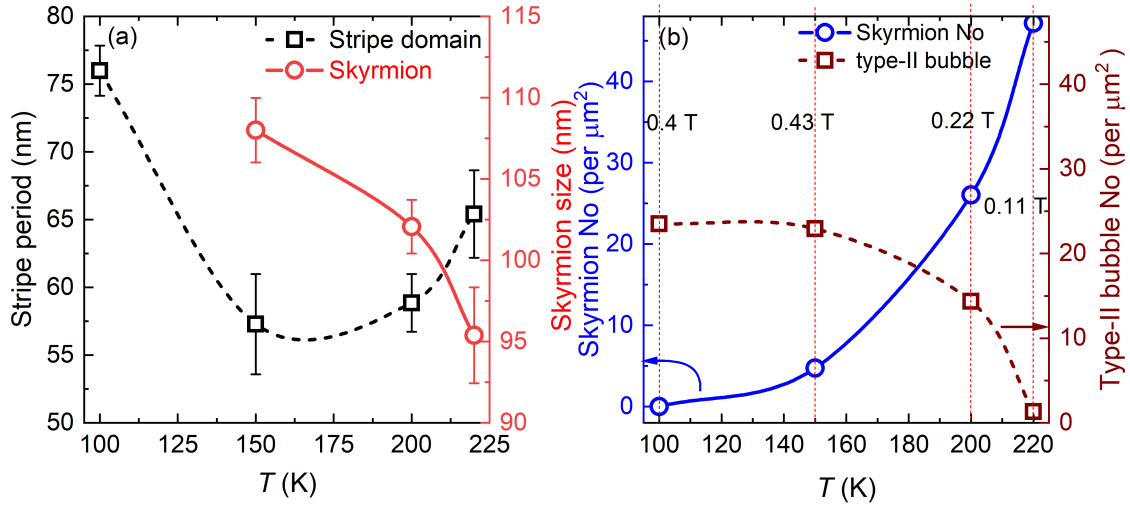


Figure 4.40: (a) Average stripe period and skyrmion size of the  $x = 0.8$  sample at different temperatures. The stripe periods are calculated at 0 T and the skyrmion size is calculated at 0.2 T. (b) The number of skyrmions and type-II bubbles observed using LTEM at different temperatures for the samples  $x = 0.8$ .

sample regions of  $27 \mu\text{m}^2$  at varying temperatures. The temperature-dependent transformation between type-II bubbles and skyrmions for the  $x = 0.8$  sample is summarized in Fig. 4.40(b).

According to the PND analysis, the collinear ferromagnetic sample with  $x = 0.8$  exhibits an easy-cone magnetic anisotropy at temperatures below  $T_{SR}$  ( $\approx 125$  K) and an out-of-plane easy-axis state at temperatures  $\geq 200$  K [see Fig. 4.25]. The collective findings from LTEM and PND investigations indicate that the application of a magnetic field along the  $c$ -axis stabilizes the type-II bubble in a ferromagnetic system with an easy-cone magnetic anisotropy. In contrast, skyrmions can emerge as a stable field-driven state in samples possessing a  $c$ -axis collinear ferromagnetic ground state. It is important to note that easy-cone magnets inherently harbor a significant in-plane anisotropy component due to the tilting of the magnetic easy-axis away from the  $c$ -axis. Consequently, at a temperature of 100 K, the presence of a finite in-plane anisotropy component results in the lower energy state of type-II bubbles rather than skyrmions in the system. Conversely, the absence of in-plane anisotropy above 200 K enhances the stability of skyrmions in the sample. A Co concentration ( $x$ ) vs. temperature ( $T$ ) phase diagram for the sample  $\text{MnFe}_{1-x}\text{Co}_x\text{Ge}$

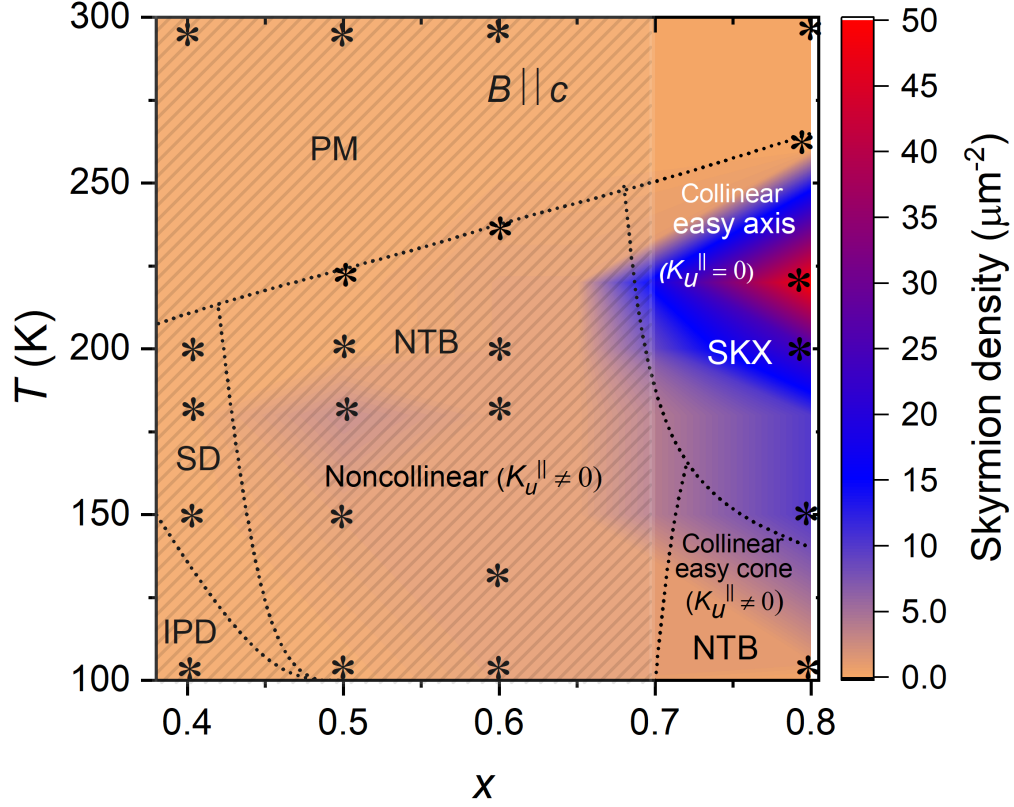


Figure 4.41: The  $x$  vs.  $T$  phase diagram for the sample  $\text{MnFe}_{1-x}\text{Co}_x\text{Ge}$ . The color bar represents the skyrmion density per  $\mu\text{m}^2$  area. PM, SD, IPD, NTB, and SKX represent paramagnetic, stripe domain, in-plane domain, non-topological bubbles, and skyrmions lattice, respectively. Dotted lines are provided as guides to the eye. The asterisk symbols mark experimental data points. The data at the magnetic field where the highest number of skyrmions are observed are considered for a given  $(x, T)$ .

is shown in Figure 4.41. This analysis uses LTEM images captured at the magnetic field corresponding to the maximum number of skyrmions at a specific  $(x, T)$  point to determine the skyrmion density for that particular condition. Notably, a robust skyrmion density is observed for the easy-axis collinear ferromagnet with zero  $K_u^{\parallel}$ , while samples with lower Co concentration up to  $x = 0.6$  predominantly exhibit type-II bubbles as the stable magnetic state. Furthermore, type-II bubbles, rather than skyrmions, are demonstrated as a stable state in the easy-cone ferromagnetic phase with a finite  $K_u^{\parallel}$ . The combined experimental findings highlight that skyrmion stability is hindered when a system contains an in-plane anisotropy component.

To determine if all of the LTEM observations provided in this chapter are truly free of the impact of an external in-plane magnetic field, the zero field remanent states of the samples are recorded after increasing the field along the zone ( $c$ )-axis. The remanent states for the samples at different temperatures are presented in Fig. 4.42, 4.43. For the  $x = 0.4$  sample, a remanent state of stripe domains is visible at 150 K, as illustrated in Fig.4.42(a). In the case of  $x = 0.5$  and  $x = 0.6$  samples, a mixed state of stripe domains and type-II bubbles, along with a small number of isolated skyrmions is observed as the remanent state. The skyrmions are marked with boxes in Fig. 4.42(b)-(c). The TIE magnetization mapping of the LTEM image for the  $x = 0.5$  sample at 150 K is shown in Fig. 4.42(d), where the arrows highlight the random orientation of the Bloch lines. For the  $x = 0.8$  sample, a mixed state of stripe domains and skyrmions with a hexagonal arrangement is observed at 220 K [see Fig.4.43(a)], while a mixed state of stripe domains and type-II bubbles is observed at 100 K [see Fig.4.43(d)]. At the intermediate temperature, 150 K, a few isolated skyrmions coexist with the state observed at 100 K. The TIE analysis of the magnetic contrasts for  $x = 0.8$  at 220 K and 100 K is shown in Fig. 4.43(e)-(f). These outcomes consistently replicate the field-dependent measurements presented earlier, confirming the robustness of our findings, which excludes the effects of in-plane magnetic fields.

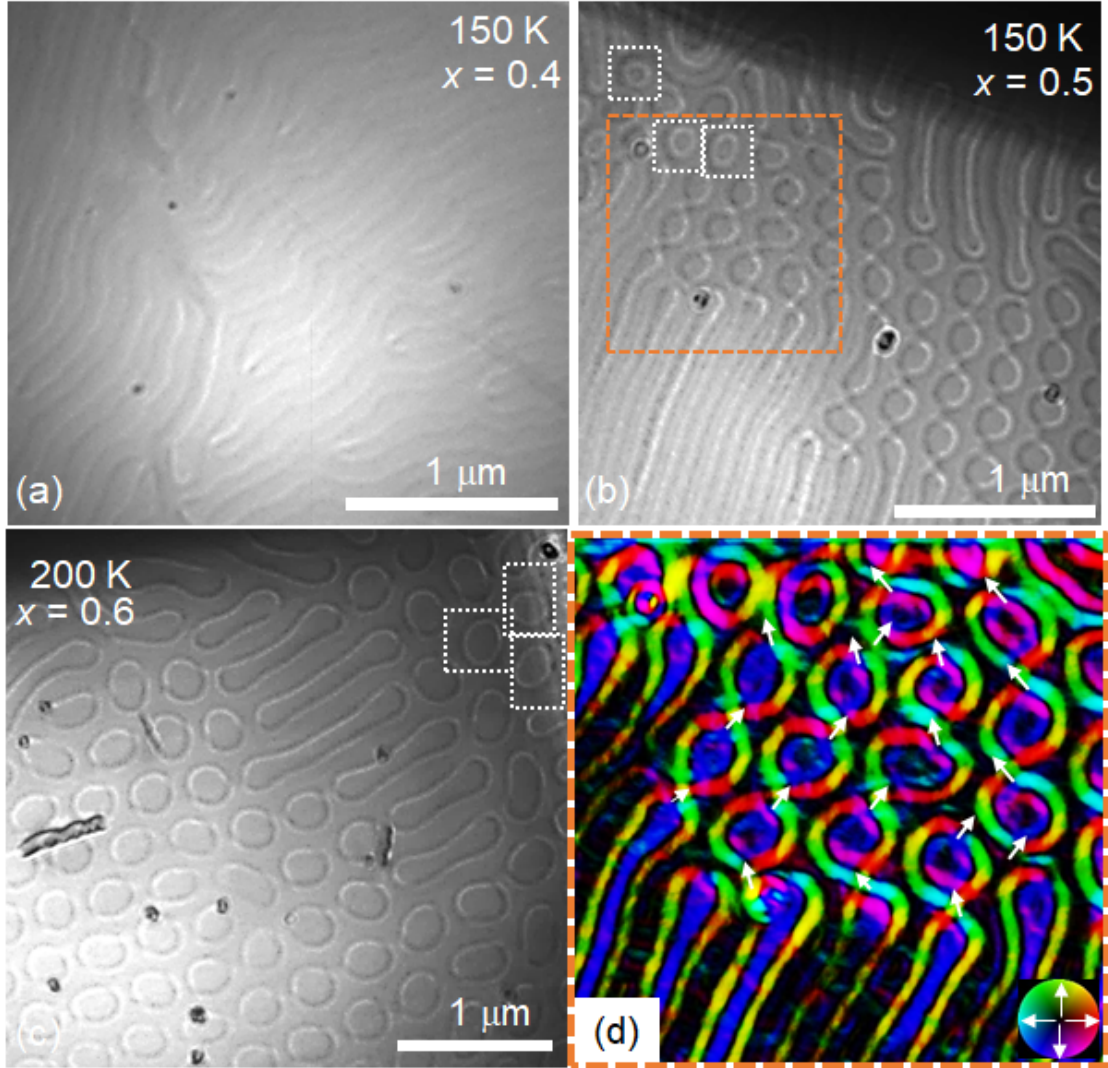


Figure 4.42: The remanent state observed in LTEM for the samples  $x = 0.4$  at 150 K (a),  $x = 0.5$  at 150 K (b),  $x = 0.6$  at 200 K, respectively. The skyrmions are marked with boxes. The TIE magnetization mapping of the marked region in (b). The color wheel represents in-plane magnetization components. The Bloch line orientations are marked with arrows.

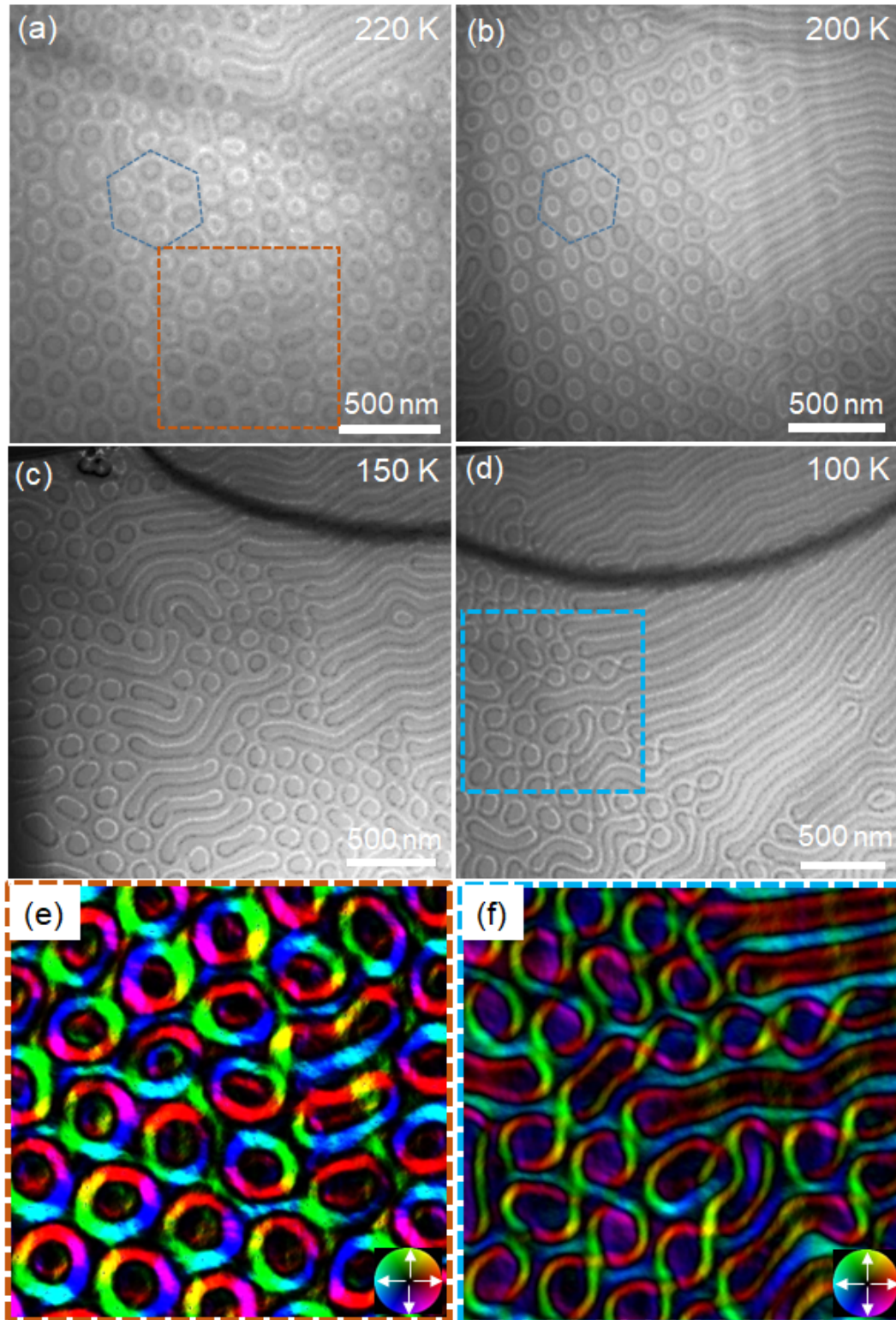


Figure 4.43: The remanent state observed in the LTEM study for the samples  $x = 0.8$  at 220 K (a), 200 K (b), 150 K (c), and 100 K (d), respectively. The remanent states are recorded with increasing field along the zone axis, then making it zero. (e)-(f) TIE magnetization mapping of the marked region in (a) and (d). The color wheel represents the in-plane magnetization components.



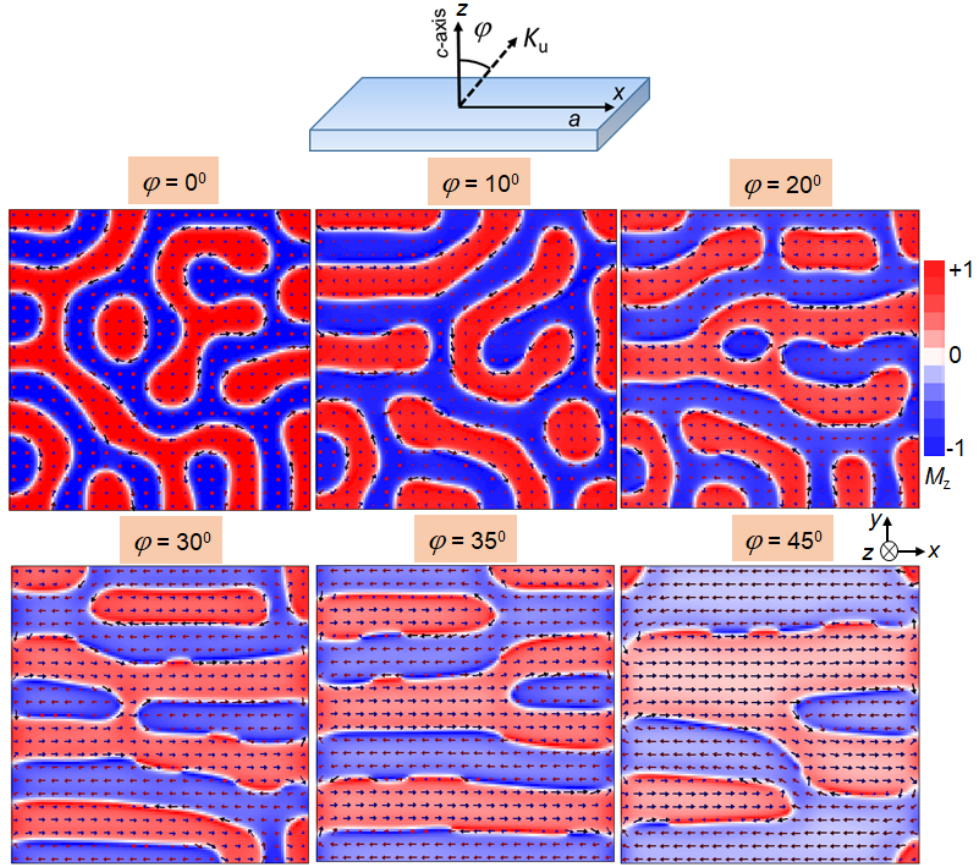


Figure 4.44: The OOMMF simulations of magnetic domains at zero magnetic fields, incorporating tilting the magnetic easy-axis away from the  $c$ -axis by an angle  $\phi$ . The simulations are conducted in the sample dimension of  $1000 \times 1000 \times 100 \text{ nm}^3$ , and cell size of  $4 \times 4 \times 4 \text{ nm}^3$ . The simulation parameters are,  $M_s = 5.8 \times 10^5 \text{ A/m}$ ,  $A = 8 \text{ pJ/m}$ ,  $K_u = 1 \times 10^5 \text{ J/m}^3$ . The color bar represents the  $z(c)$ -axis moment. The black arrows denote the in-plane moment directions.

### 4.3 Micromagnetic simulations for MnFe<sub>1-x</sub>Co<sub>x</sub>Ge sample

To better understand the experimental findings, micromagnetic simulations are conducted for the  $x = 0.8$  sample, incorporating the magnetic easy axis tilted away from the  $c$ -axis by an angle  $\phi$ . The simulated zero-field domain state for the sample is represented in Fig. 4.44 by increasing the tilting easy-axis angle  $\phi$  from  $0^\circ$  to  $45^\circ$ . An increase in angle  $\phi$  results in the alignment of the stripe domains in a certain direction. This aligning behavior resembles the stripe domain alignment observed in our experimental LTEM picture at 100K for the  $x=0.8$  sample [see Fig. 4.39(a)]. Figure 4.45 illustrates the simulated field-driven states with an applied magnetic field along the  $c$ -axis at different  $\phi$  angles. A distorted hexagonal skyrmion lattice is observed when the easy-axis is along the  $c$ -direction ( $\phi = 0^\circ$ ). As  $\phi$  increases, a gradual transformation from skyrmions to type-II bubbles occurs. At  $\phi = 25^\circ$ , only type-II bubbles are stabilized. These simulations offer valuable insights into different magnetic structures in the sample and support the interpretation of our experimental results.

Figure 4.46 schematically depicts different energy states for the stability of skyrmions and other spin textures in the MnFe<sub>1-x</sub>Co<sub>x</sub>Ge system. For both collinear and non-collinear ferromagnetic backgrounds, where the in-plane anisotropy component ( $K_u^{\parallel}$ ) exceeds the out-of-plane component ( $K_u^{\perp}$ ), in-plane domains are energetically favored. When  $K_u^{\perp}$  slightly surpasses  $K_u^{\parallel}$ , the non-collinear ferromagnet stabilizes the out-of-plane stripe domain as a lower energy state. However, the significant energy difference between stripe domains and type-II bubbles impedes field-induced transitions, observed in  $x = 0.4$  at 150 K. A decrease in the  $\frac{K_u^{\parallel}}{K_u^{\perp}}$  ratio is expected for  $x = 0.5, 0.6$  samples due to a decrease in the non-collinear canting angle as expected from the experimental and theoretical data. This decrease in the energy gap between the stripe domain and type-II bubbles results in the stabilization of type-II bubbles as a field-driven state. In this scenario, skyrmions exhibit higher

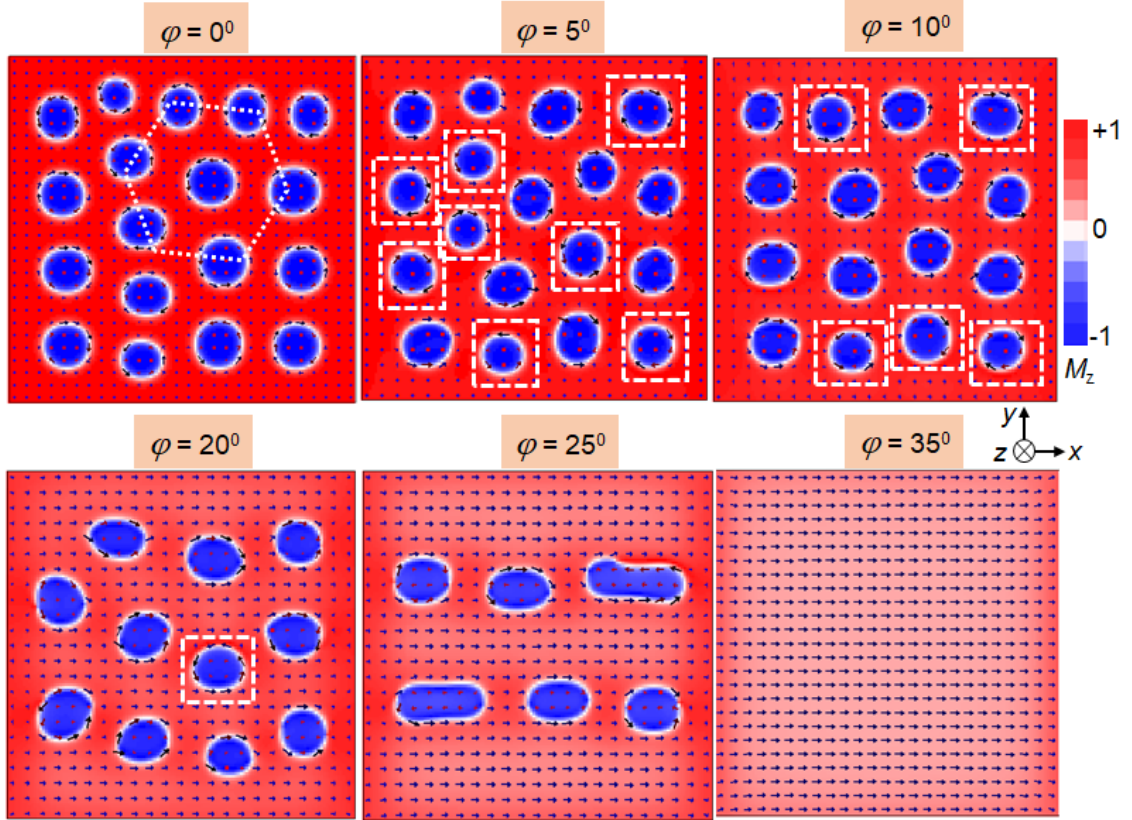


Figure 4.45: The OOMMF simulations of magnetic domains at a magnetic field of 0.2 T along the  $c$ -direction, incorporating a tilting of the magnetic easy-axis away from the  $c$ -axis by an angle  $\phi$ . The simulations are conducted in the sample dimension of  $1000 \times 1000 \times 100 \text{ nm}^3$ , and cell size of  $4 \times 4 \times 4 \text{ nm}^3$ . The simulation parameters are,  $M_S = 5.8 \times 10^5 \text{ A/m}$ ,  $A = 8 \text{ pJ/m}$ ,  $K_u = 1 \times 10^5 \text{ J/m}^3$ . The color bar represents the  $z(c)$ -axis moment. The arrows denote the in-plane moment directions. A distorted hexagonal skyrmion lattice at  $\phi = 0^\circ$  is highlighted with a hexagon, and isolated skyrmions in other cases are marked with solid boxes.



energy than type-II bubbles due to the presence of finite  $K_u^{\parallel}$  in the non-collinear ferromagnetic system. Conversely, the collinear ferromagnetic state with finite  $K_u^{\parallel}$  along with  $K_u^{\perp}$  (easy-cone ferromagnet) shows type-II bubbles as the stable state compared to that of skyrmions, as observed in the  $x = 0.8$  sample at 100 K. For the same system, by decreasing  $K_u^{\parallel}$  to zero leads to the better stabilization of skyrmions compared to the type-II bubbles.

## 4.4 Discussion and conclusion

The technological significance of skyrmion-like magnetic textures in uniaxial centrosymmetric systems stems from their distinct topological characteristics and helicity degrees of freedom. Typically, the competition between UMA and dipolar interaction is considered the primary mechanism for stabilizing skyrmions in such systems. Skyrmions with sizes of 1-2 nm are observed in some centrosymmetric systems due to frustrated magnetic interactions, including four-spin exchange interactions [13, 14, 15]. However, these extremely small skyrmions are typically observed at very low temperatures ( $< 10$  K). Investigating dipolar skyrmions by combining the effects of exchange frustration and dipolar interaction offers a possible route for achieving tiny skyrmions at room temperature. Dipolar-stabilized skyrmions in most centrosymmetric systems are conventionally studied in collinear ferromagnetic backgrounds. While prior research has explored the tunability of dipolar skyrmions through external influences like magnetic fields [43, 125, 131] and current [128, 129, 132], a comprehensive investigation into their stability amid internal energy parameter modifications is lacking. Moreover, it is still unclear how magnetic orderings and underlying interactions affect dipolar-stabilized skyrmions. This chapter thoroughly examines the stability of dipolar skyrmions, considering the impact of the associated ground state magnetic ordering and exchange frustration strength. By altering the Fe and Co atomic ratio, magnetic exchange interactions between Mn moments are manipulated, allowing in-depth analysis of dipolar skyrmion stability under different scenarios.

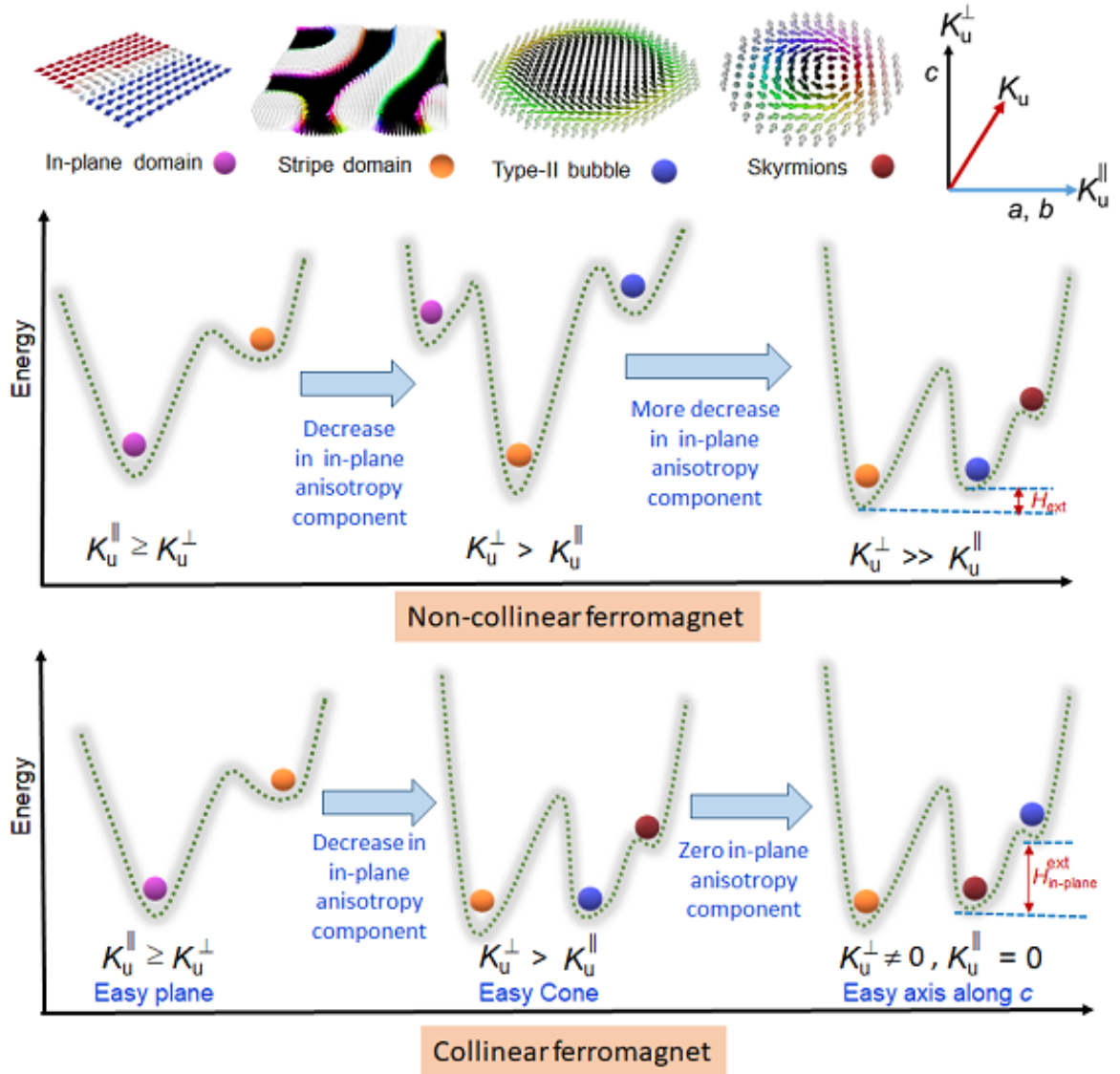


Figure 4.46: schematic energy diagram representing the stability of skyrmion and other possible spin textures in  $\text{MnFe}_{1-x}\text{Co}_x\text{Ge}$  samples.

Our combined theoretical calculations and practical findings demonstrate the presence of a noncollinear canted magnetic ground state for  $\text{MnFe}_{1-x}\text{Co}_x\text{Ge}$  samples with  $x < 0.75$ . In contrast, the ground state changes to a collinear ferromagnetic state for  $x \geq 0.75$ . In-plane domain walls for  $x = 0.4$  samples at 100 K reveal a substantial link between magnetic ordering and magnetic anisotropy components. Consequently, with a change in magnetic ordering, an anisotropy component realignment is expected for the samples. The DFT calculations predict a reduction in the canting angle ( $\theta$ ) in  $\text{MnFe}_{1-x}\text{Co}_x\text{Ge}$  with increasing Co concentration ( $x$ ). Consequently, when  $x$  increases, a drop in the ratio of  $K_u^{\parallel}$  and  $K_u^{\perp}$  is expected. Non-topological type-II bubbles are primarily stabilized as a field-driven state, overshadowing the topological skyrmions, in a noncollinear background ( $K_u^{\parallel} \neq 0$ ). Remarkably, the hexagonal skyrmion lattice becomes visible only in the collinear ferromagnetic background when a magnetic field is applied along the easy-axis direction. In contrast, the sample with easy-cone anisotropy and  $K_u^{\parallel} \neq 0$  stabilizes the hexagonal lattice of type II bubbles. Previous research shows that the presence of an in-plane magnetic field may cause a transformation between topological skyrmion and non-topological type-II bubbles in the collinear ferromagnetic background. The present work clarifies that, with an applied magnetic field along the zone axis, skyrmions in a collinear ferromagnetic background can also be transformed into type-II bubbles in the presence of a non-zero in-plane magnetic moment or  $K_u^{\parallel}$ . Our experimental findings reveal that the presence of  $K_u^{\parallel}$  limits skyrmion stability in both collinear and non-collinear magnetic backgrounds. Hence, the work offers comprehensive details on various energy parameters affecting the tunability and stability of dipolar skyrmions.

In summary, this study provides a thorough investigation of the stability and tunability of skyrmions in a series of hexagonal ferromagnets  $\text{MnFe}_{1-x}\text{Co}_x\text{Ge}$ , with a tunable magnetic ground state. A strong correlation is unveiled between the stability of skyrmions and the background spin ordering. It becomes evident that the stability of skyrmions is significantly influenced by the degree of non-collinearity and the underlying interactions in the system. A magnetic field applied along the  $c$ -direction

stabilizes the skyrmion lattice only in the  $c$ -axis collinear ferromagnet, whereas type-II bubbles are mostly stabilized in non-collinear and collinear backgrounds with  $K_u^{\parallel} \neq 0$ . The study demonstrates the importance of in-plane anisotropy component in determining skyrmion stability. These findings indicate the possibility of controlling skyrmion stability and tunability by altering material-specific characteristics, which can be a big step forward in developing skyrmion-based devices.



## Chapter 5

# Anomalous magneto-transport properties due to inter-connected real and momentum space Berry curvature in the skyrmion hosting kagome magnet $\text{Mn}_4\text{Ga}_2\text{Sn}$

Magnetic skyrmions are projected as an essential component of modern spintronics devices for their topological characteristics. In this regard, it is important to study their dynamics for any potential applications in the reading and writing of memory data. Recently, the skyrmions with helicity and vorticity degrees of freedom in centrosymmetric systems have been proposed as viable candidates for qubit generation in skyrmion-based quantum computers [67, 68, 156, 157, 158]. A few recent articles have also studied the dynamics of dipolar stabilized skyrmions with the application of electric current [128, 129, 132, 159]. In all these cases, the skyrmion dynamics are affected by unwanted joule heating. Therefore, it will be highly beneficial to identify such a system in which the joule heating effect may be avoided when studying

the skyrmion dynamics. In this direction, some theoretical studies propose that the skyrmions in a system with electronic band ( $k$ -space) topologies, such as Weyl or Dirac nodes can be moved without the application of any conduction current [76, 77, 78]. In the above-mentioned cases, a torque is generated on the spatially varying magnetic texture, such as skyrmion, due to the charge-induced spin torque, and as a result, the skyrmions can be moved with the application external magnetic field or finite gate voltage. Here, the generated torque is predicted to be proportional to the anomalous Hall conductivity (AHC) [77, 78]. In this direction, there exists only a few experimental reports where the effect of real space ( $r$ -space) topology on  $k$ -space reconstruction and vice-versa are experimentally established [79, 80]. Moreover, no experimental study exists on the correlation of both  $r$ -space topology and  $k$ -space topology. Additionally, in practice, there are very few systems that exhibit both  $r$ -space and  $k$ -space topological effects at the same time. As discussed in Chapter 3, near room temperature skyrmion lattice is observed in kagome ferromagnet  $\text{Mn}_4\text{Ga}_2\text{Sn}$ . According to the literature, the kagome magnets possess a great potential to host topological electronic band structure [70, 71, 72, 73, 74, 90, 110]. The electronic band structure of a material is always reflected in its magneto-transport properties, and many unusual phenomena, such as negative magneto-resistance due to chiral anomaly (CA) [90, 105, 106, 107, 108, 160], large anomalous Hall effect (AHE) [70, 71, 90, 107, 108, 160], quantum oscillations [161, 162, 163, 164, 165, 166], etc, can be observed. Consequently, the magneto-transport characteristics of the sample  $\text{Mn}_4\text{Ga}_2\text{Sn}$  are investigated to see whether it may serve as a platform for encasing the relationship between  $k$ -space topology and  $r$ -space topology.

The structural and magnetic characterizations are discussed in Chapter 3. The sample shows a spin reorientation transition around 90 K, and the hexagonal skyrmion lattice in this material can be observed when the magnetic field is applied along the  $c$ -axis at  $T \geq T_{SR}$ . Therefore, to achieve the  $r$  space and band topology simultaneously, a  $c$ -oriented device for the sample is prepared using FIB. The required grain for the sample is chosen using the EBSD technique. The procedure for device fabrication is described in Chapter 2 section 2.9. The micron-sized device is attached to

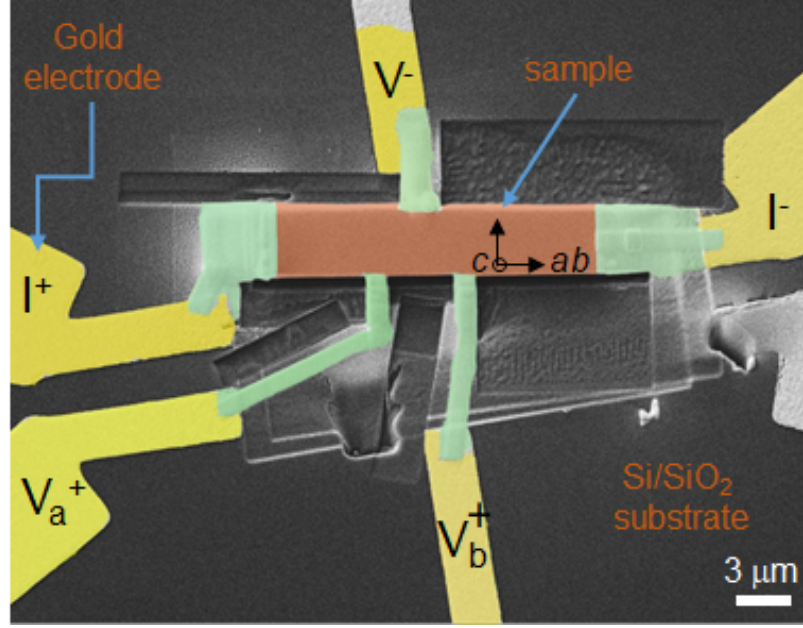


Figure 5.1: The false colored SEM image of the *c*-oriented Hall device.

a gold patterned Si/SiO<sub>2</sub> substrate and connected to the electrodes using tungsten deposition. The false-colored image of the fabricated *c*-oriented device is shown in Fig. 5.1. The sample has a thickness of around 800 nm.

## 5.1 Magneto-transport measurements:

### 5.1.1 Anomalous Hall effect:

Field dependent Hall resistivity data measured at different temperatures for the sample Mn<sub>4</sub>Ga<sub>2</sub>Sn are shown in Fig. 5.2(a). The normal Hall resistivity ( $R_0H$ ) is subtracted by linear fitting of the Hall data at high field region, as shown in Fig. 5.2(b). The extracted  $R_0$  value for the sample at different temperatures is shown in Fig. 5.2(c). The  $R_0$  values are temperature independent up to 250 K, and with further increase in temperature near  $T_C$ , the  $R_0$  value increases slightly. The extracted Anomalous Hall resistivity (AHR) is nearly 11.5  $\mu\text{ohm-cm}$  at 10 K. The temperature dependence of the AHR ( $\rho_{xy}^A$ ) along with the temperature varying longitudinal resistivity is presented in Fig. 5.2(d). The  $\rho_{xy}^A$  decreases with increasing



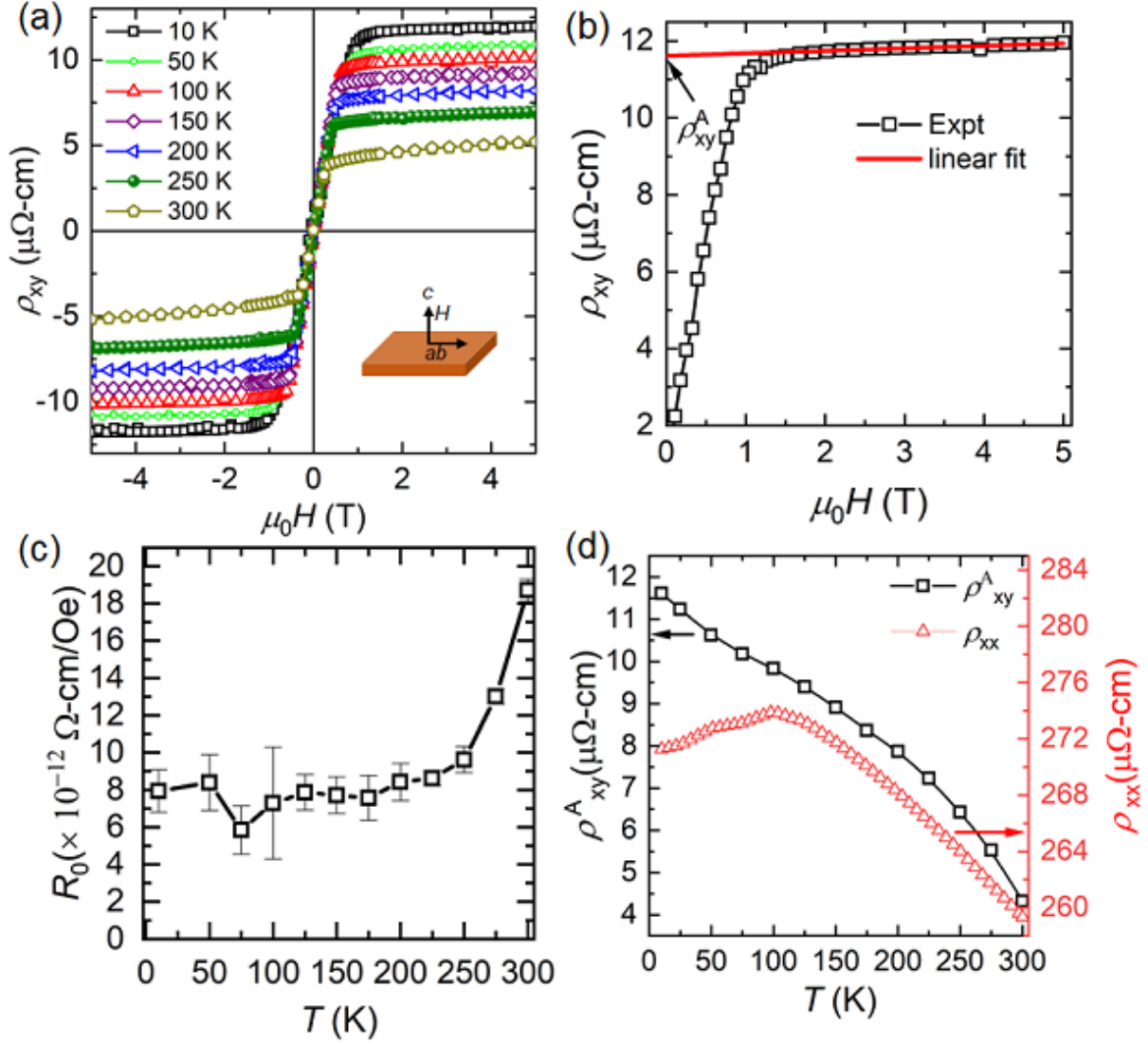


Figure 5.2: (a) The field dependent Hall resistivity for the sample  $\text{Mn}_4\text{Ga}_2\text{Sn}$  at different temperatures. (b) Extraction of anomalous Hall resistivity ( $\rho_{xy}^A$ ) by linear fitting. (c) Temperature variation of the fitting parameter  $R_0$ . (d) Temperature variation of  $\rho_{xy}^A$  and longitudinal resistivity ( $\rho_{xx}$ ) for the  $c$ -oriented device.

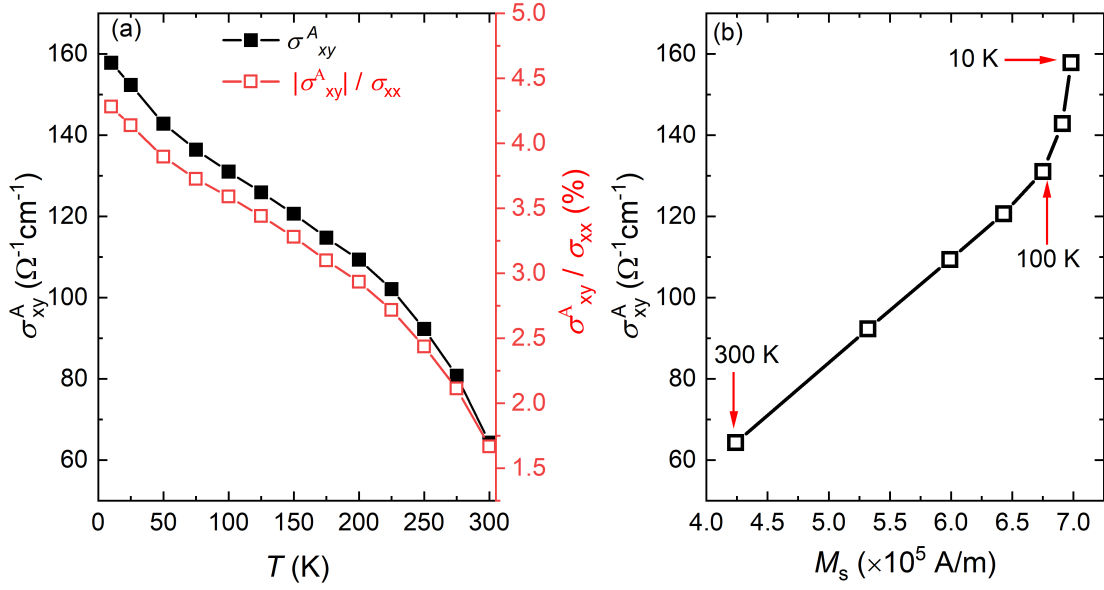


Figure 5.3: (a) Temperature dependence of anomalous Hall conductivity ( $\sigma_{xy}^A$ ), (b) Temperature dependence of scaling factor ( $\sigma_{xy}^A/M_s$ ) and anomalous Hall angle (AHA) ( $\sigma_{xy}/\sigma_{xx}$ ).

temperature. On the other hand, the temperature dependent longitudinal resistivity of the  $c$ -oriented sample shows zero-gap semiconductor or semi-metal like characteristics [107, 167, 168, 169, 170], as shown in Fig. 5.2(d).

The estimated anomalous Hall conductivity (AHC) for the sample,  $\sigma_{xy}^A \approx \frac{\rho_{xy}}{\rho_{xx}^2}$ , at different temperatures is shown in Fig. 5.3(a). A maximum AHC of  $160 \Omega^{-1}\text{cm}^{-1}$ , is observed for the sample at 10 K. As temperature rises, the AHC continually decreases, indicating that the sample exhibits a non-negligible extrinsic scattering (skew scattering and side jump) contribution [23, 169]. It is well known that the intrinsic AHC should be robust to temperature and impurities, which is being observed experimentally in several ferromagnetic materials [23, 70, 90, 96, 171]. All of the previously described samples exhibit residual conductivity ( $\sigma_{xx0}$ ) that is well inside the intrinsic zone ( $10^4 \leq \sigma_{xx0} \leq 10^6 (\Omega\text{-cm})^{-1}$ ), where the only dominating contribution is intrinsic contribution. As determined by the experimental measurement, the residual conductivity of the present material is around  $3.7 \times 10^3 (\Omega\text{-cm})^{-1}$ , falling in the boundary between the intrinsic moderate metallic regime and the dirty metallic region. Therefore, we can neglect the contribution from skew scattering for the sys-

tem. Furthermore, Fig. 5.3(a) illustrates the temperature variation of the anomalous Hall angle (AHA) for the  $c$ -oriented device. AHA is the fraction of normal conductivity that contributes to anomalous Hall conductivity and calculated using the formula  $\text{AHA}(\%) = \frac{\sigma_{xy}^A \times 100}{\sigma_{xx}}$ . A maximum AHA of 4.5 % is observed at 10 K. The magnitude of AHA in the present case is similar to that of topological semi-metals such as  $\text{Fe}_3\text{GeTe}_2$  [74],  $\text{Co}_3\text{Sn}_2\text{S}_2$  [172] and significantly larger than that of the AHA recorded in several anomalous Hall systems such as  $\text{Mn}_3\text{Sn}$ ,  $\text{Fe}_3\text{Sn}_2$ ,  $\text{Mn}_3\text{Ge}$ , and  $\text{Mn}_5\text{Ge}_3$ . Additionally, for the skew scattering-dominated AHE, the expected AHC is  $\sigma_{xy}^A \propto \sigma_{xx}$  [173]. Therefore, the AHA ( $\approx \frac{\sigma_{xy}^A}{\sigma_{xx}}$ ) is anticipated to remain constant for skew scattering dominant case [172]. As a result, the skew scattering mechanism is unable to explain the temperature dependency of AHC in this instance. The  $\sigma_{xy}^A$  vs.  $M_s$  plot for the sample in Fig. 5.3(b), on the other hand, demonstrates a linear dependency of the  $\sigma_{xy}^A$  on the  $M_s$ . Generally, the intrinsic AHC driven by the berry phase is assumed to exhibit a linear dependency on  $M$  [23, 174]. Therefore the intrinsic dominant contribution can be expected for the sample at  $T \geq 100$  K. As discussed in Chapter 3, the sample can stabilize skyrmions above the spin reorientation transition temperature of around 90 K. Consequently, it is interesting to study the intrinsic dominating AHE contribution in the skyrmion range  $T \geq 100$  K.

The following formulas [for details, see Chapter 1] can be used to determine the possible intrinsic and extrinsic contributions to AHE in a system,

$$\rho_{xy}^A = a\rho_{xx0} + \beta\rho_{xx0}^2 + b\rho_{xx}^2 \quad (5.1)$$

$$\sigma_{xy}^A = (a\rho_{xx0} + \beta\rho_{xx0}^2)\sigma_{xx}^2 + b \quad (5.2)$$

where  $b$  is the intrinsic coefficient and  $\alpha = (a\rho_{xx0} + \beta\rho_{xx0}^2)$  is the coefficient related to the extrinsic scattering (skew scattering and side jump). A linear fitting between  $\rho_{xy}^A$  vs.  $\rho_{xx}^2$  and  $\sigma_{xy}^A$  vs.  $\sigma_{xx}^2$  is presented in Figure 5.4. At low temperatures, the extrinsic AHC contribution ( $\alpha \sigma_{xx}^2 \approx 1359 \Omega^{-1} \text{ cm}^{-1}$ ) suppresses the intrinsic contribution  $b$  ( $-1201 \Omega^{-1} \text{ cm}^{-1}$ ). On the other hand, at the high temperature ( $T \geq 100$  K)

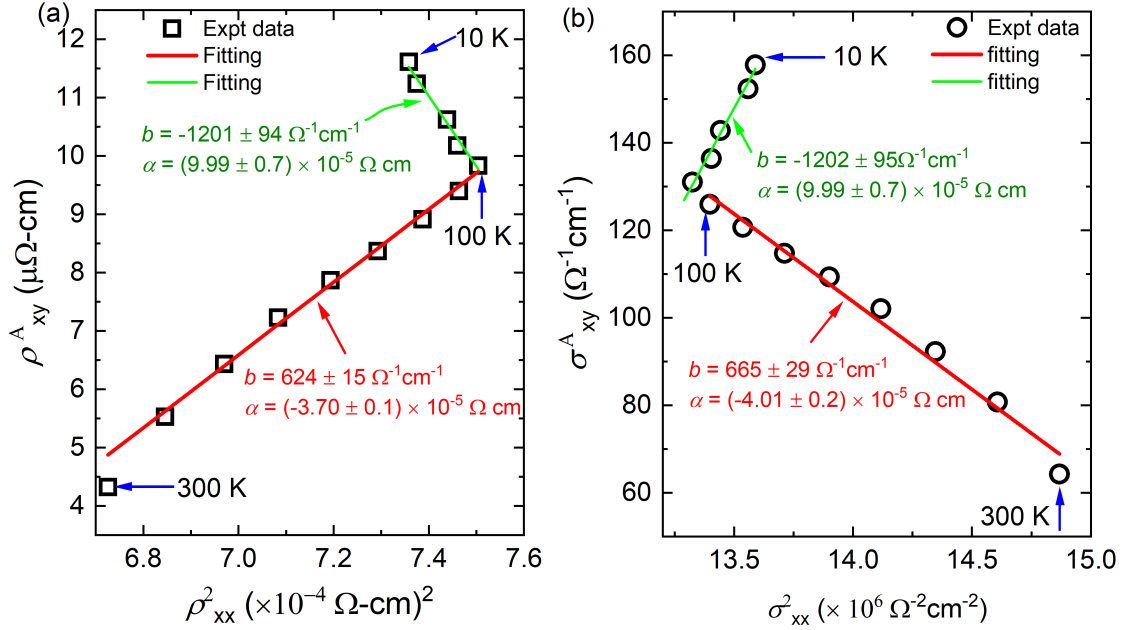


Figure 5.4: (a) Linear fitting between  $\rho^A_{xy}$  vs.  $\rho^2_{xx}$ , (b) linear fitting between  $\sigma^A_{xy}$  vs.  $\sigma^2_{xx}$ .

region ( $\approx 624 \Omega^{-1} \text{cm}^{-1}$ ), the intrinsic AHC dominates over the extrinsic AHC ( $-492 \Omega^{-1} \text{cm}^{-1}$ ) contribution. The main objective of this chapter is to identify the system in which it is feasible to see the skyrmion and intrinsic AHC simultaneously. In this direction, the present compound with skyrmion lattice ( $r$  space topology) and dominated intrinsic AHC ( $k$ -space topology) at temperature range  $T \geq 100 \text{ K}$  might be a potential choice for further study of their correlation. Although the extrinsic contribution above 100 K is quite large and non-negligible, there is no cause for concern, as theoretical predictions suggest that only the intrinsic band topology-related term plays a role in rearranging the real space topology [77, 78].

The skyrmion hosting systems are generally expected to exhibit finite topological Hall effect (THE). Details are discussed in Chapter 1. The THE for a system can be correlated with skyrmion size by the following equation,

$$\rho^T_{xy} = PR_0Q\phi_0/a_{sk}^2 \quad (5.3)$$

where  $p$  is the polarization factor,  $R_0$  is the normal Hall coefficient,  $Q$  is skyrmion

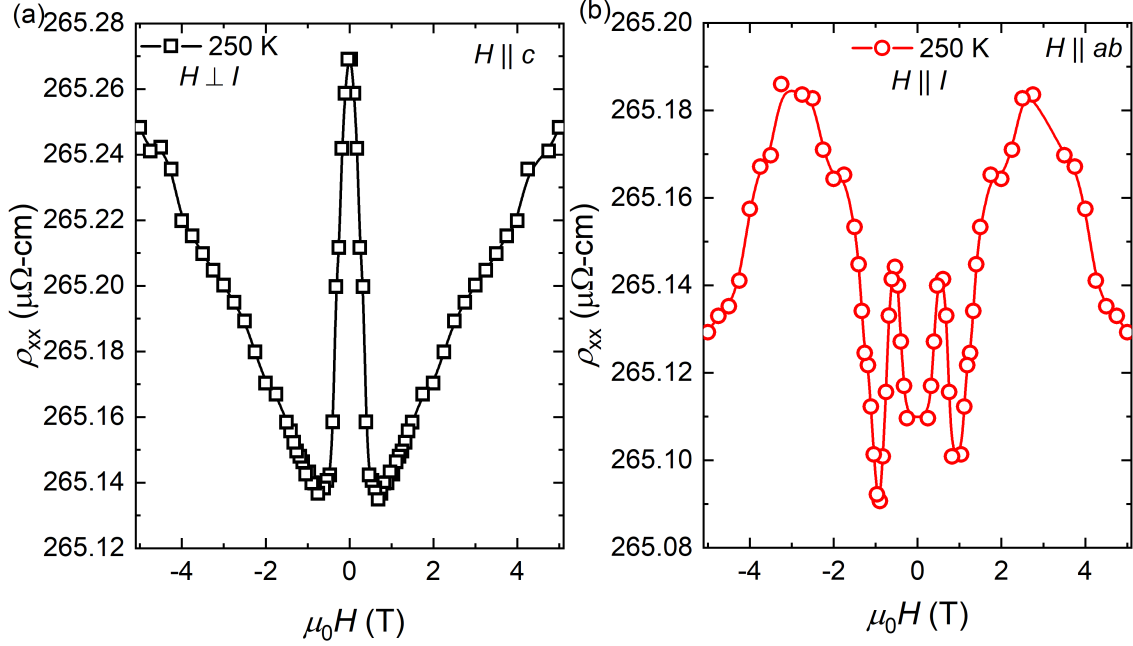


Figure 5.5: Magneto-resistance for  $c$ -oriented device of the sample  $\text{Mn}_4\text{Ga}_2\text{Sn}$  at 250 K, (a) with  $H \perp I$ , (b) with  $H \parallel I$ .

number,  $\phi_0$  is flux quanta, and  $a_{sk}$  is skyrmion size. In this situation, there are no evident hump/dip-like characteristics due to the topological Hall effect (THE). The observed skyrmion size for  $\text{Mn}_4\text{Ga}_2\text{Sn}$  is nearly 100 nm at 250 K, as discussed in Chapter 3. The normal Hall coefficient for the sample at 250 K is  $9 \times 10^{-12} \Omega\text{-cm/Oe}$  [see Fig. 5.2(c)]. The polarization factor  $P = \frac{M_{250K}}{M_s} = 0.81$ . Therefore, the calculated THE for  $\text{Mn}_4\text{Ga}_2\text{Sn}$  at 250 K is  $\approx 15 \text{ n}\Omega\text{-cm}$ . Large AHE ( $\approx 7000 \text{ n}\Omega\text{-cm}$  at 250 K) surpasses this small value of the THE in the present system.

### 5.1.2 Magneto-resistance (MR) measurements:

It has been demonstrated that the electronic band topology of a material can affect its magneto-resistance (MR), resulting in various anomalous behaviors, including chiral anomaly (CA) [90, 105, 106, 107, 108, 109] and anisotropic magneto-resistance (AMR) [175, 176, 177]. Therefore, the MR measurements of the  $\text{Mn}_4\text{Ga}_2\text{Sn}$  sample are performed to find out the possibility. Figure 5.5 shows the MR measurements on a  $c$ -oriented device of the sample at a temperature of 250 K. The MR exhibits

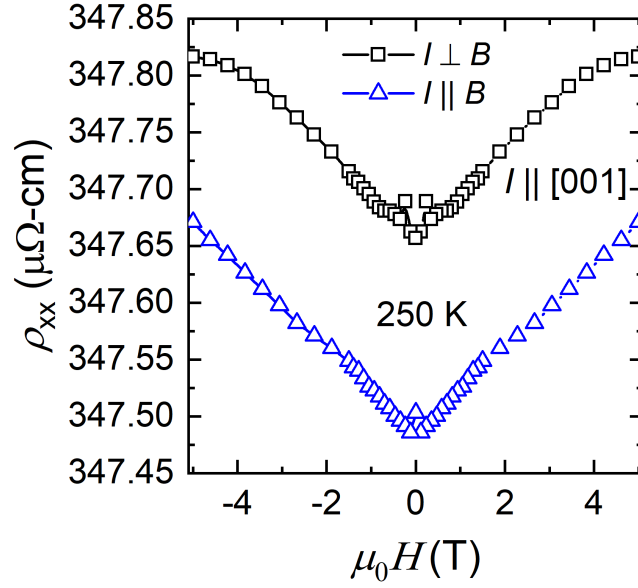


Figure 5.6: Magnetoresistance for the in-plane device of  $\text{Mn}_4\text{Ga}_2\text{Sn}$  sample at 250 K.

an increasing trend over 1 T when a magnetic field is supplied perpendicular to the current direction [see Fig. 5.5(a)]. On the other hand, the MR with  $H \parallel I$  shows an entirely different behavior; the MR follows an oscillating-like behavior with a decreasing trend at a high field [see Fig. 5.5(b)]. This type of effect in MR measurements resemble the chiral anomalously-like behavior observed in the presence of Dirac point [178], avoided band crossing [109], Weyl node [90], and other such features. The distance between two chiral band crossing locations, the crossing points' distance from the Fermi level, the concentration of carriers, etc, are the primary factors influencing the amplitude of the observed negative MR [178]. The low MR(%) value seen here may be explained by the large carrier concentration ( $6.9 \times 10^{21} \text{ cm}^{-3}$ ), or it might be that the distance between the Fermi level and the crossing points is somewhat larger in this case. However, the chiral anomaly-like behavior in the sample indicates the sample could be a potential candidate to host the band topology.

The chiral anomaly-like behavior is observed in the  $c$  [001]-oriented device, where the skyrmions can be stabilized with an applied magnetic field along the  $c$ -direction,

as shown in Chapter 3. Another in-plane ( $ac$ -plane) device is constructed where the skyrmions are not expected, to investigate if the skyrmion's presence influences the electrical band structure crossing points or, thereby, MR measurement. In this case, both  $H \parallel I$  and  $H \perp I$  show positive MR, and no chiral anomaly-like behavior is observed [see Fig. 5.6]. The observation suggests a relationship between  $k$  space electronic band structure and skyrmion ( $r$ -space topology). As a result, the  $\text{Mn}_4\text{Ga}_2\text{Sn}$  sample may be important in determining any potential correlation with future direct measurements.

## 5.2 Discussion and conclusion:

The dipolar stabilized skyrmions with tunable helicity and vorticity in centrosymmetric systems are now a days become one of the hot research topics in spintronics. The possibility of their practical applications in modern skyrmion-based memory devices is also proposed [67, 68, 156, 157, 158]. In most of the cases, the effect of dominating joule heating has been observed in the dynamics of skyrmions in centrosymmetric systems [128, 129, 132, 159]. To get rid of the heating effect, a system where the skyrmions can be moved without the application of electric current is needed. Recent theoretical studies propose that the skyrmion motion without electrical current is possible in a system containing  $k$  space topology and skyrmions [76, 77, 78]. In this chapter, a potential platform is demonstrated that supports the theoretical predictions. The practical implementation of modern skyrmion-based devices without any joule heating loss might greatly benefit from the findings.

Here, magneto-transport measurements are carried out in a skyrmion hosting centrosymmetric kagome ferromagnet  $\text{Mn}_4\text{Ga}_2\text{Sn}$ . Large AHE dominated by intrinsic contribution is observed at  $T \geq T_{SR}$ , where the hexagonal skyrmion lattice is observed using LTEM [see chapter. 3]. A chiral anomaly-like behavior in MR data is also observed for the  $c$ -oriented device of the sample. In contrast, the in- $(ac)$  plane device, where skyrmions are unexpected, does not exhibit this peculiarity. A competing out-of-plane easy-axis anisotropy and dipolar energy are required to

stabilize the skyrmion in the centrosymmetric system. Since an out-of-plane easy axis doesn't exist for the *ac* plane device, skyrmion stabilization is not possible. Although the measured MR magnitude is lower than the previously recorded cases, it may be explained by the present material's carrier concentration, band crossing point distance, etc [90, 105, 106, 107, 108, 160, 178].

Moreover, the simultaneous detection of significant AHE and chiral anomalies in MR data suggests that  $\text{Mn}_4\text{Ga}_2\text{Sn}$  might be a suitable platform for future studies on skyrmion dynamics without electric current. Furthermore, the identification of a chiral anomaly in the *c*-oriented device featuring skyrmions, its absence in the skyrmion-lacking *ac*-plane device highlights a robust correlation between the topological characteristics in real space (*r*-space) and momentum space (*k*-space) in the present system. In conclusion, this chapter identifies a possible platform for confirming the theoretically expected association between *r*-space and *k* space topology.





# Chapter 6

## Summary and Future prospective of the thesis

Magnetic skyrmions are proposed as one of the alternatives to domain walls for 3D racetrack memory devices. The skyrmions are mostly stabilized in non-centrosymmetric systems having nonzero Dzyaloshinskii–Moriya interaction. Recently, the skyrmion-like spin textures with different helicity and vorticity degrees of freedom are discovered in centrosymmetric systems. Furthermore, the recent prediction of the usage of skyrmion helicity and vorticity degrees in skyrmion-based quantum computers makes skyrmions in centrosymmetric systems much more intriguing. Although the mechanism of skyrmions' stability in non-centrosymmetric systems is well documented, its stabilization in centrosymmetric systems with additional degrees of freedom and tunability demands more investigation. As a result, the present dissertation is primarily concerned with discovering novel skyrmion-hosting centrosymmetric systems and investigating their tunable characteristics with external as well as internal factors. The first chapter of the thesis provides an overview of the topological aspects of non-collinear magnetism. A brief literature review is also provided for the skyrmion spin structures. Different internal and external characteristics that can be used to control skyrmion stability in a system are also addressed in chapter 1. A separate chapter describes the fundamental working principles of the few

experimental techniques and theoretical methodology employed in this thesis. The outcomes of the experiments are presented in three different chapters.

In the third chapter, a near room temperature hexagonal skyrmion lattice with skyrmion size  $\leq 100$  nm is discovered in a new skyrmion hosting kagome ferromagnet  $\text{Mn}_4\text{Ga}_2\text{Sn}$ , with centrosymmetric crystal structure. Here, the real space observation of skyrmions is performed using the Lorentz transmission electron microscopy technique. Due to competing uniaxial magnetic anisotropy and dipolar energy, many hexagonal centrosymmetric systems exhibit room-temperature skyrmions. However, the size of the skyrmion in these system is greater than 200 nm. In this regard, the current discovery of lower-size ( $\leq 100$  nm at 250 K) skyrmions around ambient temperature suggests the significance of our experimental result in terms of practical applicability. Furthermore, the tunability of the skyrmion spin structure relative to external factors such as magnetic field in the present case is explored. When the magnetic field is applied along the  $c$ -direction, the skyrmions are observed to be the field-driven stable state for the collinear ferromagnet with easy-axis anisotropy ( $T \geq T_{SR}$ ). The Lorentz transmission electron microscopy observations show that a controlled transformation between topological skyrmion and non-topological type-II bubbles can be achieved in the presence of an additional in-plane magnetic field and that the in-plane magnetic field can be employed by tilting the sample to the  $x$  and  $y$  axes. By controlled tilting experiments in different directions, it is also demonstrated that the in-plane magnetic field plays a key role in deciding the internal structure of type-II bubbles. The Bloch lines are aligned along the in-plane field directions. Moreover, under a specific tilting situation, such as in a finite in-plane magnetic field, the nucleated number of skyrmions increases with rising temperature to 250 K. The calculated effective uniaxial anisotropy ( $K_{eff}$ ) shows a direct correlation with the observed skyrmion numbers. Near the spin-reorientation temperature of 100 K, when the sample transitions from an out-of-plane high-temperature easy-axis state to an in-plane state, type-II bubbles are mostly seen as field-driven stable states with  $3^\circ$  sample tilting condition. In contrast, the same tilting scenario at 250 K displays many nucleate isolated skyrmions along with type-II bubbles. The

finding shows that the strength of uniaxial magnetic anisotropy plays a vital role in determining the energy barrier between skyrmion and type-II bubbles in a system. As a result, a small amount of in-plane magnetic field is sufficient to transform the skyrmion into bubbles owing to reduced anisotropy, as observed at 100 K. All these experimental results are theoretically validated by micromagnetic simulations. Moreover, the enhanced tunability of the smaller-sized skyrmion, coupled with helicity degrees of freedom within the current centrosymmetric system, represents a significant advancement toward its practical application.

There are few more recent articles exploring skyrmion tunability in terms of experimental parameters such as magnetic field, current, etc, whereas there are very small number of research on skyrmion stability in terms of internal energy parameters. Therefore, the fourth chapter of the thesis focuses on the investigation of magnetic ground state-dependent skyrmion stabilization in a series of non-collinear hexagonal magnet  $\text{MnFe}_{1-x}\text{Co}_x\text{Ge}$ , where the magnetic background can be tuned from non-collinear to collinear by varying the Co concentration ( $x$ ). According to the DFT calculation, the sample features a competing RKKY-like ferromagnetic interaction and a super exchange-like antiferromagnetic interaction, resulting in a non-collinear magnetic ground state for the sample with lower Co concentration. In the case of  $x = 0.75$ , the dominant RKKY exchange leads to the collinear ferromagnetic ground state. The neutron diffraction experiments confirm the theoretical predictions by revealing a non-collinear magnetic ground state with a  $c$ -axis ferromagnetic component and a basal plane antiferromagnetic component for the  $x = 0.4$  sample. In contrast, the sample with  $x = 0.8$  exhibits collinear magnetic ordering. Recently, atomic-size skyrmions have been experimentally observed in a few centrosymmetric systems due to frustrated exchange interaction. However, their observation temperature is very low ( $<10$  K). On the other hand, the skyrmions in the centrosymmetric system stabilized by dipolar interaction are mainly observed at room temperature. Therefore, the presence of exchange frustration in a system having dipolar skyrmions points towards the possibility of stabilizing the small-sized skyrmions at room temperature. The real space LTEM measurements reveal the

presence of in-plane domain walls for the sample  $x = 0.4$  at 100 K, which signifies the role of the present in-plane AFM component in deciding the in-plane anisotropy component. Therefore, the realignment of anisotropy components according to the magnetic background is expected for the systems. For the sample  $x = 0.4$ , neutron diffraction indicates a reduction in non-collinear canting angle or in-plane AFM component with rising temperature. As a result, increasing the temperature to 150 K causes a slight decrease in the in-plane anisotropy component, stabilizing the stripe domain as zero field domains. The stripe domains begin to disappear as the field increases, and the sample eventually becomes field-polarized. In this case, the findings indicate a larger energy difference between stripe domains and bubbles/skyrmions. The sample with  $x = 0.8$ , on the other hand, exhibits a hexagonal skyrmion lattice as a stable field-driven state at 220 K with an applied magnetic field along the  $c$ -direction. Whereas type-II bubbles are mainly found as stable field-driven states for  $x = 0.8$  sample at  $T = 100$  K, even without an in-plane magnetic field. The mixed condition of skyrmion and type-II bubble is observed at intermediate temperatures. The neutron diffraction experiments show an easy-cone magnetic state for the material with  $x = 0.8$  at temperature  $T < 125$  K. As a result, type-II bubble state is stabilized as the lower energy state at the easy-cone state with non-zero in-plane anisotropy components. On the other hand, skyrmions appear to be a more stable condition for easy-axis configurations with no in-plane anisotropy component. At all temperature ranges with an applied magnetic field along the  $c$ -direction, the samples with  $x = 0.5$ , and  $0.6$  primarily display type-II bubbles with very few skyrmions. To determine if the in-plane magnetic field impacts all of these experimental results, the remanent states of the samples are recorded with zero magnetic field after the application of a magnetic field along the  $c$ -direction. The observations closely mirror the samples field-dependent readings. As a result, it can be concluded that the domain states are not influenced by the in-plane magnetic field effect. All the observations suggest that the skyrmions are stable in a hexagonal centrosymmetric system with easy-axis anisotropy, whereas the presence of in-plane anisotropy components hinder the skyrmion stability in both collinear and non-collinear magnets,

and stabilize type-II bubbles as a lower energy state. Micromagnetic simulations experimentally validate all the experimental results. The present study explores that the skyrmion spin texture in a centrosymmetric system can also be tuned with internal material-specific parameters. Chapter 3 reveals that the skyrmions can be transformed into type-II bubbles with an in-plane magnetic field. In the fourth chapter, with both experimental and simulated results it is observed that in the hexagonal system, the skyrmions can also be transformed to type II bubbles, due to the presence of non-zero in-plane anisotropy with  $c$ -axis magnetic field without the presence of in-plane field. The discovery points to a new avenue for researchers looking for more controllable features of skyrmion spin texturing.

The helicity degree of freedom of centrosymmetric skyrmion can be used as a potential choice for quantum qubit development. As a result, their dynamics are critical for future data reading and writing. Although there exists a few reports that investigate the dynamics of dipolar stabilized skyrmions, the joule heating effect in most of the cases influences their dynamics and stability. A different method of moving the skyrmion without the applied current and joule heating is necessary to solve this issue. In this regard, a few recent publications propose that skyrmion motion is achievable in the presence of  $k$ -space topology without the need for electric current. In this situation, the torque produced on a skyrmion will be proportionate to the inherent band topology-driven AHC. However, there are no experimental reports on this fact due to the lack of systems where both properties can be observed simultaneously. Hence, the fifth chapter of this thesis makes a concerted effort to identify a system in which skyrmion and band topology may be observed simultaneously. The third chapter shows a hexagonal skyrmion lattice in the kagome ferromagnet  $\text{Mn}_4\text{Ga}_2\text{Sn}$ . Meanwhile, other sources assert that kagome ferromagnets are widely known to have band topology and intrinsic AHC. As a result, magnetotransport measurements are carried out on the sample's site-specific devices to determine this possibility. For the  $c$ -oriented device of the sample at temperature  $T \geq 100$  K, where the hexagonal skyrmion lattice is observed, a substantial anomalous Hall conductivity ( $170 \text{ } \Omega^{-1}\text{-cm}^{-1}$ ) dominated by intrinsic contribution ( $\approx 600 \text{ } \Omega^{-1}\text{-cm}^{-1}$ )

$\text{cm}^{-1}$ ) is detected. The decreasing trend of AHC with rising temperature suggests the presence of some sort of external influence. However, it is theoretically shown that only the intrinsic AHC can influence the skyrmion dynamics without extrinsic contribution. Hence, extrinsic contribution is not a significant issue in the present case. In the  $c$ -oriented sample, where the skyrmions are observed, chiral anomaly-like behavior in MR measurement is observed. Conversely, the anomaly disappears in the  $bc$  plane device where the skyrmions are unexpected. The chiral anomaly is most commonly noticed in systems with electronic band topology. The observations demonstrate the close connection between skyrmion and  $k$ -space band structure. The observation of low MR value in the present system can be related to the high carrier concentration. As a result, our findings indicate a viable platform for further investigating skyrmion dynamics without joule heating and direct visualization of the predicted correlation between  $r$ -space and  $k$ -space topology is also possible in the present system.

In conclusion, the present thesis explores new skyrmion hosting centrosymmetric systems that can exhibit smaller skyrmions near room temperature. Additionally, the tunability of the skyrmions using both external and internal parameters is investigated. A controlled transformation between topological skyrmion and non-topological type-II bubbles is also extensively explored. Additionally, the stability of skyrmion based on various magnetic backgrounds is investigated for the first time. Furthermore, a potential skyrmion system is found in which the dynamics of skyrmions may be examined without the need for electric current, i.e., without the joule heating effect. In light of this, the current thesis presents great significance for investigating skyrmion physics in centrosymmetric systems.

## 6.1 Future outlook:

The skyrmions in centrosymmetric systems, exhibiting both right-handed and left-handed helicity, are proposed as potential candidates for qubit generation in skyrmion-based quantum computers. Although the room temperature skyrmions are already

observed in centrosymmetric systems, in most cases, the skyrmion size is  $> 200$  nm. In this context, the present thesis explores new centrosymmetric ferromagnets with smaller skyrmions ( $< 100$  nm) at room temperature, holding significant implications for practical applications. The extensive investigation of the controlled transformation between topological skyrmions and non-topological type-II bubbles in a centrosymmetric system  $\text{Mn}_4\text{Ga}_2\text{Sn}$  with external factors, such as in-plane magnetic field, indicates the superior tunability of dipolar stabilized skyrmions. Consequently, the prospect of tunable room temperature skyrmions, characterized by smaller sizes and helicity degrees of freedom, offers significant promise for advancements in modern spintronics. Furthermore, the elucidation of the role of UMA strength in the transformation between skyrmions and type-II bubbles contributes fundamentally to understanding the stabilization mechanisms of skyrmions in centrosymmetric systems.

While the stability and tunability of skyrmions in centrosymmetric systems have been extensively investigated using external factors like magnetic fields and currents, there is a noticeable dearth of research on skyrmion stability in the context of material-specific parameters. In this direction, a thorough investigation of skyrmion stabilization in exchange-frustrated centrosymmetric magnets with diverse magnetic ground states become crucial for advancing our understanding of skyrmion physics. It is found that the skyrmions exhibit greater stability in a collinear background than in a non-collinear background. This observation implies that the tuning of skyrmions can also be accomplished by manipulating material-specific parameters, including magnetic background and underlying interactions. The experimental results additionally demonstrate how magnetic anisotropy components play an essential role in skyrmion stability in a centrosymmetric system. The thesis also explores a potential platform that can host both  $r$ -space topology and  $k$ -space topology at the same time. Consequently, according to the theoretical prediction, the system can be a potential platform for studying the dynamics of a skyrmion without electric current, which can solve the problem of joule heating. Therefore, the present thesis makes a great impact on the fundamental study of skyrmion physics, as it investigates the



possible extensive controls on the skyrmions in centrosymmetric systems, making this topic more interesting.

The findings within the field are undeniably intriguing, yet numerous technical and experimental limitations hinder our ability to realize some of the key ideas on the present subject. Specifically, the real-space observation of skyrmions via Transmission Electron Microscopy (TEM) is impeded by laborious sample preparation techniques, especially when we always start with polycrystalline samples. In addition, TEM lamellas, typically less than 100 nm thick, are susceptible to bending during polishing or handling of the TEM lamella, further complicating the observation process.

Although skyrmions in centrosymmetric systems exhibit higher tunability, their stability, often determined by potential barriers, is compromised due to the absence of symmetry breaking. Consequently, external perturbations can readily manipulate or destabilize the skyrmion state in such systems. The challenge lies in identifying centrosymmetric systems that strike a delicate balance between stability and tunability for practical applications.

Despite proposals suggesting the potential of different helicity skyrmions for qubit formation, the practicality of effectively controlling the trajectories of skyrmions with varying helicity remains exceedingly challenging.

Although some literature discusses the dynamics of dipolar skyrmions, their effectiveness in dynamic applications remains elusive. However, certain studies indicate that applied currents can induce helicity changes and topological transformations in dipolar-stabilized skyrmions, offering glimpses into their potential dynamical behavior.

The larger size of dipolar-stabilized skyrmions presents a formidable challenge in the formation of racetrack memory, complicating efforts to integrate these skyrmions into practical memory devices.

# References

- [1] Mario Norberto Baibich et al., *Physical review letters*, **61**, 2472 (1988).
- [2] Grünberg Binasch et al., *Physical review B*, **39**, 4828 (1989).
- [3] Michel Julliere, *Physics letters A*, **54**, 225–226 (1975).
- [4] Stuart SP Parkin, Masamitsu Hayashi, and Luc Thomas, *Science*, **320**, 190–194 (2008).
- [5] João Sampaio et al., *Nature nanotechnology*, **8**, 839–844 (2013).
- [6] Riccardo Tomasello et al., *Scientific reports*, **4**, 1–7 (2014).
- [7] Zhipeng Hou et al., *Advanced Materials*, **29**, 1701144 (2017).
- [8] Xiuzhen Yu et al., *Proceedings of the National Academy of Sciences*, **109**, 8856–8860 (2012).
- [9] XZ Yu et al., *Nature Communications*, **5**, 1–7 (2014).
- [10] Wenhong Wang et al., *Advanced Materials*, **28**, 6887–6893 (2016).
- [11] Xiaofei Xiao et al., *Applied Physics Letters*, **114**, 142404 (2019).
- [12] Shulan Zuo et al., *Advanced Materials*, **33**, 2103751 (2021).
- [13] Takashi Kurumaji et al., *Science*, **365**, 914–918 (2019).
- [14] Max Hirschberger et al., *Nature communications*, **10**, 1–9 (2019).
- [15] Nguyen Duy Khanh et al., *Nature Nanotechnology*, **15**, 444–449 (2020).
- [16] Rina Takagi et al., *Nature communications*, **13**, 1–7 (2022).

- [17] T Nagamiya, S Tomiyoshi, and Y Yamaguchi, *Solid State Communications*, **42**, 385–388 (1982).
- [18] Olga Meshcheriakova et al., *Physical review letters*, **113**, 087203 (2014).
- [19] RJ Elliott and FA Wedgwood, *Proceedings of the Physical Society (1958-1967)*, **84**, 63 (1964).
- [20] Sebastian Muhlbauer et al., *Science*, **323**, 915–919 (2009).
- [21] XZ Yu et al., *Nature*, **465**, 901–904 (2010).
- [22] István Kézsmárki et al., *Nature materials*, **14**, 1116–1122 (2015).
- [23] Naoto Nagaosa et al., *Reviews of modern physics*, **82**, 1539 (2010).
- [24] A Neubauer et al., *Physical review letters*, **102**, 186602 (2009).
- [25] Joseph E Avron, Daniel Osadchy, and Ruedi Seiler, *Physics today*, **56**, 38–42 (2003).
- [26] Ya M Blanter, Moisei I Kaganov, and DV Posvyanskii, *Physics-Uspekhi*, **38**, 203 (1995).
- [27] Arnold Markovich Kosevich, BA Ivanov, and AS Kovalev, *Physics Reports*, **194**, 117–238 (1990).
- [28] N David Mermin, *Reviews of Modern Physics*, **51**, 591 (1979).
- [29] J Ping Liu, Zhidong Zhang, and Guoping Zhao. *Skyrmions: topological structures, properties, and applications*. CRC Press, 2016.
- [30] Karin Everschor-Sitte and Matthias Sitte, *Journal of Applied Physics*, **115**, 172602 (2014).
- [31] T. H. R. Skyrme and Basil Ferdinand Jamieson Schonland, *Proceedings of the Royal Society of London. Series A. Mathematical and Physical Sciences*, **260**, 127–138 (1961).
- [32] Tony Hilton Royle Skyrme, *Nuclear Physics*, **31**, 556–569 (1962).

- [33] AN Bogdanov and D Yablonskii, *Zh. Eksp. Teor. Fiz*, **95**, 182 (1989).
- [34] A Bogdanov and A Hubert, *Journal of magnetism and magnetic materials*, **138**, 255–269 (1994).
- [35] Ulrich K Roessler, AN Bogdanov, and C Pfleiderer, *Nature*, **442**, 797–801 (2006).
- [36] XZ Yu et al., *Nature communications*, **3**, 1–6 (2012).
- [37] Wanjun Jiang et al., *Science*, **349**, 283–286 (2015).
- [38] XZ Yu et al., *Nature materials*, **10**, 106–109 (2011).
- [39] Shinichiro Seki et al., *Science*, **336**, 198–201 (2012).
- [40] Constance Moreau-Luchaire et al., *Nature nanotechnology*, **11**, 444–448 (2016).
- [41] Anjan Soumyanarayanan et al., *Nature materials*, **16**, 898–904 (2017).
- [42] Abhay K Srivastava et al., *Advanced Materials*, **32**, 1904327 (2020).
- [43] Bei Ding et al., *Nano Letters*, **20**, 868–873 (2019).
- [44] Ajaya K Nayak et al., *Nature*, **548**, 561–566 (2017).
- [45] Subir Sen et al., *Physical Review B*, **99**, 134404 (2019).
- [46] Jagannath Jena et al., *Nano letters*, **20**, 59–65 (2019).
- [47] Kosuke Karube et al., *Nature Materials*, **20**, 335–340 (2021).
- [48] Y Fujishiro et al., *Nature communications*, **10**, 1–8 (2019).
- [49] XZ Yu et al., *Nature*, **564**, 95–98 (2018).
- [50] Yang Gao et al., *Advanced Materials*, **32**, 2005228 (2020).
- [51] Zhuolin Li et al., *Nature communications*, **12**, 5604 (2021).
- [52] Xiaowei Lv et al., *ACS nano*, **16**, 19319–19327 (2022).

- 
- [53] Brian W Casas et al., *Advanced Materials*, 2212087 (2023).
  - [54] Xiuzhen Yu et al., *Advanced Materials*, 2306441 (2023).
  - [55] Mathias Getzlaff. *Fundamentals of magnetism*. Springer Science & Business Media, 2007.
  - [56] Stephen Blundell. *Magnetism in condensed matter*. 2003.
  - [57] John MD Coey. *Magnetism and magnetic materials*. Cambridge university press, 2010.
  - [58] Ralph Skomski. *Simple models of magnetism*. Oxford university press, 2008.
  - [59] BD Cullity and CD Graham, *New Jersey*, (2009).
  - [60] TCEP Squier. *Wohlfarth-Handbook of Magnetic Materials, Volume*. 1986.
  - [61] RL Stamps et al., *Journal of applied physics*, **81**, 4751–4753 (1997).
  - [62] Holger Stillrich et al., *Journal of Applied Physics*, **105**, (2009).
  - [63] Tsuyoshi Okubo, Sungki Chung, and Hikaru Kawamura, *Physical review letters*, **108**, 017206 (2012).
  - [64] Souvik Paul et al., *Nature communications*, **11**, 1–12 (2020).
  - [65] Naoto Nagaosa and Yoshinori Tokura, *Nature nanotechnology*, **8**, 899–911 (2013).
  - [66] Xiuzhen Yu et al., *Advanced Materials*, **29**, 1603958 (2017).
  - [67] Christina Psaroudaki and Christos Panagopoulos, *Physical Review Letters*, **127**, 067201 (2021).
  - [68] Jing Xia et al., *Physical Review Letters*, **130**, 106701 (2023).
  - [69] EH Hall. *Am. J. Math.* 1879.
  - [70] Qi Wang et al., *Physical Review B*, **94**, 075135 (2016).
  - [71] Hiroaki Tanaka et al., *Physical Review B*, **101**, 161114 (2020).

- [72] Yihao Wang et al., *Physical Review B*, **96**, 134428 (2017).
- [73] Qi Wang et al., *Nature communications*, **9**, 1–8 (2018).
- [74] Kyoo Kim et al., *Nature materials*, **17**, 794–799 (2018).
- [75] Hang Li et al., *Applied Physics Letters*, **114**, 192408 (2019).
- [76] Yasufumi Araki, *Annalen der Physik*, **532**, 1900287 (2020).
- [77] Kentaro Nomura and Daichi Kurebayashi, *Physical review letters*, **115**, 127201 (2015).
- [78] Daichi Kurebayashi and Kentaro Nomura, *Physical Review Applied*, **6**, 044013 (2016).
- [79] Pascal Puphal et al., *Physical review letters*, **124**, 017202 (2020).
- [80] Zhuolin Li et al., *Advanced Materials*, 2211164 (2023).
- [81] Yuki Shiomi. *Anomalous and Topological Hall Effects in Itinerant Magnets*. Springer Science & Business Media, 2013.
- [82] EH Hall, *Philos. Mag*, **12**, 157–172 (1881).
- [83] Emerson M Pugh and TW Lippert, *Physical Review*, **42**, 709 (1932).
- [84] Yugui Yao et al., *Physical review letters*, **92**, 037204 (2004).
- [85] Robert Karplus and JM Luttinger, *Physical Review*, **95**, 1154 (1954).
- [86] Michael Victor Berry, *Proceedings of the Royal Society of London. A. Mathematical and Physical Sciences*, **392**, 45–57 (1984).
- [87] Ming-Che Chang and Qian Niu, *Physical Review B*, **53**, 7010 (1996).
- [88] Ganesh Sundaram and Qian Niu, *Physical Review B*, **59**, 14915 (1999).
- [89] Satya N Guin et al., *Advanced Materials*, **33**, 2006301 (2021).
- [90] Enke Liu et al., *Nature physics*, **14**, 1125–1131 (2018).
- [91] Kiran Kumar Vudya Sethu, *vol. Belgium*, (2017).

- 
- [92] Jan Smit, *Phys. Rev. B*, **8**, 2349 (1973).
  - [93] J Smit, *The Theory of Atomic Collisions*, (1964).
  - [94] Luc Berger, *Physical Review B*, **2**, 4559 (1970).
  - [95] R Schad et al., *Journal of Physics: Condensed Matter*, **10**, 6643 (1998).
  - [96] T Miyasato et al., *Physical review letters*, **99**, 086602 (2007).
  - [97] Lingling Gao et al., *Applied Physics Letters*, **119**, (2021).
  - [98] Hidemi Toyosaki et al., *Nature materials*, **3**, 221–224 (2004).
  - [99] Amalio Fernández-Pacheco et al., *Physical Review B*, **77**, 100403 (2008).
  - [100] Deepak Venkateshvaran et al., *Physical Review B*, **78**, 092405 (2008).
  - [101] Xiong-Jun Liu, Xin Liu, and Jairo Sinova, *Physical Review B*, **84**, 165304 (2011).
  - [102] Yuan Tian, Li Ye, and Xiaofeng Jin, *Physical review letters*, **103**, 087206 (2009).
  - [103] Stephen L Adler, *Physical Review*, **177**, 2426 (1969).
  - [104] John Stewart Bell and Roman W Jackiw, *Nuovo cimento*, **60**, 47–61 (1969).
  - [105] Xiaochun Huang et al., *Physical Review X*, **5**, 031023 (2015).
  - [106] Jun Xiong et al., *Science*, **350**, 413–416 (2015).
  - [107] Chandra Shekhar et al., *Proceedings of the National Academy of Sciences*, **115**, 9140–9144 (2018).
  - [108] NP Ong and Sihang Liang, *Nature Reviews Physics*, **3**, 394–404 (2021).
  - [109] Yanglin Zhu et al., *Physical Review B*, **101**, 161105 (2020).
  - [110] Linda Ye et al., *Nature*, **555**, 638–642 (2018).
  - [111] Seonghoon Woo et al., *Nature communications*, **8**, 15573 (2017).

- [112] Daichi Kurebayashi and Kentaro Nomura, *Scientific reports*, **9**, 5365 (2019).
- [113] Joseph I Goldstein et al. *Scanning electron microscopy and X-ray microanalysis*. Springer, 2017.
- [114] Tim Maitland and Scott Sitzman, *Scanning microscopy for nanotechnology: techniques and applications*, 41–75 (2007).
- [115] Angus J Wilkinson and T Ben Britton, *Materials today*, **15**, 366–376 (2012).
- [116] Adam J Schwartz et al. *Electron backscatter diffraction in materials science*. Vol. 2. Springer, 2009.
- [117] Bernard Dennis Cullity. *Elements of X-ray Diffraction*. Addison-Wesley Publishing, 1956.
- [118] Richard J Harrison, *Reviews in mineralogy and geochemistry*, **63**, 113–143 (2006).
- [119] Helmut Kohl and Ludwig Reimer, *Springer Series in Optical Sciences*, **36**, (2008).
- [120] Li-cong Peng et al., *Chinese physics B*, **27**, 066802 (2018).
- [121] L Eichenberger, B Malaman, and JH Huang, *Journal of Applied Physics*, **116**, (2014).
- [122] Takashi Tonegawa, *Journal of the Physical Society of Japan*, **17**, 1398–1401 (1962).
- [123] Sk Jamaluddin et al., *Advanced Functional Materials*, **29**, 1901776 (2019).
- [124] Licong Peng et al., *Applied Physics Letters*, **113**, 142408 (2018).
- [125] James C Loudon et al., *Advanced Materials*, **31**, 1806598 (2019).
- [126] David B Williams et al. *The transmission electron microscope*. Springer, 1996.
- [127] SV Andreev et al., *Journal of alloys and compounds*, **260**, 196–200 (1997).



- 
- [128] Yaodong Wu et al., *Applied Physics Letters*, **118**, 122406 (2021).
- [129] Wensen Wei et al., *Advanced Materials*, **33**, 2101610 (2021).
- [130] Licong Peng et al., *Nature nanotechnology*, **15**, 181–186 (2020).
- [131] Yaodong Wu et al., *Applied Physics Letters*, **119**, (2021).
- [132] Zhipeng Hou et al., *Advanced Science*, **10**, 2206106 (2023).
- [133] A Szytuła et al., *Journal of Magnetism and Magnetic Materials*, **25**, 176–186 (1981).
- [134] Yurong You et al., *Intermetallics*, **106**, 88–93 (2019).
- [135] Elizabeth Decolvenaere et al., *Physical Review B*, **96**, 165109 (2017).
- [136] E Şaşıoğlu, LM Sandratskii, and P Bruno, *Physical Review B*, **77**, 064417 (2008).
- [137] Zhu-Pei Shi, Peter M Levy, and John L Fry, *Physical Review B*, **49**, 15159 (1994).
- [138] Adam A Aczel et al., *Physical Review B*, **88**, 014413 (2013).
- [139] Joya A Cooley et al., *Physical Review Materials*, **4**, 044405 (2020).
- [140] JL Wang et al., *Journal of Applied Physics*, **104**, 103911 (2008).
- [141] JL Wang et al., *Journal of Physics: Condensed Matter*, **25**, 386003 (2013).
- [142] Olivier Isnard and Eder J Kinast, *Engineering*, **6**, 154–158 (2020).
- [143] Fang Yuan et al., *Journal of Solid State Chemistry*, **257**, 1–8 (2018).
- [144] R Welter et al., *Journal of alloys and compounds*, **218**, 204–215 (1995).
- [145] Yangkun He et al., *Applied Physics Letters*, **116**, 102404 (2020).
- [146] Zhan Wang et al., *Applied Physics Letters*, **122**, (2023).
- [147] Simon R Larsen et al., *Inorganic Chemistry*, **61**, 17673–17681 (2022).

- 
- [148] Mai Komabuchi et al., *Journal of Magnetism and Magnetic Materials*, **498**, 166115 (2020).
- [149] Mai Komabuchi et al., *Physical Review B*, **100**, 094406 (2019).
- [150] Willie Sucksmith and Jo E Thompson, *Proceedings of the Royal Society of London. Series A. Mathematical and Physical Sciences*, **225**, 362–375 (1954).
- [151] RM Grechishkin et al., *IEEE Transactions on Magnetics*, **53**, 1–4 (2017).
- [152] Li Huai-Shan and Juang Rui-Wang, *Journal of magnetism and magnetic materials*, **117**, 29–32 (1992).
- [153] MI Bartashevich et al., *Physica B: Condensed Matter*, **183**, 369–378 (1993).
- [154] EA Tereshina and AV Andreev, *Intermetallics*, **18**, 641–648 (2010).
- [155] N Scheludko, *Journal of magnetism and magnetic materials*, **117**, 138–140 (1992).
- [156] Xichao Zhang et al., *Nature communications*, **8**, 1717 (2017).
- [157] Xiaoyan Yao, Jun Chen, and Shuai Dong, *New Journal of Physics*, **22**, 083032 (2020).
- [158] Yuan Yao et al., *nature communications*, **13**, 5991 (2022).
- [159] Jialiang Jiang et al., *Advanced Functional Materials*, 2304044 (2023).
- [160] Prineha Narang, Christina AC Garcia, and Claudia Felser, *Nature Materials*, **20**, 293–300 (2021).
- [161] J Hu et al., *Physical Review B*, **95**, 205134 (2017).
- [162] YH Kwan et al., *Physical Review Research*, **2**, 012055 (2020).
- [163] Jin Hu et al., *Physical Review B*, **97**, 155101 (2018).
- [164] J Klotz et al., *Physical Review B*, **93**, 121105 (2016).

- 
- [165] Weiyao Zhao et al., *npj Quantum Materials*, **4**, 56 (2019).
  - [166] AA Taskin and Yoichi Ando, *Physical Review B*, **80**, 085303 (2009).
  - [167] Max Hirschberger et al., *Nature materials*, **15**, 1161–1165 (2016).
  - [168] Junli Zhang et al., *New Journal of Physics*, **23**, 083041 (2021).
  - [169] Nisha Shahi et al., *Physical Review B*, **106**, 245137 (2022).
  - [170] Cheng Zhang et al., *Journal of Applied Physics*, **134**, (2023).
  - [171] Peigang Li et al., *Nature communications*, **11**, 3476 (2020).
  - [172] Jianlei Shen et al., *Advanced Functional Materials*, **30**, 2000830 (2020).
  - [173] Jie Chen et al., *Applied Physics Letters*, **118**, (2021).
  - [174] A Husmann and LJ Singh, *Physical Review B*, **73**, 172417 (2006).
  - [175] Jie Chen et al., *NPG Asia Materials*, **15**, 34 (2023).
  - [176] FL Zeng et al., *Physical review letters*, **125**, 097201 (2020).
  - [177] NJ Ghimire et al., *Physical Review Materials*, **2**, 081201 (2018).
  - [178] Cai-Zhen Li et al., *Nature communications*, **6**, 10137 (2015).